KIT SCIENTIFIC REPORTS 7634

Results of the QUENCH-16 Bundle Experiment on Air Ingress

J. Stuckert, M. Große, Z. Hózer, M. Steinbrück

KIT Scientific Publishing

J. Stuckert, M. Große, Z. Hózer, M. Steinbrück

Results of the QUENCH-16 Bundle Experiment on Air Ingress

Karlsruhe Institute of Technology
KIT SCIENTIFIC REPORTS 7634

Results of the QUENCH-16 Bundle Experiment on Air Ingress

by
J. Stuckert
M. Große
Z. Hózer
M. Steinbrück

KIT Scientific Publishing

Report-Nr. KIT-SR 7634

Hinweis
Die vorliegende wissenschaftliche Kurzdarstellung wurde im Auftrag
des Umweltministeriums Baden-Württemberg durchgeführt.
Die Verantwortung für den Inhalt dieser Veröffentlichung liegt bei den Autoren.

Impressum

Karlsruher Institut für Technologie (KIT)
KIT Scientific Publishing
Straße am Forum 2
D-76131 Karlsruhe
www.ksp.kit.edu

KIT – Universität des Landes Baden-Württemberg und
nationales Forschungszentrum in der Helmholtz-Gemeinschaft

Diese Veröffentlichung ist im Internet unter folgender Creative Commons-Lizenz
publiziert: http://creativecommons.org/licenses/by-nc-nd/3.0/de/

KIT Scientific Publishing 2013
Print on Demand

ISSN 1869-9669
ISBN 978-3-7315-0008-7

Zusammenfassung

Das Experiment QUENCH-16 mit Lufteinbruch wurde im Juli 2011 in der QUENCH-Anlage mit einem elektrisch beheizten 21-Stab Bündel durchgeführt. Der Versuch fand im Rahmen des von der EU gesponserten LACOMECO Programms statt; er wurde von AEKI Budapest vorgeschlagen und in Kooperation mit weiteren Institutionen (PSI, EdF, GRS) geplant.

QUENCH-16 war der zweite Versuch mit Lufteinbruchphase im Rahmen des QUENCH Programms. Im Unterschied zu QUENCH-10 waren bei QUENCH-16 1) die während der Voroxidationsphase in Dampf gebildete Oxidschicht deutlich geringer, 2) die Sauerstoffmangelphase während des Lufteinbruchs signifikant länger und 3) die Temperatur bei der Initiierung des Flutens geringer. Trotzdem wurde während des Flutens signifikante Temperatureskalation gemessen, verbunden mit der Freisetzung von deutlich größeren Mengen an Wasserstoff, verglichen mit der Quench-Phase des QUENCH-10-Tests.

In metallographischen Nachuntersuchungen des Bündels, und insbesondere auch der während des Versuchs gezogenen Eckstäbe, wurde die Bildung von Zirkoniumnitrid über weite Bündelbereiche beobachtet. Diese ZrN Phasen wurden vorzugsweise während der Sauerstoffmangelphase gebildet. Während des Flutens des Bündels wurde ein Großteil der Nitride wieder oxidiert, was zur Bildung von extrem porösen und somit nicht-schützenden Oxidschichten geführt hat. Die erhöhte Wasserstoffproduktion während des Flutens hängt ursächlich mit dem Lufteinbruch zusammen und wurde verursacht durch 1) die schnelle Oxidation von ZrN, 2) die Reaktion von Zirkonium mit Dampf, der durch die nichtschützende poröse Oxidschicht zum Metall gelangt und 3) die Oxidation von Metallschmelze.

Abstract

The out-of-pile bundle experiment QUENCH-16 on air ingress was conducted in the electrically heated 21-rod QUENCH facility at KIT in July 2011. It was proposed by AEKI Budapest and performed in the framework of the EC supported LACOMECO program. The test scenario was based on coordinated planning analyses by PSI, EdF and GRS.

The primary aims were to examine the oxidation of the Zircaloy-4 claddings in air following a limited pre-oxidation in steam, and to achieve a long period of oxygen starvation to promote interaction with the nitrogen. QUENCH-16 was thus a companion test to the earlier air ingress experiment, QUENCH-10, which was performed with strongly pre-oxidized bundle. Unlike QUENCH-10, significant temperature escalation and intensive hydrogen release were observed during the reflood phase.

Post-test investigations of bundle cross sections reveal many residual nitride traces at various elevations. The nitrides were formed during the oxygen starvation stage of air ingress. The upper oxide scales above nitrides have a porous structure due to re-oxidation of nitrides during reflood. Under this outer scale the relative thick oxide layer was formed during reflood. At lower bundle elevations frozen partially oxidized melt was detected, relocated from upper elevations. Three contributors for intensive hydrogen production during reflood were identified: 1) re-oxidation of nitrides, 2) secondary oxidation of cladding metal by steam penetrated through the porous re-oxidized scales and 3) melt oxidation.

Content

Introduction 1

1 Test facility 3

2 Instrumentation and data acquisition 5

3 Test performance 7

3.1 Test conduct and results of on-line measurements 7

3.2 Corner rods withdrawn from the bundle 9

3.3 Neutron radiography examinations of corner rods 9

4 Posttest investigations 10

4.1 Metallographic examination of corner rods 10

4.2 Videoscope inspection 11

4.3 Metallographic examination of bundle cross sections 11

5 Estimation of hydrogen release by different oxidation mechanisms 13

5.1 Melt oxidation 13

5.2 Oxidation of solid metal cladding 13

5.3 Oxidation of nitrides during reflood 14

6 Summary 15

Acknowledgements 16

References 16

List of Tables

Table 1: QUENCH test matrix

Table 2: Design characteristics of the QUENCH-16 test bundle

Table 3: Main characteristics of the ZrO_2 pellet material, yttria-stabilized (type FZY)

Table 4: QUENCH-16; Electrical resistances of rods [mΩ]

Table 5: Properties of zirconia fiber insulating boards

Table 6: List of instrumentation for the QUENCH-16 test

Table 7: QUENCH-16; map of TFS and TCRC thermocouples.

Table 8: Diameters of the materials used for the QUENCH high-temperature thermocouples

Table 9: Main characteristics of the HfO2 thermocouple insulator

Table 10: QUENCH-16; Failure of thermocouples

Table 11: QUENCH-16; Sequence of events

Table 12: QUENCH-16; Water/steam balance

Table 13: Cross sections of the QUENCH-16 test bundle for metallographic examination

Table 14: Thickness of α-Zr(O)- and prior β-Zr-layers at four circumferential positions (in µm)

Table 15: Thickness of α-Zr(O)- and prior β-Zr-layers averaged circumferentially (in µm)

Table 16: Thickness of outer and inner oxide layers at four circumferential positions (in µm)

Table 17: Thickness of outer and inner oxide layers averaged circumferentially (in µm)

Table 18: Thickness of outer secondary oxide layer averaged for eight circumferential positions (in µm)

Table 19: Estimated contribution mechanisms for hydrogen release

List of Figures

Fig. 1: QUENCH facility - main components.

Fig. 2: Flow diagram of the QUENCH test facility.

Fig. 3: QUENCH facility - containment and test section.

Fig. 4: QUENCH-16; Test section with flow lines.

Fig. 5: QUENCH-16; Fuel rod simulator bundle (cross section) including rod type indications.

Fig. 6: QUENCH-16; Heated fuel rod simulator.

Fig. 7: QUENCH-16; Unheated fuel rod simulator.

Fig. 8: QUENCH-16; Test bundle; TC instrumentation and rod designation (top view).

Fig. 9: Axial temperature measurement locations in the QUENCH test section.

Fig. 10: QUENCH-16; High-temperature thermocouple.

Fig. 11: QUENCH-16; Concept for TC fastening at the test rod.

Fig. 12: QUENCH-16; Arrangement of the thermocouples inside the corner rods.

Fig. 13: QUENCH Facility; H_2 measurement with the GAM 300 Mass spectrometer.

Fig. 14: Mass spectrometer sampling position at the off-gas pipe of the QUENCH test facility.

Fig. 15: QUENCH-16; Mounting of high temperature thermocouples.

Fig. 16: QUENCH-16; Test conduct showing electric power input and selected temperatures.

Fig. 17: QUENCH-16; Temperatures measured by (TFS 4/1) and shroud (TSH 1/0) thermocouples at -250 mm elevation.

Fig. 18: QUENCH-16; Temperatures measured by TFS 6/2 thermocouples at -150 mm elevation.

Fig. 19: QUENCH-16; Temperatures measured by rod cladding (TFS) and shroud (TSH 3/180) thermocouples at -50 mm elevation.

Fig. 20: QUENCH-16; Temperatures measured by rod cladding (TFS) and shroud (TSH) thermocouples at 50 mm elevation.

Fig. 21: QUENCH-16; Temperatures measured by rod cladding (TFS) and shroud (TSH) thermocouples at 150 mm elevation.

Fig. 22: QUENCH-16; Temperatures measured by rod cladding (TFS) and shroud (TSH) thermocouples at 250 mm elevation.

Fig. 23: QUENCH-16; Temperatures measured by rod cladding (TFS and TCR 7) and shroud (TSH) thermocouples at 350 mm elevation.

Fig. 24: QUENCH-16; Temperatures measured by rod cladding (TFS) thermocouples at 450 mm elevation.

Fig. 25: QUENCH-16; Temperatures measured by rod cladding (TFS and TCR) and shroud (TSH) and thermocouples at 550 mm elevation.

Fig. 26: QUENCH-16; Temperatures measured by rod cladding (TFS) and shroud (TSH) and centerline (TCRC 10) thermocouples at 650 mm elevation.

Fig. 27: QUENCH-16; Temperatures measured by rod cladding (TFS) and shroud (TSH) thermocouples at 750 mm elevation.

Fig. 28: QUENCH-16; Temperatures measured by rod cladding (TFS and TCR), shroud (TSH), and corner rod internal (TIT C/12) thermocouples at 850 mm elevation.

Fig. 29: QUENCH-16; Temperatures measured by rod cladding (TFS and TCR), shroud (TSH), corner rod internal (TIT A/13) and central rod centerline (TCRC 13) thermocouples at 950 mm elevation.

Fig. 30: QUENCH-16; Temperatures measured by rod cladding (TFS) and shroud (TSH) thermocouples at 1050 mm elevation.

Fig. 31: QUENCH-16; Temperatures measured by rod cladding (TFS) and shroud (TSH) thermocouples at 1150 mm elevation.

Fig. 32: QUENCH-16; Temperatures measured by rod cladding (TFS) and shroud (TSH) thermocouples at 1250 mm elevation.

Fig. 33: QUENCH-16; Temperature measured by rod cladding thermocouples TFS 13/17 at 1350 mm elevation.

Fig. 34: QUENCH-16; Overview of the TFS, top, and TSH temperatures, bottom.

Fig. 35: QUENCH-16; Axial temperature profile TFS inner ring and TFS outer ring together with TSH, left, and axial temperature profile of all TFS, right, at 6300 s (intermediate cooling).

Fig. 36: QUENCH-16; Axial temperature profile TFS inner ring and TFS outer ring together with TSH, left, and axial temperature profile of all TFS, right, at 11330 s (end of air ingress).

Fig. 37: QUENCH-16; Consumption of oxygen and nitrogen during air ingress.

Fig. 38: QUENCH-16; Residual steam flow and corresponding hydrogen release.

Fig. 39: QUENCH-16; Quench water mass flow rate (F 104), top, measurement of collapsed water level (L 501), center, off-gas flow rate (F 601), bottom.

Fig. 40: QUENCH-16; Argon and system pressure.

Fig. 41: QUENCH-16; Condensed water in the collection vessel.

Fig. 42: QUENCH-16; Indication of rod failure by Kr measurement at MS.

Fig. 43: QUENCH-16; Hydrogen production during reflood.

Fig. 44: QUENCH-16; withdrawn corner rods

Fig. 45: QUENCH-16; Photographs of corner rod B withdrawn from the bundle before air ingress, 300-800 mm elevation.

Fig. 46: QUENCH-16; Photographs of corner rod B withdrawn from the bundle before air ingress, 800-1100 mm elevation.

Fig. 47: QUENCH-16; Photographs of corner rod D withdrawn from the bundle before quenching, 200-700 mm elevation.

Fig. 48: QUENCH-16; Photographs of corner rod D withdrawn from the bundle before quenching, 700-1100 mm elevation.

Fig. 49: QUENCH-16; Photographs of corner rod A withdrawn from the bundle after the test, 200-550 mm elevation.

Fig. 50: QUENCH-16; axial distribution of oxide layer thickness for corner rods B (withdrawn before air ingress) and D (withdrawn before quench). Values for rods D and A are calculated according to the Pilling-Bedworth coefficient on the basis of residual metal.

Fig. 51: QUENCH-16; metallography of corner rod B withdrawn before air ingress.

Fig. 52: QUENCH-16; formation of nitrides for corner rod D (withdrawn before reflood initiation) at different bundle elevations with indication of temperature reached on the withdrawal time point.

Fig. 53: QUENCH-16; metallography of corner rod A (tube up to 950 mm) withdrawn after the test.

Fig. 54: Neutron radiograph of rod B (axial range: 365 < z < 395 mm)

Fig. 55: Neutron radiograph of rod D (axial range: 355 < z < 385 mm)

Fig. 56: Neutron radiograph of rod A (axial range: 210 < z < 480 mm)

Fig. 57: QUENCH-16; Post-test visual investigations by endoscope introduced at the position of the corner rod B: front view.

Fig. 58: QUENCH-16; Post-test visual investigations by endoscope introduced at the position of the corner rod B: side view.

Fig. 59: QUENCH-16; Post-test visual investigations by endoscope introduced at the position of the corner rod B: side view 2.

Fig. 60: QUENCH-16; Post-test visual investigations by endoscope introduced at the position of the corner rod D: front view

Fig. 61: QUENCH-16; Post-test visual investigations by endoscope introduced at the position of the corner rod D: side view.

Fig. 62: QUENCH-16; Post-test visual investigations by endoscope introduced at the position of the corner rod D: side view 2.

Fig. 63: QUENCH-16; Bundle (with shroud and partially ZrO2 insulation) withdrawn from cooling jacket.

Fig. 64: QUENCH-16; middle part of bundle (with shroud and ZrO2) withdrawn from cooling jacket.

Fig. 65: QUENCH-16; Bundle (with shroud and partially ZrO2 insulation) withdrawn from cooling jacket.

Fig. 66: QUENCH-16; middle part of bundle after dismounting of ZrO2 insulation (deleted together with shroud parts).

Fig. 67: QUENCH-16; Bundle cross sections at 80 mm, 100 mm, 230 mm and 250 mm.

Fig. 68: QUENCH-16; Bundle cross sections at 330 mm and 350 mm (normal magnification); 430 mm and 450 mm (reduced magnification).

Fig. 69: QUENCH-16; Bundle cross sections at 530 mm, 550 mm, 630 mm and 650 mm (reduced magnification).

Fig. 70: QUENCH-16; Bundle cross sections at 730 mm, 750 mm, 830 mm and 850 mm.

Fig. 71: QUENCH-16; Bundle cross sections at 930 mm, 950 mm, 1030 mm and 1050 mm.

Fig. 72: QUENCH-16; thermocouple TCRC 10 inside the central rod.

Fig. 73: QUENCH-16; Cross section at elevation 250 mm depicting individual test rods 1-6.

Fig. 74: QUENCH-16; Cross section at elevation 250 mm depicting individual test rods 7-12.

Fig. 75: QUENCH-16; Cross section at elevation 250 mm depicting individual test rods 13-18.

Fig. 76: QUENCH-16; Cross section at elevation 250 mm depicting individual test rods 19-21.

Fig. 77: QUENCH-16; cladding structure at 250 mm with melt fragments relocated from upper elevations between pellet and cladding.

Fig. 78: QUENCH-16; EDX analysis of shroud, cladding and relocated melt at elevation 250 mm.

Fig. 79: QUENCH-16; Cross section at elevation 350 mm depicting individual test rods 1-6.

Fig. 80: QUENCH-16; Cross section at elevation 350 mm depicting individual test rods 7-12.

Fig. 81: QUENCH-16; Cross section at elevation 350 mm depicting individual test rods 13-18.

Fig. 82: QUENCH-16; Cross section at elevation 350 mm depicting individual test rods 19-21.

Fig. 83: QUENCH-16; cladding structure of rod #1 at elevation of 350 mm with nitrides (light strips) at the interface between two oxide sub-layers.

Fig. 84: QUENCH-16; cladding structure of internal rods #2 - #9 with outer oxide sub-layer (yellowish by epoxy resin) at elevation of 350 mm.

Fig. 85: QUENCH-16; structure of outer oxide layer with re-oxidized porous sublayer coloured by epoxy resin for claddings at elevation of 350 mm.

Fig. 86: QUENCH-16; structure of inner (concave) surface of shroud at bundle elevation 350 mm.

Fig. 87: QUENCH-16; Frozen melt at elevation 350 mm: not oxidized and oxidized melt.

Fig. 88: QUENCH-16; EDX analysis of shroud, cladding and relocated melt at elevation 350 mm.

Fig. 89: QUENCH-16; Cross section at elevation 450 mm depicting individual test rods 1-6.

Fig. 90: QUENCH-16; Cross section at elevation 450 mm depicting individual test rods 7-12.

Fig. 91: QUENCH-16; Cross section at elevation 450 mm depicting individual test rods 13-18.

Fig. 92: QUENCH-16; Cross section at elevation 450 mm depicting individual test rods 19-21.

Fig. 93: QUENCH-16; cladding structure at elevation 450 mm.

Fig. 94: QUENCH-16; structure of inner (concave) surface of shroud at bundle elevation 450 mm.

Fig. 95: QUENCH-16; Frozen melt at elevation 450 mm: mostly oxidized melt.

Fig. 96: QUENCH-16; Cross section at elevation 550 mm depicting individual test rods 1-6.

Fig. 97: QUENCH-16; Cross section at elevation 550 mm depicting individual test rods 7-12.

Fig. 98: QUENCH-16; Cross section at elevation 550 mm depicting individual test rods 13-18.

Fig. 99: QUENCH-16; Cross section at elevation 550 mm depicting individual test rods 19-21.

Fig. 100: QUENCH-16; cladding structure at 550 mm with two outer ZrO2 sub-layers, frozen molten layer and inner ZrO2-x layer.

Fig. 101: QUENCH-16; Cross section at elevation 650 mm depicting individual test rods 1-6.

Fig. 102: QUENCH-16; Cross section at elevation 650 mm depicting individual test rods 7-12.

Fig. 103: QUENCH-16; Cross section at elevation 650 mm depicting individual test rods 13-18.

Fig. 104: QUENCH-16; Cross section at elevation 650 mm depicting individual test rods 19-21.

Fig. 105: QUENCH-16; strong oxidation of claddings at 650 mm.

Fig. 106: QUENCH-16; Cross section at elevation 750 mm depicting individual test rods 1-6.

Fig. 107: QUENCH-16; Cross section at elevation 750 mm depicting individual test rods 7-12.

Fig. 108: QUENCH-16; Cross section at elevation 750 mm depicting individual test rods 13-18.

Fig. 109: QUENCH-16; Cross section at elevation 750 mm depicting individual test rods 19-21.

Fig. 110: QUENCH-16; cladding structure at 750 mm with significant melt formation.

Fig. 111: QUENCH-16; Cross section at elevation 850 mm depicting individual test rods 1-6.

Fig. 112: QUENCH-16; Cross section at elevation 850 mm depicting individual test rods 7-12.

Fig. 113: QUENCH-16; Cross section at elevation 850 mm depicting individual test rods 13-18.

Fig. 114: QUENCH-16; Cross section at elevation 750 mm depicting individual test rods 19-21.

Fig. 115: QUENCH-16; sequence of structure elements for different rods of elevation 850 mm.

Fig. 116: QUENCH-16; Cross section at elevation 950 mm depicting individual test rods 1-6.

Fig. 117: QUENCH-16; Cross section at elevation 950 mm depicting individual test rods 7-12.

Fig. 118: QUENCH-16; Cross section at elevation 950 mm depicting individual test rods 13-18.

Fig. 119: QUENCH-16; Cross section at elevation 950 mm depicting individual test rods 19-21.

Fig. 120: QUENCH-16; structure of simulator rods at elevation 950 mm: absence of nitrides; formation of axial wedge-shape cracks predetermine the “flowering effect”.

Fig. 121: QUENCH-16; Cross section at elevation 1050 mm depicting individual test rods 1-6.

Fig. 122: QUENCH-16; Cross section at elevation 1050 mm depicting individual test rods 7-12.

Fig. 123: QUENCH-16; Cross section at elevation 1050 mm depicting individual test rods 13-18.

Fig. 124: QUENCH-16; Cross section at elevation 1050 mm depicting individual test rods 19-21.

Fig. 125: QUENCH-16; structure of simulator rods and grid spacer at elevation 1050 mm.

Fig. 126: QUENCH-16; Alpha-phase layer thickness at bundle elevation 250 mm (Cross section QUE-2-250).

Fig. 127: QUENCH-16; Alpha-phase layer thickness at bundle elevation 350 mm (Cross section QUE-3-350).

Fig. 128: QUENCH-16; Alpha-phase layer thickness at bundle elevation 450 mm (Cross section QUE-4-450).

Fig. 129: QUENCH-16; Alpha-phase layer thickness at bundle elevation 550 mm (Cross section QUE-5-550).

Fig. 130: QUENCH-16; Alpha-phase layer thickness at bundle elevation 750 mm (Cross section QUE-7-750).

Fig. 131: QUENCH-16; Alpha-phase layer thickness at bundle elevation 850 mm (Cross section QUE-8-850).

Fig. 132: QUENCH-16; Alpha-phase layer thickness at bundle elevation 950 mm (Cross section QUE-9-950).

Fig. 133: QUENCH-16; Alpha-phase layer thickness at bundle elevation 1050 mm (Cross section QUE-10-1050).

Fig. 134: QUENCH-16; Beta-phase layer thickness at bundle elevation 250 mm (Cross section QUE-2-250).

Fig. 135: QUENCH-16; Beta-phase layer thickness at bundle elevation 350 mm (Cross section QUE-3-350).

Fig. 136: QUENCH-16; Beta-phase layer thickness at bundle elevation 850 mm (Cross section QUE-8-850).

Fig. 137: QUENCH-16; Beta-phase layer thickness at bundle elevation 950 mm (Cross section QUE-9-950).

Fig. 138: QUENCH-16; Beta-phase layer thickness at bundle elevation 1050 mm (Cross section QUE-10-1050).

Fig. 139: QUENCH-16; Oxide layer thickness at bundle elevation 250 mm (Cross section QUE-2-250).

Fig. 140: QUENCH-16; Oxide layer thickness at bundle elevation 350 mm (Cross section QUE-3-350).

Fig. 141: QUENCH-16; Oxide layer thickness at bundle elevation 450 mm (Cross section QUE-4-450).

Fig. 142: QUENCH-16; Oxide layer thickness at bundle elevation 550 mm (Cross section QUE-5-550).

Fig. 143: QUENCH-16; Oxide layer thickness at bundle elevation 650 mm (Cross section QUE-6-650).

Fig. 144: QUENCH-16; Oxide layer thickness at bundle elevation 750 mm (Cross section QUE-7-750).

Fig. 145: QUENCH-16; Oxide layer thickness at bundle elevation 850 mm (Cross section QUE-8-850).

Fig. 146: QUENCH-16; Oxide layer thickness at bundle elevation 950 mm (Cross section QUE-9-950).

Fig. 147: QUENCH-16; Oxide layer thickness at bundle elevation 1050 mm (Cross section QUE-10-1050).

Fig. 148: QUENCH-16; axial distribution of cladding oxidation rate.

Introduction

Air ingress issues have received considerable attention in recent years in view of the likely acceleration of the cladding oxidation, fuel rod degradation, and the release of some fission products, most notable ruthenium. The Paks NPP cleaning tank incident and the accident at Fukushima Daiichi drew attention to the possibility of overheated fuel assemblies becoming exposed to air outside of the reactor.

Experimental and analytical works on air ingress were performed within the EC 4th and 6th Framework Programs [1, 2]. Numerous single effect tests on cladding oxidation in air were performed at ANL [3] (temperatures 300-900°C; alloys Zircaloy-4, ZIRLO, M5), AEKI [4] (temperatures 600-1500°C), IRSN [5] and KIT [6, 7] (temperatures 700-1600°C). The recent OECD/NEA project SFP investigated the performance of full-scale 17x17 PWR assemblies in air with special emphasis on thermal-hydraulic and ignition phenomena [8]. A number of previous out-of-pile bundle air ingress tests have been performed under a range of configurations and oxidizing conditions, namely CODEX AIT-1, AIT-2 with small 9-rod bundles [9], QUENCH-10 with 21-rod strong pre-oxidized bundle [10, 11] and PARAMETER-SF4 with finally molten 19-rod bundle [12]. The accumulated data have demonstrated that air oxidation of cladding is a quite complicated phenomenon governed by numerous processes whose role can depend on the oxidizing conditions, the oxidation history and the details of the cladding material specification. The models for air oxidation do not yet cover the whole range of representative conditions. The main aims of new bundle tests should be the investigation of areas where data were mostly missing.

The QUENCH-16 bundle test was proposed by AEKI (MTA EK / Hungary) in the framework of the EC-sponsored LACOMECO program [13] as part of the collective investigation of air ingress into overheated nuclear fuel assemblies. The experiment focused specifically on the following phenomena:

- air oxidation after rather moderate pre-oxidation in steam;
- slow oxidation and nitriding of cladding in high heated air and transition to rapid oxidation and temperature excursion;
- role of nitrogen under oxygen-starved conditions,
- formation of oxide and nitride layers on the surface of cladding;
- release of hydrogen from oxidized zirconium during air ingress scenario;
- reflooding of the oxidized and nitrided bundle by water, release of nitrogen.

The proposal included a target scenario characterized by:

- a long period of oxygen starvation to promote the occurrence of the above phenomena;
- reflood quench initiated at temperatures well below the melting point of the cladding to provide the opportunity of avoiding a major oxidation, to facilitate post-test inspection of the bundle.

Concerning the second objective, it was realized that avoiding such an excursion could not be guaranteed, especially in the light of previous experiments such as PARAMETER-SF4 which showed clearly how a starvation period can promote an excursion. The outcome would in any case yield valuable data on this phenomenon.

QUENCH-16 was successfully performed on 27 July 2011 in the QUENCH facility at KIT. The facility is well qualified for such kind of large-scale bundle experiments and was approved during long period of operation, during which a lot of experiments with different test parameters were conducted (Table 1). The QUENCH-16 experiment was performed according to a test protocol following the outcome of discussions among the participants and based on coordinated planning analyses by GRS, EDF and PSI using independent simulation tools.

1 Test facility

The main components of the QUENCH test facility are presented in Fig. 1. The test section is enclosed by a safety containment with a wall thickness of 5.6 mm and an inner diameter of 801.8 mm. The facility can be operated in two modes: a forced-convection mode depicted in the flow diagram of Fig. 2 and a boil-off mode. In the forced-convection mode (relevant for QUENCH-16) superheated steam from the steam generator and superheater together with argon as a carrier gas enter the test bundle at the bottom (Figs. 3 and 4). The system pressure in the test section is around 0.2 MPa. The quenching water is injected through a separate line marked “bottom quenching” in Fig. 3.

The argon, the steam and air not consumed, and the hydrogen produced in the zirconium-steam reaction flow from the bundle outlet at the top through a temperature-controlled off-gas pipe to the condenser where the steam is separated from the non-condensable gases. The water cooling circuits for bundle head and off-gas pipe are temperature-controlled to guarantee that the steam/gas temperature is high enough so that condensation at test section outlet and inside the off-gas pipe can be avoided. The temperature at the bundle head is kept at 348 K, and the flow rate of the cooling water is 250 g/s.

The off-gas pipe system (Fig. 14) contains a water-cooled outer jacket with a water flow rate of 370 g/s. The water inlet temperature for the jacket is controlled at 393 K. Between the inner off-gas pipe and inner tube of the cooling jacket there is stagnant off-gas (yellow gap in Fig. 14). The main dimensions of the tubes that make up the off-gas pipe are:

Inner pipe: outer diameter 139.7 mm, wall thickness 4.5 mm, total length 3256 mm, material: stainless steel.
Inner tube of cooling jacket: outer diameter 154 mm, wall thickness 2 mm, material: stainless steel.
Outer tube of cooling jacket: outer diameter 168.3 mm, wall thickness 5 mm; material: stainless steel.

The design characteristics of the test bundle are given in Table 2. The test bundle is made up of 21 fuel rod simulators, each with a length of approximately 2.5 m, and of four corner rods (see cross section in Fig. 5). The fuel rod simulators (Figs. 6 and 7) are held in their positions by five grid spacers, four of Zircaloy-4, and one of Inconel 718 in the lower bundle zone. All test rods, excluding the rod in the bundle center, are heated electrically with tungsten heaters over a length of 1024 mm and are filled with Kr at a pressure of approx. 0.22 MPa. The heated rods (Fig. 6) were connected to a controlled feeding system that compensated minor gas losses and allowed observation of a first cladding failure as well as a progression of rod failure. The rod cladding of the heated and unheated fuel rod simulator is Zircaloy-4 with 10.75 mm outside diameter and 0.725 mm wall thickness (see also Table 2).

Tungsten heating elements of 6 mm diameter are installed in the center of the heated rods and are surrounded by annular ZrO_2 pellets. The physical properties of the ZrO_2 pellets are described in Table 3. The tungsten heaters (chemically clean tungsten) are connected to electrodes made of molybdenum (chemically clean molybdenum) and copper (material 2.1293 with Cr 0.8, Zr 0.08 and rest Cu) at each end of the heater. The molybdenum and copper electrodes are joined by high-frequency/high-temperature brazing under vacuum ($2x10^{-3}$ mbar) using an AuNi 18 powder (particle size <105 µm). The electrical resistance of

internal rod heating system, combined from W heater and Mo-copper electrodes, was measured before (at the end of bundle assembling) and after the test (Table 4). The measured electric resistance of a single heater (W+Mo+Cu sections) is 3.4 mΩ at room temperature. This value increases significantly with temperature. The additional resistance of the external electric circuit between the axial end of the single heater and the connection to the generator (sliding contacts, cables, and bolts) is 1.46 mΩ + 0.22 mΩ = 1.68 mΩ. This value can be taken as constant because the external electric circuit remains at ambient temperature throughout the experiment.

For electrical insulation the surfaces of both types of electrodes are plasma-coated with 0.2 mm ZrO_2. To protect the copper electrodes and the O-ring-sealed wall penetrations against excessive heat they are water-cooled (lower and upper cooling chambers filled with demineralized water). The copper electrodes are connected to the DC electric power supply by means of special sliding contacts at the top and bottom. The maximum total heating power available is 70 kW. The distribution of the electric power within the two groups is as follows: about 40 % of the power is released into the inner rod circuit consisting of eight fuel rod simulators (in parallel connection) and 60 % in the outer rod circuit (12 fuel rod simulators in parallel connection).

The lower boundary for the lower cooling chamber is a sealing plate made of stainless steel with plastic inlays for electrical insulation, sealed toward the system by O-shaped rings. The upper boundary of the lower cooling chamber is a sealing plate of stainless steel. An insulation plate made of plastic (PEEK) forms the top of the upper cooling chamber, and a sealing plate of Al_2O_3, functioning as a heat-protection shield, is the lower boundary of the upper cooling chamber (see Fig. 6).

In the region below the upper Al_2O_3 plate the copper electrode is connected firmly to the cladding. This is done by rotary swaging the cladding onto the electrode. In the swaging region a sleeve of boron nitride is put between electrode and cladding for electrical insulation. The axial position of the fuel rod simulator in the test bundle is fixed by a groove and a locking ring in the top Cu electrodes. Referred to the test bundle the fixing point of the fuel rod simulators is located directly above the upper edge of the upper insulation plate. So, during operation the fuel rod simulators are allowed to expand downwards. Clearance for expansion of the test rods is provided in the region of the lower sealing plate. Also in this region, relative movement between cladding and internal heater/electrode can take place.

The test bundle is surrounded by a 3.05 mm thick shroud (82.8 mm ID) made of Zr 702 with a 34 mm thick ZrO_2 fiber insulation (physical properties are given in Table 5) and an annular cooling jacket made of Inconel 600 (inner tube) and stainless steel (outer tube); see Fig. 5. The annulus between shroud and cooling jacket was filled (after several cycles of degasing) with stagnant argon of 0.22 MPa and was connected to a flow-controlled argon feeding system in order to prevent steam access to the annulus after shroud failure. The 6.7 mm annulus of the cooling jacket is cooled by an argon flow. Above the heated zone, i.e. above the 1024 mm elevation there is no ZrO_2 fiber insulation to allow for higher radial heat losses. This region of the cooling jacket is cooled by a water flow (Figs. 3 and 4). Both the lack of ZrO_2 insulation above the heated region and the water cooling force the axial temperature maximum downward.

Insertion of four corner rods avoids an atypically large flow cross section at the outer positions and hence helps to obtain a rather uniform radial temperature profile. There are four corner rods installed in the bundle. Two of them, i.e. rods “A” and “C” are made of a Zircaloy-4 solid rod Ø 6 mm at the top and a Zircaloy-4 tube (outer Ø 6 mm, inner Ø 4.2 mm) at the bottom and are used for thermocouple instrumentation. The other two rods, i.e. rods “B” and “D” (solid Zircaloy-4 rods of 6 mm diameter) are particularly determined to be withdrawn from the bundle to check the degree of oxidation and hydrogen uptake at specific times. In QUENCH-16 three corner rods were used for analysis of the oxide layer thickness. Rod B was pulled out of the bundle before air ingress, rod D before quenching and rod A was removed after test termination.

2 Instrumentation and data acquisition

For **temperature** measurements the test bundle, shroud, and cooling jackets are equipped with thermocouples at orientations and elevations as illustrated in Fig. 8 and Fig. 9 correspondingly, and listed in Table 6. An overview of the positions of the bundle thermocouples is given in Table 7. There are 40 high-temperature (W/Re) thermocouples in the upper hot bundle region (bundle and shroud thermocouples between elevations 650 and 1350 mm) and 32 low-temperature (NiCr/Ni) thermocouples in the lower “cold” bundle region (bundle and shroud thermocouples between –250 and 550 mm).

The dimensions of the thermocouple components are provided in Table 8, some properties of the thermocouple insulator in Table 9. The thermocouples attached to the outer surface of the rod cladding at elevations between -250 and 1350 mm are designated “TFS” for all heated rods.

In the lower bundle region, i.e. up to 550 mm elevation, NiCr/Ni thermocouples with stainless steel sheath/MgO insulation and an outside diameter of 1.0 mm are used for measurements of the rod cladding and shroud temperatures. The thermocouples in the hot zone and above are high-temperature thermocouples with W5Re/W26Re wires, HfO_2 insulation, and a duplex sheath of tantalum (inside) and Zircaloy (outside) with an outside diameter of about 2.2-2.3 mm (Fig. 10).

The thermocouple attachment technique for the surface-mounted high-temperature TCs is shown in Fig. 11 and Fig. 15. The TC tip is held in place by two clamps of zirconium (0.2 mm thick). As these clamps are prone to oxidation and embrittlement in a steam environment an Ir-Rh wire of 0.25 mm diameter is additionally used in test QUENCH-16. The leads of the thermocouples from the -250 mm to the 850 mm level leave the test section at the bottom whereas the TCs above 850 mm are routed to the top avoiding to route TC cables through the hot zone (see Fig. 9).

Additionally, the cables of shroud thermocouples (designated TSH xx/x “I”) were routed toward outside the shroud insulation to avoid heat transfer from the shroud into the TC cable, apart from the TC junction. The shroud thermocouples are mounted at the outer surface between -250 mm and 1250 mm.

The thermocouples that are installed inside the Zircaloy instrumentation rods at the two corner positions of the bundle (positions A, and C) are designated “TIT” (see Fig. 12). All “TIT” thermocouples are of the high-temperature type. The thermocouples of the cooling jacket (TCI and TCO) are 1 mm NiCr/Ni thermocouples with stainless steel sheath for all levels. The thermocouples of the cooling jacket are installed inside the wall of the inner cooling tube (from -250 mm to 1150 mm, designation “TCI”) and at the outer surface of the outer cooling tube (from -250 mm to 950 mm, designation “TCO”) as illustrated in Fig. 8.

The thermocouples which failed during the experiment are listed in Table 10.

The off-gas including Ar, H_2, O_2, N_2 and steam is analysed by a state-of-the-art mass spectrometer “Balzers GAM300” (Fig. 13) whose sampling tube is connected with the off-gas pipe. The mass spectrometer allows also indicating the failure of rod simulators by detection of Kr release.

The **mass spectrometer** “BALZERS GAM 300“ is a completely computer-controlled quadrupole MS with an 8 mm rod system which allows accurate quantitative measurement of gas concentrations down to about 10 ppm. For the MS measurement a sampling tube is inserted in the off-gas pipe located approx. 2.7 m downstream from the test section outlet (see Fig. 2 and 4). It has several holes at different elevations to guarantee that the sampling of the gas to be analyzed is representative (Fig. 14). To avoid steam condensation in the gas pipes between the sampling position and the MS the temperature of the gas at the MS inlet is controlled by heating tapes to be between 110 and 150 °C (the upper operating temperature of the MS inlet valves). This allows the MS to analyze the steam production rate. Besides, the concentrations of the following species were continuously measured by the mass spectrometer during all test phases: argon, hydrogen, steam, nitrogen, oxygen, and krypton. The fuel rod simulators are filled with krypton which can be used as an indicator for a cladding failure. Additionally, the MS is used to control the atmosphere in the facility, e.g., to monitor the gas composition at the beginning of the test.

The temperature and pressure of the analyzed gas are measured near the inlet valve of the MS. The MS is calibrated for hydrogen, oxygen and nitrogen with well-defined argon/gas mixtures and for steam with mixtures of argon and steam supplied by a Bronkhorst controlled evaporator mixing (CEM) device. The MS off-gas is released into the atmosphere because the amount of hydrogen taken out of the system is negligible. A heated measuring gas pump was used to ensure a continuous flow of the steam-gas mixture from the off-gas pipe to the mass spectrometer.

For the MS device the mass flow rates of the gases of interest are calculated by referring the measured concentrations to the known argon mass flow rate according to equation (1):

$$\dot{m}_i = \frac{M_i}{M_{Ar}} \cdot \frac{C_i}{C_{Ar}} \cdot \dot{m}_{Ar} \qquad (1)$$

with M representing the molecular masses, i the index of the gas, C the concentrations in vol-% and $\dot{m}$ the mass flow rates of the corresponding gases. Instead of argon other gas with known flow rate can be used (e.g. steam, as applied for the quench phase of the QUENCH-16 test due to switch-off the argon as carrier gas).

The data of the main **data acquisition** system and of the mass spectrometer were stored on different computers. All computers were synchronized against each other. The data of the main acquisition system as well as those of the mass spectrometer data were stored at a frequency of 1 Hz, the ones with the MS with approximately 1.1 Hz. The latter were interpolated to 1 Hz for further data processing.

3 Test performance

3.1 Test conduct and results of on-line measurements

The test was performed with a bundle similar to that used in the QUENCH-10. The experience of the QUENCH-10 test provided very valuable information for test preparation and for this reason the QUENCH-16 scenario was specified with the modification of QUENCH-10 scenario. Two important changes were considered in the QUENCH-16 scenario:

• The pre-oxidation period was shortened compared to QUENCH-10 to produce thinner oxide scale on the cladding (100-200 µm instead of 500 µm). The oxidation temperature and power were kept similar to QUENCH-10.

• The air ingress phase lasted longer and the maximum temperature was lower than in QUENCH-10. During the specification of the test conditions it was emphasized that oxygen starvation should be established in the upper part of the bundle. To reach such conditions the electrical power, the air and argon flow rates were reduced. It was proposed to have an average heat-up rate in this phase between 0.1-0.2 K/s.

In summary the QUENCH-16 test was conducted with the following tests phases:

Preparation	Heat-up in a flow of 3.4 g/s superheated steam and 3 g/s argon to peak cladding temperature T_{pct} = 873 K.
Phase I	Stabilization in a flow of 3.4 g/s superheated steam and 3 g/s argon at 873 K; facility checks.
Phase II	Heat-up in a flow of 3.4 g/s superheated steam and 3 g/s argon with 0.1-0.4 K/s to 1300 K during 2300 s
Phase III	Pre-oxidation of the test bundle in a flow of 3.4 g/s superheated steam and 3 g/s argon during 4000 s at temperatures increasing from 1300 K to 1430 K
Phase IV	Intermediate cooling from 1430 K to 1000 K during 1000 s in the same flow of steam and argon.
Phase V	Air ingress and transient heat-up from 1000 K to 1873 K with slow heating rate of 0.2 K/s in a flow of 0.2 g/s of air and 1 g/s argon for 4040 s. Total oxygen consumption during 835 s before end of this phase.
Phase VI	Quenching of the bundle by a flow of 53 g/s of water; argon was switched off. Temperature escalation to 2420 K with intensive hydrogen release.

The detailed sequence of the test events is described in Table 11. Fig. 16 illustrates the phases of test performance. The readings of all cladding and shroud thermocouples are presented in Figs. 17 – 33 separately for each elevation.

In the pre-oxidation phase and following slow cooling phase the claddings were oxidized in superheated steam (3.4 g/s). The maximal ZrO_2 thickness measured at corner rod B withdrawn after phase IV was 130 µm (Fig. 50). In the subsequent air ingress phase, which lasted 4035 s, the steam flow was replaced by 0.2 g/s of air. Fig. 34 presents an overview of thermocouple readings during the end of this and the beginning of quench phases. The change in flow conditions had the immediate effect of reducing the heat transfer so that the temperatures began to rise again. The generally limited rate of temperature increase was the result of a rather low air flow rate, probably not untypical for reactor or spent fuel pool conditions. The faster temperature increase was most marked at the mid elevations of the bundle (Fig. 16 and Fig. 34). As result, the axial temperature maximum was shifted from elevation 950 to 550…750 mm (Figs. 35 – 36). After some time measurements demonstrated gradually an increasing consumption of oxygen, accompanied by acceleration of the temperature increase at certain locations.

Oxygen was completely consumed at about 3200 s after beginning of air ingress (Fig. 37). Shortly before that time, partial consumption of the nitrogen was first observed, indicating local oxygen starvation which promoted the onset of nitriding. Following this, the temperature continued to increase until water injection was initiated when the maximum observed temperature was about 1873 K. Thus there was a period of about 835 s complete oxygen consumption and hence starvation in upper part of the bundle. During this time period the residual steam has reacted with bundle materials, resulting in negligible release of hydrogen (Fig. 38). The total hydrogen release measured before reflood initiation was about *16 g*. The total *uptakes of oxygen and nitrogen* were about ***58*** and ***29 g***, respectively.

Reflood was initiated by injecting 53 g/s of water (Fig. 39). The quench initiation was indicated also with system pressure oscillations (Fig. 40) and sharp increase of condensed water (Fig. 41). Almost immediately after the start of reflood there was a ***temperature excursion*** in the mid to upper regions of the bundle (*500 to 1400 mm*, see Figs. 26 – 34), leading to maximum measured temperatures of about 2420 K. Cooling was established at the hottest location ca. 70 s after the start of injection, but was delayed further at other locations. Reflood progressed rather slowly, perhaps due to the high temperatures and partial degradation, and final quench was achieved after about 500 s. Thereafter the water supply was terminated. The water balance for the whole test is presented in Table 12.

In line with the temperature escalations, a significant quantity of ***hydrogen (128 g)*** was generated during the reflood. Fig. 43 shows two curves for hydrogen release, calculated on the basis of 1) steam flow rate measured by the L701 device, and 2) argon flow rate (measured by the Fm406 gauge) into the bundle through the shroud which failed 40 s after the reflood initiation. There are also indications of *nitrogen release* during the quench phase: ***24 g*** from 29 g consumed during oxygen starvation period were released again due to the oxidation of nitrides (Fig. 37).

3.2 Corner rods withdrawn from the bundle

Three corner rods were withdrawn from the bundle to investigate the degree of oxidation for different phases of the experiment (Fig. 44). Rod B was extracted before air ingress. Its surface has a dark smoothly oxidized structure typical for relative thin dense oxide layers (Figs. 45 – 46).

Rod D withdrawn at the end of the air ingress phase exhibits gray or white oxide scale at elevations between 300 and 900 mm (Figs. 47 – 48). The white scales were spalled in the region between 350 and 650 mm, the lower sublayer has a yellow-brown color typical for zirconium nitride. The estimated content of nitrogen in this sublayer defined by EDX analysis was between 30 and 40 at% (with about 50 at% zirconium and between 20 and 10 at% oxygen).

Similar spalling nitrided surface structure was observed for the corner rod A partially withdrawn after the test (upper part of the rod remained in the bundle). However, only some spots of the sublayer under spalled oxide scales have yellow-brown color (Fig. 49). The largest area of this sublayer has a dark-grey color, typical for zirconium oxide. This oxide was formed by re-oxidation of nitrides during the reflood.

3.3 Neutron radiography examinations of corner rods

Neutron radiography was successfully applied for the post-test examination in former QUENCH tests. In the system steam - zirconium the concentration of absorbed hydrogen can be quantitatively and non-destructively determined with a spatial resolution of about 25 µm. The method was applied to the post test examinations of the QUENCH-16 test too. Neutron radiographs of the corner rods A, B and D were taken. The system of this test is more difficult than those of former tests. During oxidation in wet air we have to deal with zirconium, hydrogen, oxygen and additionally nitrogen which has a significant higher neutron cross section than oxygen. Therefore, the total macroscopic neutron cross section Σ_{total} of specimens withdrawn from the QUENCH-16 test after initiation of the air ingress has to be described by:

$$\Sigma_{total}(x,y) = \frac{-\ln(T(x,y))}{s(x,y)} \tag{2}$$

$$= \sum_i \sigma_i \cdot N_i \tag{3}$$

$$= \underbrace{N_{Zry}(x,y)\,\overline{\sigma_{Zry}}}_{\Sigma_{sample\ as\ reseived}} + N_O(x,y)\,\sigma_O + N_H(x,y)\,\sigma_H + N_N(x,y)\,\sigma_N \tag{4}$$

where *T* is the neutron transmission, *x* and *y* the pixel positions, *s* the path length through the sample, *i* the isotop number, *σ* the microscopic total neutron cross section of the isotope and *N* the number density of the isotope.

From these radiography measurements a separation of the contributions of oxygen, hydrogen and nitrogen is not possible. Therefore, no concentrations can be determined.

Rod B withdrawn before air ingress was initiated shows homogeneous neutron attenuation over the whole length. Fig. 54 gives a typical radiograph taken from this rod. The total macroscopic neutron cross section varies between 0.2098 and 0.2219 cm^{-1}, indicating that no significant amount of hydrogen was absorbed in the pre-oxidation phase in steam.

Rod D was withdrawn at the end of the air oxidation phase before quenching. The neutron radiograph given in Fig. 55 shows a laminar breakaway of the oxide/nitride layer. Small differences in the total macroscopic neutron cross section were determined for various elongations. The highest values of about 0.25 cm^{-1} were found for the axial positions between 550 and 640 mm. At the upper (910 < z < 1030 mm) and lower end (0 < z < 250 mm) values of $\Sigma_{total} \approx 0.21$ cm were calculated. It can be assumed that the differences in the total macroscopic neutron cross section are caused by differences in the oxidation and nitriding level at these positions. In contrast to rod A (below), no small dark spots are obvious in the radiographs of rod D.

Unfortunately, in rod A withdrawn after the test the thermocouple and inner surface of the rod is welded with the rod because of melt formation (Fig. 53). It could not be removed. Between z = 450 and 510 mm the rod is completely filled with relocated melt. An example is given in Fig. 56d. Radial cracks in this melt are visible. In Fig. 56c a large hole is visible indicating the brittleness of the remaining tube walls. At lower elongations z the oxide layer is vary porous (see Fig. 56b). At elongations z ~ 230 mm a lot of small darker spots of different dimensions are visible in Fig. 56a. It cannot be excluded that these spots are hydrogen enriched. Possibly, steam has reached the remaining metal through the porous oxide/nitride layer at these positions during the quench phase. The “hydrogen pump effect” occurring in zirconium alloys covered by oxide layers containing a large amount of open cracks [14] would result in very local hydrogen enrichments. However, the larger neutron attenuation of these spot can also be explained by the formation of dense nitride accumulations.

4 Posttest investigations

4.1 Metallographic examination of corner rods

A maximum oxide layer thickness of 135 µm was determined for rod B at bundle elevation of 950 mm (Fig. 50) with direct metallographic measurements (Fig. 51). Due to partial scale spalling the axial distribution of the oxide layer thickness for rods D and A was calculated on the basis of measurements of residual metal diameter.

Metallographic investigations of corner rod D, withdrawn before reflood initiation, showed formation of porous nitrides inside the oxide layer as well as on the interface between oxide layer and α-Zr(O)-layer (Fig. 52). The nitrides were formed at elevations above 300 mm under local or full oxygen starvation conditions. If the gas phase in the gas channel does not contain oxygen, the oxygen of the oxide layer is transported into the metal cladding part not only from the ZrO_2/metal boundary, but also from the oxide bulk. As a result, the formation of α-Zr(O) clusters in the oxide layer is observed [15]. The nitrogen diffused from the gas phase through the oxide scales and reacted with α-Zr(O), resulting in the formation of zirconium nitride clusters. No nitride formation was observed at and above elevation 950 mm with saturated α-Zr(O) layer. Due to the higher density of ZrN in comparison to ZrO_2 density

(about 25% difference), the structure of the formed nitrides is very porous. The stresses induced during formation of nitrides cause formation of cracks going through the cladding. Indeed, the first rod failures were detected about 80 s after beginning of full oxygen starvation and the corresponding formation of nitrides (Fig. 42).

The investigation of the corner rod A withdrawn from the bundle after the test showed that nitrides were re-oxidized during the reflood with the formation of porous outer oxide sublayer at elevations 300 – 800 mm and growth of thick secondary inner oxide sublayer, formed due to steam penetration through the outer porous structure (Fig. 53). Due to the strong temperature escalation during reflood a part of the corner rod A was molten and relocated to lower positions (melt inside the corner rod at 450 mm in Fig. 53).

4.2 Videoscope inspection

The videoscope inspection at positions of withdrawn corner rods B (Figs. 57 – 59) and D (Figs. 60 – 62) showed an intensive degradation of the oxide layer with partial spalling at bundle elevations between 450 and 850 mm. The oxide layers between 250 and 750 mm have a white color – typical for the porous oxide structure. Yellowish oxide scales at the outer surface of claddings were observed at elevations between 750 and 1050 mm. The yellow coloring of the cladding surfaces can be caused by 1) small nitride traces inside the oxide and 2) oxidized tantalum particles from destroyed high-temperature thermocouples installed at elevations above 650 mm (such phenomenon with formation of yellow Ta_2O_5 spots was observed also for the QUENCH-15 bundle).

The status of grid spacers was checked in details. Only some remnants of the grid spacer #3 (originally installed at 550 mm) were observed at lower elevations (Fig. 60, 450 mm), whereas the significantly oxidized grid #4 was geometrically stable and not relocated (Fig. 57, 1050 mm and Fig. 59, 1050 mm).

The axial movement of the camera inside the bundle allows to achieve the imagination of 3D melt distribution. Frozen melt droplets and rivulets with oxidized surface were observed between rods at lower elevations between -60 and 420 mm.

4.3 Metallographic examination of bundle cross sections

After videoscope investigations the bundle (together with shroud and heat insulation) was extracted from the facility (Figs. 63, 64), dismantled from heat insulation (Figs. 65, 66) and filled with the epoxy resin, which was hardened during two weeks. Then the bundle was cut at different elevations. The cross sections were ground and polished (Table 13). Metallographic investigation of cross sections (Figs. 67 – 71) showed the formation of pools of partially oxidized frozen melt between 300 and 500 mm relocated from upper elevations 500 – 800 mm.

The melting of Zr cladding of high-temperature thermocouples, relocation and oxidation of the corresponding melt at different elevations is depicted in Fig. 72. The TC cladding melting took place at elevations above 500 mm. The melt inside the central pellet hole was

significantly oxidized at elevations above 600 mm by steam penetrated into the rod simulator through the failed cladding tube.

All 21 claddings at *elevation 250 mm* were not damaged (Figs. 73 – 76). The cladding surface is only insignificantly oxidized and reveals traces of metallic melt relocated from upper elevations (Fig. 77). The presence of Hf in the shroud (alloy Zr 702) allows the identification of the contributions of different bundle elements to the formation of the melt relocated to elevation 250 mm. Results of EDX analysis depicted in Fig. 78 show that the metallic melt pools consist of more than 50% of shroud melt. Similar EDX results were found for elevation 350 mm (Fig. 88).

Some claddings at *elevations 350 and 450 mm* have through-going cracks (Figs. 79 – 82 and Figs. 89 – 92). The oxide layers at the outer surfaces of most of the claddings reveal typical two-sublayer-structure: 1) the outer porous oxide formed during the pre-oxidation, nitrided during the oxygen starvation stage at the end of air ingress and re-oxidized during reflood; 2) the secondary internal dense oxide formed during the reflood due to the steam penetration through the porous outer sublayer (Figs. 83 – 85 and Fig. 93). Some nitrides formed relatively deep inside the prior α-Zr(O) layer did not react with steam and are surrounded by secondary oxide layer growth during reflood (e.g. rod 5 in Fig. 84). The surface of few claddings, intensively oxidized at the beginning of reflood, was blocked later by melt relocated downwards along the cladding. In such cases of local steam starvation the oxygen was partially transported from the oxide layer to adjacent α-Zr(O) layer and melt. As a result, metallic α-Zr(O) precipitates inside the oxide layer were formed (rod 6 in Fig. 84) according to mechanism described in [15].

The concave inner surface of shroud shows the presence of only relatively thin outer porous scales (Figs. 86, 94). It can be supposed that a part of the porous outer layer was spalled under larger compressive stresses at the concave inner shroud surface in comparison to stresses at the convex outer cladding surface. Relatively thin porous oxide scales without residual nitride traces were observed also at higher elevations.

The molten pools between 230 and 530 mm were formed by melt relocated from *elevations 550, 650 and 750 mm.* The metallographic observations reveal the formation of corresponding voids below the residual oxide layer (Figs. 96 – 99, Figs. 101 – 104 and Figs. 106 – 109). Relative thick inner oxide layers were formed at inner cladding surface between melt and pellet at these elevations (Figs. 100, 105, 110). These layers were developed as the result of the reaction with steam penetrated under the cladding after its failure (some claddings failed yet before reflood – see chapter 3). No remains of grid spacer were detected at elevation 550 mm. The spacer was partially oxidized, partially melted and relocated to lower elevations.

At *elevation 850 mm* only few claddings were locally molten (Fig. 111 - 114). However all claddings at this elevation were significantly damaged due to nitriding, re-oxidation of outer oxide layer and formation of thick secondary oxide layer formed during quench (Fig. 115).

No melt was formed at *elevation 950 and 1050 mm* (Figs. 116 – 119 and Figs. 121 – 124). The oxide structure at these elevations is typical for cladding oxidation in steam without

intermediate air oxidation (Figs. 120, 125). No reaction with nitrogen took place at elevations above 900 mm. Two factors prevented nitrogen attack at these elevations: 1) relative thick oxide layer formed during preoxidation (Fig. 50), and 2) relative low temperatures during the oxygen starvation phase (compare e.g. Figs. 29 and 28). The grid spacer at elevation 1050 mm was markedly oxidized but not destroyed, and kept the intact geometry at original position.

5 Estimation of hydrogen release by different oxidation mechanisms

5.1 Melt oxidation

The melt was formed due to strong temperature escalation during the reflood. Its oxidation contributed significantly to the hydrogen production during this test phase. The image analysis of frozen melt structures (Figs. 87, 95) allows defining the degree of oxidation of the melt on the basis of the correlation between relative area of ceramic precipitations and content of oxygen transported into the melt [16]. The average oxygen content of the melt at elevation 350 mm was measured to be about 8 wt% (corresponding relative ceramic area 10%), at elevation 450 mm about 11 wt% (corresponding relative ceramic area 25%).

The measurement of melt areas of molten pools at elevations 350 and 450 mm and extrapolation of these data to axial region 300 – 500 mm allows estimating the mass of hydrogen produced by bulk oxidation of pools to be 3 g. According to the EDX measurements, the pools contain 50% shroud material. Therefore the oxidation of the cladding part inside melts gives 1.5 g hydrogen. Oxide scale development at the melt surface gives additionally 3 g (1.5 g from cladding melt and 1.5 g from shroud melt). The oxidation of melt located inside claddings at elevations between 450 and 950 mm gives 16 g released hydrogen.

The similar estimation procedure for the hydrogen release during the oxidation of the shroud melt located radially outside bundle and axially between elevations 430 and 550 mm gives the hydrogen mass of 11 g. Therefore, the total hydrogen production by melt oxidation is about 33 g (***19 g*** *from claddings* and 14 g from shroud).

5.2 Oxidation of solid metal cladding

Measurements of the thicknesses of α- and prior β-layers as well as of oxide scales of the cladding are made at four points of each simulator rod with an azimuth interval of 90° and at each elevation according to Tables 14 and 16. Table 16 includes separately two types of oxide layers: 1) oxide layer at the outer cladding surface formed during the whole test, and 2) oxide layer at inner cladding surface formed mostly at higher elevations between melt and pellet (marked by red color). Fig. 126 to Fig. 147 illustrate the results of the layer thickness measurements for the respective bundle elevations. All these figures indicate scatter in the data due to the radial temperature gradient from the center of bundle to its periphery.

Averaged results of these measurements are summarized in Table 15 and Table 17. Again the thicknesses of the inner oxide layers between melt and pellet are marked with red color

in Table 17. Fig. 148 shows the corresponding axial distribution of final cladding oxidation. The maximum of oxidation lies at 550 mm. According to metallographic investigations the oxide layer at the outer cladding surface for elevations between 300 and 900 mm has a clear double structure: 1) porous outer sublayer formed before reflood and 2) dense and relative thick secondary sublayer formed during the reflood due to steam penetration through the outer porous sublayer.

The total mass of cladding outer sublayer corresponds approximately 9 g hydrogen released during the bundle pre-oxidation phase. Additionally about 4 g hydrogen was released during this test phase due to oxidation of shroud and corner rods (the estimation is based on the fact that the total surface of shroud and four corner rods corresponds effectively to surface of ten claddings). According to the mass spectrometer measurement, 16 g hydrogen were released before reflood. The difference of 16 – 9 – 4 = 3 g hydrogen should be connected with formation of the α-Zr(O) layer and oxidation of other construction elements (grid spacers, thermocouples, heaters).

On the basis of data for thicknesses of the *secondary oxide sublayer* formed at the rod simulator claddings during the quench phase between elevations 300 and 900 mm (Table 18), the corresponding hydrogen release was estimated to be ***46 g*** (considering combined α-Zr(O) layer). Additionally 6 g hydrogen were released during the quench phase by steam oxidation of the inner surface of ruptured claddings (corresponding layer thicknesses are marked in Table 16 in red color). A similar estimation for the oxidation of the solid part of the shroud between 300 and 900 mm during reflood gives 26 g hydrogen. The consideration of the oxidation at elevations above 900 mm gives 5 g hydrogen released from bundle and 1 g from shroud.

5.3 Oxidation of nitrides during reflood

A very intensive nitride formation was observed at elevations 350 – 850 mm. The upper oxide scales above nitrides have a porous structure due to re-oxidation of nitrides during reflood:

$$2\ ZrN + 4\ H_2O = 2\ ZrO_2 + 4\ H_2 + N_2 \qquad (5)$$

Only some nitride traces at the boundary between the inner dense and the spalled outer porous oxide scales were observed. On the basis of measured nitrogen release during the quench phase (24 g) and according to formula (5), the mass of hydrogen released during *nitride re-oxidation* was about ***7 g***. Because the surface of shroud and the remaining corner rods is equivalent to about nine cladding surfaces, the mass of hydrogen released due to cladding nitride oxidation should be about 5 g.

Hence, a significant part of the hydrogen release during the quench phase was produced by intensive oxidation of the rod cladding and shroud metal (with formation of dense oxide sublayer as shown in Fig. 85) by steam penetrated through the outer porous scale formed during the air ingress phase at the beginning of reflood.

6 Summary

The QUENCH-16 bundle test with Zry-4 claddings was performed with three typical features before initiation of reflood: moderate pre-oxidation to maximal 135 µm of oxide layer (instead ca. 500 µm for QUENCH-10), a long period of oxygen starvation during the air ingress phase (about 800 s instead 80 s for QUENCH-10), and reflood initiation at temperatures significantly below the melting point of the cladding (about 1800 K instead of 2200 K for QUENCH-10).

The change in flow conditions during the air ingress phase in comparison to the pre-oxidation phase had the immediate effect of reducing the heat transfer so that the temperatures began to rise and the axial temperature maximum was shifted from elevation 950 to 550…750 mm. A total oxygen starvation during 800 s before reflood initiation was observed at bundle elevations above 300 mm. The corresponding total oxygen uptake at the lower bundle elevations during that phase was 58 g.

A partial consumption of nitrogen during the oxygen starvation, accompanied by acceleration of the temperature increase at mid bundle elevations, caused the formation of zirconium nitrides inside the oxide layer at bundle elevations between 350 and 850 mm. Due to a noticeable difference between zirconium nitride and zirconium oxide densities, the structure of formed nitride containing clusters is very porous.

Immediate temperature escalations after reflood initiation, leading to maximum measured temperatures of about 2420 K, were caused by massive steam penetration through the porous oxide/nitride scales and intensive reaction with nitrides and especially with metallic cladding. Very thick oxide sub-layers up to 400 µm developed during the reflood phase. The cooling phase up to the final quench lasted ca. 500 s after achievement of peak temperatures.

A relatively high concentration of residual nitrides was observed mostly at elevations 350 - 550 mm. Spalled oxide scales with a re-oxidized porous structure were observed at elevations between 350 and 850 mm.

24 g nitrogen from 29 g, consumed during oxygen starvation period, were released during the quench phase. This quantity of released nitrogen corresponds to 7 g hydrogen produced during re-oxidation of nitrides (5 g bundle + 2 g shroud).

Metallographic investigation of cross sections between 300 and 500 mm showed partially oxidized frozen melt, relocated from upper elevations 500 – 800 mm. Image analysis of frozen Zr-O melt regions allows estimating the hydrogen release due to melt oxidation to be 33 g (19 g bundle + 16 g shroud).

A significant part of hydrogen released during reflood of the QUENCH-16 bundle was generated due to oxidation of the cladding metal by steam penetrated through the porous oxide layer formed due to re-oxidation of ZrN. Estimation made on the basis of corresponding layer thicknesses between elevations 300 and 900 mm gives 46 g hydrogen generated by oxidation of bundle and 26 g by shroud. The damaging of claddings by

through-going cracks caused the steam penetration under cladding with oxidation of inner cladding surface; the corresponding hydrogen release was estimated to be 6 g. Oxidation of non-nitrided surfaces of claddings and shroud at elevations above 900 mm causes hydrogen production of about 5 and 1 g correspondingly. Table 19 summarizes contributions of different oxidation mechanisms in the hydrogen production.

According to measurements by mass spectrometer, the total hydrogen production during QUENCH-16 was higher compared to QUENCH-10, i.e., 144 g (QUENCH-10: 53 g), 128 g of which were released during reflood (QUENCH-10: 5 g). The estimated contribution of claddings oxidation in the hydrogen release during reflood is 81 g.

Acknowledgements

The LACOMECO program is performed by KIT with financial support from the HGF Program NUKLEAR and the European Commission. The authors thank all colleagues involved in the investigations, particularly J. Moch and C. Rössger for bundle preparation, U. Stegmaier and U. Peters for metallographic analysis, J. Laier for data processing, M. Heck for very detailed draft review and corrections. Furthermore the very valuable support of the test planning by pre-test calculations performed at PSI, GRS, and EdF is strongly acknowledged.

References

1. Shepherd et al., “Oxidation Phenomena in Severe Accidents (OPSA)”, Final Report, INV-OPSA(99)-P008, 2000.

2. T. Albiol et al., “SARNET: Severe Accident Research Network of Excellence”. ICONE-15, Nagoya, Japan, April 22-26, 2007, paper 10429. http://www.sar-net.org/upload/icone15-10429_final_sarnet.pdf

3. K. Natesan and W.K. Soppet, “Air Oxidation Kinetics for Zr-Based Alloys”, Report NUREG/CR-6846, ANL-03/32, US NRC, Washington, DC (2004). http://pbadupws.nrc.gov/docs/ML0419/ML041900069.pdf

4. L. Matus, N. Vér, M. Kunstár, M. Horváth, A. Pintér, Z. Hózer: “Summary of separate effect tests with E110 and Zircaloy-4 in high temperature air, oxygen and nitrogen”, Report AEKI-FL-2008-401-04/01 (2008).

5. C. Duriez, M. Steinbrück, D. Ohai, T. Meleg, J. Birchley, T. Haste. „Separate-effect tests on zirconium cladding degradation in air ingress situations”. Nuclear Engineering and Design 239 (2009) 244–253.

6. M. Steinbrück and M. Böttcher, „ Air oxidation of Zircaloy-4, M5 and ZIRLO cladding alloys at high temperatures”, Journal of Nuclear Materials 414 (2011) 276–285.

7. M. Steinbrück, Prototypical experiments relating to air oxidation of Zircaloy-4 at high temperatures, Journal of Nuclear Materials 392 (2009) 276–285.

8. http://sacre.web.psi.ch/current-projects/main-frames/documents/oecd-projects/SandiaFuelProjectSFPDescription.pdf

9. Z. Hózer, P. Windberg, I. Nagy, L. Maróti, L. Matus, M. Horváth, A. Pintér, M. Balaskó, A. Czitrovszky, P. Jani, “Interaction of failed fuel rods under air ingress conditions”, Nucl. Technology, 141, p. 244 (2003).

10. J. Stuckert, J. Birchley, C. Homann, S. Horn, Z. Hozer, A. Miassoedov, J. Moch, G. Schanz, L. Sepold, U. Stegmaier, L. Steinbock, M. Steinbrueck: “Main results of the bundle test QUENCH-10 on air ingress”. 10th International QUENCH Workshop, Karlsruhe, October 26-28, 2004.

11. G. Schanz, M. Heck, Z. Hozer, L. Matus, I. Nagy, L. Sepold, U. Stegmaier, M. Steinbrück, H. Steiner, J. Stuckert, P. Windberg, “Results of the QUENCH-10 experiment on air ingress”. Wissenschaftliche Berichte, FZKA-7087, Karlsruhe, Mai 2006. http://bibliothek.fzk.de/zb/berichte/FZKA7087.pdf

12. A. Kiselev, D. Ignatiev, V. Konstantinov, D. Soldatkin, V. Nalivaev, V. Semishkin, "Main results and conclusions of the VVER fuel assemblies tests under severe accident conditions in the large-scale PARAMETER test facility". 16th International QUENCH Workshop, Karlsruhe, 16-18 November, 2010, ISBN 978-3-923704-74-3

13. A. Miassoedov, M. Kuznetsov, M. Steinbrück: “Overview of Severe Accident Research Activities Performed in the LACOMECO Project At Karlsruhe Institute of Technology.” 9th International Conference on Heat Transfer, Fluid Mechanics and Thermodynamics (HEFAT 2012), 16 – 19 July 2012, Saint-Julian, Malta. http://edas.info/web/hefat2012/authors.html#M

14. Mirco Große, Eberhard Lehmann, Martin Steinbrück, Guido Kühne, Juri Stuckert. Influence of oxide layer morphology on hydrogen concentration in tin and niobium containing zirconium alloys after high temperature steam oxidation. Journal of Nuclear Materials, Volume 385, Issue 2, 31 March 2009, Pages 339–345.

15. J. Stuckert, M. Veshchunov, “Behaviour of Oxide Layer of Zirconium-Based Fuel Rod Cladding under Steam Starvation Conditions”, Wissenschaftliche Berichte, FZKA-7373, Karlsruhe, April 2008. http://bibliothek.fzk.de/zb/berichte/FZKA7373.pdf

16. P. Hofmann, J. Stuckert, A. Miassoedov, M. Veshchunov, A. Berdyshev, A. Boldyrev, “ZrO_2 dissolution by molten Zircaloy and cladding oxide shell failure. New experimental results and modeling”, scientific report FZKA 6383, Karlsruhe (1999). http://bibliothek.fzk.de/zb/berichte/FZKA6383.pdf

Table 1: QUENCH Test Matrix

Test	Quench medium and injection rate	Temp. at onset of flooding[1)]	Max. ZrO_2 before transient[2)]	Max. ZrO_2 (X s) before flooding[2)]	Posttest average ZrO_2 thickness[3)]	H_2 production before / during cooldown	Remarks, objectives
QUENCH-00 Oct. 9 - 16, 97	Water 80 g/s	≈ 1800 K			completely oxidized		Commissioning tests.
QUENCH-01 Febr 26, 98	Water 52 g/s	≈ 1830 K	312 µm		500 µm at 913 mm	36 / 3	COBE Project; partial fragmentation of pre-oxidized cladding.
QUENCH-02 July 7, 98	Water 47 g/s	≈ 2400 K			completely oxidized	20 / 140	COBE Project; no additional pre-oxidation; quenching from high temperatures.
QUENCH-03 January 20, 99	Water 40 g/s	≈ 2350 K			completely oxidized	18 / 120	No additional pre-oxidation, quenching from high temperatures.
QUENCH-04 June 30, 99	Steam 50 g/s	≈ 2160 K	82 µm		280 µm	10 / 2	Cool-down behavior of slightly pre-oxidized cladding by cold steam injection.
QUENCH-05 March 29, 2000	Steam 48 g/s	≈ 2020 K	160 µm		420 µm	25 / 2	Cool-down behavior of pre-oxidized cladding by cold steam injection.
QUENCH-06 Dec 13 2000	Water 42 g/s	≈ 2060 K	207 µm[5)]	300 µm, (60 s), SVECHA modeling	630 µm[4)]	32 / 4	OECD-ISP 45; prediction of H_2 source term by different code systems.
QUENCH-07 July 25, 2001	Steam 15 g/s	≈ 2100 K	230 µm		completely oxidized	66 / 120	COLOSS Project; impact of B_4C absorber rod failure on H_2, CO, CO_2, and CH_4 generation.

Test	Quench medium and injection rate	Temp. at onset of flooding[1)]	Max. ZrO_2 before transient[2)]	Max. ZrO_2 (*X s*) before flooding[2)]	Posttest average ZrO_2 thickness[3)]	H_2 production before / during cooldown	Remarks, objectives
QUENCH-09 July 3, 2002	Steam 49 g/s	≈ 2100 K			completely oxidized	60 / 400	As QUENCH-07, steam-starved conditions prior to cooldown.
QUENCH-08 July 24, 2003	Steam 15 g/s	≈ 2090 K	274 µm		completely oxidized	46 / 38	As QUENCH-07, no absorber rod.
QUENCH-10 July 21, 2004	Water 50 g/s	≈ 2200 K	514 µm	613 µm (at 850 mm)	completely oxidized	48 / 5	LACOMERA Project; Air ingress.
QUENCH-11 Dec 08, 2005	Water 18 g/s	≈ 2040 K		170 µm	completely oxidized	9 / 132	LACOMERA Project; Boil-off.
QUENCH-12 Sept 27, 2006	Water 48 g/s	≈ 2100 K	160 µm, breakaway	300 µm, (110 s), breakaway	completely oxidized	34 / 24	ISTC Project #1648.2; VVER bundle with E110 claddings
QUENCH-13 Nov 7, 2007	Water 52 g/s	≈ 1820 K		400 µm,after AgInCd rod failure	750 µm	42 / 1	SARNET; impact of AgInCd absorber rod failure on aerosol generation.
QUENCH-14 July 2, 2008	Water 41 g/s	≈ 2100 K	170 µm[6)]	470 µm[6)] (30 s)	900 µm	34 / 6	ACM series: M5® cladding
QUENCH-15 May 27, 2009	Water 48 g/s	≈ 2100 K	145 µm[6)]	380 µm[6)] (30 s)	620 µm	41 / 7	ACM series: ZIRLO™ cladding
QUENCH-16 July 27, 2011	Water 53 g/s	≈ 1870 K*	135 µm	130 µm at 450-950 mm, breakaway	1075 µm at 550-650 mm	144 / 128	LACOMECO Project; Air ingress.

[1)] Maximum measured bundle temperature at 950 mm elevation (* at 650 – 850 mm).
[2)] Measured at the withdrawn corner rod at 950 mm elevation.
[3)] Measured posttest at the bundle elevation of maximum temperature, i.e. 950 mm.
[4)] Some claddings were completely oxidized at 950 mm elevation.
[5)] Oxide thickness during transient phase.
[6)] Zircaloy-4 corner rods (no M5® and ZIRLO® values available).

Revised: 01/2013

Table 2: Design characteristics of the QUENCH-16 test bundle

Bundle type		PWR
Bundle size (heated rods)		21 rods (20)
Pitch		14.3 mm
Coolant channel area		33.65 cm^2
Hydraulic diameter		12.9 mm
Cladding material		Zircaloy-4
Cladding outside diameter		10.75 mm
Cladding thickness		0.725 mm
Cladding length (levels)	heated rod unheated rod	2278 mm (-595 to 1683 mm) 2203 mm (-595 to 1608 mm)
Rod length (levels)	heated rod unheated rod	2480 mm (-690 to 1790 mm) 2610 mm (-820 to 1790 mm)
Heater material		Tungsten (W)
Heater length		1024 mm
Heater diameter		6 mm
Annular pellet	material heated rod unheated rod	ZrO_2, Y_2O_3-stabilized ∅ 9.15/6.15 mm; L=11 mm ∅ 9.15/2.5 mm; L=11 mm
Pellet stack heated/unheated		0 mm to 1024/1590 mm
Internal rod pressure (gas)		0.22 MPa abs. (Kr)
Corner rod (4)	material instrumented (A, C) not instrumented (B, D)	Zircaloy-4 tube ∅ 6x0.9 (bottom: -1140 mm) rod ∅ 6 mm (top: +1300 mm) rod ∅ 6 mm (-1350 to +1155 mm)
Grid spacer	material length location of lower edge	Zircaloy-4, Inconel 718 Zircaloy: 42 mm, Inconel: 38 mm Inc: -100; Zry: 150, 550, 1050, 1410 mm
Shroud	material wall thickness outside/inside diameter length (extension)	Zr 702 (flange: Zry-4) 3.05 mm 88.9/82.8 mm 1600 mm (-300 mm to 1300 mm)
Shroud insulation	material insulation thickness elevation	ZrO_2 fiber ZIRCAR 34 mm -300 mm to 1024 mm
Molybdenum-copper electrodes	length of upper electrodes length of lower electrodes diameter of electrodes: - prior to coating - after coating with ZrO_2	766 mm (576 Mo, 190 mm Cu) 690 mm (300 Mo, 390 mm Cu) 8.6 mm 9.0 mm
Cooling jacket	Material: inner/outer tube inner tube outer tube	Inconel 600 (2.4816) / SS (1.4571) ∅ 158.3 / 168.3 mm ∅ 181.7 / 193.7 mm

Table 3: Main characteristics of the ZrO_2 pellet material, yttria-stabilized (type ZYK3)

Property	Data
Y_2O_3 content	5 %
Density	6.07 ± 0.03 g/cm^3
Open porosity	0
Average crystallite size	0.8 µm
Specific heat at 20 °C	400 J/kg K
Thermal conductivity at 100 °C	2.5 W/m K
Linear expansion, 20-1000 °C	11 x 10^{-6}/K
Vickers Hardness HV10	> 12000 N/mm^2
Bending strength	> 1150 MPa
Elastic modulus	> 200 GPa
Weibull modulus	20
Fracture toughness K_{1C}	12 MPa•m$^{1/2}$

According to Barat Ceramics GmbH, 07955 Auma

Table 4: QUENCH-16; Electrical resistances of rods [mΩ] at 20 °C

Rod #	2	3	4	5	6	7	8	9	*ave-rage*	***8 rods parallel***
Pre-test	3.3	3.4	3.3	3.4	3.4	3.4	3.3	3.6	*3.4*	***0.42***
Post-test	3.1	3.0	3.1	3.3	3.2	3.2	3.1	3.3	*3.1*	***0.39***

Rod #	10	11	12	13	14	15	16	17	18	19	20	21	*ave-rage*	***12 rods parallel***
Pre-test	3.5	3.4	3.5	3.5	3.5	3.4	3.5	3.4	3.4	3.3	3.3	3.9	*3.5*	***0.29***
Post-test	48.1	3.2	4.0	3.3	3.3	3.2	3.3	3.2	3.2	3.2	3.2	3.3	*7.0*	***0.30***

Table 5: Properties of zirconia fiber insulating boards of type ZYFB3

Chemical composition

Oxide	ZrO_2	Y_2O_3	HfO_2	TiO_2	SiO_2	CaO	MgO	Fe_2O_3	Al_2O_3	Na_2O
typical wt%	88	10	2	0.14	0.12	0.09	0.03	0.04	0.01	0.01

Physical properties

bulk density	porosity	shrinkage		thermal expansion coefficient @298-1453K	melting point	max service temperature	flexural strength	compressive strength @10% compression
		(1 hour @1925 K)	(24 hours @1925 K)					
g/cm³	%	%		1/K	K	K	MPa	MPa
0.48	92	1.2	2.8	$10.7*10^{-6}$	2866	2500	0.59	0.29

Thermal conductivity

temperature, K	673	1073	1373	1673	1923
conductivity, W/(m*K)	0.08	0.11	0.14	0.19	0.24

Specific heat capacity

temperature, K	366	2644
specific heat capacity, J/(kg*K)	544	754

According to specifications of manufacturer ZIRCAR PRODUCTS

Table 6: List of instrumentation for the QUENCH-16 test

Chan-nel	Designation	Instrument, location	Unit
0	TFS 8/13	TC (W/Re) fuel rod simulator 8 (type 2), 950 mm, 225°	K
1	TFS 11/13	TC (W/Re) fuel rod simulator 11 (type 4), 950 mm, 315°	K
2	TFS 17/13	TC (W/Re) fuel rod simulator 17 (type 4), 950 mm, 135°	K
3		Reserve (W/Re)	K
4	TFS 13/17	TC (W/Re) fuel rod simulator 13 (type 5), 1350 mm, 45°	K
5	TSH 15/180 I	TC (W/Re) shroud outer surface, 1150 mm, 206°, behind shroud insulation	K
6	TFS 5/11	TC (W/Re) fuel rod simulator 5 (type 3), 750 mm, 45°	K
7	TFS 3/16	TC (W/Re) fuel rod simulator 3 (type 3), 1250 mm, 315°	K
8	TCR 13	TC (W/Re) fuel rod simulator 1 (type 1), 950 mm, 135°	K
9	TFS 2/14	TC (W/Re) fuel rod simulator 2 (type 2), 1050 mm, 315°	K
10	TFS 14/14	TC (W/Re) fuel rod simulator 14 (type 4), 1050 mm, 45°	
11	TFS 4/13	TC (W/Re) fuel rod simulator 4 (type 2), 950 mm, 45°	K
12	TFS 6/10	TC (W/Re) fuel rod simulator 6 (type 2), 650 mm, 135°	K
13	TFS 20/14	TC (W/Re) fuel rod simulator 20 (type 4), 1050 mm, 135°	K
14	TFS 9/15	TC (W/Re) fuel rod simulator 9 (type 3), 1150 mm, 225°	K
15	TFS 15/15	TC (W/Re) fuel rod simulator 15 (type 5), 1150 mm, 315°	K
16	TFS 6/14	TC (W/Re) fuel rod simulator 6 (type 2), 1050 mm, 135°	K
17	TSH 16/180 I	TC (W/Re) shroud outer surface, 1250 mm, 206°, behind shroud insulation	K
18	TSH 13/90 I	TC (W/Re) shroud outer surface, 950 mm, 116°, behind shroud insulation	K
19	TSH 14/90 I	TC (W/Re) shroud outer surface, 1050 mm, 116°, behind shroud insulation	K
20	TSH 11/0 I	TC (W/Re) shroud outer surface, 750 mm, 26°, behind shroud insulation	K
21	TSH 12/0 I	TC (W/Re) shroud outer surface, 850 mm, 26°, behind shroud insulation	K
22	TFS 2/5	TC (NiCr/Ni) fuel rod simulator 2 (type 2), 150 mm, 315°	K
23	TCR 7	TC (NiCr/Ni) fuel rod simulator 1 (type 1), 350 mm, 225°	K
24..31		Reserve (20 mA)	
26..31		Reserve (W/Re)	
32	TIT A/13	TC (W/Re) corner rod A, center, 950 mm	K
33	TCRC 13	TC (W/Re) central rod, center, 950 mm	K
34	TCRC 10	TC (W/Re) central rod, center, 650 mm	K
35	TSH 9/90	TC (NiCr/Ni) shroud outer surface, 550 mm, 116°	K

Chan-nel	Designation	Instrument, location	Unit
36	TSH 9/270	TC (NiCr/Ni) shroud outer surface, 550 mm, 296°	K
37		Reserve (W/Re), channel defect?	
38	TFS 8/9	TC (NiCr/Ni) fuel rod simulator 8 (type 2), 550 mm, 225°	K
39	TFS 11/9	TC (NiCr/Ni) fuel rod simulator 11 (type 4), 550 mm, 135°	K
40	TIT C/12	TC (W/Re) corner rod C, center, 850 mm	K
41	TCR 12	TC (W/Re) fuel rod simulator 1 (type 1), 850 mm, 315°	K
42	TFS 9/8	TC (NiCr/Ni) fuel rod simulator 9 (type 3), 450 mm, 225°	K
43	TFS 4/8	TC (NiCr/Ni) fuel rod simulator 4 (type 2), 450 mm, 315°	K
44	TCR 9	TC (NiCr/Ni) fuel rod simulator 1 (type 1), 550 mm, 315°	K
45	T 304	TC (NiCr/Ni) outer surface of pipe after V302	K
46	TFS 11/5	TC (NiCr/Ni) fuel rod simulator 11 (type 4), 150 mm, 45°	K
47	TFS 5/15	TC (W/Re) fuel rod simulator 5 (type 3), 1150 mm, 45°	K
48	TFS 7/16	TC (W/Re) fuel rod simulator 7 (type 3), 1250 mm, 135°	K
49..50		Reserve (W/Re)	K
51	TFS 18/11	TC (W/Re) fuel rod simulator 18 (type 5), 750 mm, 45°	K
52	TSH 13/270 I	TC (W/Re) shroud outer surface, 950 mm, 296°, behind shroud insulation	K
53	TSH 14/270 I	TC (W/Re) shroud outer surface, 1050 mm, 270°, behind shroud insulation	K
54	TSH 11/180 I	TC (W/Re) shroud outer surface, 750 mm, 206°, behind shroud insulation	K
55	TSH 12/180 I	TC (W/Re) shroud outer surface, 850 mm, 206°, behind shroud insulation	K
56	TFS 10/12	TC (W/Re) fuel rod simulator 10 (type 5), 850 mm, 315°	K
57	TFS 2/10	TC (W/Re) fuel rod simulator 2 (type 2), 650 mm, 315°	K
58..59		Reserve	
60	TFS 3/12	TC (W/Re) fuel rod simulator 3 (type 3), 850 mm, 315°	K
61..62		Reserve	
63	**R001 air**	**Flow rate air 0.08…2 g/s**	g/s
64	T 402b	Temperature of the tube surface after gas heater	K
65		Reserve	
66	TSH 15/0 I	TC (W/Re) shroud outer surface, 1150 mm, 26°, behind shroud insulation	K
67	TSH 16/0 I	TC (W/Re) shroud outer surface, 1250 mm, 26°, behind shroud insulation	K
68	T 512	Gas temperature bundle outlet	K
69		Reserve	
70	TFS 7/12	TC (W/Re) fuel rod simulator 7 (type 3), 850 mm, 135°	K

Chan-nel	Designation	Instrument, location	Unit
71	Ref. T 01	Reference temperature 1	K
72	TFS 4/1	TC (NiCr/Ni) fuel rod simulator 4 (type 2), -250 mm, 315	K
73	TFS 6/2	TC (NiCr/Ni) fuel rod simulator 6 (type 2), -150 mm, 45	K
74	TFS 7/3	TC (NiCr/Ni) fuel rod simulator 7 (type 3), -50 mm, 135°	K
75	TFS 4/3,5	TC (NiCr/Ni) fuel rod simulator 4 (type 2), 0 mm, 135°	K
76	TFS 9/6	TC (NiCr/Ni) fuel rod simulator 4 (type 2), 250 mm, 315	K
77		Reserve TC (NiCr/Ni)	K
78	TFS 12/4	TC (NiCr/Ni) fuel rod simulator 12 (type 5), 50 mm, 225°	K
79	TFS 20/4	TC (NiCr/Ni) fuel rod simulator 20 (type 4), 50 mm, 225°	K
80	TFS 17/5	TC (NiCr/Ni) fuel rod simulator 17 (type 4), 150 mm, 135°	K
81	TFS 15/6	TC (NiCr/Ni) fuel rod simulator 15 (type 5), 250 mm, 315°	K
82	TFS 12/7	TC (NiCr/Ni) fuel rod simulator 12 (type 5), 350 mm, 225°	K
83	TSH 4/270	TC (NiCr/Ni) shroud outer surface, 50 mm, 296°	K
84	TSH 3/180	TC (NiCr/Ni) shroud outer surface, -50 mm, 206°	K
85	TSH 4/180	TC (NiCr/Ni) shroud outer surface, 50 mm. 206°	K
86	TSH 7/180	TC (NiCr/Ni) shroud outer surface, 350 mm, 206°	K
87	TSH 4/90	TC (NiCr/Ni) shroud outer surface, 50 mm, 116°	K
88	TSH 1/0	TC (NiCr/Ni) shroud outer surface, -250 mm, 26°	K
89	TSH 4/0	TC (NiCr/Ni) shroud outer surface, 50 mm, 26°	K
90	TSH 7/0	TC (NiCr/Ni) shroud outer surface, 350 mm, 26°	K
91	TCI 9/270	TC (NiCr/Ni) cooling jacket inner tube wall, 550 mm, 270°	K
92	TCI 10/270	TC (NiCr/Ni) cooling jacket inner tube wall, 650 mm, 270°	K
93	TCI 11/270	TC (NiCr/Ni) cooling jacket inner tube wall, 750 mm, 270°	K
94	TCI 13/270	TC (NiCr/Ni) cooling jacket inner tube wall, 950 mm, 270°	K
95	TFS 13/8	TC (NiCr/Ni) fuel rod simulator 13 (type 5), 450 mm, 45°	K
96	TCI 1/180	TC (NiCr/Ni) cooling jacket inner tube wall, -250 mm, 180°	K
97	TCI 4/180	TC (NiCr/Ni) cooling jacket inner tube wall, 50 mm, 180°	K
98	TCI 7/180	TC (NiCr/Ni) cooling jacket inner tube wall, 350 mm, 180°	K
99	TCI 11/180	TC (NiCr/Ni) cooling jacket inner tube wall, 750 mm, 180°	K
100	TCI 12/180	TC (NiCr/Ni) cooling jacket inner tube wall, 850 mm, 180°	K
101	TCI 13/180	TC (NiCr/Ni) cooling jacket inner tube wall, 950 mm, 180°	K
102	TCI 15/180	TC (NiCr/Ni) cooling jacket inner tube wall, 1150 mm, 180°	K
103	T002 inlet	Cooling water, inlet of off-gas tube	K
104	T 309	Ar bundle top	K
105	TSH 10/90	TC (NiCr/Ni) shroud outer surface, 650 mm, 96°	K

Chan-nel	Designation	Instrument, location	Unit
106	TCI 11/90	TC (NiCr/Ni) cooling jacket inner tube wall, 750 mm, 90°	K
107	TCI 13/90	TC (NiCr/Ni) cooling jacket inner tube wall, 950 mm, 90°	K
108	*T 305 flange*	*TC (NiCr/Ni) bundle inlet flange*	K
109	TCI 1/0	TC (NiCr/Ni) cooling jacket inner tube wall, -250 mm, 0°	K
110	TCI 4/0	TC (NiCr/Ni) cooling jacket inner tube wall, 50 mm, 0°	K
111	TCI 7/0	TC (NiCr/Ni) cooling jacket inner tube wall, 350 mm, 0°	K
112	TCI 11/0	TC (NiCr/Ni) cooling jacket inner tube wall, 750 mm, 0°	K
113	TCI 12/0	TC (NiCr/Ni) cooling jacket inner tube wall, 850 mm, 0°	K
114	TCI 13/0	TC (NiCr/Ni) cooling jacket inner tube wall, 950 mm, 0°	K
115	TCI 15/0	TC (NiCr/Ni) cooling jacket inner tube wall, 1150 mm, 0°	K
116	T003	Cooling water, outlet of off-gas tube	K
117		Reserve (NiCr/Ni)	K
118	TSH 10/270	TC (NiCr/Ni) shroud outer surface, 650 mm, 296°	K
119	*T 306 foot*	*TC (NiCr/Ni) outer surface of bundle foot*	K
120	TCO 1/0	TC (NiCr/Ni) cooling jacket outer tube surface, -250 mm, 0°	K
121	TCO 7/0	TC (NiCr/Ni) cooling jacket outer tube surface, 350 mm, 0°	K
122	TCO 13/0	TC (NiCr/Ni) cooling jacket outer tube surface, 950 mm, 0°	K
123	T 601	Temperature before off-gas flow instrument (orifice) F 601	K
124	T 513	Outer wall of bundle head	K
125	*T 514*	Cooling water bundle head	
126	T307 off-gas	TC (NiCr/Ni) inner surface of inlet of off-gas pipe	K
127	TFS 20/9	TC (NiCr/Ni) fuel rod simulator 20 (type 4), 550 mm, 225°	K
128	T 104	Temperature quench water	K
129	T 201	Temperature steam generator heating pipe	K
130	T 204	Temperature before steam flow instrument location 50 g/s	K
131	T 205	Temperature before steam flow instrument location 10 g/s	K
132	T 301A	Temperature behind superheater	K
133	T 302	Temperature superheater heating pipe	K
134	T 303	Temperature before total flow instrument (orifice) location	K
135	T 401	Temperature before gas flow instrument (orifice) location	K
136	T 403	Temperature of Ar at inlet cooling jacket	K
137	T 404	Temperature of Ar at outlet cooling jacket	K
138	T 501 cont-t	Temperature in containment (near from bundle head)	K
139	T 502	Temperature at outer surface of containment, 0°, 2.4 m	K
140	T 503	Temperature at outer surface of containment, 270°, 2.2 m	K

Chan-nel	Designation	Instrument, location	Unit
141	T 504	Temperature at outer surface of containment, 270°, 3.2 m	K
142	T 505	Temperature at outer surface of containment, 90°, 3.2 m	K
143	T 506	Temperature at outer surface of containment, 270°, 3.6 m	K
144	T 507	Temperature at outer surface of containment, 90°, 3.6 m	K
145	T 508	Temperature at outer surface of containment, 180°, 4.0 m	K
146	T 310	TC (NiCr/Ni) aerosol extraction tube in off-gas pipe	K
147	T 510	Temperature at outer surface of containment, 270°, 4.4 m	K
148	T 511	Gas temperature at bundle inlet	K
149	T 901	Temperature before off-gas flow instrument F 901	K
150	TFS 4/9	TC (NICr/Ni) fuel rod simulator 4 (type 2), 550 mm, 45°	K
151	Ref. T 02	Reference temperature 2	K
152	P 201	Pressure steam generator	bar
153		Reserve	
154	P 205	Pressure at steam flow instrument location 10 g/s	bar
155	P 303	Pressure before total flow instrument (orifice) location	bar
156	P 401	Pressure before gas flow instrument location	bar
157	P 511	Pressure at bundle inlet	bar
158	P 512	Pressure at bundle outlet	bar
159	P 601	Pressure before orifice of off-gas pipe	bar
160	P 901	Pressure after condenser (end of off-gas system)	bar
161	L 201	Liquid level steam generator	mm
162	L 501	Liquid level quench water	mm
163	L 701	Liquid level of condensation vessel	mm
164	**Fm 401B**	Argon flow rate (Bronkhorst device)	g/s
165	P 411	Pressure **Kr** supply (rod filling)	bar
166	P 403	Pressure Ar cooling of cooling jacket	bar
167	P 406	Pressure insulation shroud/cooling jacket	bar
168	Fm 104	Flow rate quench water	l/h
169		Reserve	g/s
170	**Fm 205**	Flow rate steam 10 g/s	g/s
171	F 303	Flow rate at bundle inlet (steam + argon), orifice	mbar
172		Reserve	
173	F 403	Flow rate cooling gas	Nm^3/h
174	F 601	Flow rate off-gas (orifice)	mbar
175	**Fm 406**	Flow rate argon into room between shroud and cooling jacket	g/s

Chan-nel	Designation	Instrument, location	Unit
176	E 201	Electric current steam generator	A
177	E 301	Electric current superheater	A
178	E 501	Electric current inner ring of fuel rod simulators	A
179	E 502	Electric current outer ring of fuel rod simulators	A
180	E 503	Electric voltage inner ring of fuel rod simulators	V
181	E 504	Electric voltage outer ring of fuel rod simulators	V
182	Hub_V302	Gas supply valve lift	%
183	Ref. T 03	Reference temperature 3	K
:			
250	E 505	Electric power inner ring of fuel rod simulators	W
251	E 506	Electric power outer ring of fuel rod simulators	W

Indications:

TFS – TC at the surface of fuel rod simulators;
TCR – TC at the surface of the central rod;
TCRC – TC inside the central rod;
TSH – TC at the outer surface of shroud;
TIT – TC inside corner rods.

Groups of rods:

type 1: rod 1 (central rod);
type 2: rods 2, 4, 6, 8;
type 3: rods 3, 5, 7, 9;
type 4: rods 11, 14, 17, 20;
type 5: rods 10, 12, 13, 15, 16, 18, 19, 21.

Table 7: QUENCH-16; map of TFS and TCRC thermocouples

elevation, mm	-250	-150	-50	50	150	250	350	450	550	650	750	850	950	1050	1150	1250	1350
elev. No. / rod No.	1	2	3	4	5	6	7	8	9	10	11	12	13	14	15	16	17
1							N		N	W		W	W, W				
2					N					W				W			
3												W				W	
4	N							N	N				W				
5											W				W		
6		N								W				W			
7			N									W				W	
8									N				W				
9						N		N							W		
10												W					
11									N				W				
12				N			N										
13								N									W
14														W			
15						N									W		
16																	
17					N								W				
18											W						
19																	
20				N					N					W			
21																	
TC quantity:	1	1	1	2	2	2	2	3	5	3	2	4	6	4	3	2	1

heated rods

unheated rod

TC to bottom: 9 W/Re+20 NiCr/Ni

TC to top: 16 W/Re

N NiCr/Ni (totally 19)

W W/Re (totally 23)

W W/Re TCRC (2)

Table 8: Diameters of the materials used for the QUENCH High-Temperature Thermocouples [mm]

Material	As-received	Final
W/Re wires	0.254	
HfO_2 insulation OD (see drawing below)	1.1	
Ta tube OD / ID	2.15 / 1.65	1.4 / 0.94
Zr tube OD / ID	2.5 / 1.65 ± 0.05	2.2-2.3 / ~1.4

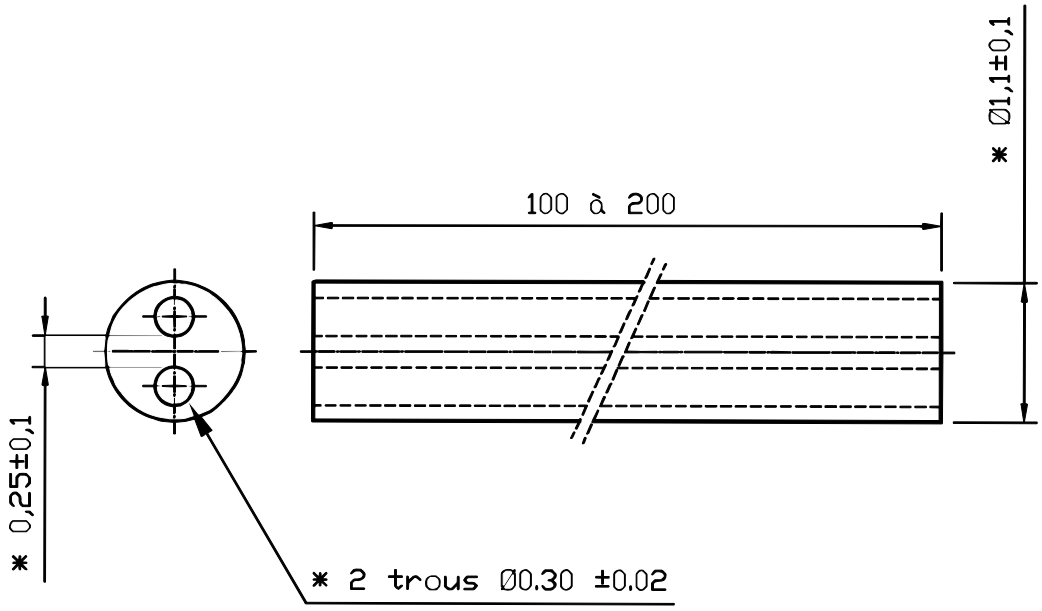

Table 9: Main characteristics of the HfO_2 thermocouple insulator

Property	Data
Composition of basic material	99 % HfO_2
Melting temperature	2840 °C
Max. use temperature	2500 °C
Density	8.4 g/cm^3
Thermal conductivity at 20-1000 °C	1.14 W/m K
Linear expansion	5.8 x 10^{-6}/K

According to Saint-Gobain ceramics, 1997

Table 10: QUENCH-16; Failure of thermocouples

Bundle

#	Thermocouple	Elevation [mm]	Time [s]	T [K]
1	TFS 11/9	550	10652	1701
2	TFS 4/9	550	10688	1728
3	TFS 8/9	550	10706	1715
4	TFS 20/9	550	10770	1705
5	TFS 13/8	450	10897	1725
6	TCR 9	550	10915	1758
7	TFS 4/8	450	10962	1765
8	TFS 9/8	450	11120	1766
9	TCR 7	350	11250	1758
10	TFS 12/7	350	11307	1754
11	TFS 4/13	950	11347	1482
12	TFS 6/14	1050	11351	1443
13	TFS 18/11	750	11380	2057
14	TCR 12	850	11409	2390
15	TFS 5/11	750	11450	1506
16	TFS 2/10	650	11477	701
17	TFS 3/12	850	11478	822
18	TCRC 10	650	11587	395
19	TIT C/12	850	11611	395
20	TFS 7/12	850	11648	395*
21	TFS 8/13	950	11681	993
22	TCR 13	950	11675	906
23	TFS 11/13	950	11765	395*
24	TFS 2/14	1050	11879	395*
25	TFS 15/15	1150	11900	395*

*estimated fluid temperature

Shroud

#	Thermocouple	Elevation [mm]	Time [s]	T [K]
1	TSH 9/270	550	11346	1769
2	TSH 10/90	650	11361	1742
3	TSH 9/0	550	11372	406
4	TSH 10/270	650	11414	1772
5	TSH 7/180	350	11427	386

NiCr/Ni
W/Re

Table 11: QUENCH-16; Sequence of events

Time [s]	Event
0 (10:41:35h)	Start data recording, T_{max}=TFS 6/14=871 K, el. power switched from 4.3 to 9.7 kW. Start of ***pre-oxidation phase*** in gas mixture of overheated steam (Fm 205 = 3.4 g/s) and argon (Fm 401B = 3 g/s).
2291	El. power switched from 9.8 to 10.8 kW. T_{max} = TFS 4/13 = 1306 K.
3002	El. power switched from 10.8 to 11.3 kW. T_{max} = TFS 4/13 = 1360 K.
6301 (12:26:34h)	Start of ***cooling phase***. Reduction of el. power from 11.3 to 3.9 kW. T_{max} = TFS 4/13 = 1428 K.
7249	Corner rod B withdrawn.
7307 (12:43:22h)	Start of ***air ingress phase***. Turn on the air flow with flow rate 0.2 g/s. Switch of argon flow from 3 g/s to 1 g/s. Switch-off of steam supply (0 g/s at 7319 s). T_{max} = TFS 6/14 = 998 K.
7321	First indication of air at mass spectrometer.
10270… …10400	Accelerated temperature increase at bundle elevation 9 (550 mm). TCR 9 increased from 1445 to 1620 K.
10300… …10800	Accelerated temperature increase at bundle elevation 8 (450 mm). TFS 4/8 increased from 1290 to 1700 K.
10350… …10650	Transition to *complete oxygen starvation* and to *partial nitrogen consumption*. Decrease of nitrogen flow rate through the off-gas pipe from 0.16 to 0.13 g/s.
10500… 11120	Accelerated temperature increase at bundle elevation 7 (350 mm). TCR 7 increased from 1205 to 1700 K.
10587	First rod failure: Kr indication at mass spectrometer.
10900… …11341	Accelerated temperature increase at bundle elevation 6 (250 mm). TFS 15/6 increased from 1115 to 1400 K.
11330	Corner rod D withdrawn. Maximal bundle temperature TCR 12 = TFS 18/11 = TFS 2/10 = **1870 K**
11341	Initiation **of *fast water*** injection. Stop of overheated gas and argon supply (closing of the V 302 valve). Reaction of the T511 bundle inlet thermocouple.
11350… 11413	Initiation of ***quench water*** supply (Fm 104 increased from 0 to 53 g/s).
11352… …11560	*Release of hydrogen and nitrogen*.
11380	Shroud failure: flow of argon from the shroud annulus into the bundle (Fm 406 increase).
11395… …11530	Intensive water boiling in bundle (evaporation rate ca. 53 g/s): indication by increased off-gas flow rate (F 601); constant collapsed water level at elevation L 501 = 530 mm.
11530… …11780	Constant evaporation rate ca. 47.3 g/s (according to coolant channel of 33.65 cm²). Increase of collapsed water level from elevation L 501 = 570 mm to L 501 = 995 mm.
11830	Thermocouples TFS 13/17 and T 512 at bundle elevation 1350 mm wetted with double-phase fluid. Collapsed water level at elevation L 501 = 1194 mm.
12047… …12080	Shut down of the quench pump (Fm 104 decreased from 53 to 0 g/s).
14625	Shut down of electrical power supply (power reduction from 3.6 to 0 kW).
14640 (14:45:36h)	End of data recording. Stop of Ar flow into shroud annulus. Bundle T_{max} = TFS 10/12 = 390 K; shroud T_{max} = TSH 16/180 = 405 K. L 501 = 1020 mm. Total collected condensed water 33602 g (according to summarised L 701 = 2350 mm).
(28.07.11)	L 501 = 654 mm – corresponding water mass inside bundle is 6590 g (measured after bundle dismounting). Water mass inside shroud annulus: 7264 g. Increase of L 701 = 1103 mm.

Table 12: QUENCH-16; Water/steam balance

Accumulated mass of water [g]	
Total steam injected (Fm 205)	24853
Total quench water injected (F 104)	36691
Quench water from fast injection system	4000
Total used water	**65544**
Condensed water collected (L 701 = 2350+1103 = 3453 mm)*	49378
Water/steam consumed by metal oxidation (144 g released H_2)	1296
Water found posttest in the test bundle (L501 = +654 mm)	6590
Water found posttest retained in the ZrO_2 fiber insulation**	7264
Water found posttest in the annulus of the upper plenum	450
Total posttest water	**64978**

*) water column of 1 mm corresponds to 14.3 g

**) post-test insulation weight (between -300 mm and 1000 mm): 13614 g; weight of the dry insulation (10 annuli): 10 x 900 g = 9000 g; 2650 g collected as water

Table 13: Cross sections of the QUENCH-16 test bundle for metallographic examination

Sample	Sample length (mm)	Axial position (mm)		Remarks
		bottom	top	
			80	Remainder
Cut	4	80	84	
QUE-16-1	16	**84**	**100**	Spacer 2, 84 mm, 100 mm polished
Cut	4	100	104	
QUE-16-a	126	104	230	
Cut	4	230	234	
QUE-16-2	16	234	**250**	TC elevation 6, 250 mm polished
Cut	4	250	254	
QUE-16-b	76	254	330	
Cut	4	330	334	
QUE-16-3	16	334	**350**	TC elevation 7, 350 mm polished
Cut	4	350	354	
QUE-16-c	76	354	430	
Cut	4	430	434	
QUE-16-4	16	434	**450**	TC elevation 8, 450 mm polished
Cut	4	450	454	
QUE-16-d	76	454	530	
Cut	4	530	534	
QUE-16-5	16	534	**550**	Spacer 3, 550 mm polished
Cut	4	550	554	
QUE-16-e	76	554	630	
Cut	4	630	634	
QUE-16-6	16	634	**650**	TC elevation 10, 650 mm polished
Cut	4	650	654	
QUE-16-f	76	654	730	
Cut	4	730	734	
QUE-16-7	16	734	**750**	TC elevation 11, 750 mm polished
Cut	4	750	754	
QUE-16-g	76	754	830	
Cut	4	830	834	
QUE-16-8	16	834	**850**	TC elevation 12, 850 mm polished
Cut	4	850	854	
QUE-16-h	76	854	930	
Cut	4	930	934	
QUE-16-9	16	934	**950**	TC elevation 13, 950 mm polished
Cut	4	950	954	
QUE-16-i	76	954	1030	
Cut	4	1030	1034	
QUE-16-10	16	1034	**1050**	TC elevation 14, 1050 mm polished
Cut	4	1050	1054	
		1054		Remainder

Table 14: Thickness of α-Zr(O)- and prior β-Zr-layers at four circumferential positions (in μm)

Elevation, mm		250		350		450	550	750	850		950		1050	
rod	angle	α	β	α*	β	α	α	α	α	β	α	β	α	β
Rod 1	0°	22	710	30	620	400	0	720	350	0	200	420	170	470
	90°			150	450	400	200	0	400	0	190	410	160	480
	180°	22	700	200	390	360	700	-	300	0	210	430	150	500
	270°			200	440	400	0	-	250	250	200	430	150	490
Rod 2	0°	24	690	200	420	400	0	0	200	350	200	410	130	510
	90°			220	390	440	0	0	200	300	220	390	170	460
	180°	24	680	220	430	450	180	0	300	300	220	430	130	520
	270°			200	410	350	300	0	200	350	200	420	130	520
Rod 3	0°	22	690	180	420	500	-	-	280	280	220	400	150	490
	90°			210	410	500	0	0	250	300	220	400	190	450
	180°	22	690	200	410	500	0	0	250	300	200	420	160	470
	270°			190	410	450	0	0	530	0	220	400	150	500
Rod 4	0°	24	690	200	420	450	720	330	170	350	240	380	190	450
	90°			210	430	450	0	400	170	300	280	320	180	460
	180°	24	700	120	400	320	300	0	350	0	260	350	180	470
	270°			160	440	350	0	0	250	250	250	350	180	450
Rod 5	0°	24	680	600	0	580	600	460	200	350	250	370	170	470
	90°			200	400	400	0	500	200	300	250	390	170	480
	180°	26	660	230	380	420	0	440	210	210	250	400	180	450
	270°			600	0	300	0	300	250	250	290	330	170	470
Rod 6	0°	26	670	180	420	330	150	420	250	170	270	320	180	440
	90°			170	400	-	0	0	280	0	490	0	180	430
	180°	24	670	220	350	-	200	0	400	0	220	300	170	500
	270°			220	390	300	0	0	420	0	210	370	170	450
Rod 7	0°	24	700	250	390	-	0	0	450	0	250	280	160	480
	90°			200	400	-	0	0	0	0	200	0	190	420
	180°	24	690	150	480	-	-	0	50	0	240	0	160	440
	270°			150	450	270	0	0	350	0	500	0	160	480
Rod 8	0°	22	690	200	400	380	300	0	350	0	200	380	160	480
	90°			150	450	630	0	0	500	0	530	0	160	470
	180°	24	680	170	430	290	0	0	380	0	520	0	150	470
	270°			160	450	470	200	0	400	0	210	370	160	470
Rod 9	0°	24	700	190	450	400	200	0	220	330	200	450	140	520
	90°			170	430	420	0	-	530	0	200	420	140	510
	180°	22	700	170	480	300	0	300	420	0	200	430	130	430
	270°			190	460	300	900	350	180	300	170	480	130	550
Rod 10	0°	22	690	200	430	520	450	400	200	350	170	480	90	590
	90°			200	430	470	480	0	250	250	170	470	100	580
	180°	22	690	180	450	450	350	200	250	250	160	490	80	600
	270°			170	470	470	450	0	150	350	160	500	80	610
Rod 11	0°	22	700	200	430	420	0	0	250	300	170	460	100	570
	90°			240	370	520	350	0	220	300	190	440	100	100
	180°	22	670	180	420	520	400	1020	220	230	160	490	80	80
	270°			200	420	440	200	0	150	400	140	430	80	610

*600 – only α-Zr(O)

Table 14 (cont.): **Thickness of α-Zr(O)- and prior β-Zr-layers at four circumferential positions (in µm)**

Elevation, mm		250		350		450	550	750	850		950		1050	
rod	angle	α	β	α	β	α	α	α	α	β	α	β	α	β
Rod 12	0°	22	710	160	450	480	250	-	120	120	180	470	100	600
	90°			170	430	500	400	0	300	300	190	460	110	560
	180°	22	710	200	440	500	500	0	200	200	170	500	100	580
	270°			160	430	430	750	300	150	150	170	520	80	610
Rod 13	0°	22	690	160	440	500	500	620	200	400	200	550	100	570
	90°			220	420	500	450	630	200	400	170	460	120	550
	180°	24	700	180	440	500	0	0	250	300	230	410	140	530
	270°			170	470	530	350	0	150	350	200	450	120	560
Rod 14	0°	20	720	210	400	420	360	480	120	430	220	430	120	550
	90°			200	410	540	380	480	150	370	220	400	110	550
	180°	24	690	200	500	500	100	100	200	300	250	370	140	500
	270°			210	410	580	700	360	200	350	220	400	120	540
Rod 15	0°	22	710	220	390	420	800	460	120	120	200	420	110	560
	90°			220	400	450	360	560	150	150	210	400	120	550
	180°	22	700	210	420	430	0	550	250	250	220	400	140	510
	270°			220	400	500	0	420	220	220	200	420	130	530
Rod 16	0°	22	690	210	410	400	150	550	130	300	220	410	120	560
	90°			200	430	200	470	520	150	350	200	410	130	550
	180°	24	690	180	420	350	0	450	200	300	250	360	140	510
	270°			210	430	470	0	580	200	300	230	390	160	500
Rod 17	0°	22	670	180	390	350	0	190	400	0	250	350	150	490
	90°			220	330	280	0	280	420	0	230	350	120	520
	180°	24	680	300	330	-	0	0	450	0	420	0	160	440
	270°			160	420	200	0	0	280	0	490	0	160	460
Rod 18	0°	22	690	280	360	-	0	0	600	0	370	0	180	400
	90°	_	_	350	330	0	0	-	330	0	450	0	160	490
	180°	20	680	300	400	0	0	-	0	0	270	0	170	420
	270°			200	300	-	0	0	0	0	270	0	200	380
Rod 19	0°	22	680	100	460	-	0	0	0	0	310	0	180	370
	90°	_	_	130	460	0	0	-	0	0	230	0	170	380
	180°	20	690	170	490	550	0	0	200	0	350	0	140	460
	270°			170	470	-	0	0	150	0	420	0	150	430
Rod 20	0°	20	690	170	490	300	0	150	500	0	500	0	120	510
	90°			180	470	420	0	0	300	0	450	0	140	500
	180°	20	710	170	430	400	250	0	450	0	510	0	100	560
	270°			180	470	250	300	0	500	0	230	340	100	560
Rod 21	0°	22	690	170	490	400	0	-	220	300	190	410	110	560
	90°			180	470	250	0	-	520	0	190	360	100	570
	180°	20	690	170	480	320	150	-	260	260	200	400	90	590
	270°			170	480	200	0	-	200	330	200	450	90	590

Table 15: Thickness of α-Zr(O)- and prior β-Zr-layers averaged circumferentially (in μm)

Elevation, mm	250		350		450	550	750	850		950		1050	
Rod	α	β	α	β	α	α	α	α	β	α	β	α	β
Rod 1	22	705	145	475	390	450	720	325	250	200	423	158	485
Rod2	24	685	210	413	410	240	0	225	325	210	413	140	503
Rod 3	22	690	195	413	488	0	0	328	293	215	405	163	478
Rod 4	24	695	173	423	393	510	365	235	300	258	350	183	458
Rod 5	25	670	408	390	425	600	425	215	278	260	373	173	468
Rod 6	25	670	198	390	315	175	420	338	170	298	330	175	455
Rod 7	24	695	188	430	270	0	0	283	0	298	280	168	455
Rod 8	23	685	170	433	443	250	0	408	0	365	375	158	473
Rod 9	23	700	180	455	355	550	325	338	315	193	445	135	503
Rod 10	22	690	188	445	478	433	300	213	300	165	485	88	595
Rod 11	22	685	205	410	475	317	1020	210	308	165	455	90	340
Rod 12	22	710	173	438	478	475	300	193	193	178	488	98	588
Rod 13	23	695	183	443	508	433	625	200	363	200	468	120	553
Rod 14	22	705	205	430	510	385	355	168	363	228	400	123	535
Rod 15	22	705	218	403	450	580	498	185	185	208	410	125	538
Rod 16	23	690	200	423	355	310	525	170	313	225	393	138	530
Rod 17	23	675	215	368	277	0	235	388	0	348	350	148	478
Rod 18	21	685	283	348	0	0	0	465	0	340	0	178	423
Rod 19	21	685	143	470	550	0	0	175	0	328	0	160	410
Rod 20	20	700	175	465	343	275	150	438	0	423	340	115	533
Rod 21	21	690	173	480	293	150	0	300	297	195	405	98	578
Average	23	691	201	427	409	391	436	274	290	252	411	139	494

Table 16: Thickness of outer and inner oxide layers at four circumferential positions (in μm)

Elevation [mm]		250	350	450		550		650		750		850		950		1050
rod	angle	out	out	out	in	out*	in*	out	in	out	in	out	in	out	in	out
Rod 1	0°	14	90	500		950	170	850		800	120	370		160		110
	90°		150	650		820	150	~		450		500		150		106
	180°	14	100	520		650	100	~		~		400		150		108
	270°		210	500	20	950		330		~		300		150		112
Rod 2	0°	14	120	300	40	450	130	~		240		150		150		110
	90°		130	400		700		450		270		350		170		114
	180°	12	~	300	15	650		320		600		110		130		100
	270°		120	600	30	750	100	~		300		100		130		88
Rod 3	0°	14	150	300	10	~		900		~		120		150		100
	90°		150	300		550	80	~		700		150		160		120
	180°	10	140	300	30	700		480		700		150		150		112
	270°		150	350		1200		700		600		150		140		92
Rod 4	0°	16	120	480		950	160	~		400	30	120		170		118
	90°		140	450		900		300		550	20	220		180		128
	180°	14	120	550		350	250	400		800		400		180		134
	270°		150	350		550		~		680		200		170		130
Rod 5	0°	14	150	450	20	750	130	460		400	40	100		170		112
	90°		140	400		400	100	250		130	40	120		180		110
	180°	14	130	400		800		800		450	40	400		190		130
	270°		150	500		900		~		400	40	200		170		128
Rod 6	0°	14	160	500	20	800	150	970		400		480		200		134
	90°		210	~		400		600		1150		600		320		128
	180°	14	180	~		830	150	~		230		550		290		124
	270°		190	580	20	550		~		800		450		190		128
Rod 7	0°	14	140	~		300		550		950		480		320		140
	90°		200	~	180	1230		750		500		800		600	120	160
	180°	16	180	~		~		~		800		1050		550	120	170
	270°		180	470	120	760		450		250		680		290		128
Rod 8	0°	14	200	550		800	100	~		520		450		200		116
	90°		120	450	100	1100	80	~		200		400		310		116
	180°	14	120	550	100	1050		~		170		500		320		118
	270°		140	520	40	900	80	~		170		550		200		108
Rod 9	0°	12	170	400		700	100	350		470		150		150		94
	90°		120	480		550	50	250		~		270		170		98
	180°	14	110	600		850		600		450		370		150		80
	270°		130	800		570	100	650		380		250		130		72
Rod 10	0°	14	130	300		400		950	50	620		250		80		42
	90°		~	350		450		600	120	550	150	300		100		50
	180°	12	120	350	20	500		820		650		300		100		40
	270°		120	300		400		800		430		320		80		32
Rod 11	0°	14	130	300		950		~		250		220		90		50
	90°		140	250		550	120	350		350		250		120		60
	180°	10	120	250		450		500		600		300		90		42
	270°		130	400		620		~		700		100		90		32
Rod 12	0°	14	70	200		600		200		~		350		100		50
	90°		120	350		650		~		400		120		120		66
	180°	12	110	300		600		650		350		120		100		56
	270°		120	350		750		750		630		60		90		34

* 450 – no metal layer

Table 16 (cont.): Thickness of outer and inner oxide layers at four circumferential positions (in μm)

Elevation, mm		250	350	450		550		650		750		850		950		1050
rod	angle	out	out	out	in	out	in	out	in	out	in	out	in	out	in	out
Rod 13	0°	12	130	300		550		950		450		120		130		48
	90°		140	300		600		350		450		100		120		68
	180°	16	150	350		500	120	~		500		120		150		80
	270°		150	250		550	100	~		220		220		120		60
Rod 14	0°	12	140	400	30	500		500		300		130		120		60
	90°		140	250	30	450		650		270	80	120		150		80
	180°	16	150	300	10	900	90	220		390	250	60		150		98
	270°		140	220	20	500		500		350	250	100		140		80
Rod 15	0°	14	140	300	20	380		800		130		100		140		58
	90°		140	380		700	80	800	180	150		150		150		70
	180°	14	140	400	12	500		800		300		200		170		92
	270°		140	300		500		700		300	100	100		150		82
Rod 16	0°	14	140	500	10	750		550		150		300		150		70
	90°		150	450		650		450		200		170		150		68
	180°	16	130	380	20	850		160		330	50	450		170		90
	270°		140	350		950		250		200		150		170		98
Rod 17	0°	14	150	450	120	950	150	~		500	40	520		190		108
	90°		210	850	200	550		1800		630	120	470		200		92
	180°	12	~	~	100	700		250		830		700		420		134
	270°		180	900	100	1000	100	~		560		640		330		126
Rod 18	0°	14	~	~		400	100	~		1450		600	110	450		190
	90°		~	1000	150	1070	50	~		~		550		400		106
	180°	14	~	750		400		1000		~		970		620		182
	270°		300	~	150	900		120		400		860		600		200
Rod 19	0°	16	200	~		1180		650		550		1020		540		180
	90°		220	720	200	850		~		~		450				186
	180°	12	130	750	200	1160		600		450		700	110	520		104
	270°		140	~		1100		1200		480	500	780				130
Rod 20	0°	14	100	550	150	1000		800		680		500		300		118
	90°		100	300	20	500	150	450		220		870		690	30	102
	180°	10	160	550	50	600	150	400		650		400		330		72
	270°		110	600	100	850	100	400		500		600		440		80
Rod 21	0°	14	100	500		400		350		~		270		130		68
	90°		~	750	170	900		600	130	~		250		430		68
	180°	10	110	500	120	600		600		~		150		150		50
	270°		~	550	100	600	100	850		~		320		260		48
Rod A	0°											300		90		24
	90°											350		90		30
	180°											320		90		24
	270°											300		90		20
Rod C	0°	10	~											650		
	90°		160											590		
	180°	12	180											670		
	270°		300											720		

Table 17: Thickness of outer and inner oxide layers averaged circumferentially (in μm)

Elevation, mm	250	350	450		550		650		750		850		950		1050
Rod	out	out	out	in	out*	in*	out	in	out	in	out	in	out	in	out
Rod 1	14	138	543	20	843	140	590		625	120	393		153		109
Rod2	13	123	400	28	638	115	385		353		178		145		103
Rod 3	12	148	313	20	817	80	693		667		143		150		106
Rod 4	15	133	458		688	205	350		608	25	235		175		128
Rod 5	14	143	438	20	713	115	503		345	40	205		178		120
Rod 6	14	185	540	20	645	150	785		645		520		250		129
Rod 7	15	175	470	150	763		583		625		753		440	120	150
Rod 8	14	145	518	120	963	87	~		265		475		258		115
Rod 9	13	133	570		668	83	463		433		260		150		86
Rod 10	13	433	325	20	438		793	85	563	150	293		90		41
Rod 11	12	130	300		643	120	425		475		218		98		46
Rod 12	13	105	300		650		533		460		163		103		52
Rod 13	14	143	300		550	110	650		405		140		130		64
Rod 14	14	143	293	23	588	90	468		328	193	103		140		80
Rod 15	14	140	345	16	520	80	775	180	220	100	138		153		76
Rod 16	15	140	420	15	800		353		220	50	268		160		82
Rod 17	13	180	733	130	800	125	1025		630	80	583		285		115
Rod 18	14	300	875	150	693	75	560		925		745	110	518		170
Rod 19	14	173	735	200	1073		817		493	500	738	110	530		150
Rod 20	12	118	500	80	738	133	513		513		593		440	30	93
Rod 21	12	105	575	130	625	100	600	130	~		248		243		59
average	14	163	474	71	**707**	113	593	132	490	**140**	352	110	228	75	99
max	15	433	875	200	**1073**	205	1025	180	925	**500**	753	110	530	120	170
st.deviation	1	74	162	64	145	34	178	48	177	**146**	**220**	0	138	64	36
Rod A											318		90		25
Rod C	11	213											658		

Table 18: Thickness of outer secondary oxide layer averaged for eight circumferential positions (in μm)

Elevation	350 mm		450 mm		550 mm		650 mm		750 mm		850 mm	
rod	δ	σ	δ	σ	δ	σ	δ	σ	δ	σ	δ	σ
1	**80**	40	**424**	148	**513**	338	**317**	173	**619**	386	**280**	173
2	**64**	45	**361**	136	**550**	207	**380**	190	**291**	311	**164**	101
3	**121**	80	**184**	134	**451**	227	**414**	223	**322**	305	**128**	91
4	**55**	41	**361**	150	**495**	197	**230**	116	**360**	158	**141**	85
5	**67**	49	**354**	96	**564**	259	**241**	166	**266**	153	**188**	130
6	**106**	49	**374**	181	**728**	213	**453**	293	**351**	251	**317**	160
7	**107**	59	**263**	108	**515**	271	**432**	283	**350**	201	**431**	270
8	**79**	81	**403**	153	**826**	36	**465**	340	**237**	200	**319**	174
9	**34**	30	**369**	141	**455**	277	**300**	143	**309**	221	**250**	187
10	**54**	42	**211**	160	**492**	240	**672**	272	**538**	214	**200**	100
11	**54**	35	**243**	167	**412**	270	**330**	320	**383**	193	**173**	113
12	**56**	49	**299**	160	**435**	149	**364**	211	**399**	279	**110**	86
13	**57**	40	**231**	160	**431**	182	**534**	378	**377**	186	**93**	55
14	**66**	72	**183**	133	**420**	258	**366**	259	**287**	123	**110**	92
15	**61**	62	**284**	151	**287**	201	**527**	355	**239**	163	**92**	43
16	**84**	50	**289**	151	**587**	240	**288**	167	**236**	139	**195**	121
17	**123**	70	**434**	290	**612**	272	**406**	258	**578**	193	**400**	197
18	**123**	76	**579**	326	**537**	344	**342**	231	**943**	623	**503**	240
19	**69**	35	**634**	384	**730**	343	**405**	312	**403**	219	**490**	220
20	**58**	26	**371**	146	**564**	272	**344**	216	**358**	197	**517**	225
21	**34**	25	**424**	134	**417**	144	**567**	303	**57**	41	**297**	138
elevation average	***74***	*50*	***346***	*172*	***525***	*235*	***399***	*248*	***376***	*226*	***257***	*143*

δ – thickness;

σ – standard deviation.

Table 19: Estimated contribution mechanisms for hydrogen release

Mechanism	H_2 mass, g
Oxidation of claddings before reflood initiation	9
Oxidation of shroud and 4 corner rods before reflood initiation	4
Total hydrogen production before reflood initiation measured by mass spectrometer	16
Hydrogen release during reflood	
Re-oxidation of nitrides inside claddings	5
Oxidation of melt relocated from claddings	3
Oxidation of melt inside claddings	16
Oxidation of solid cladding metal by steam penetrated through the porous re-oxidized layer at elevations 300 – 900 mm (secondary oxidation of outer cladding surface)	46
Oxidation of inner surface of cladding by steam penetrated through damaged cladding	6
Oxidation of not nitrided claddings at elevation above 900 mm	5
Total contribution of claddings during reflood	**81**
Re-oxidation of nitrides inside shroud and 2 corner rods	*2*
Oxidation of melt relocated from shroud	*3*
Oxidation of shroud melt outside bundle	*11*
Oxidation of shroud and 2 corner rods metal by steam penetrated through the porous re-oxidized layer at elevations 300 – 900 mm	*26*
Oxidation of not nitrided shroud at elevation above 900 mm	*1*
Total contribution of shroud and corner rods during reflood	***43***
Total hydrogen production during reflood: by metallography / by mass spectrometer	124 (81+43) / 128

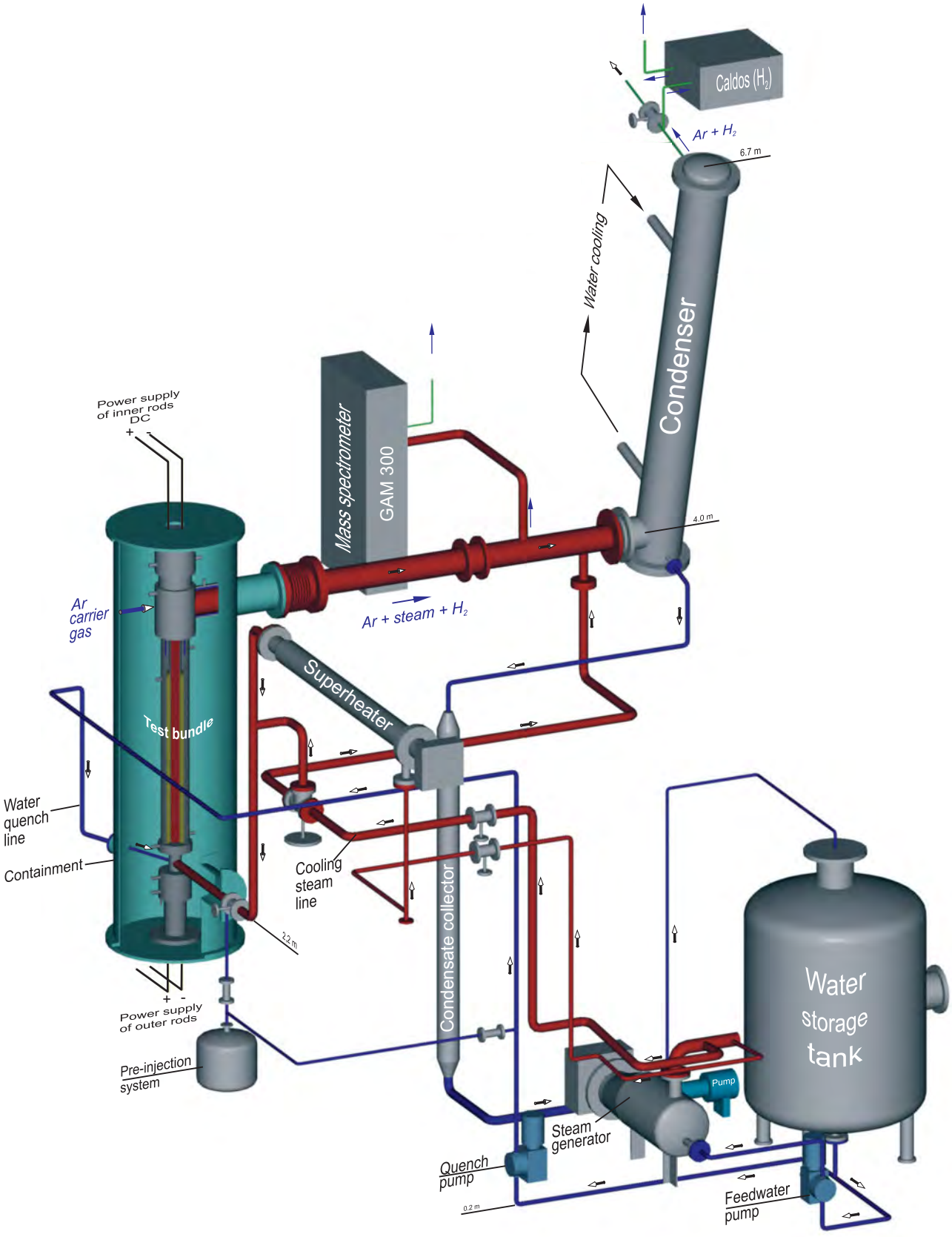

Fig. 1: QUENCH Facility - Main components.

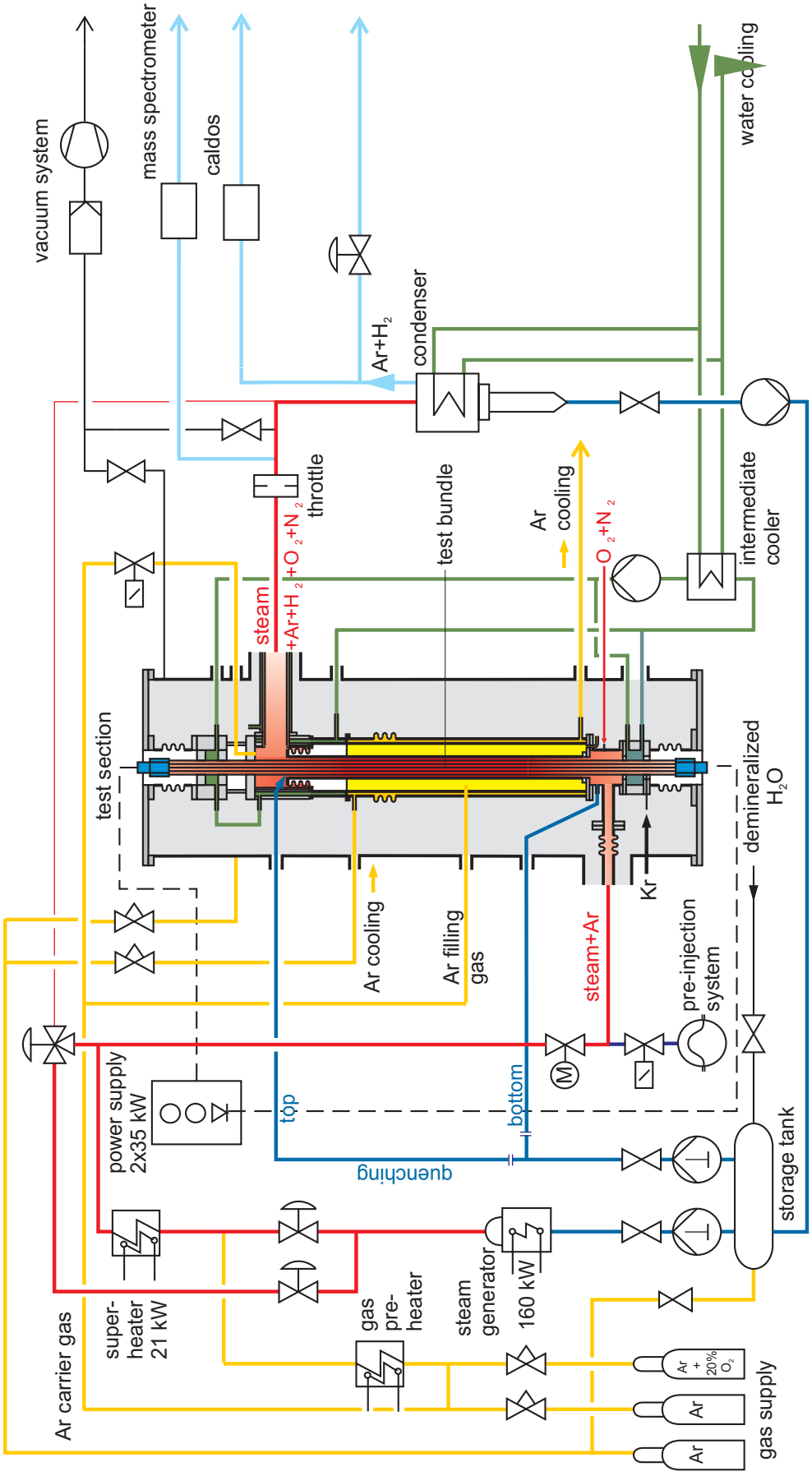

Fig. 2: Flow diagram of the QUENCH test facility.

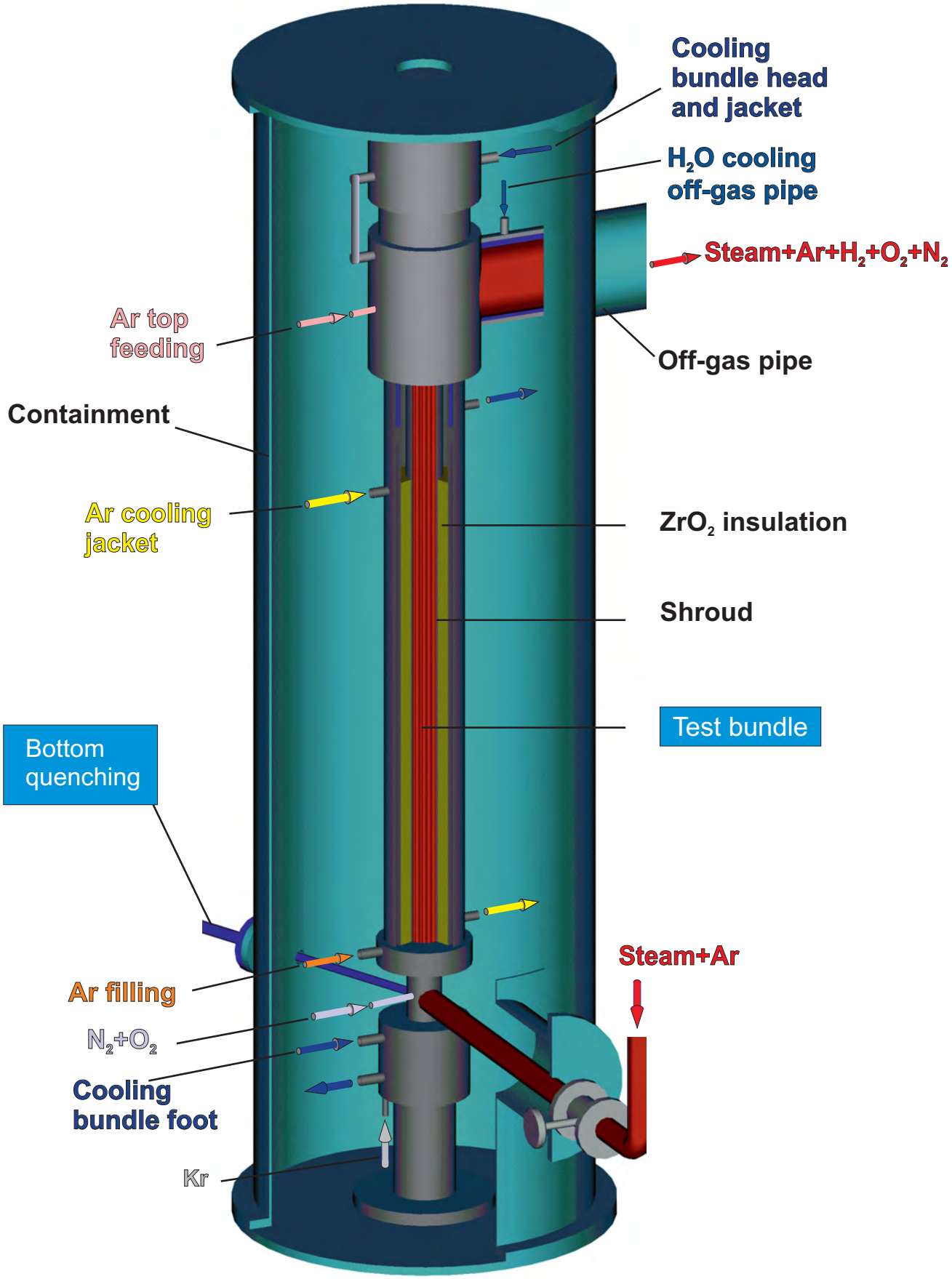

Fig. 3: QUENCH Facility; Containment and test section.

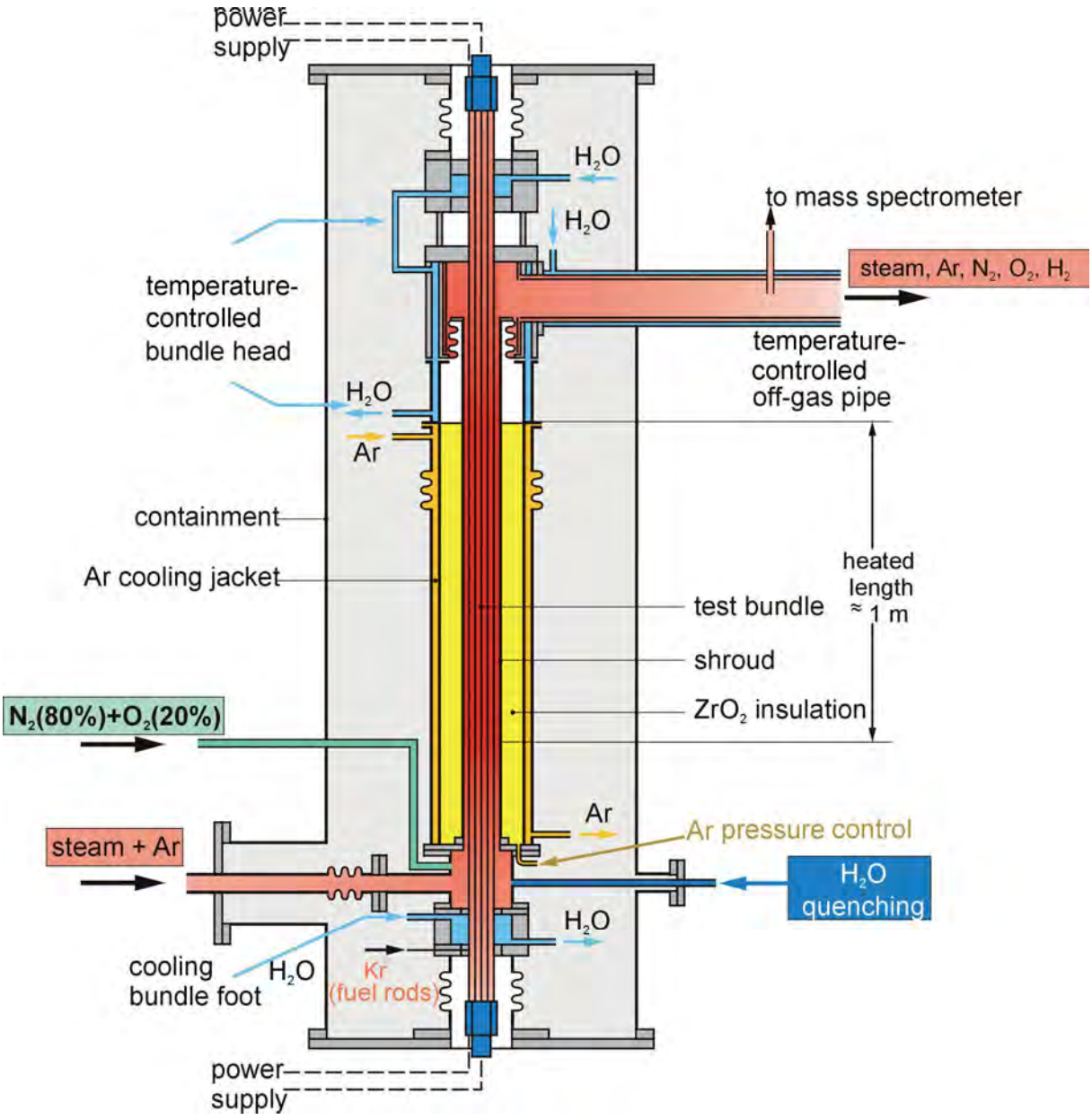

Fig. 4: QUENCH-16; Test section with flow lines.

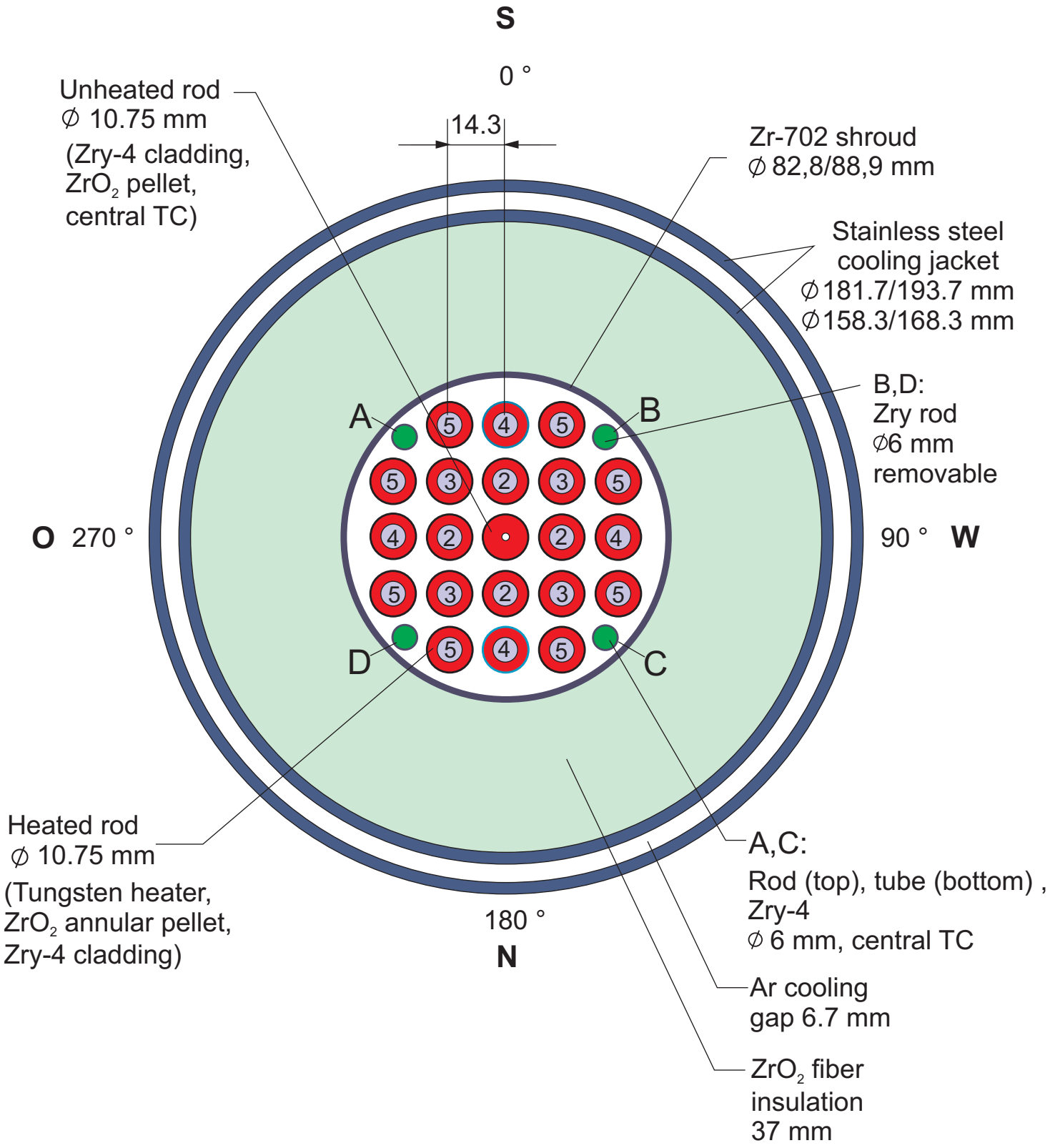

Fig. 5: QUENCH-16; Fuel rod simulator bundle (cross section, top view) including rod type indications.

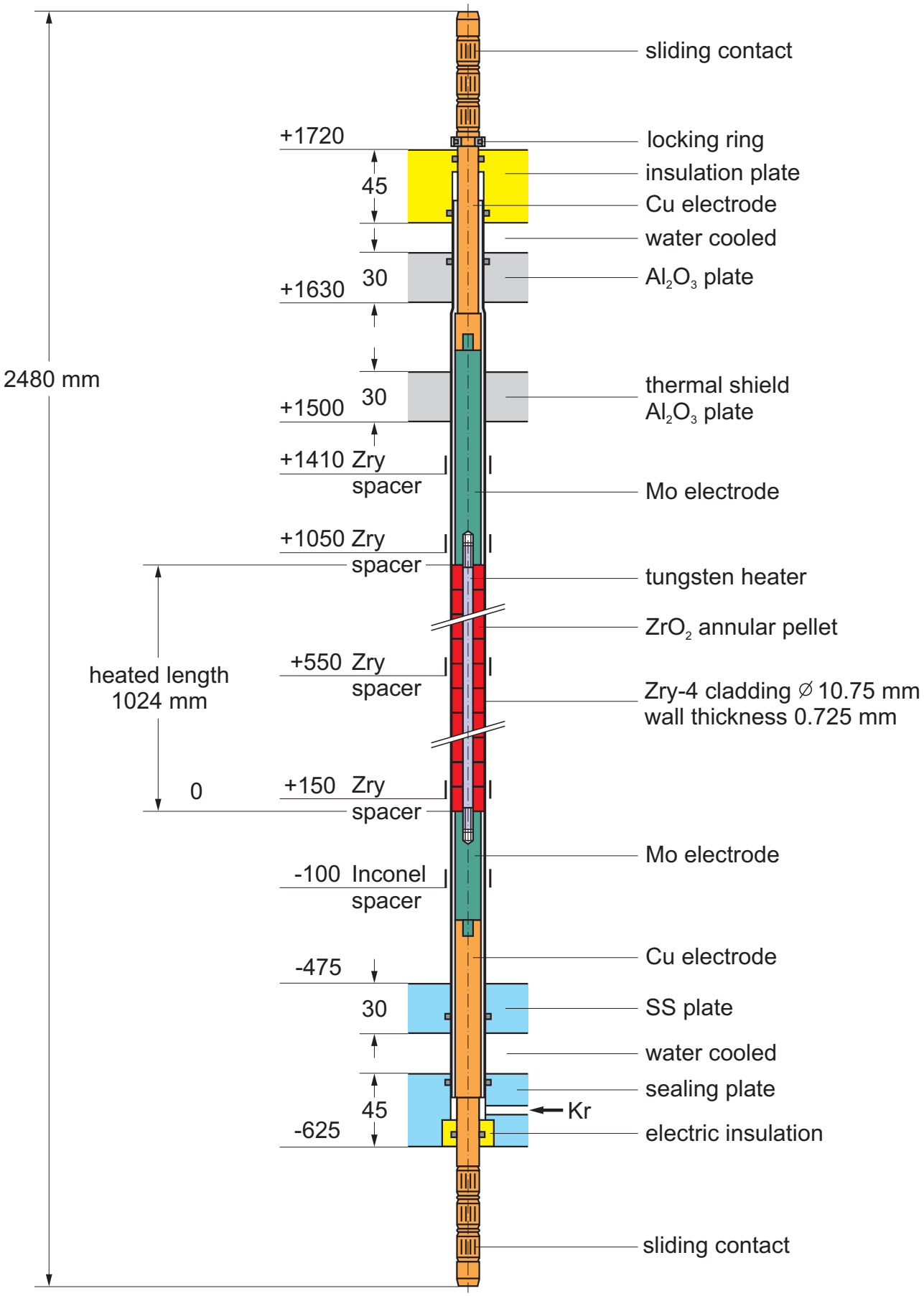

Fig. 6: Heated fuel rod simulator.

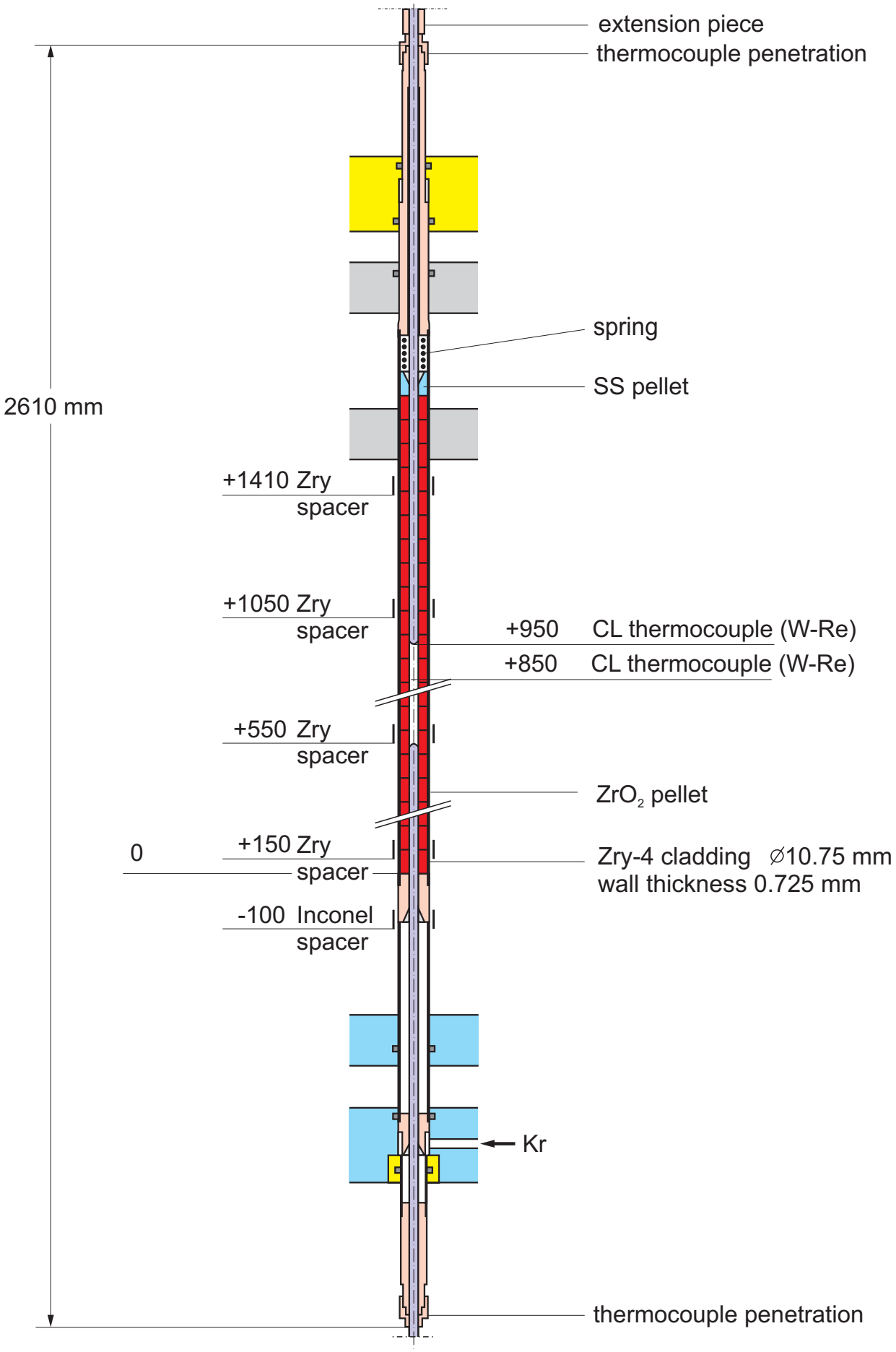

Fig. 7 : Unheated fuel rod simulator.

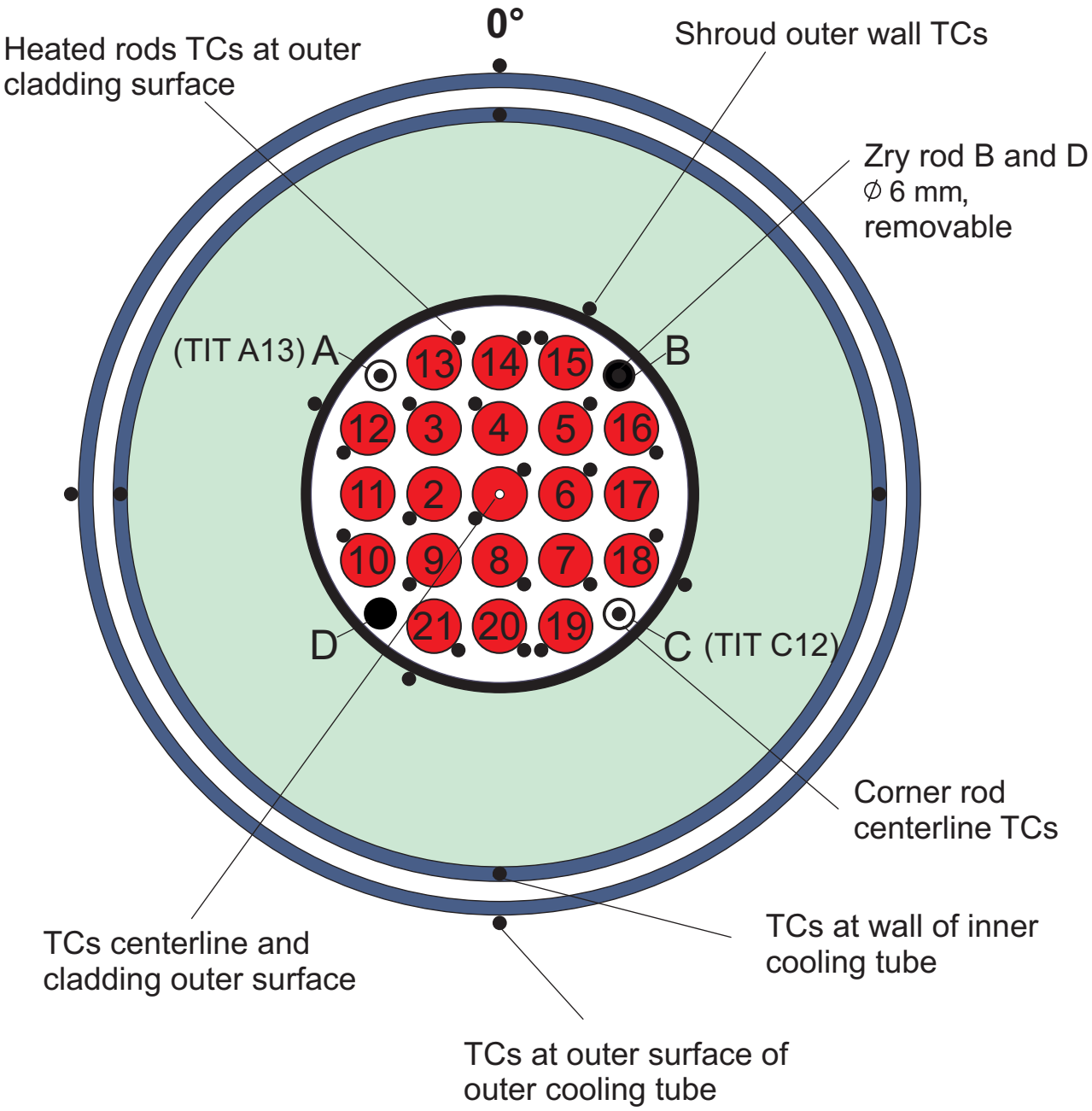

Fig. 8: QUENCH-16; Test bundle; TC instrumentation and rod designation (top view).

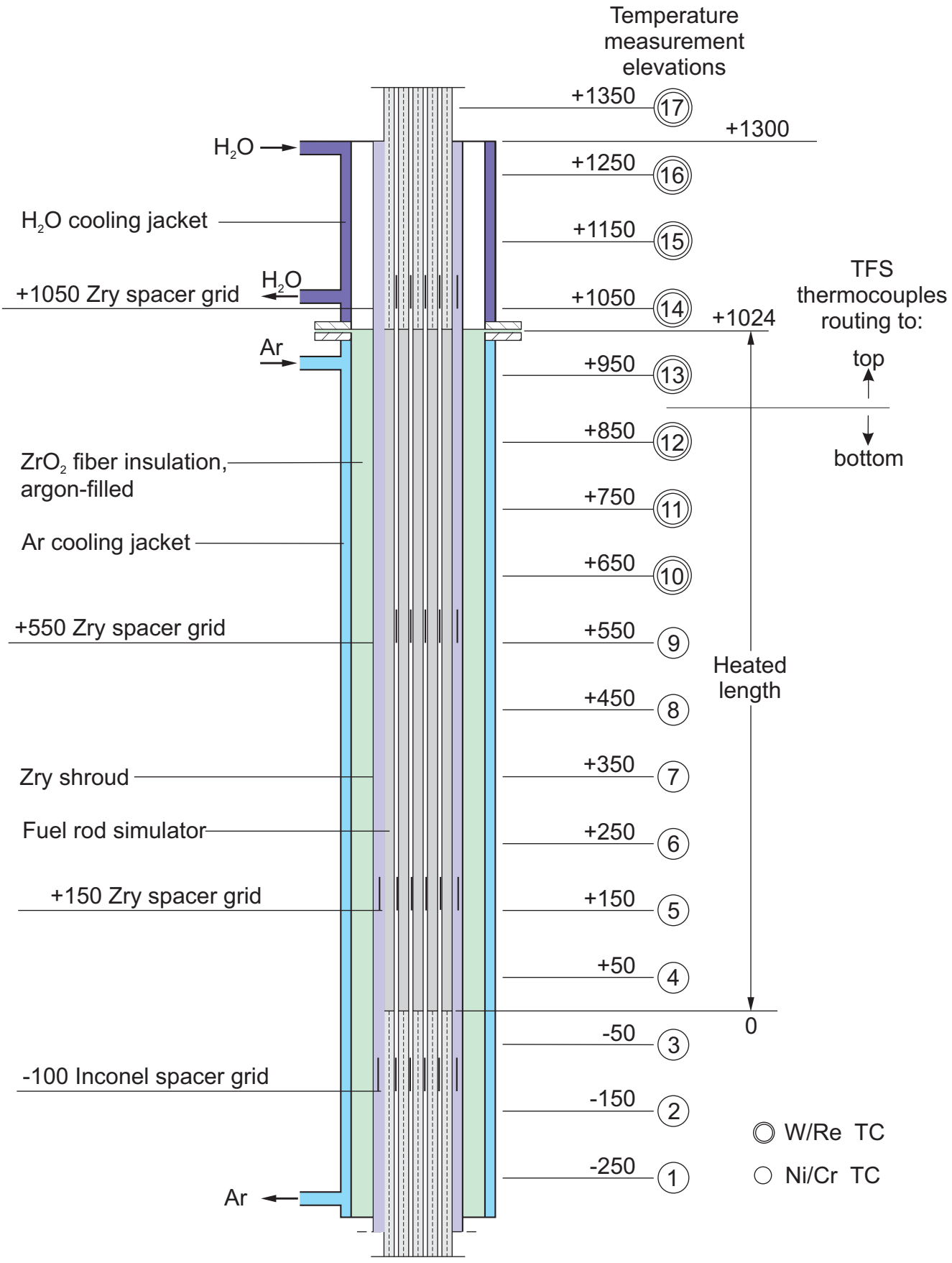

Fig. 9: Axial temperature measurement locations in the QUENCH test section.

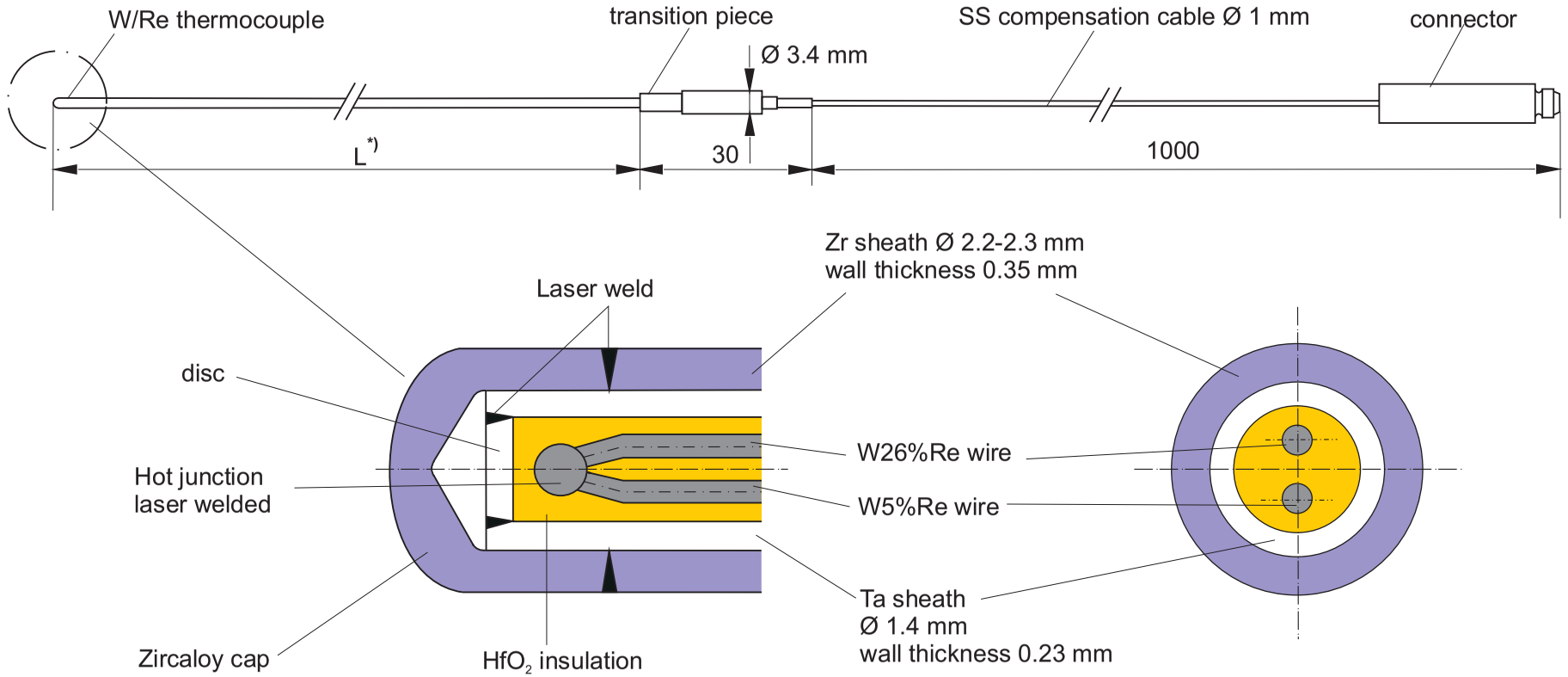

*) L: high-temperature section length dependent on the TC position in the test bundle: 500-1700 mm

Fig. 10: QUENCH; High-temperature thermocouple.

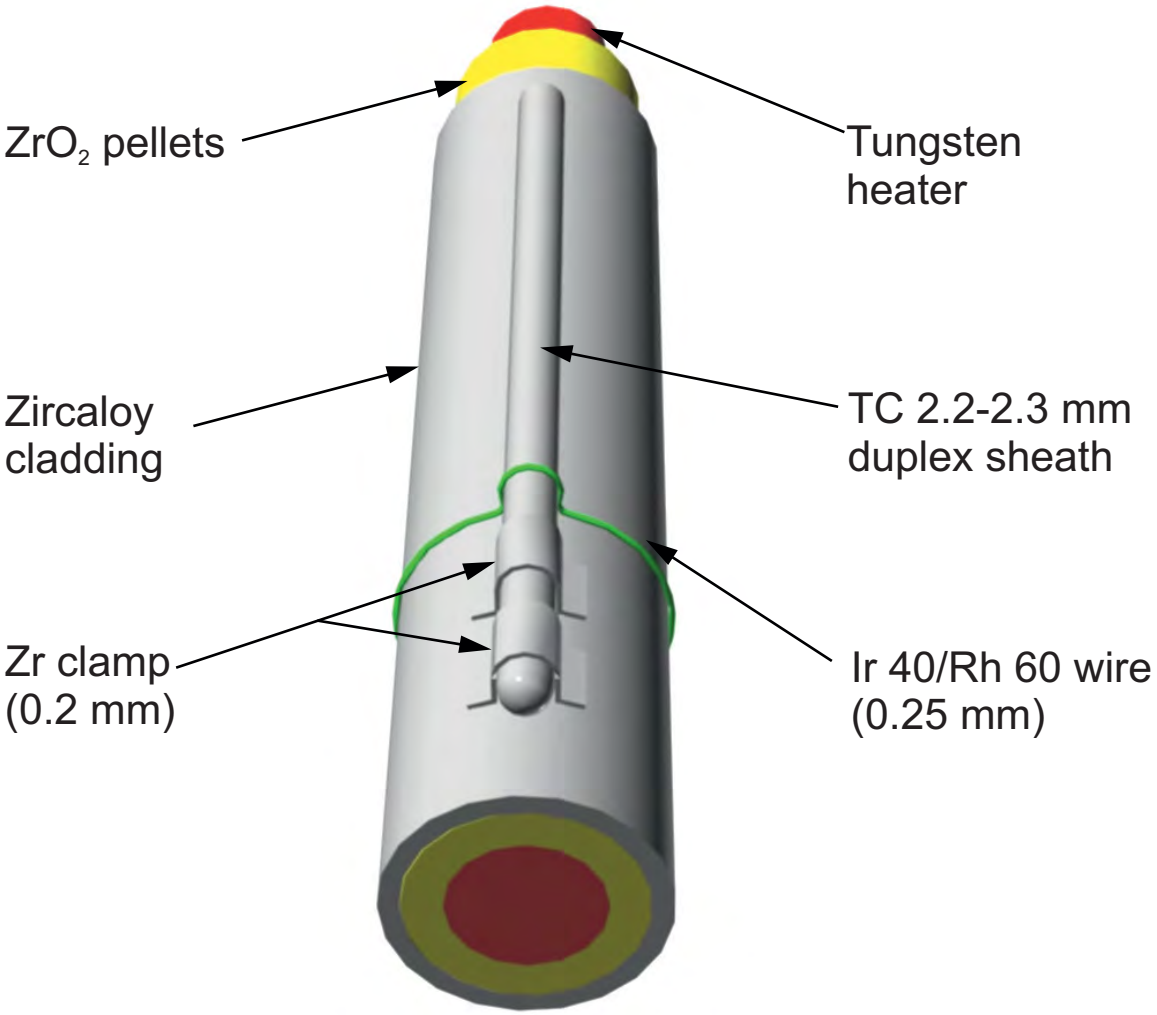

Fig. 11: QUENCH-16; Concept for TC fastening at the test rod.

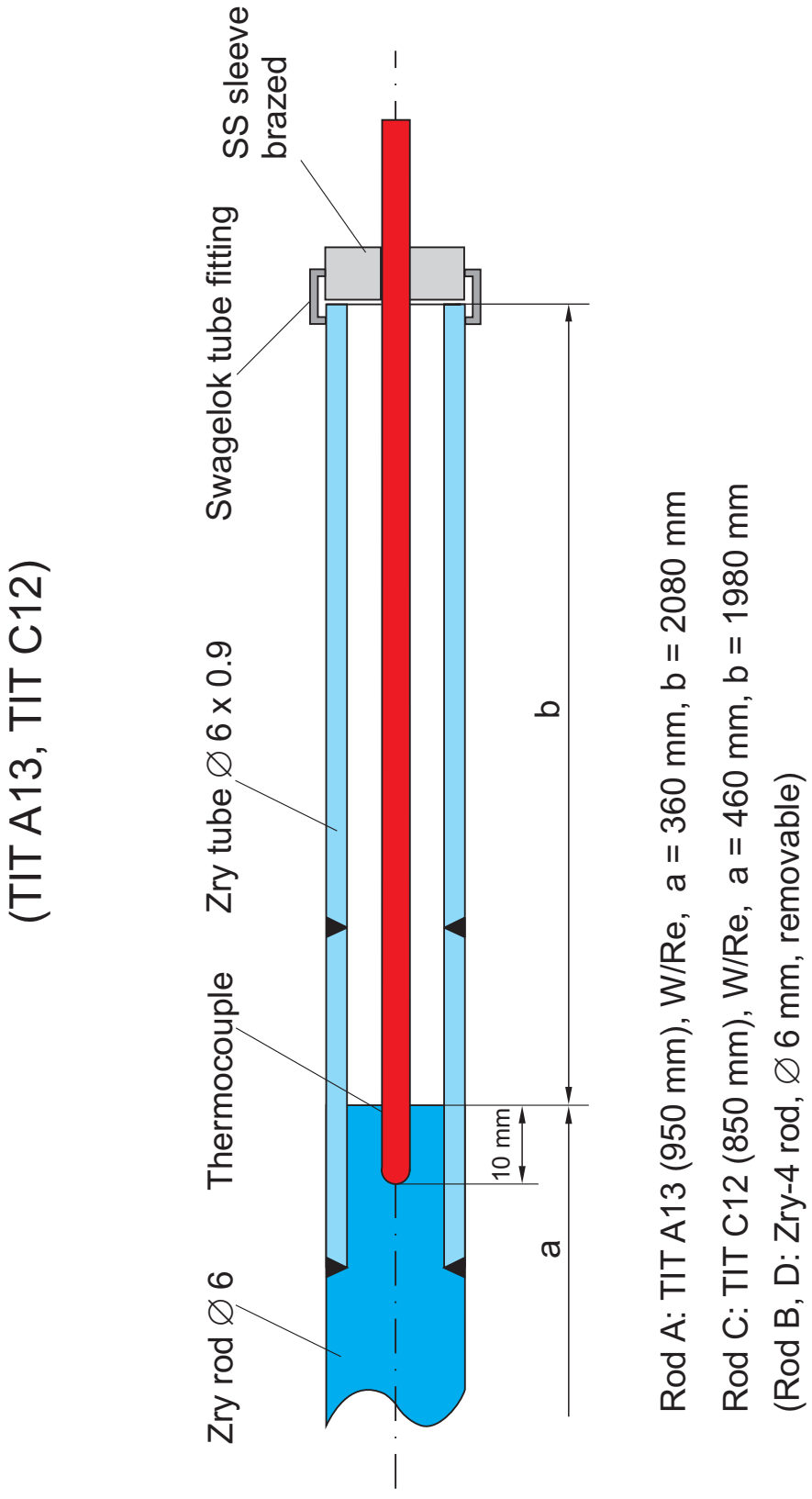

Fig. 12: QUENCH-16; Arrangement of the thermocouples inside the corner rods.

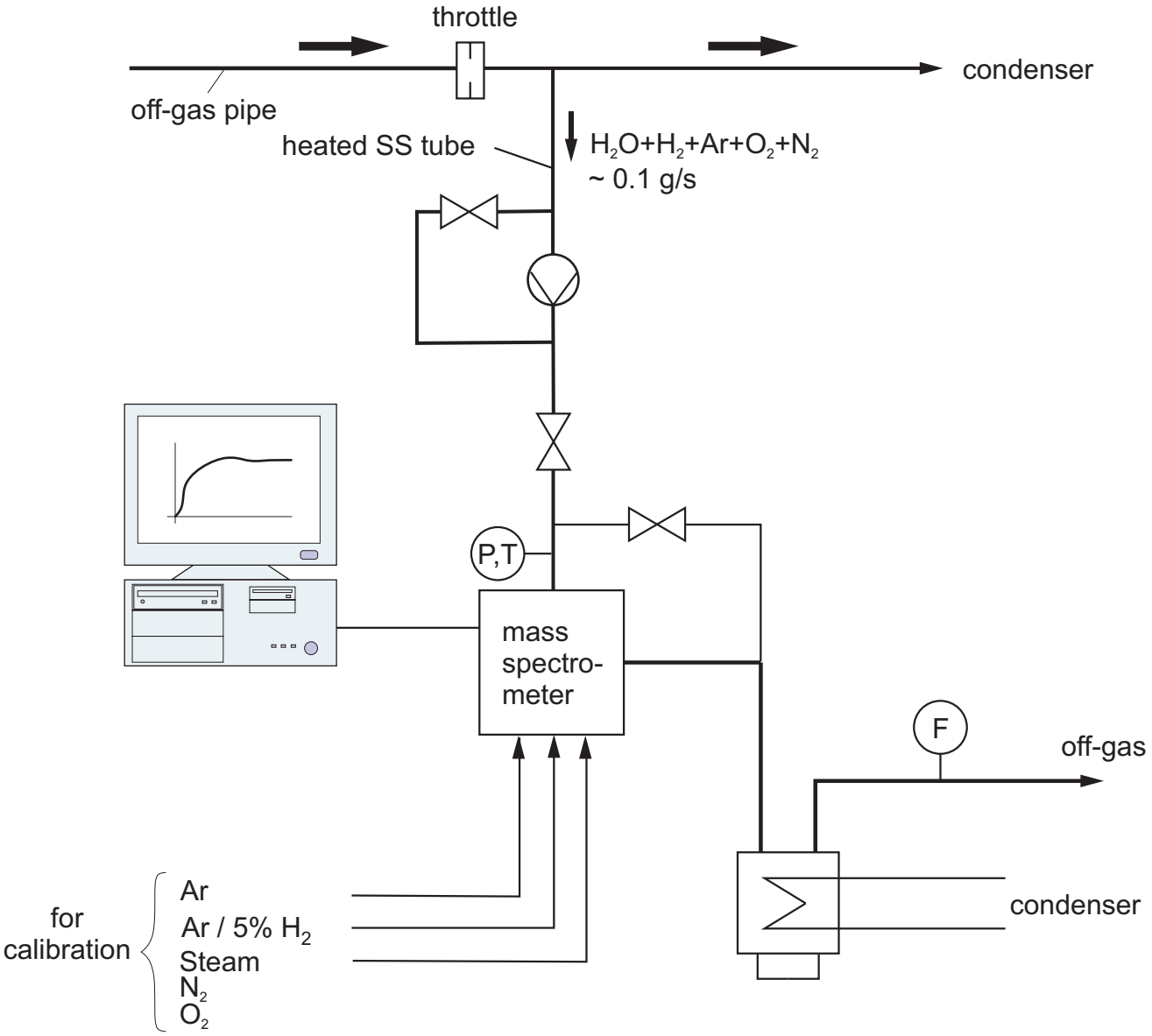

Fig. 13: QUENCH Facility; gas measurement with the GAM 300 mass spectrometer.

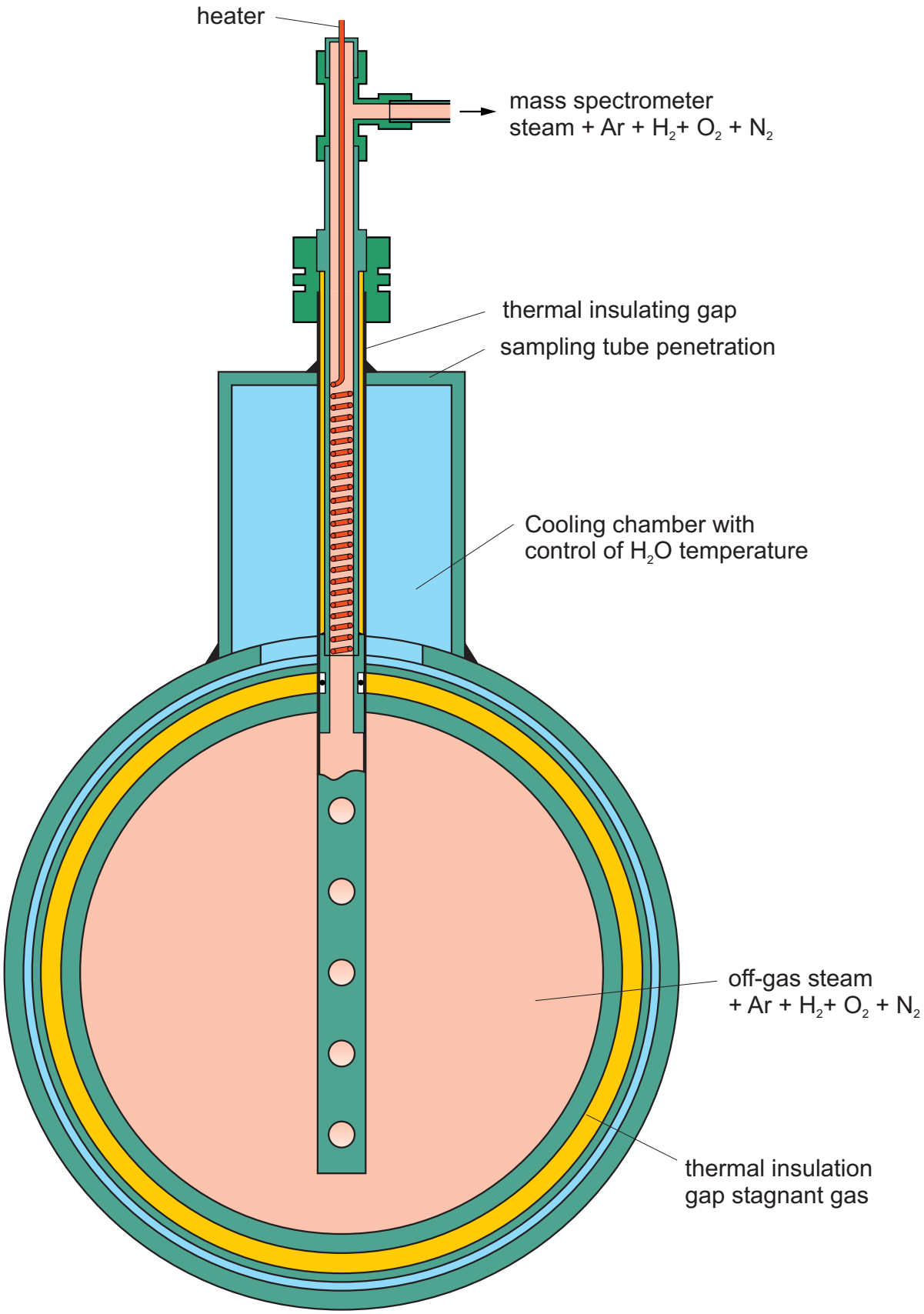

Fig. 14: Mass spectrometer sampling position at the off-gas pipe of the QUENCH test facility.

TC inserted from bundle bottom up to 850 mm

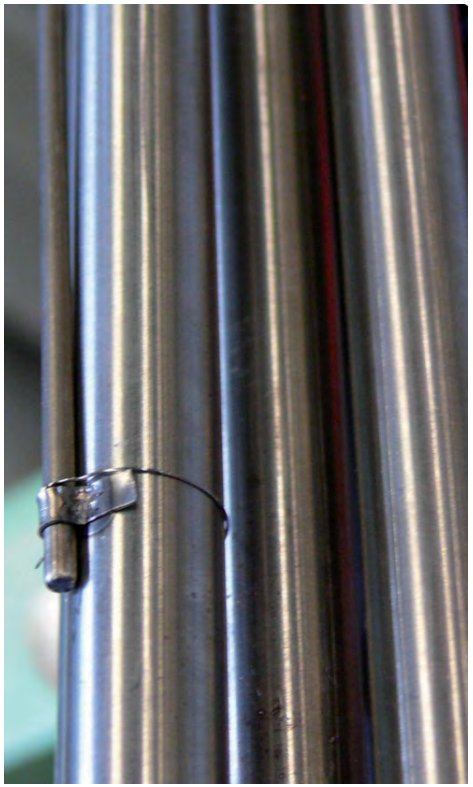

TC inserted from bundle top above 850 mm

TC inserted from bundle top under GS4 (1150 mm)

Cladding surface thermocouples TFS

TC installed at shroud

Shroud thermocouples TSH

Fig.15: QUENCH-16; Mounting of high temperature thermocouples.

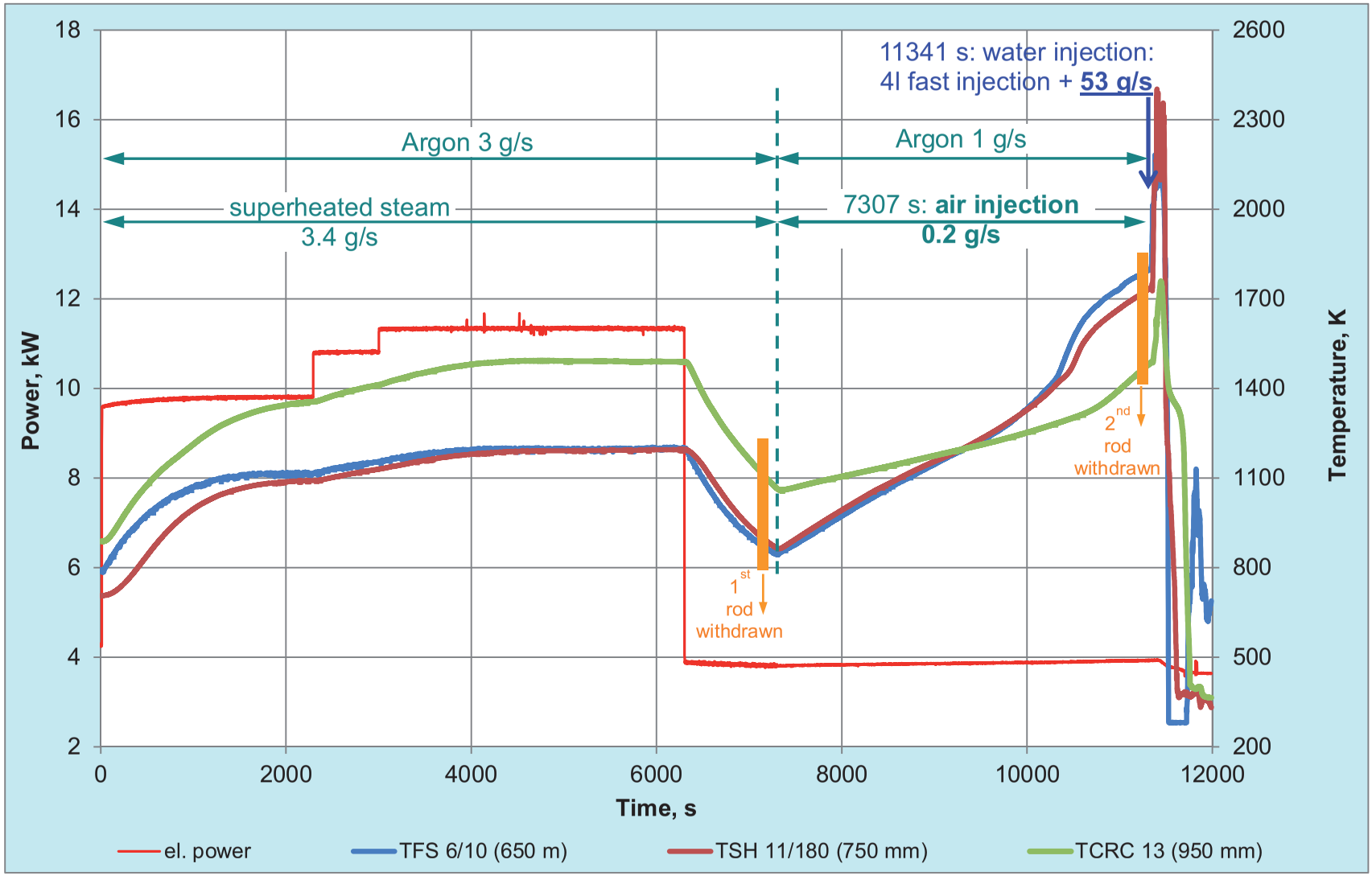

Fig.16: QUENCH-16; Test conduct showing electric power input and selected temperatures.

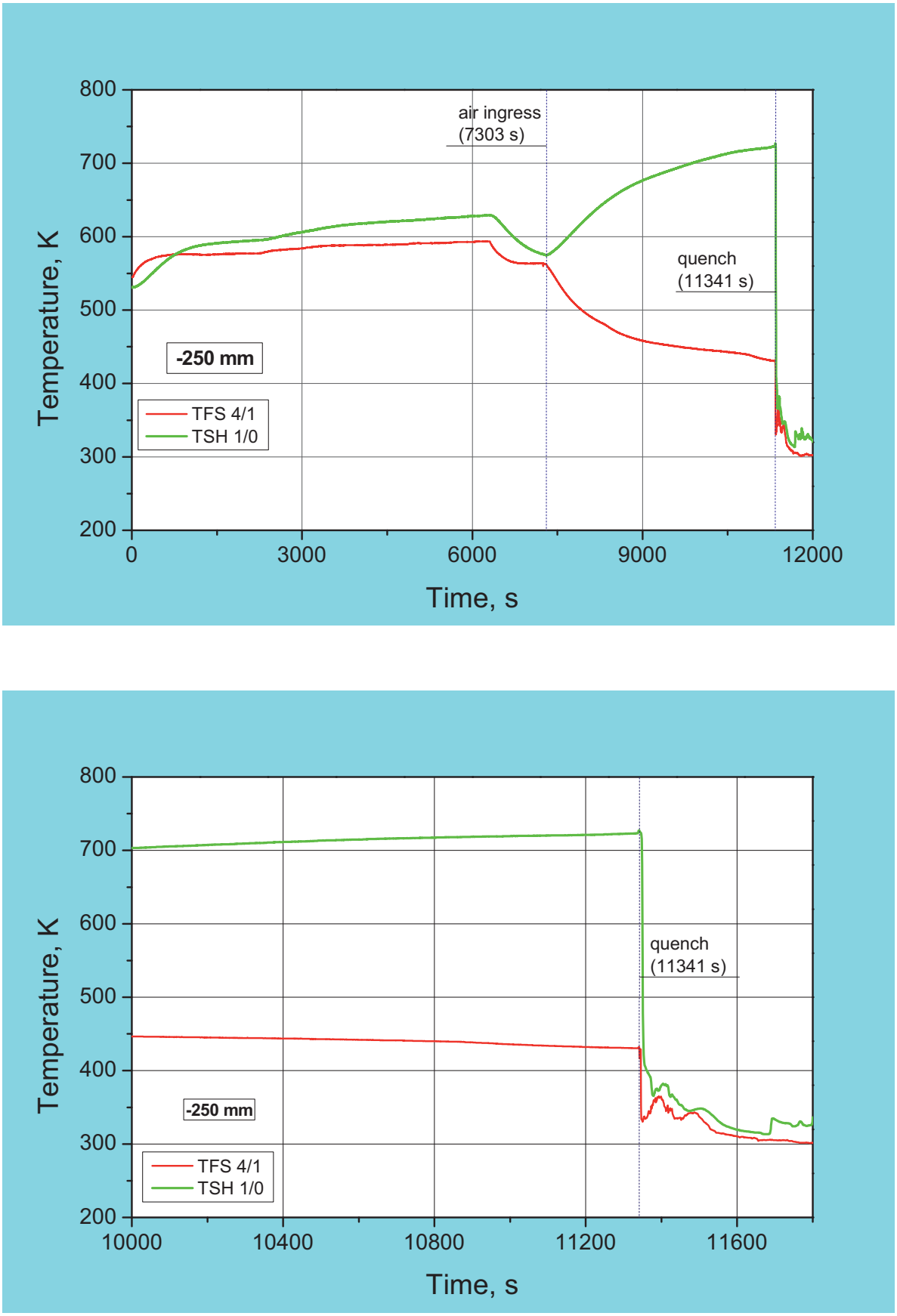

Fig.17: QUENCH-16; Temperatures measured by (TFS 4/1) and shroud (TSH 1/0) thermocouples at -250 mm elevation.

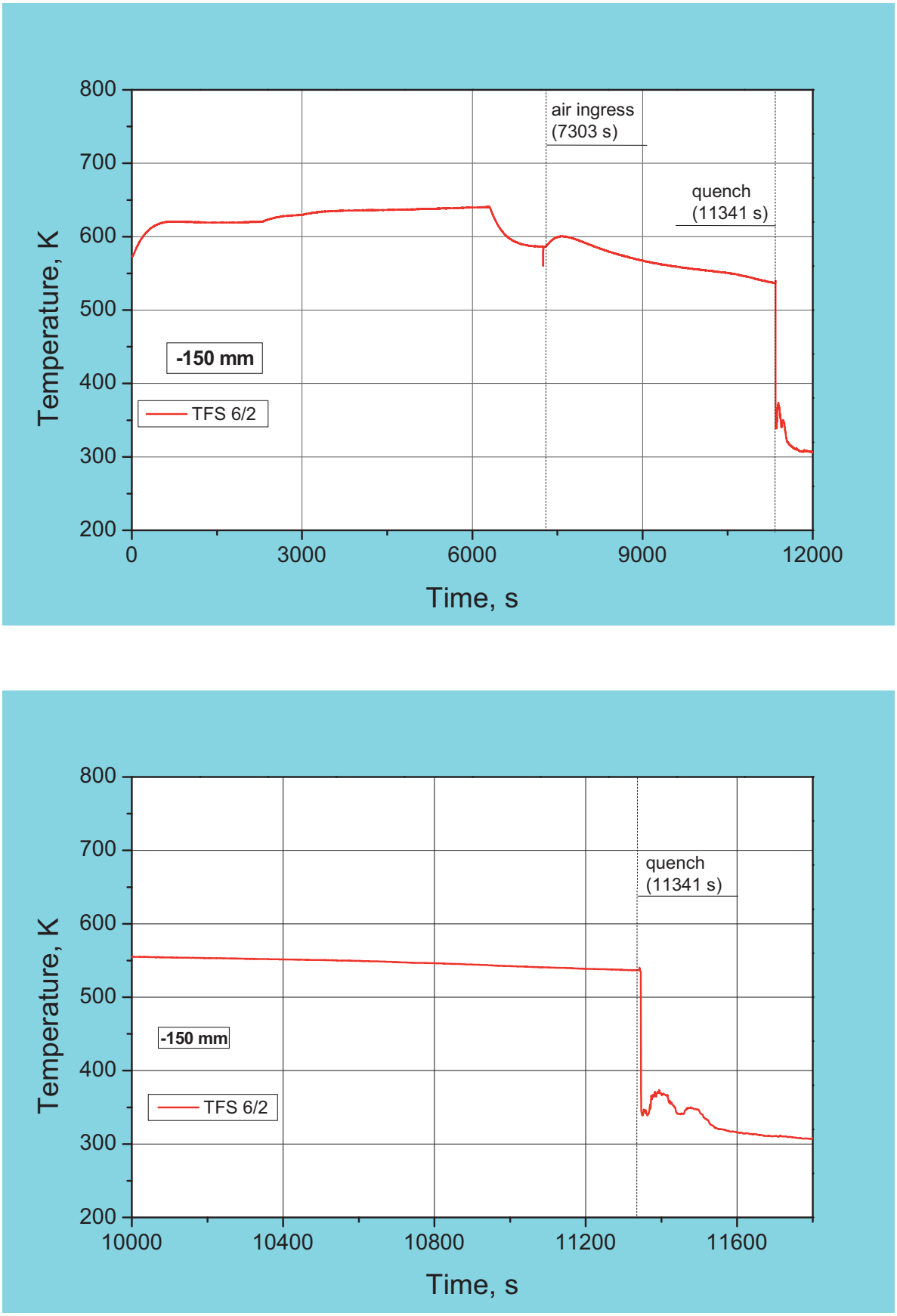

Fig.18: QUENCH-16; Temperatures measured by TFS 6/2 thermocouples at -150 mm elevation.

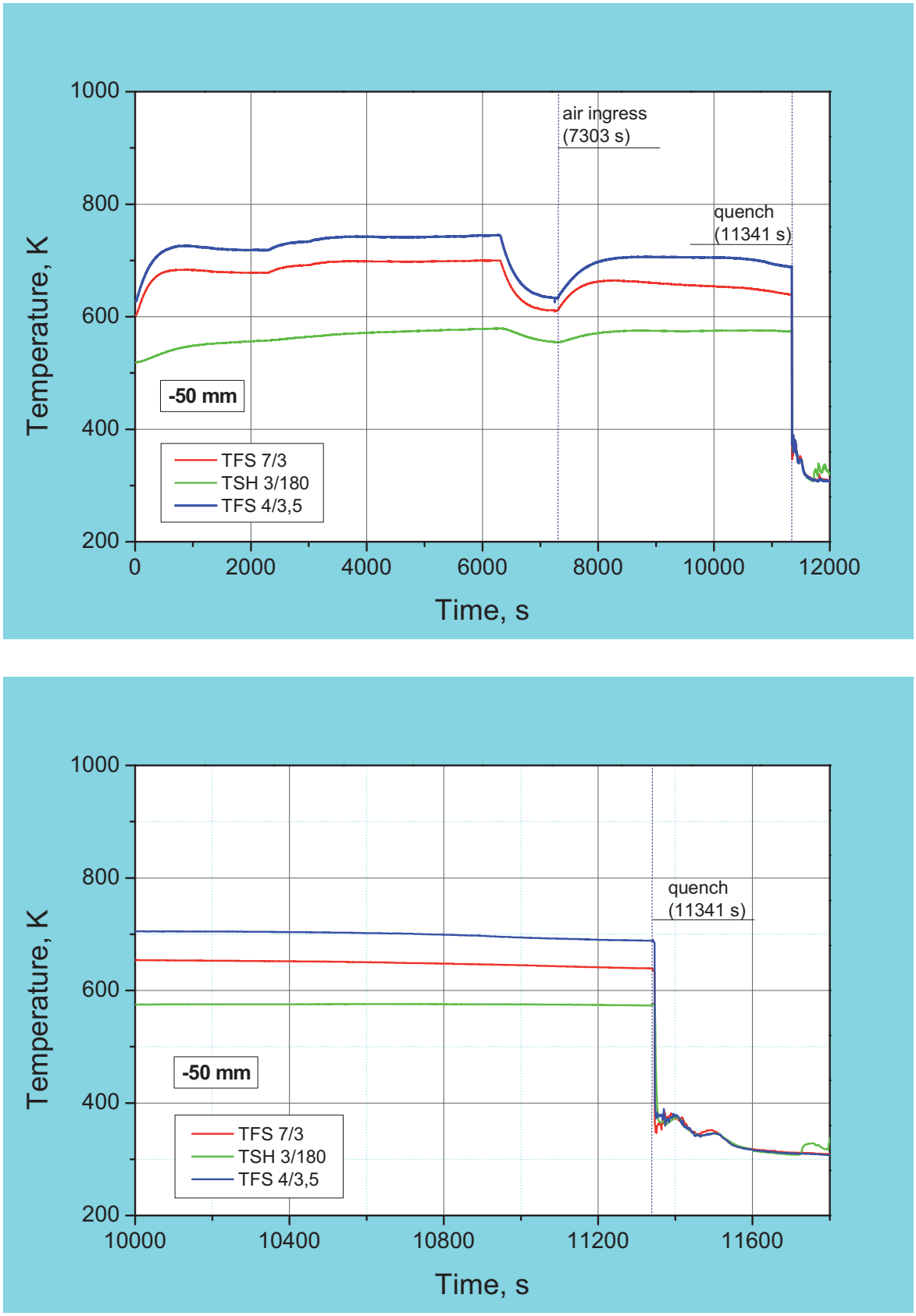

Fig.19: QUENCH-16; Temperatures measured by rod cladding (TFS) and shroud (TSH 3/180) thermocouples at -50 mm elevation.

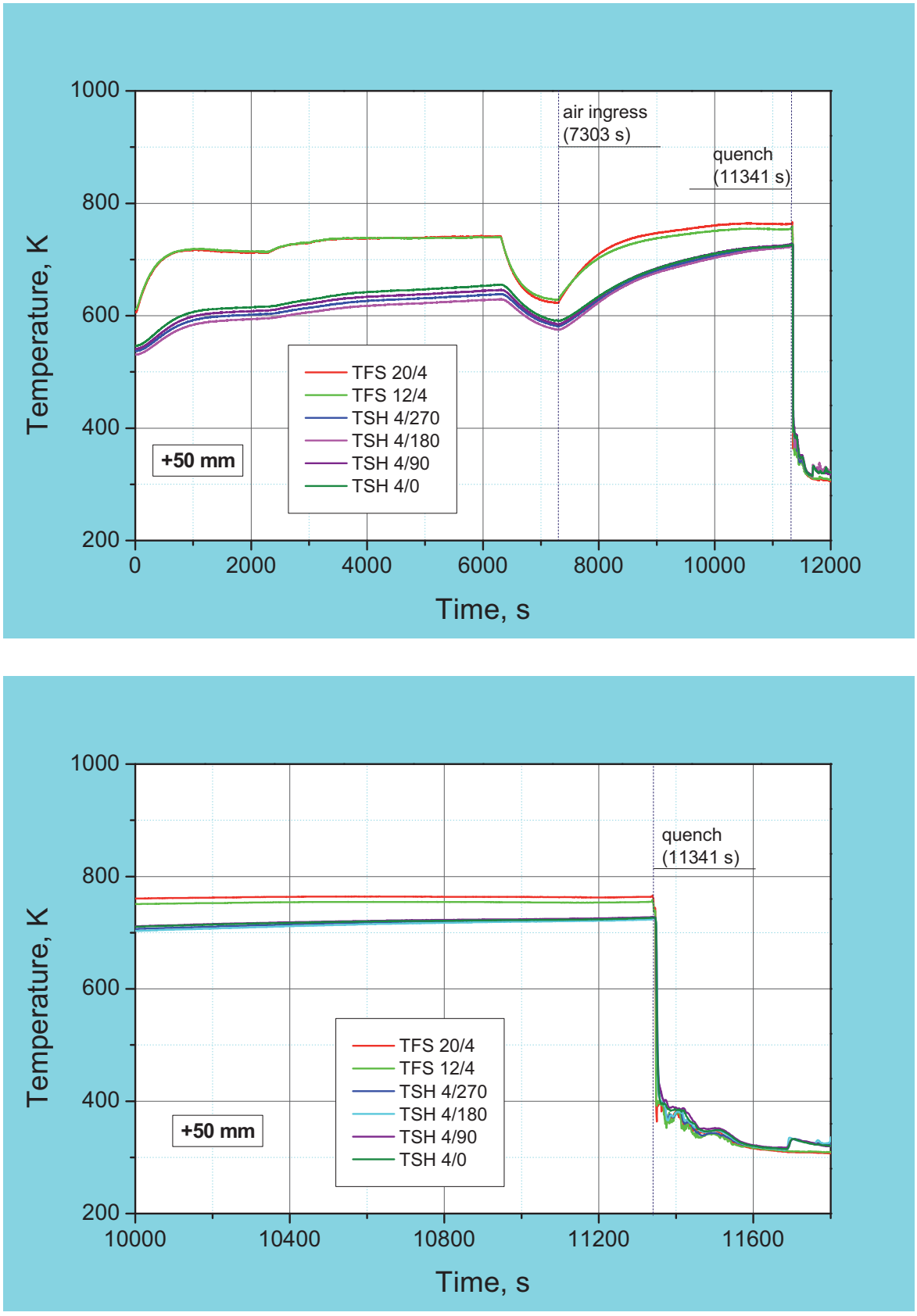

Fig. 20: QUENCH-16; Temperatures measured by rod cladding (TFS) and shroud (TSH) thermocouples at 50 mm elevation.

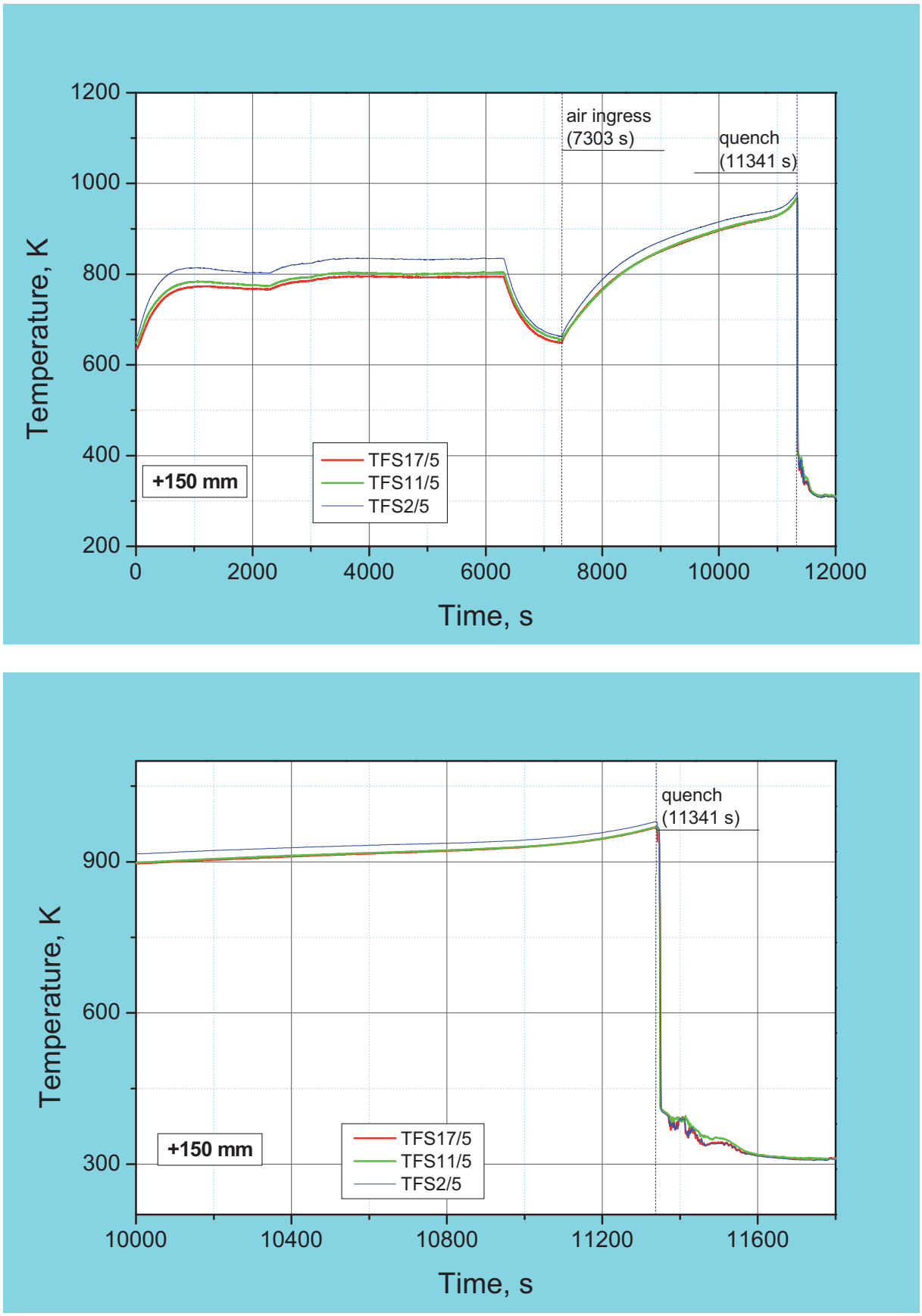

Fig. 21: QUENCH-16; Temperatures measured by rod cladding (TFS) and shroud (TSH) thermocouples at 150 mm elevation.

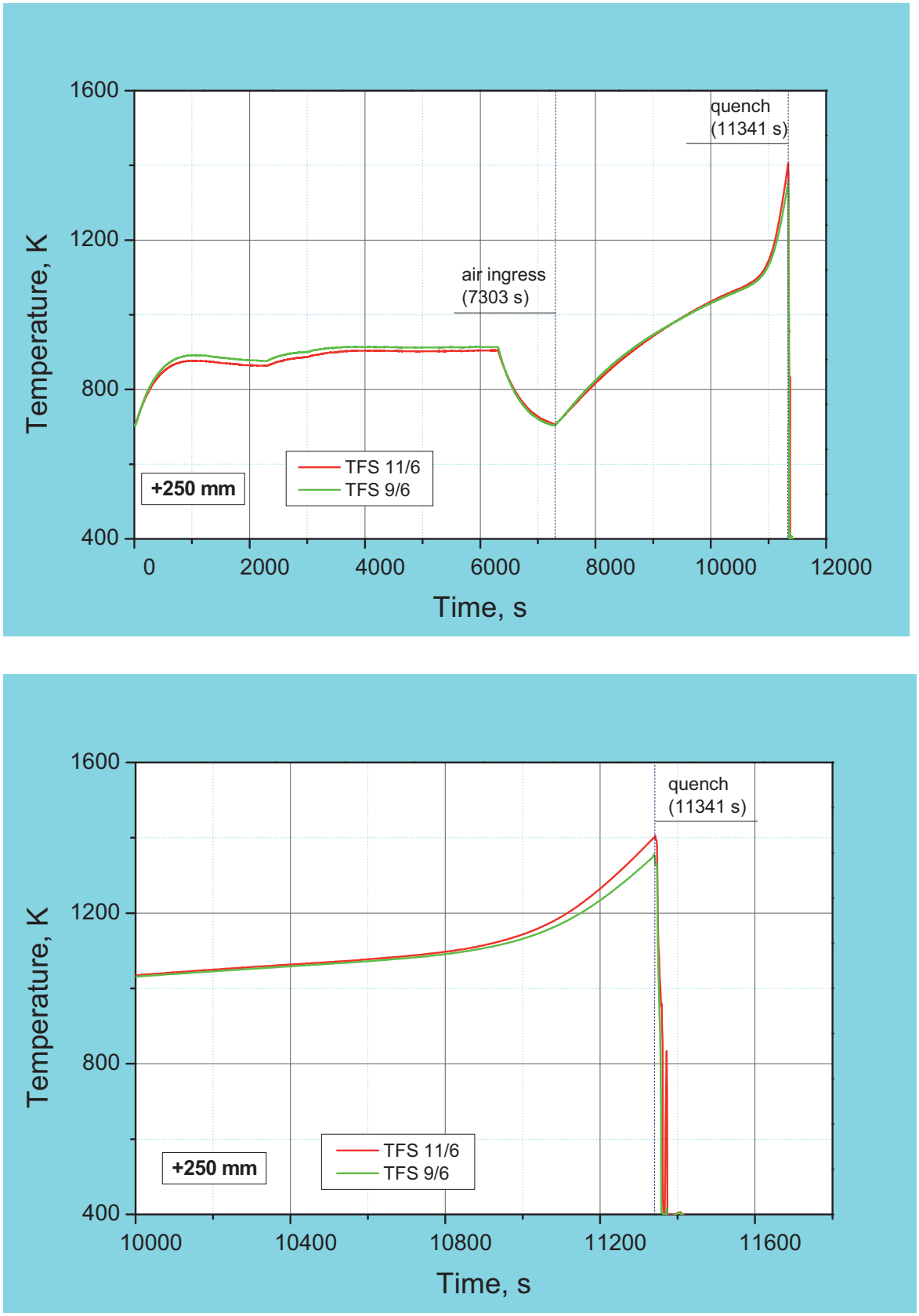

Fig. 22: QUENCH-15; Temperatures measured by rod cladding (TFS) and shroud (TSH) thermocouples at 250 mm elevation.

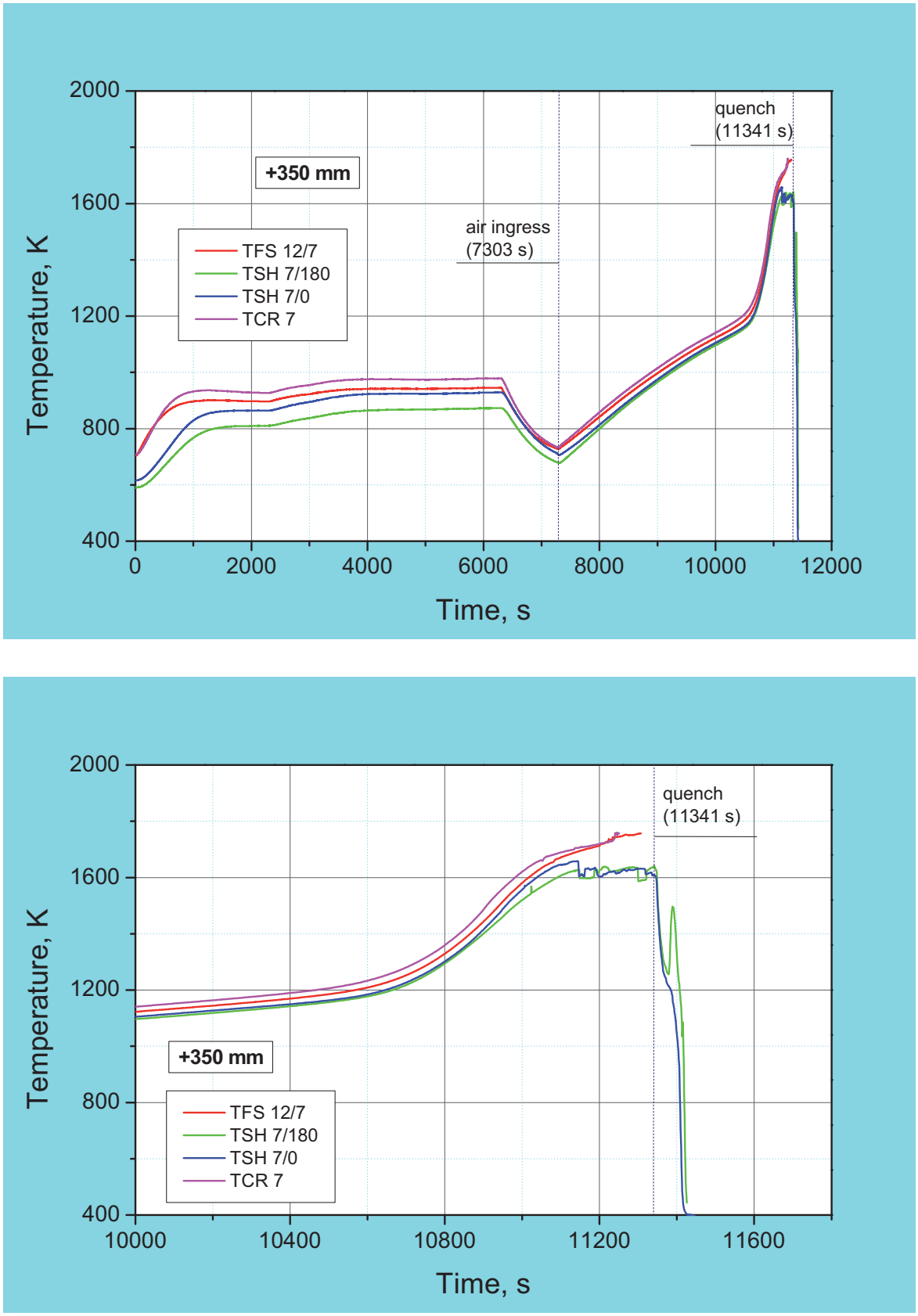

Fig. 23: QUENCH-16; Temperatures measured by rod cladding (TFS and TCR 7) and shroud (TSH) thermocouples at 350 mm elevation.

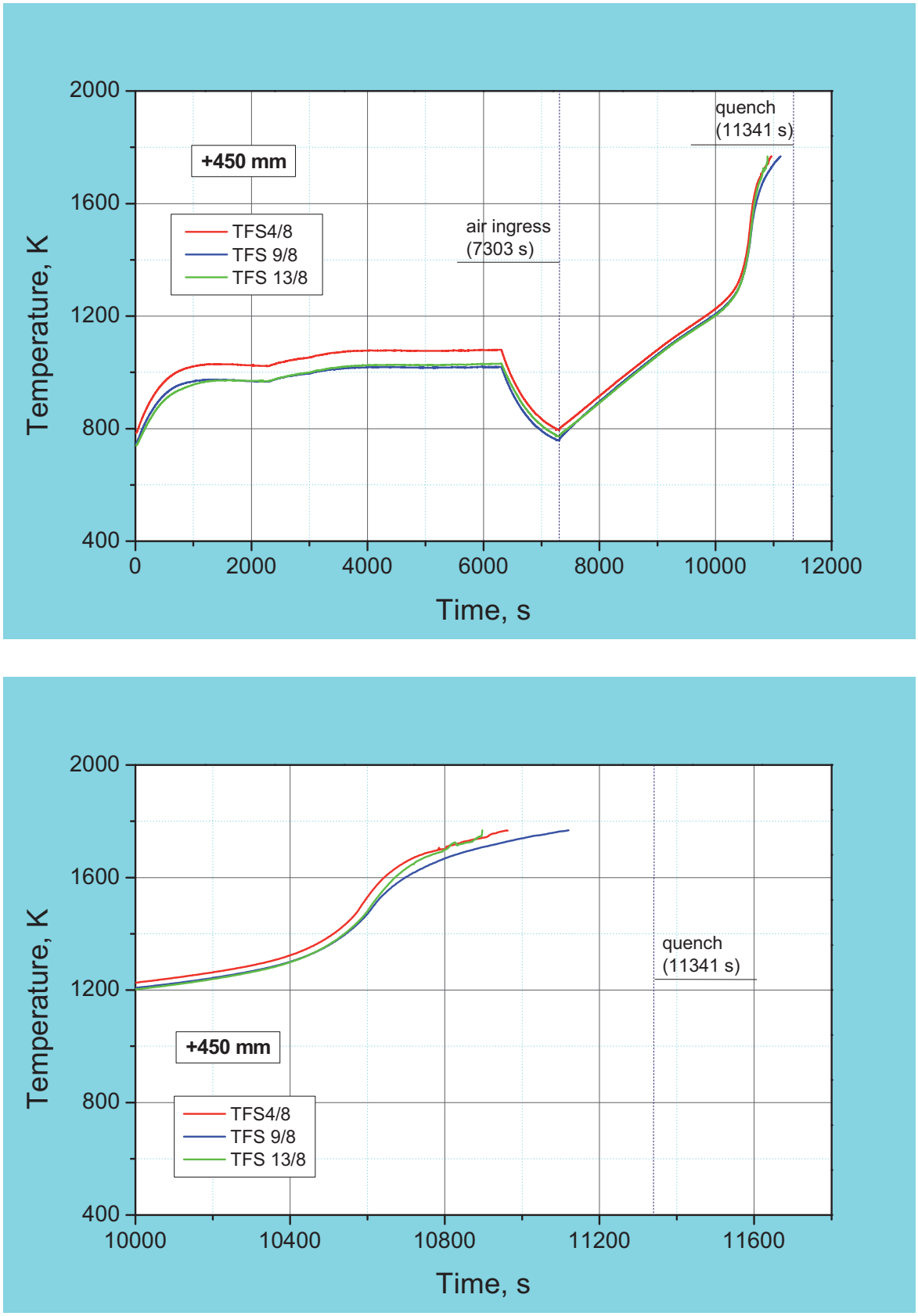

Fig. 24: QUENCH-16; Temperatures measured by rod cladding (TFS) thermocouples at 450 mm elevation.

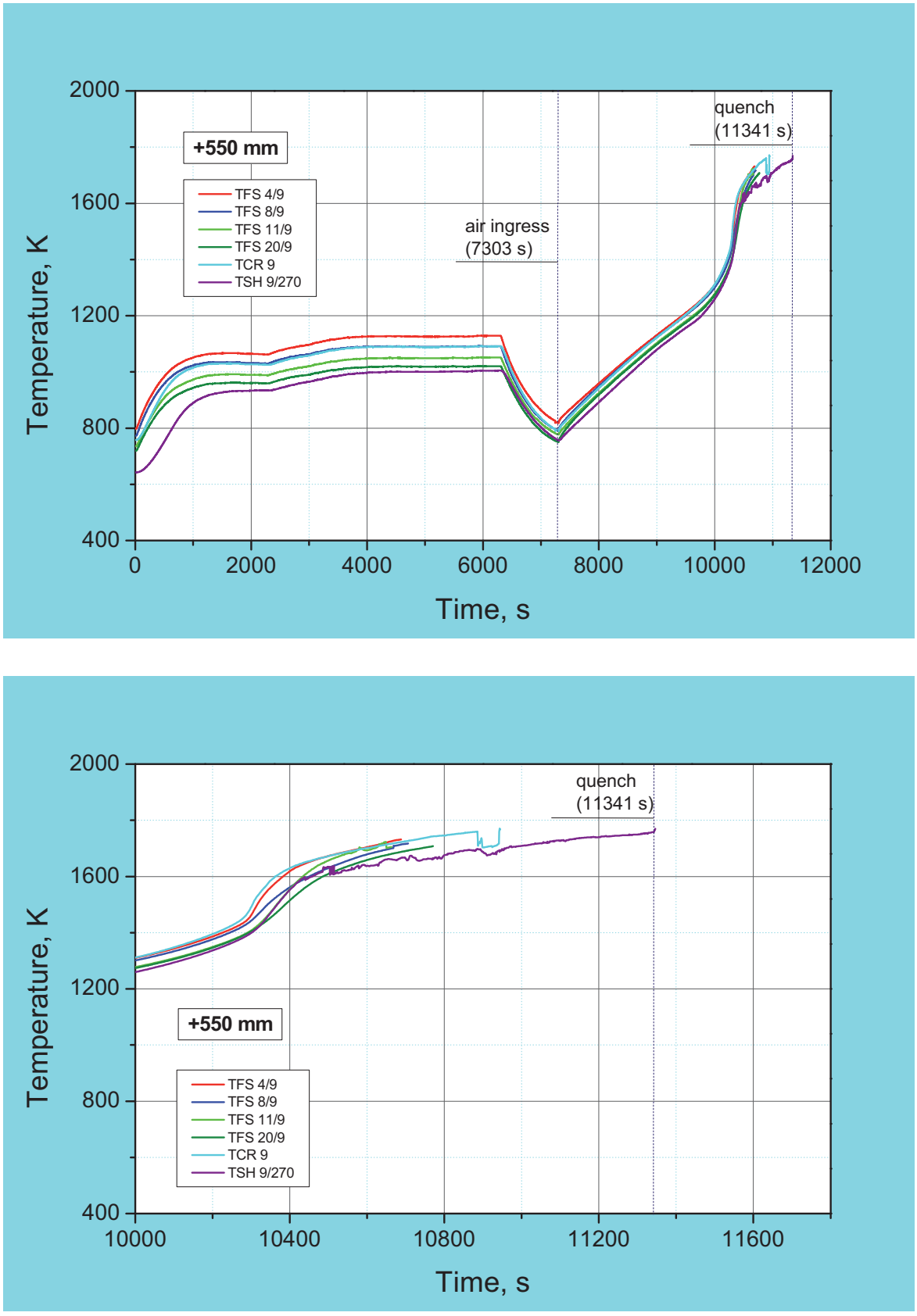

Fig. 25: QUENCH-16; Temperatures measured by rod cladding (TFS and TCR) and shroud (TSH) and thermocouples at 550 mm elevation.

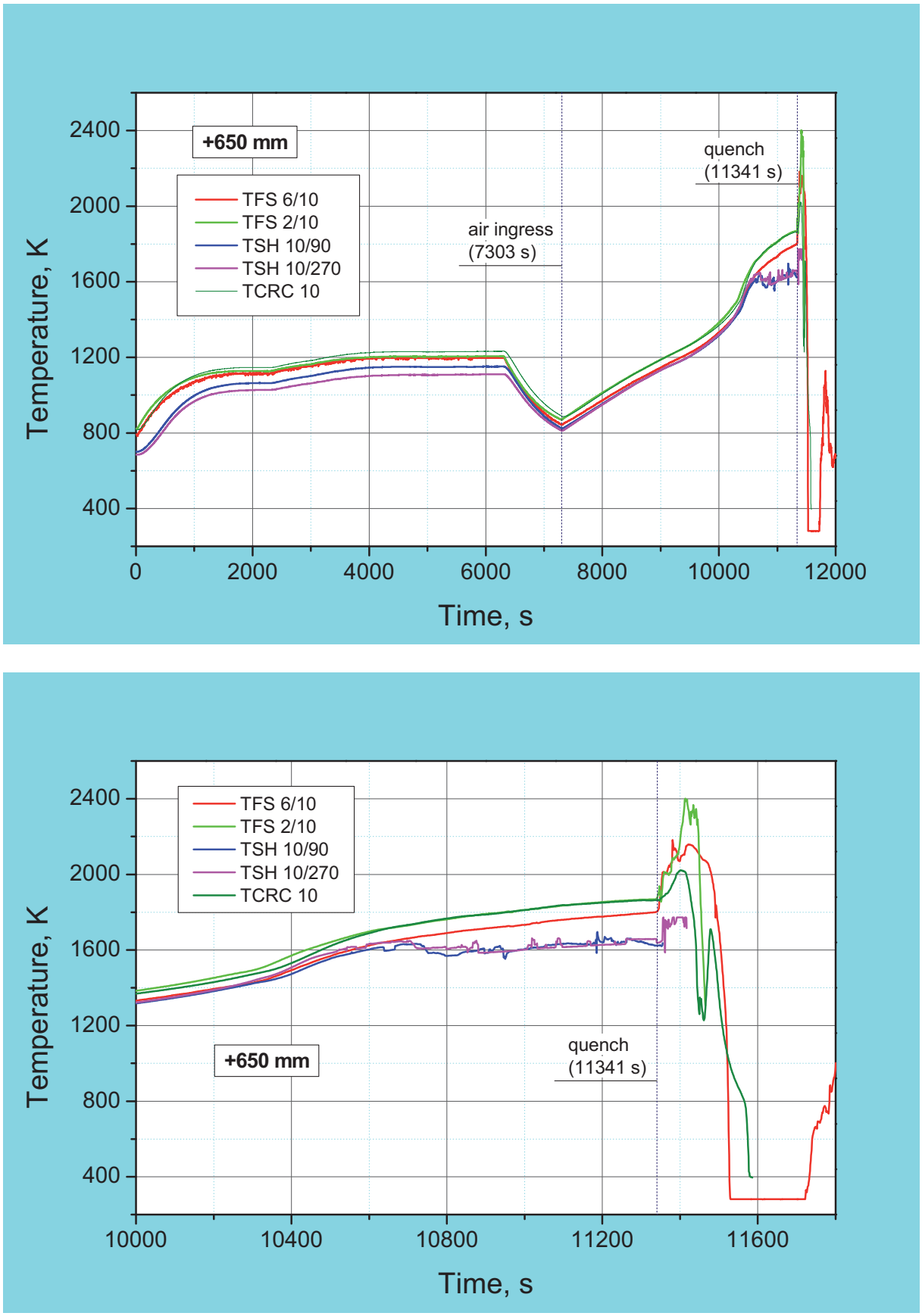

Fig. 26: QUENCH-16; Temperatures measured by rod cladding (TFS) and shroud (TSH) and centerline (TCRC 10) thermocouples at 650 mm elevation.

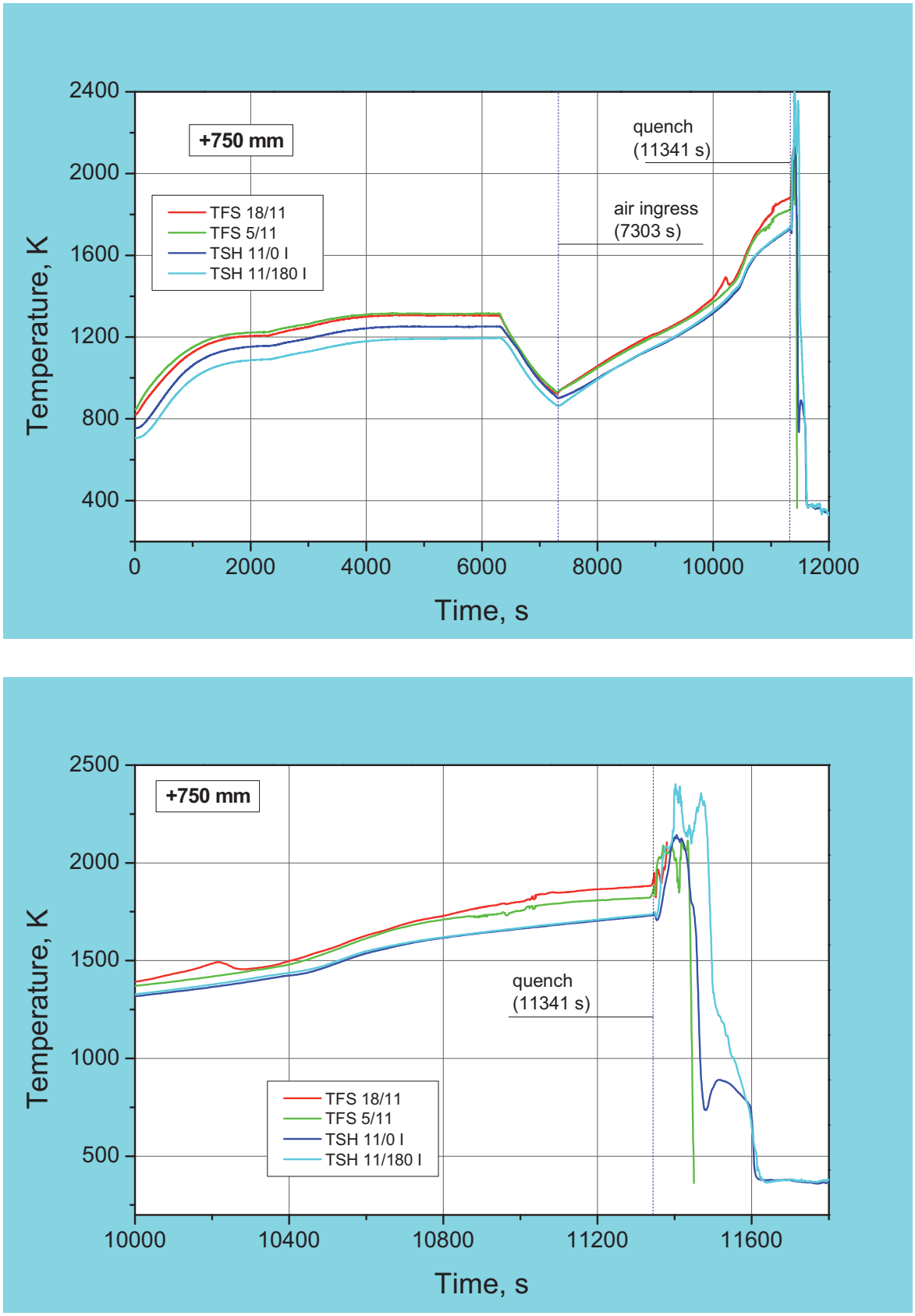

Fig. 27: QUENCH-16; Temperatures measured by rod cladding (TFS) and shroud (TSH) thermocouples at 750 mm elevation.

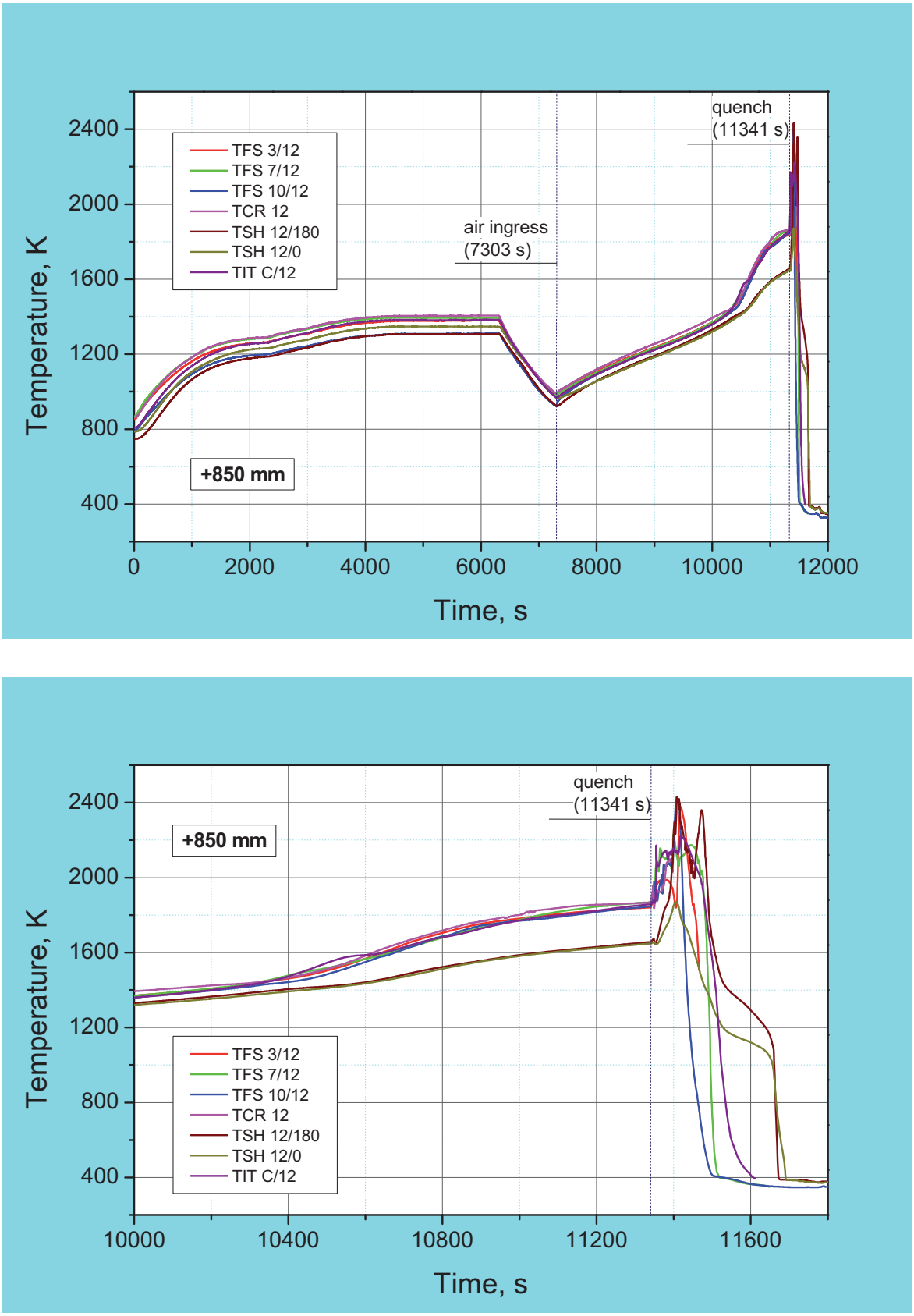

Fig. 28: QUENCH-16; Temperatures measured by rod cladding (TFS and TCR), shroud (TSH), and corner rod internal (TIT C/12) thermocouples at 850 mm elevation.

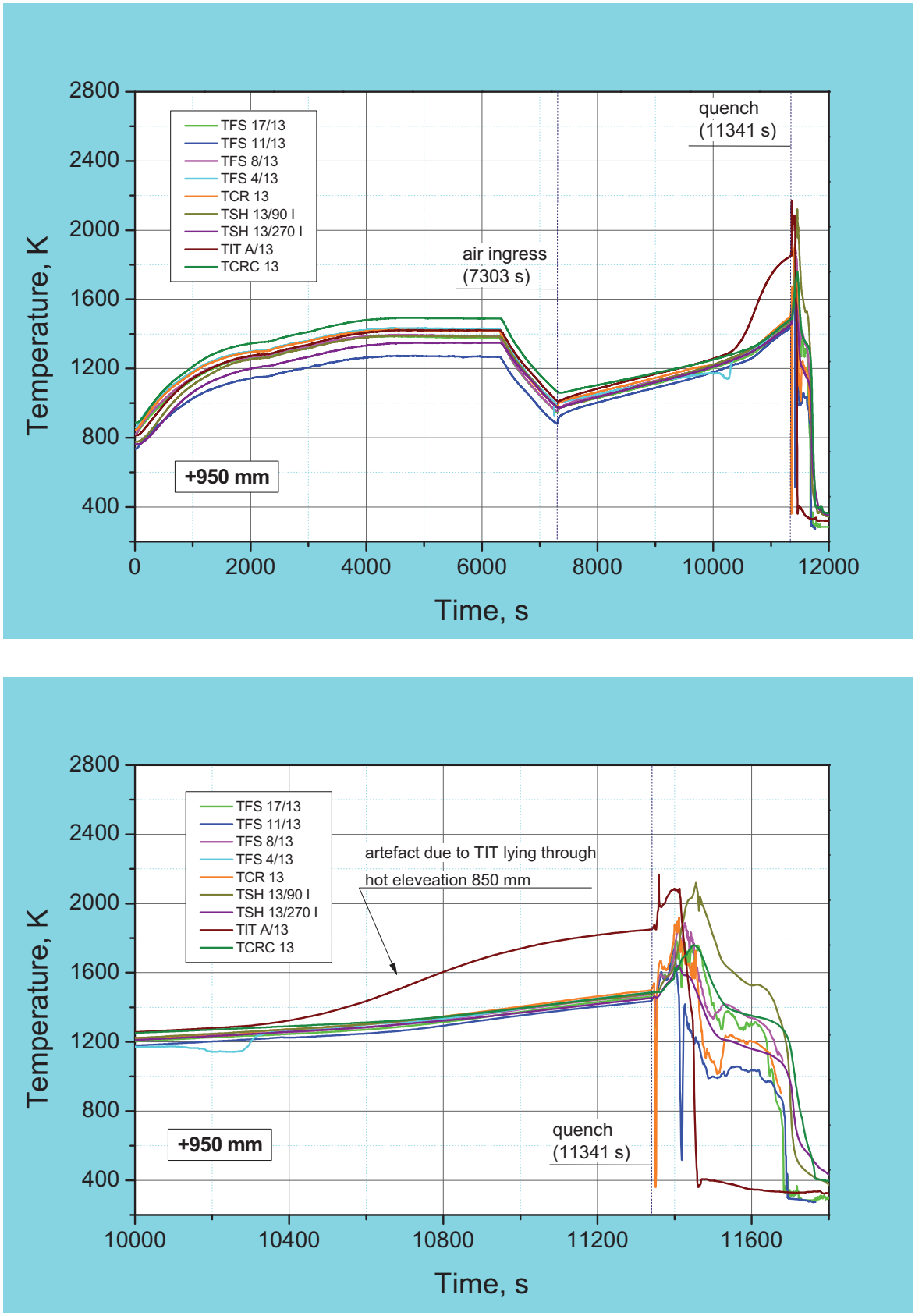

Fig. 29: QUENCH-16; Temperatures measured by rod cladding (TFS and TCR), shroud (TSH), corner rod internal (TIT A/13) and central rod centerline (TCRC 13) thermocouples at 950 mm elevation.

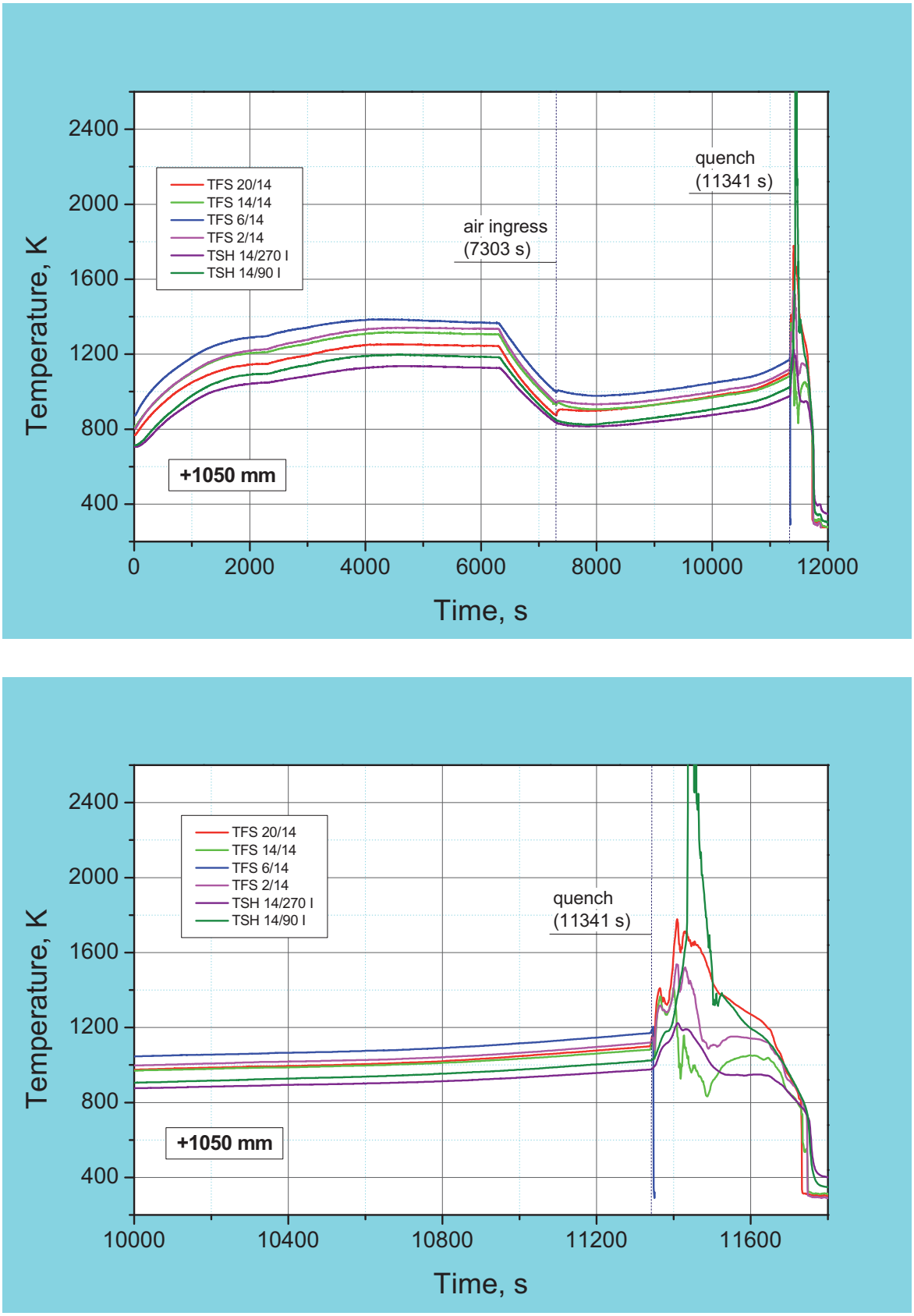

Fig. 30: QUENCH-16; Temperatures measured by rod cladding (TFS) and shroud (TSH) thermocouples at 1050 mm elevation.

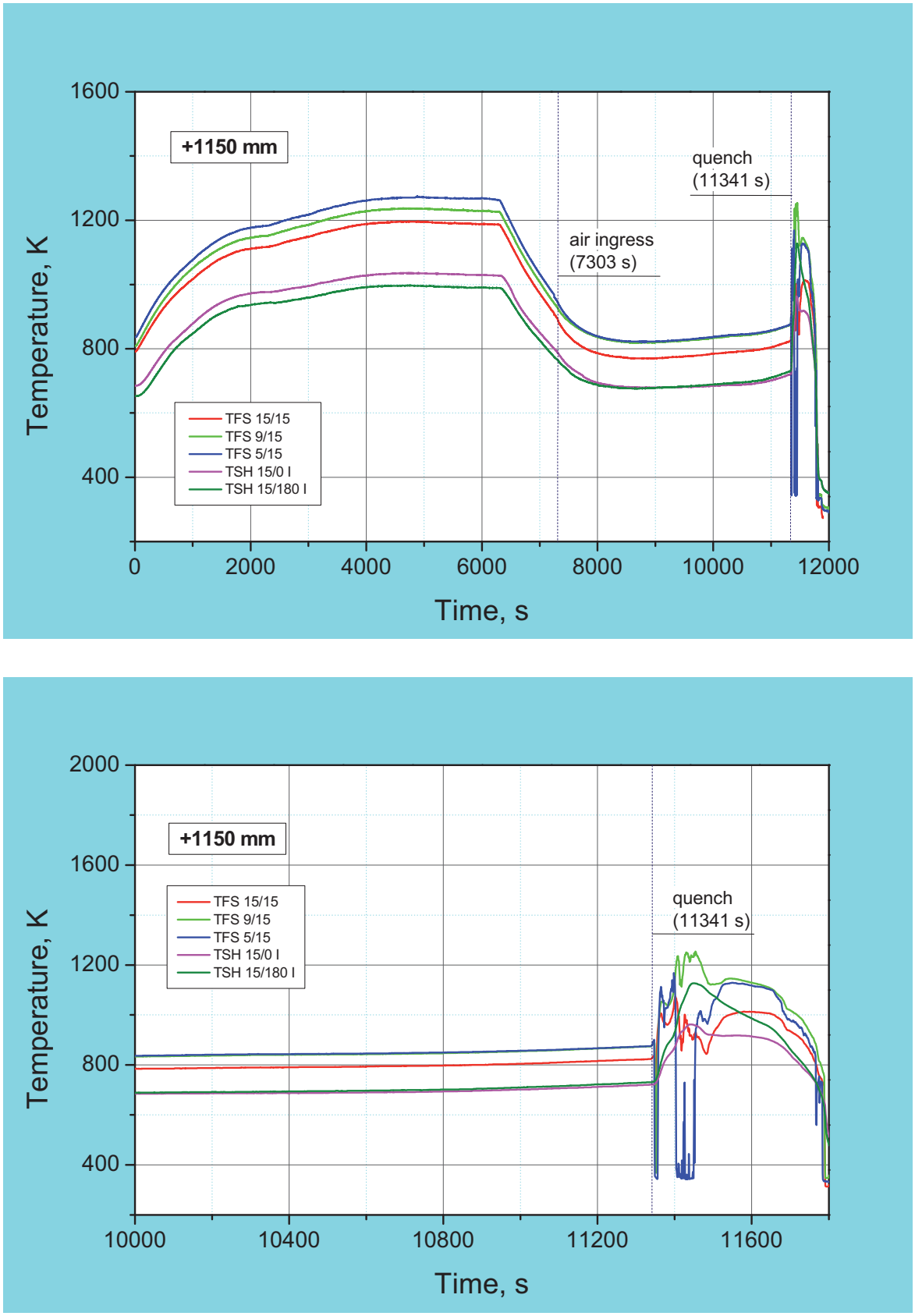

Fig. 31: QUENCH-16; Temperatures measured by rod cladding (TFS) and shroud (TSH) thermocouples at 1150 mm elevation.

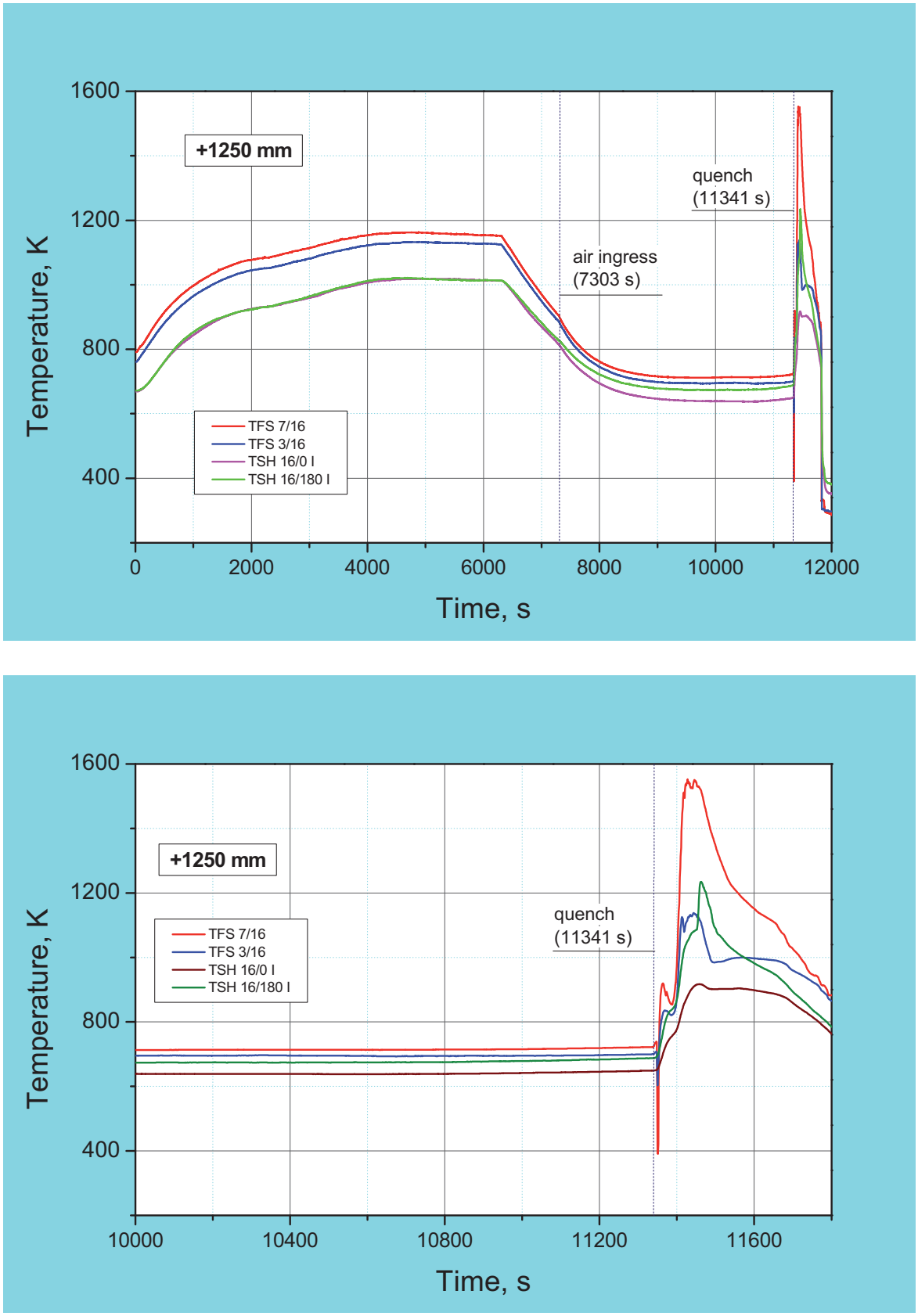

Fig. 32: QUENCH-16; Temperatures measured by rod cladding (TFS) and shroud (TSH) thermocouples at 1250 mm elevation.

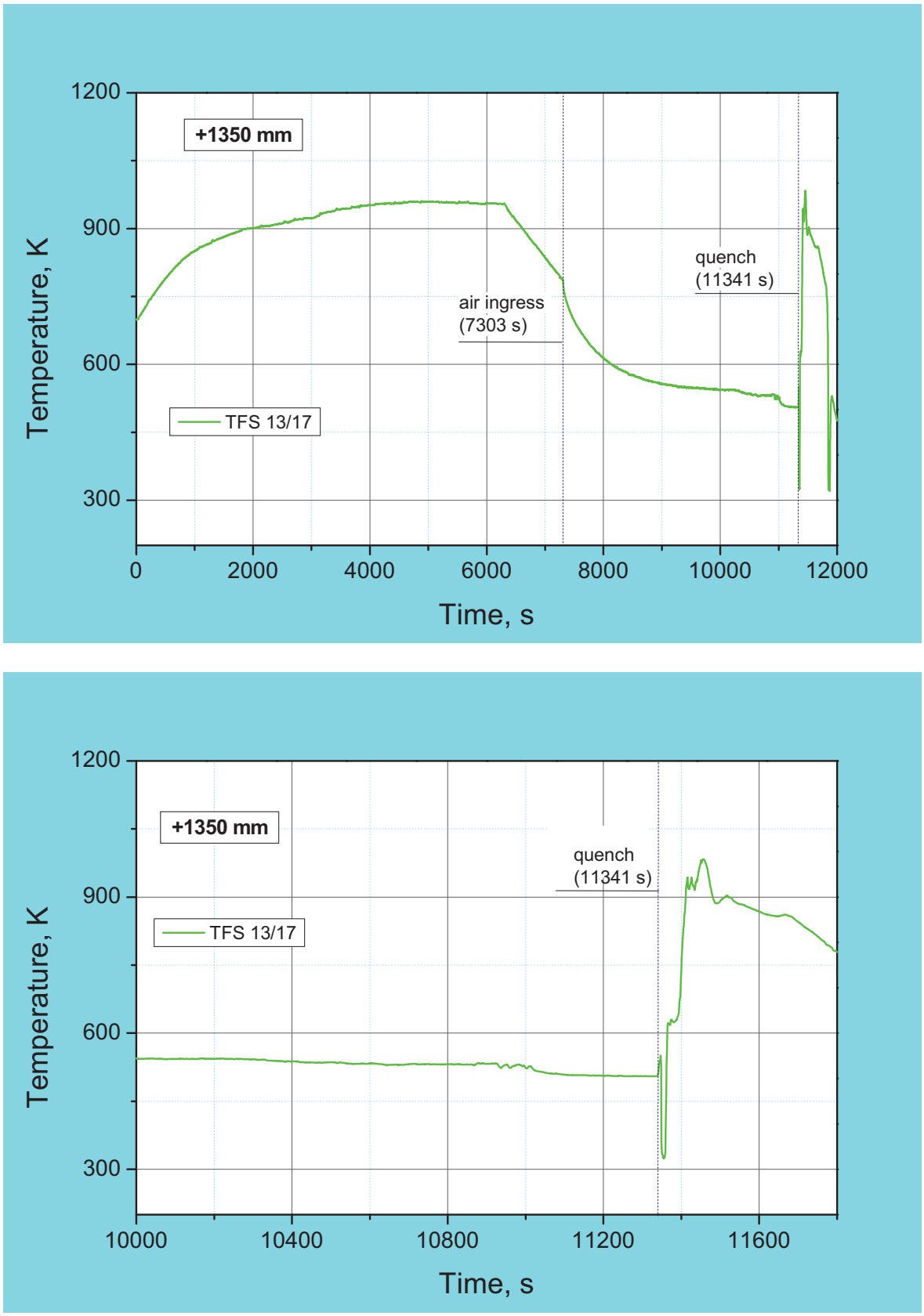

Fig. 33: QUENCH-16; Temperature measured by rod cladding thermocouple TFS 13/17 at 1350 mm elevation.

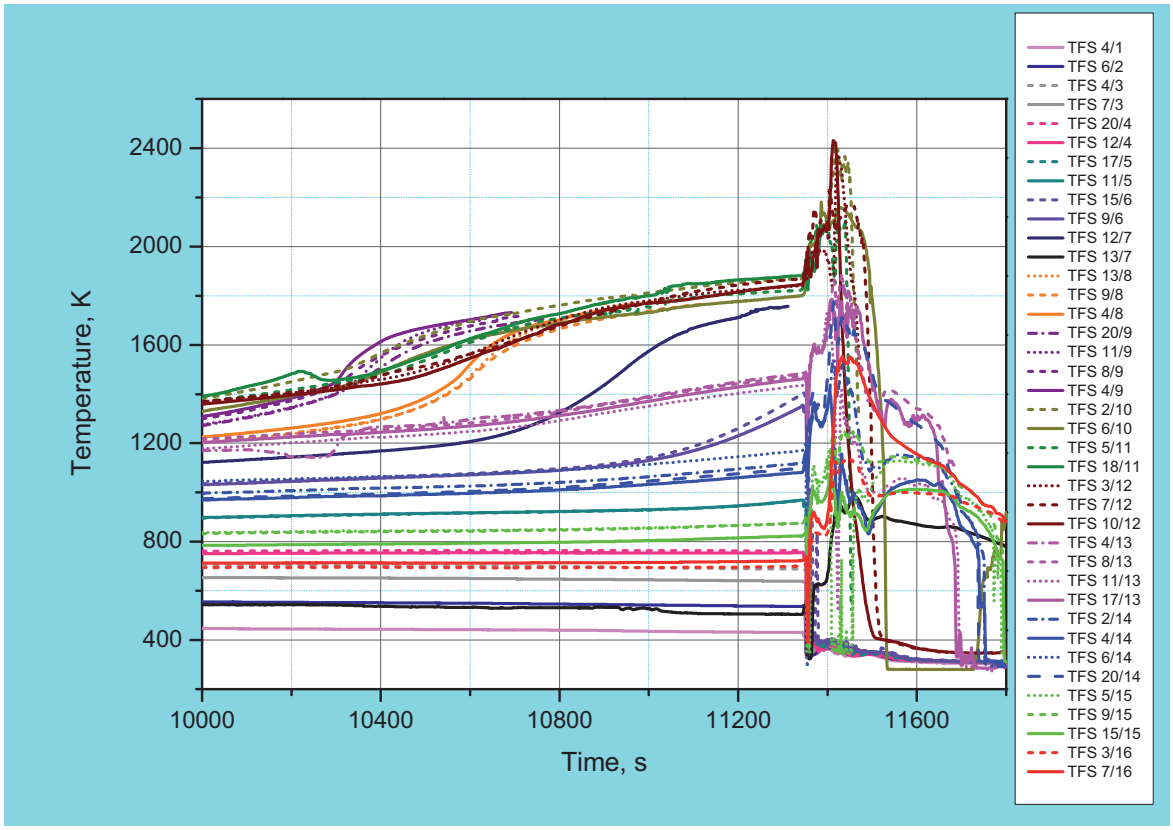

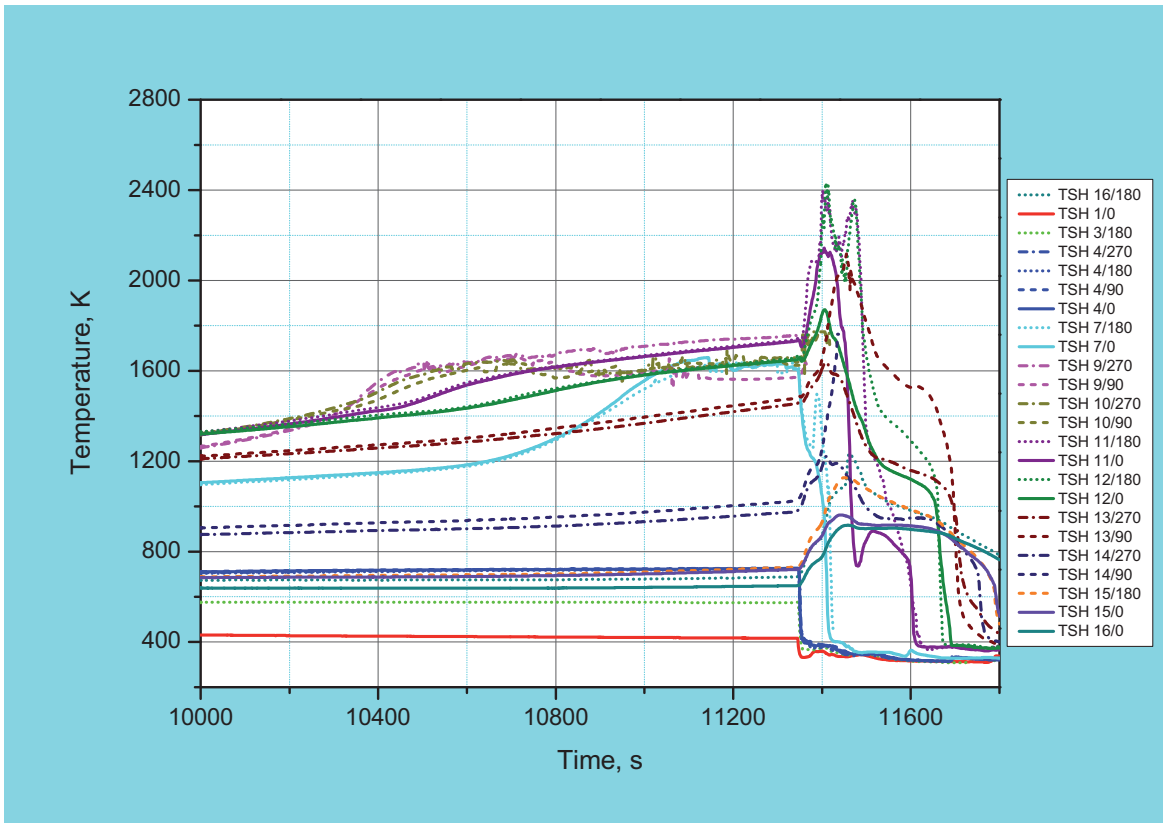

Fig. 34: QUENCH-16; Overview of the TFS, top, and TSH temperatures, bottom.

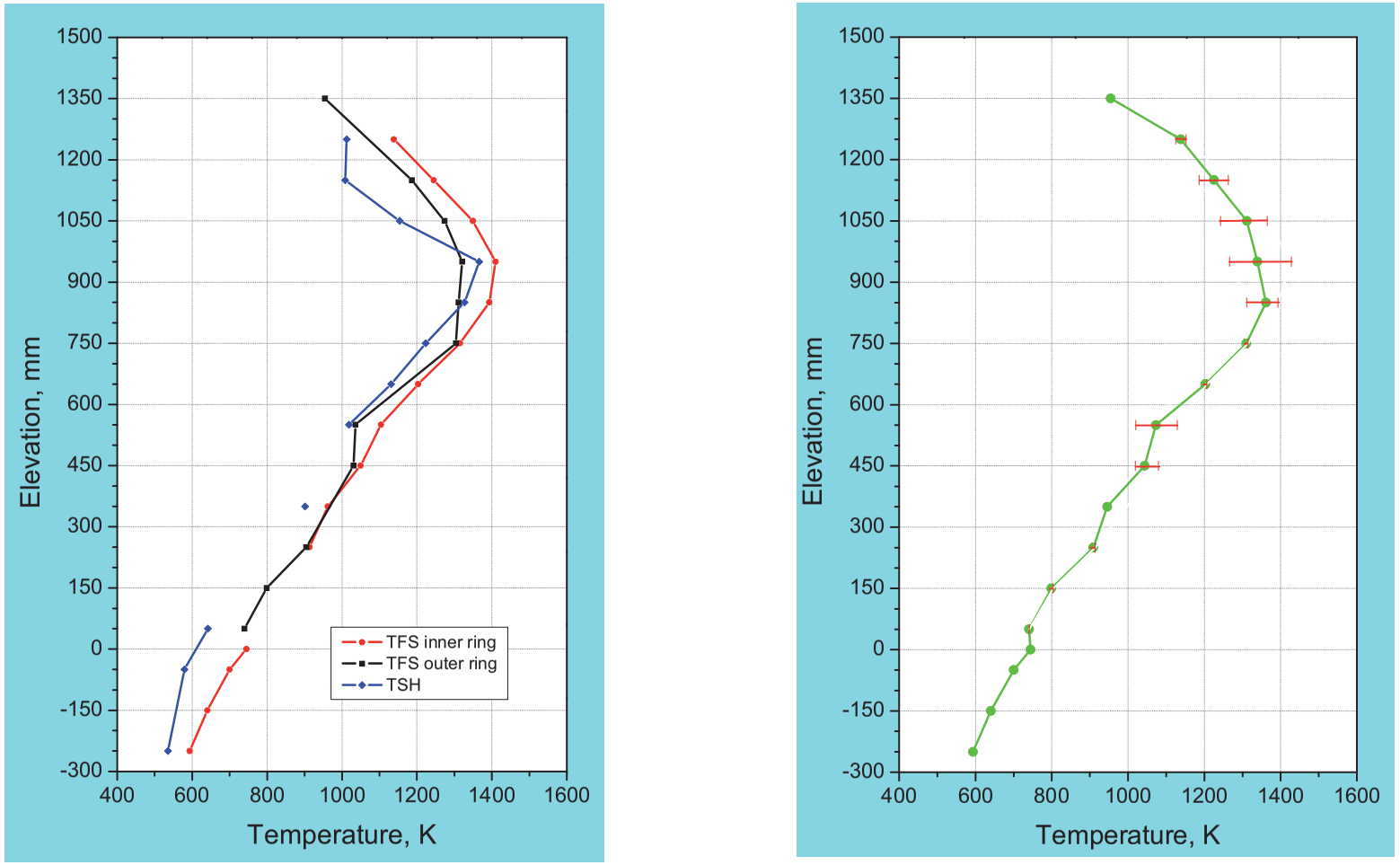

Fig. 35: QUENCH-16; Axial temperature profile TFS inner ring and TFS outer ring together with TSH, left, and axial temperature profile of all TFS, right, at 6300 s (intermediate cooling).

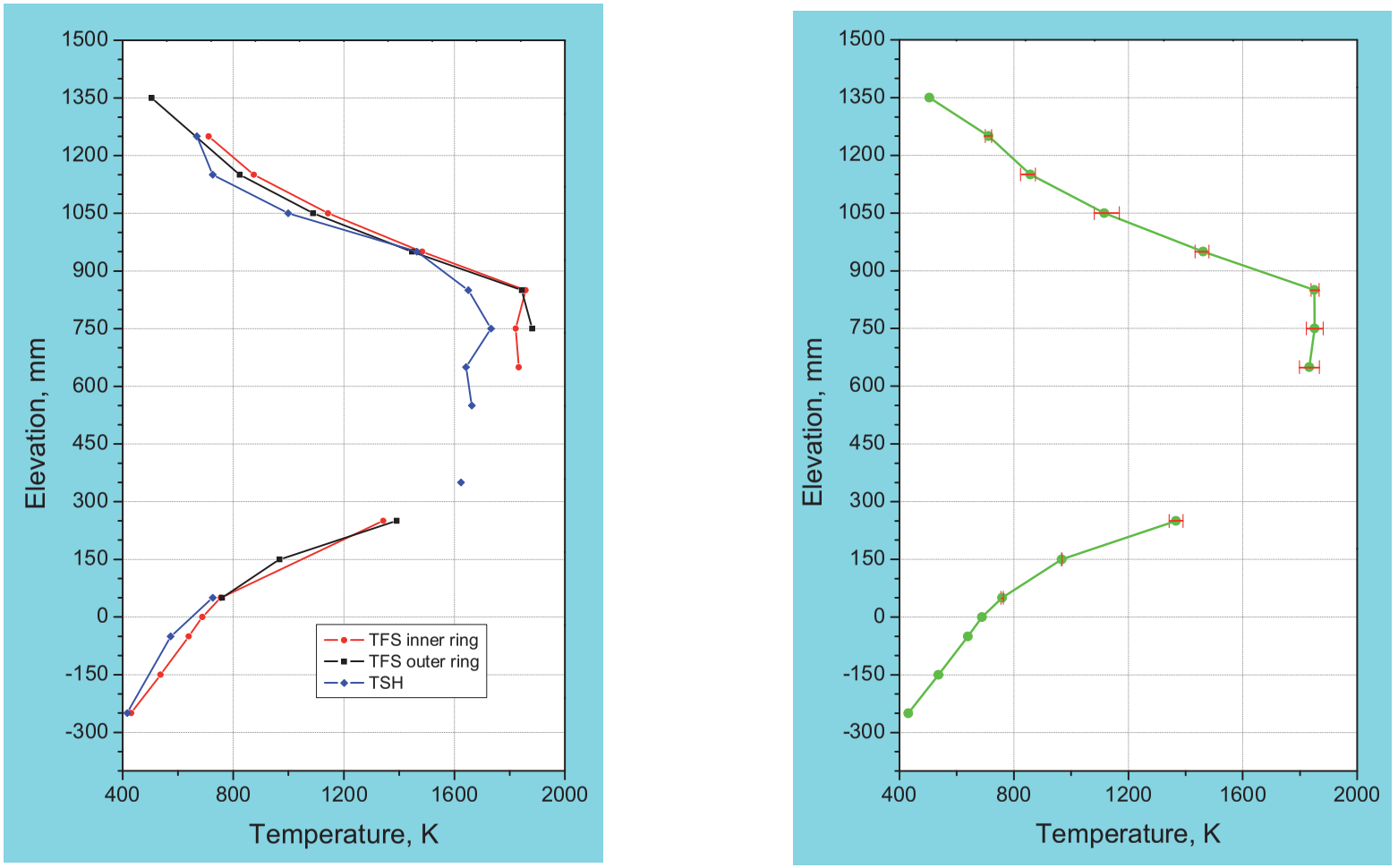

Fig. 36: QUENCH-16; Axial temperature profile TFS inner ring and TFS outer ring together with TSH, left, and axial temperature profile of all TFS, right, at 11330 s (end of air ingress).

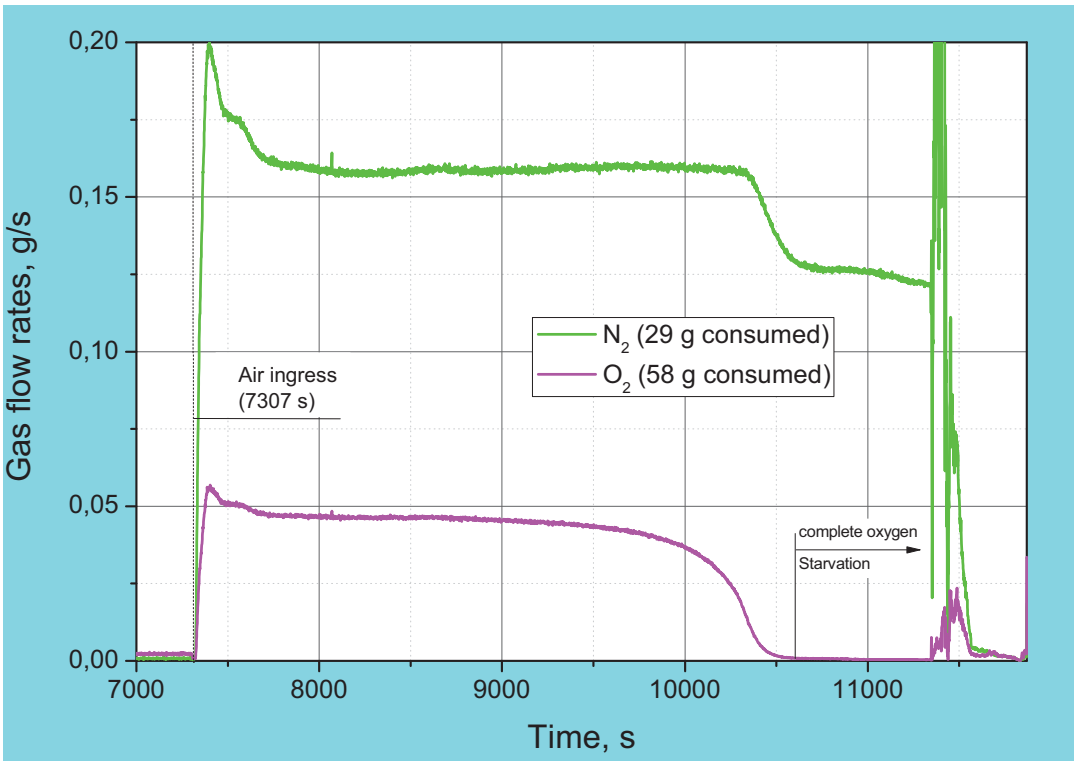

Fig. 37: QUENCH-16; Consumption of oxygen and nitrogen during air ingress.

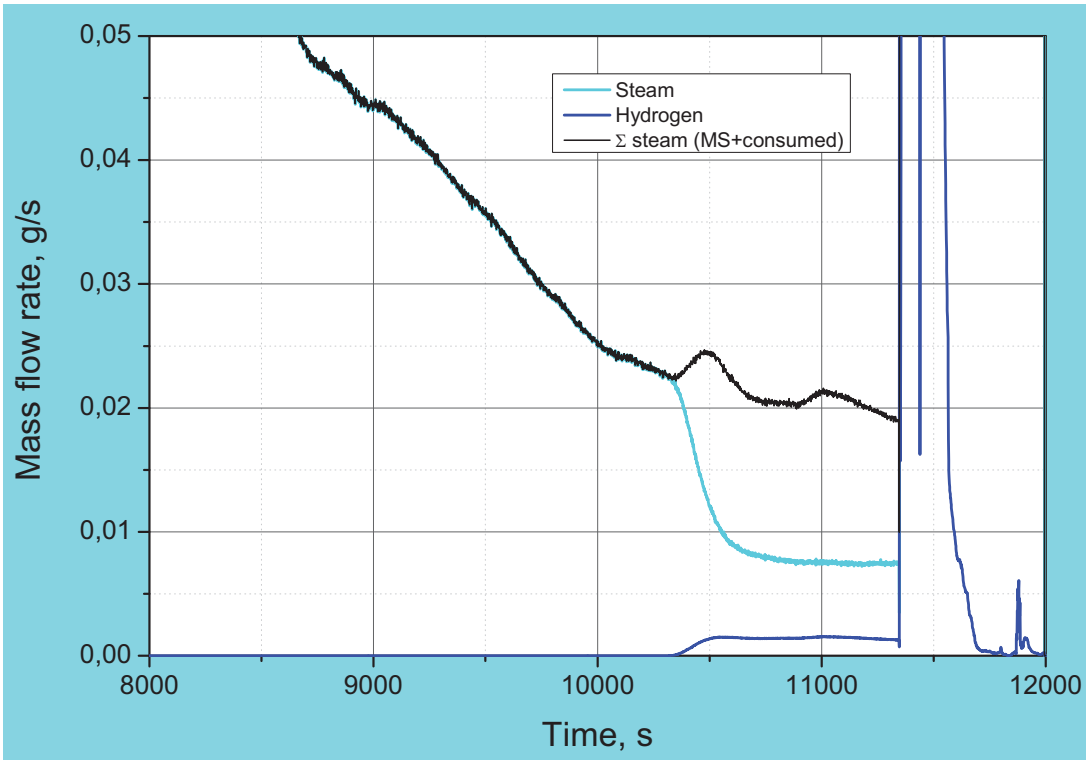

Fig. 38: QUENCH-16; Residual steam flow and corresponding hydrogen release.

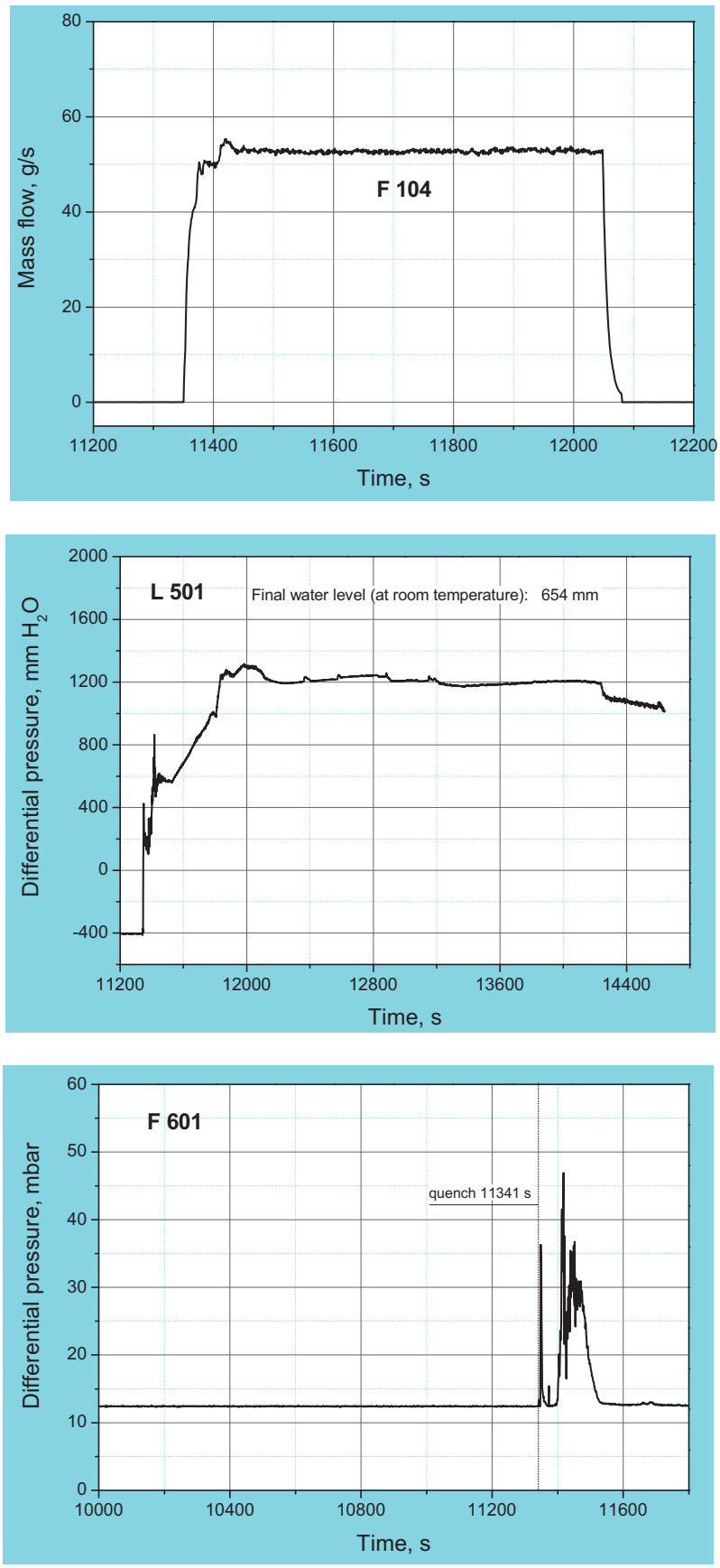

Fig. 39: QUENCH-16; Quench water mass flow rate (F 104), top, measurement of collapsed water level (L 501), center, off-gas flow rate (F 601), bottom.

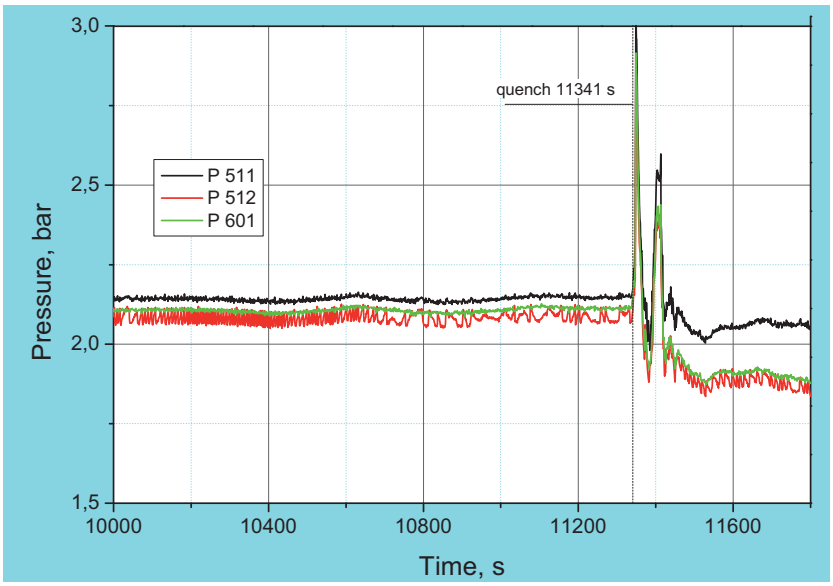

System pressure measured at test section inlet P 511, at outlet P 512, and in the off-gas pipe P 601.

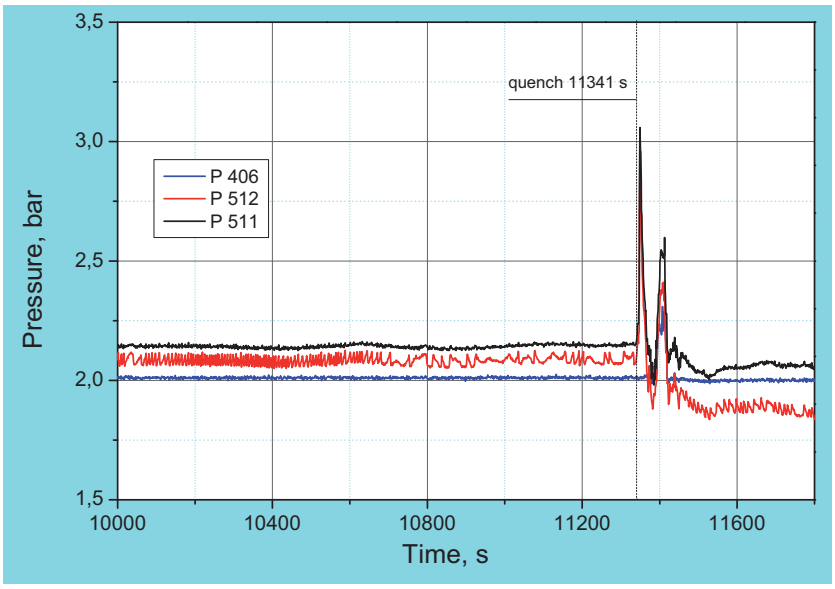

Argon pressure measured at shroud insulation P 406, together with system pressure at the test section inlet P 511 and outlet P 512 (the constant pressure P 406 indicates that there was no shroud failure).

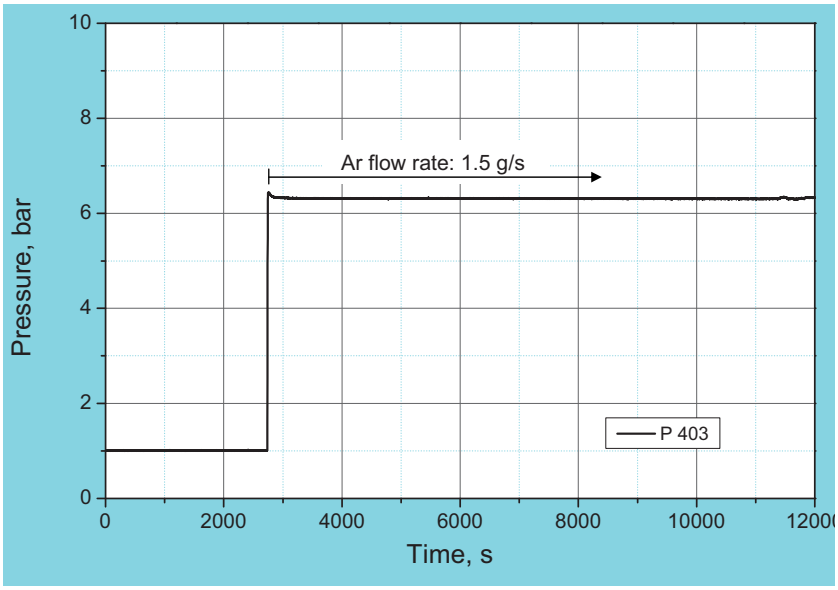

Argon coolant pressure of the cooling jacket P 403 demonstrates tightness of the inner cooling jacket.

Fig. 40: QUENCH-16; Argon and system pressure.

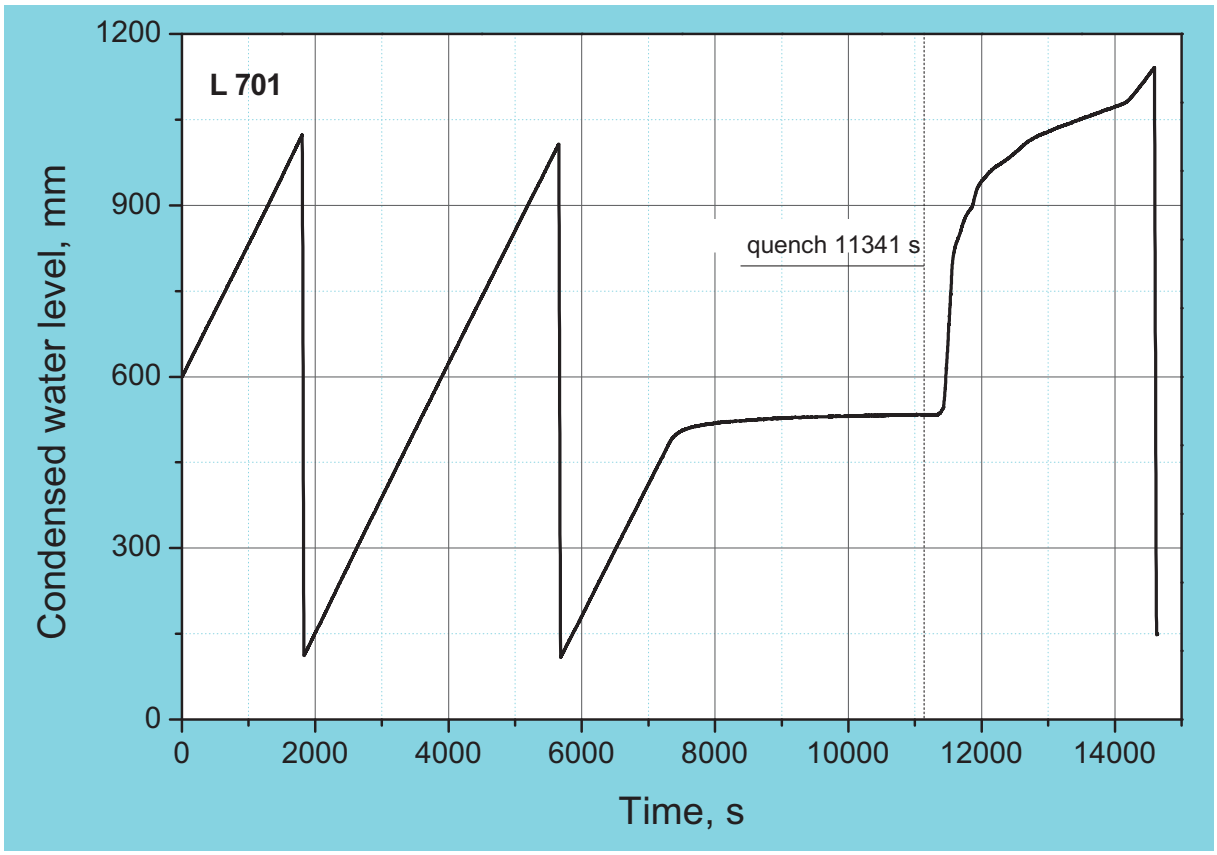

Fig. 41: QUENCH-16; Condensed water in the collection vessel.

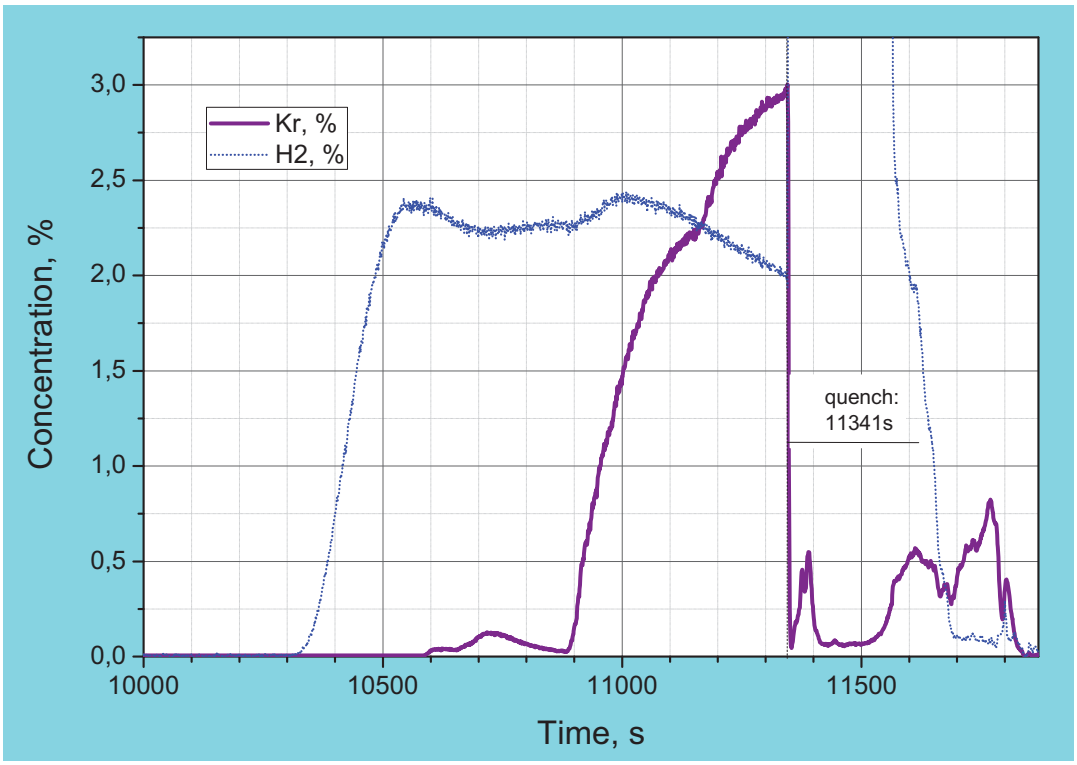

Fig. 42: QUENCH-16; Indication of rod failure by Kr measurement at MS.

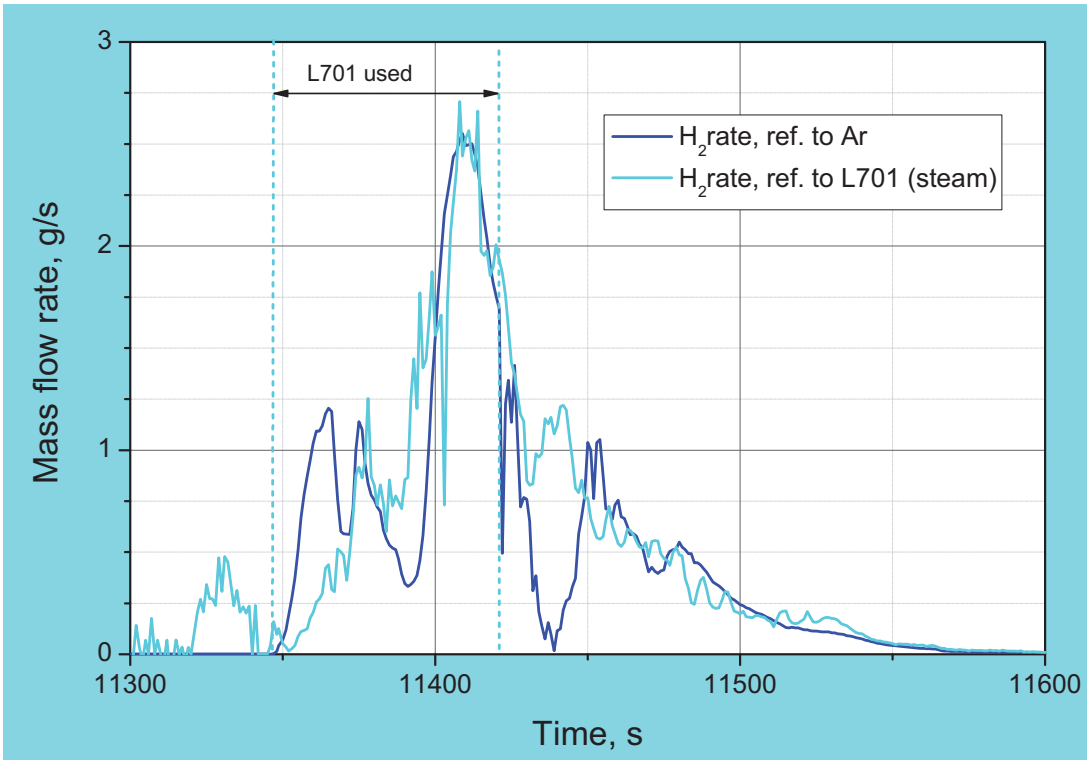

Fig. 43: QUENCH-16; Hydrogen production during reflood.

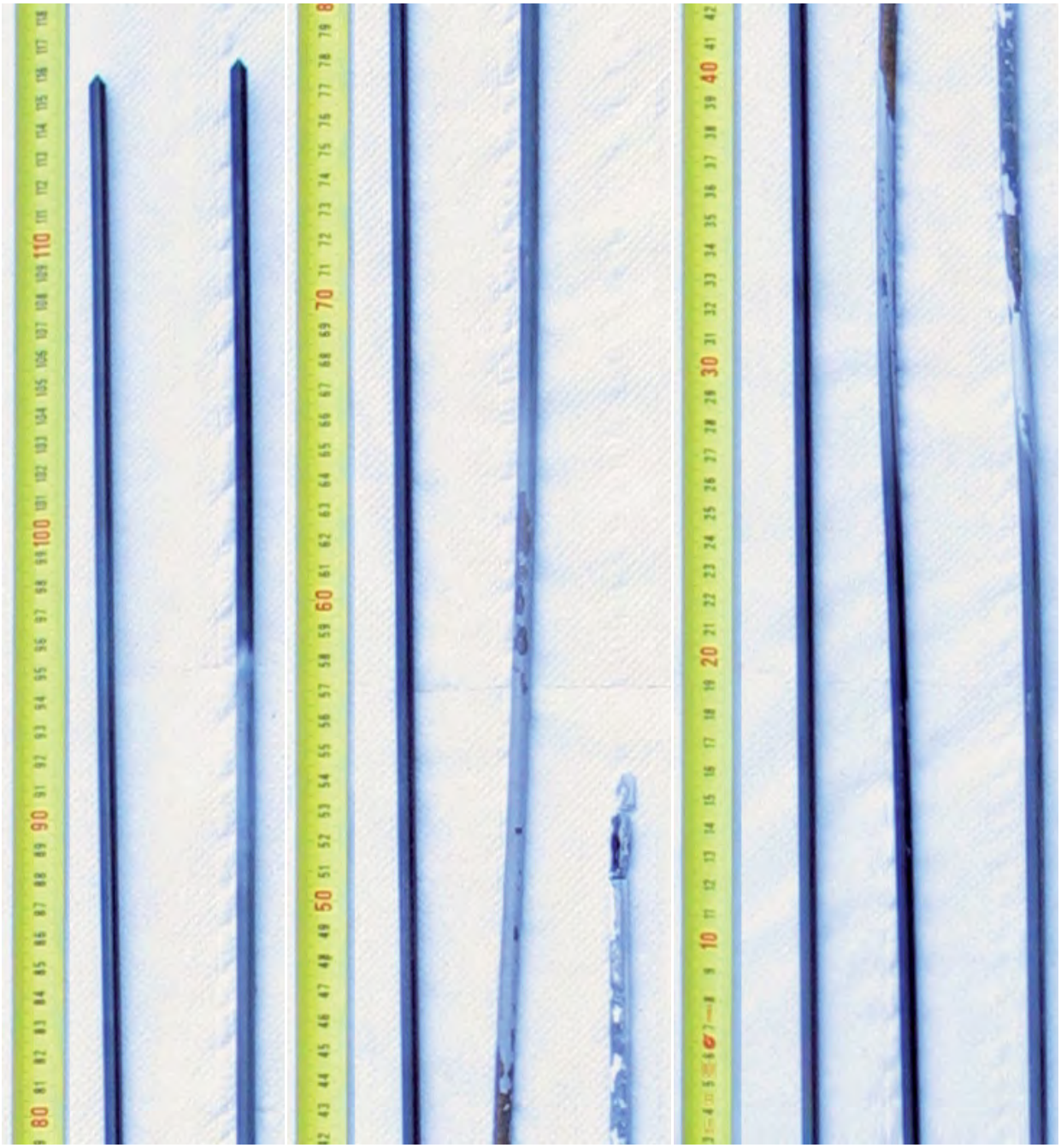

bundle top: rods B and D (from left)

bundle middle: rods B, D and A (from left)

bundle bottom: rods B, D and A (from left)

Fig.44: QUENCH-16; withdrawn corner rods.

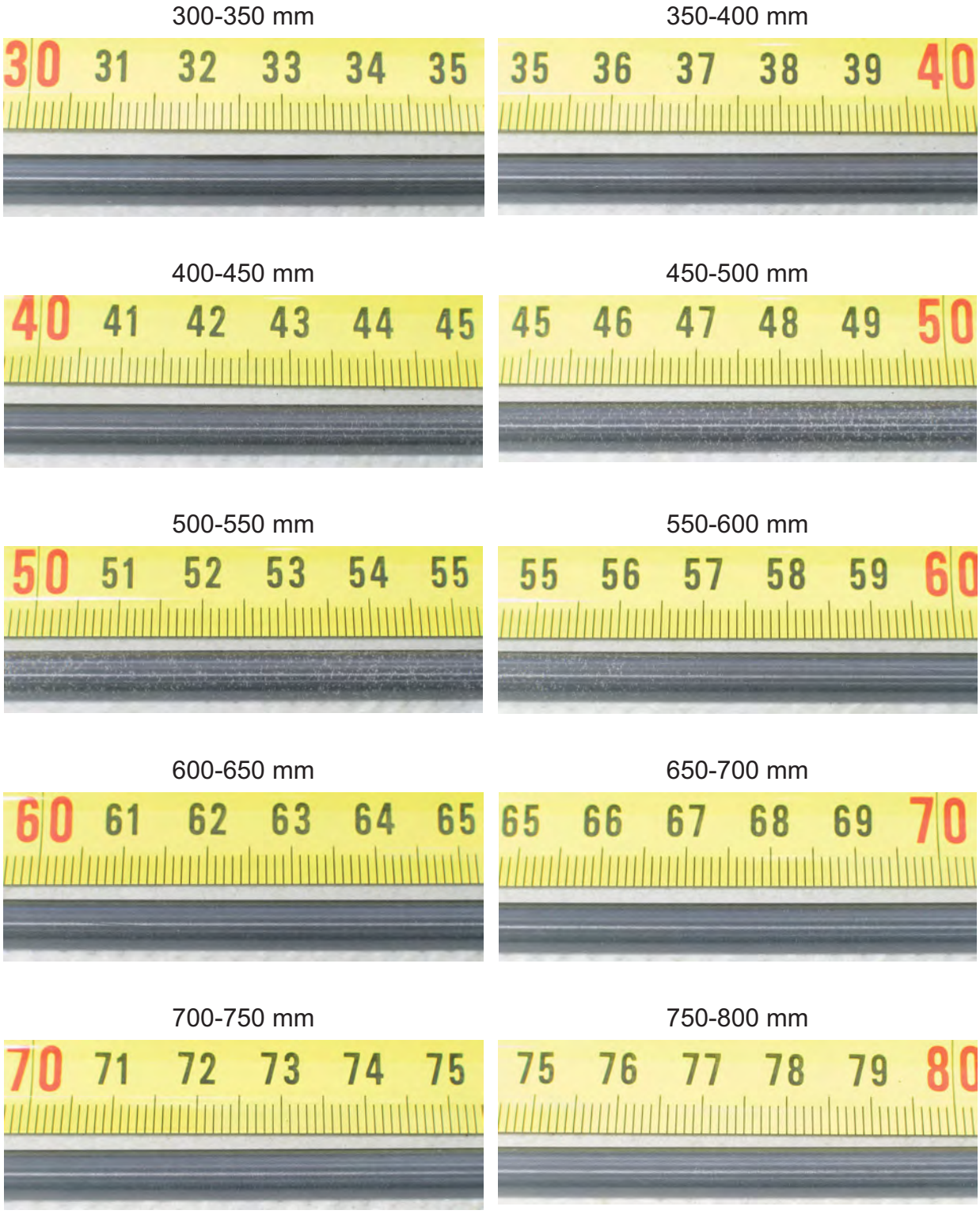

Fig. 45: QUENCH-16; Photographs of corner rod B withdrawn from the bundle before air ingress, 300-800 mm elevation.

800-850 mm

850-900 mm

900-950 mm

950-1000 mm

1000-1050 mm

1050-1100 mm

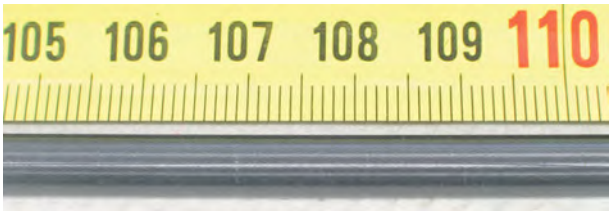

1100-1150 mm

Fig. 46: QUENCH-16; Photographs of corner rod B withdrawn from the bundle before air ingress, 800-1100 mm elevation.

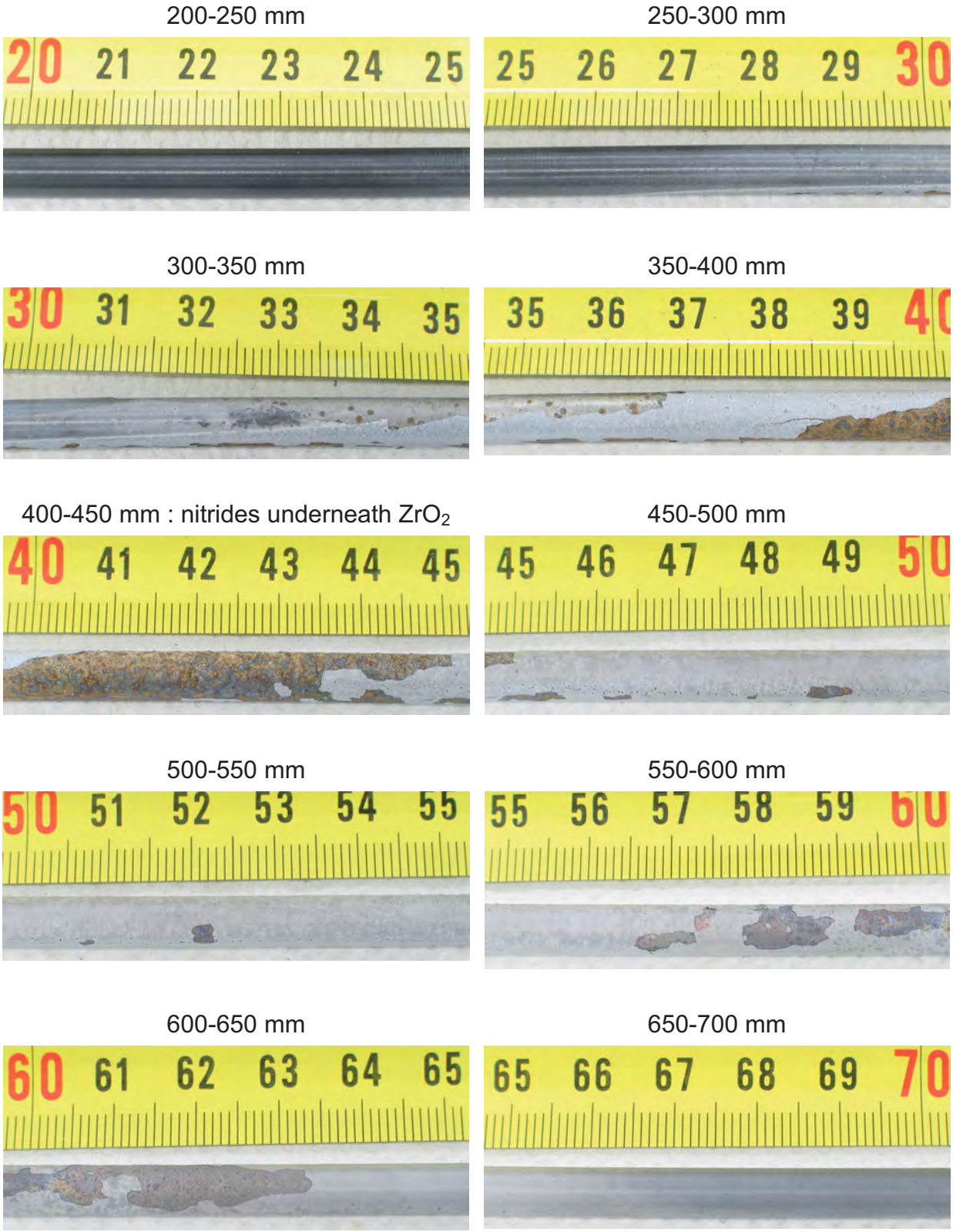

Fig. 47: QUENCH-16; Photographs of corner rod D withdrawn from the bundle before quenching, 200-700 mm elevation.

700-750 mm

750-800 mm

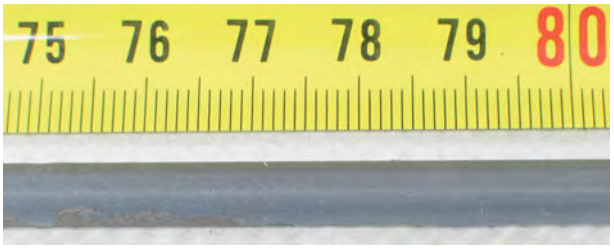

800-850 mm

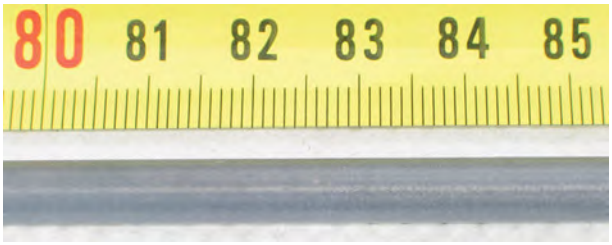

850-900 mm

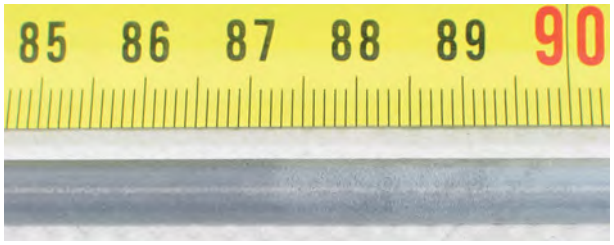

900-950 mm

950-1000 mm

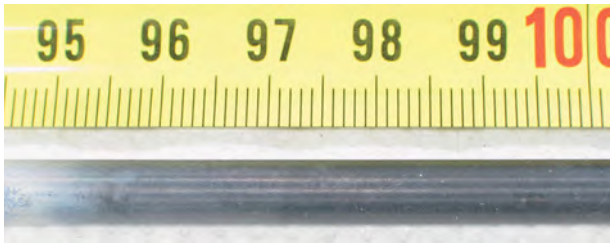

1000-1050 mm

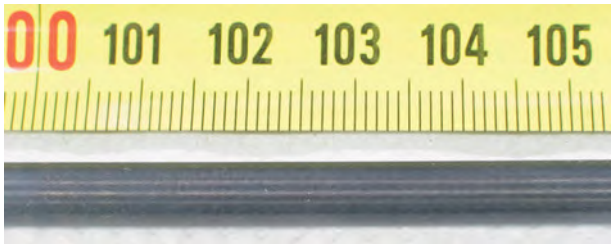

1050-1100 mm

1100-1150 mm

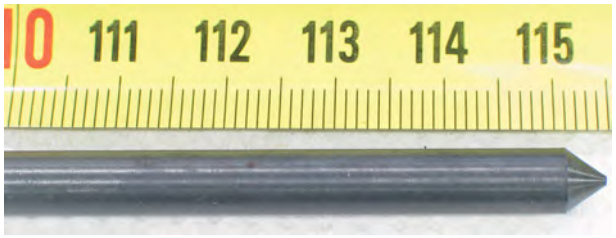

Fig. 48: QUENCH-16; Photographs of corner rod D withdrawn from the bundle before quenching, 700-1100 mm elevation.

200-250 mm

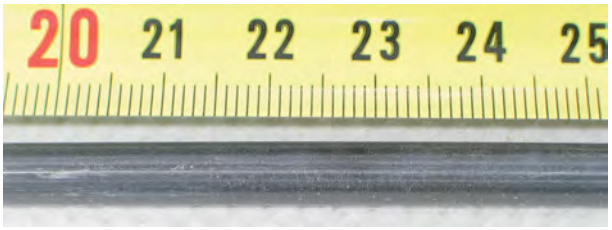

250-300 mm

300-350 mm

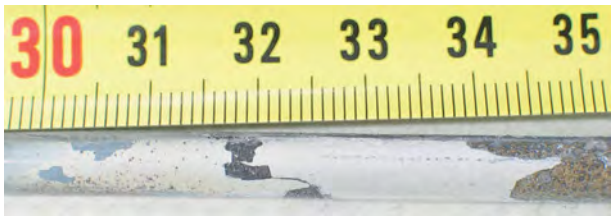

350-400 mm

400-450 mm

450-500 mm

500-550 mm

Fig. 49: QUENCH-16; Photographs of corner rod A withdrawn from the bundle after the test, 200-550 mm elevation.

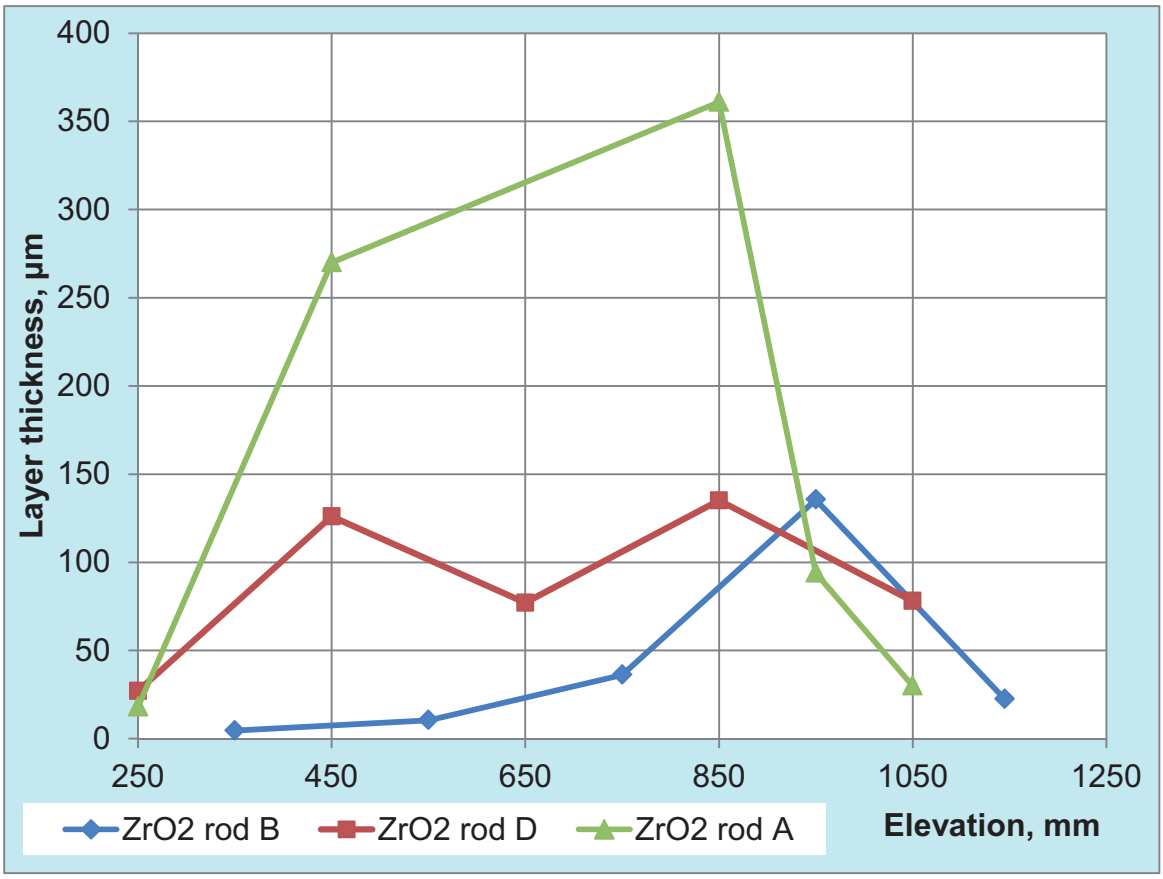

Fig. 50: QUENCH-16; axial distribution of oxide layer thickness for corner rods B (withdrawn before air ingress), D (withdrawn before quench) and A (after test). Values for rods D and A are calculated according to the Pilling-Bedworth coefficient on the basis of residual metal.

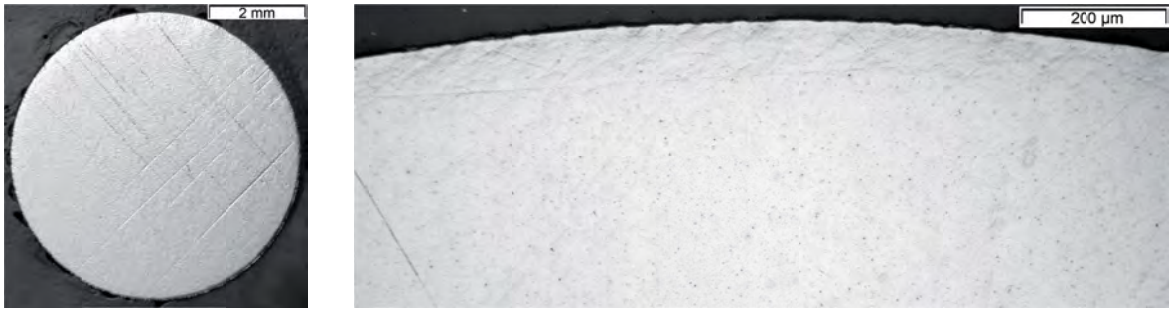

350 mm: δ_{ZrO2}=4.5 µm; α-Zr(O)=2.5 µm; T_{max}=945 K (TFS 12/7)

550 mm: δ_{ZrO2}=10 µm; α-Zr(O)=9 µm; T_{max}=1129 K (TFS 4/9)

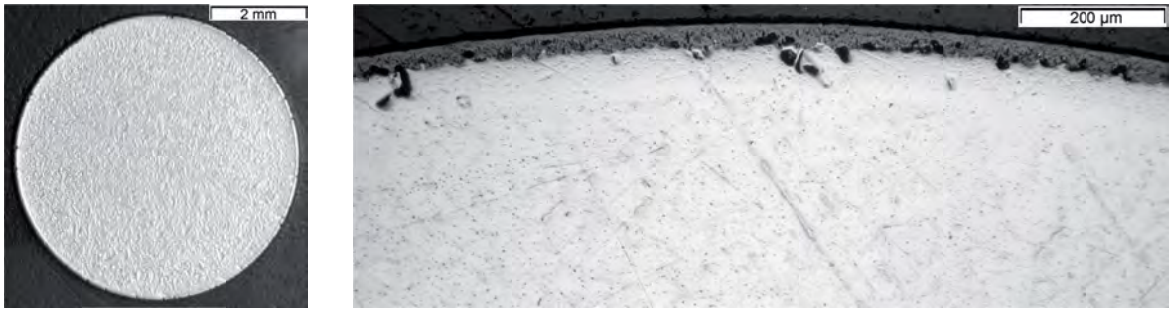

750 mm: δ_{ZrO2}=36 µm; α-Zr(O)=65 µm; T_{max}=1315 K (TFS 5/11)

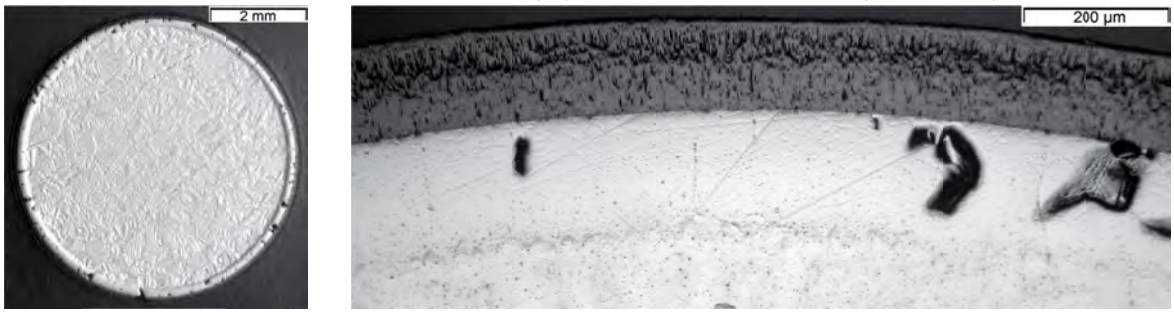

950 mm: δ_{ZrO2}=135 µm; α-Zr(O)=164 µm; T_{max}=1376 K (TFS 17/13)…1430 K (TFS 4/13)

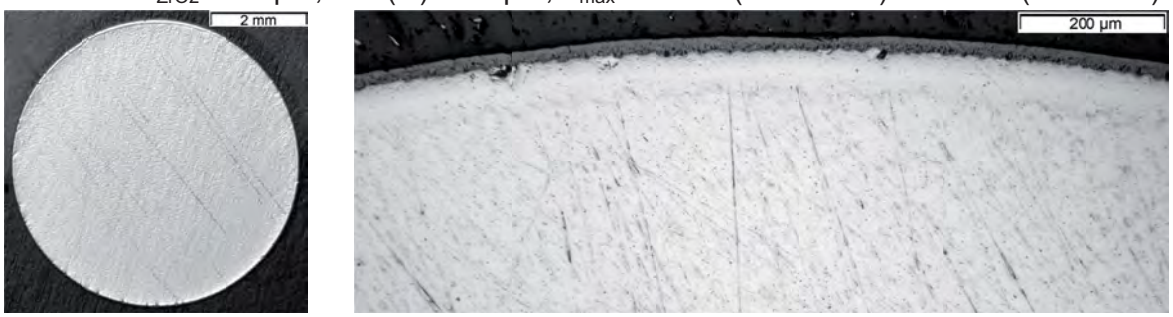

1145 mm: δ_{ZrO2}=23 µm; α-Zr(O)=51 µm; T_{max}=1271 K (TFS 5/15)

Fig.51: QUENCH-16; metallography of corner rod B withdrawn before air ingress.

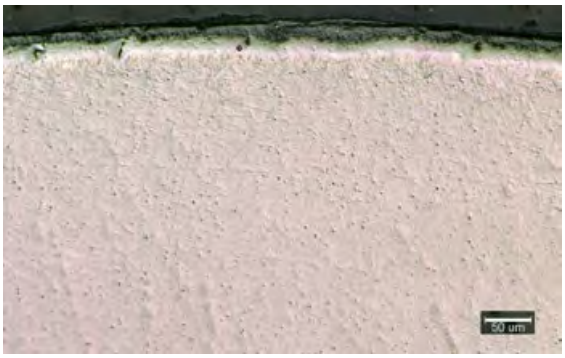

250 mm, 90°; T=1343 K (TFS 9/6): no nitrides

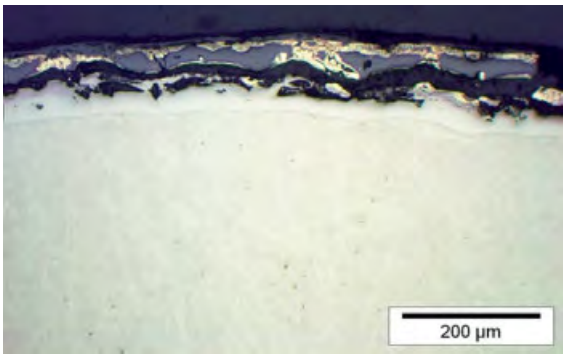

350 mm, 135°; 1760 K (TFS 12/7): moderate corrosion

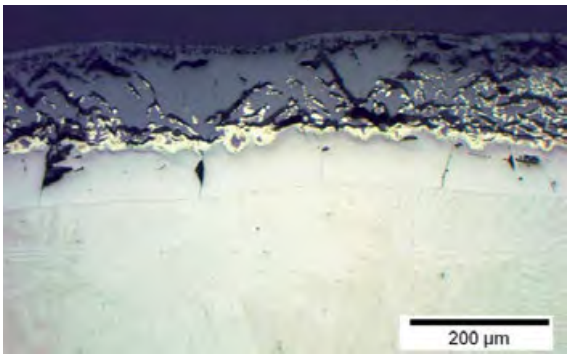

450 mm, 135°; 1800 K (TFS 9/8): strong corrosion

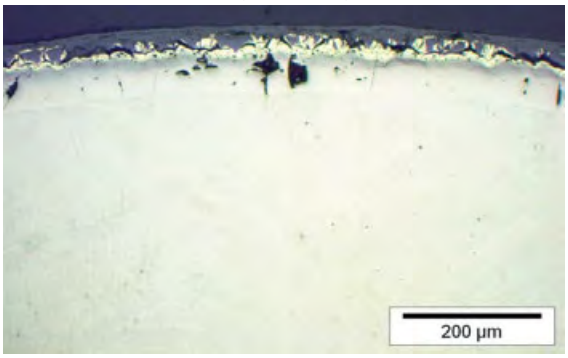

550 mm, 315°; 1760 K (TSH 9): moderate corrosion

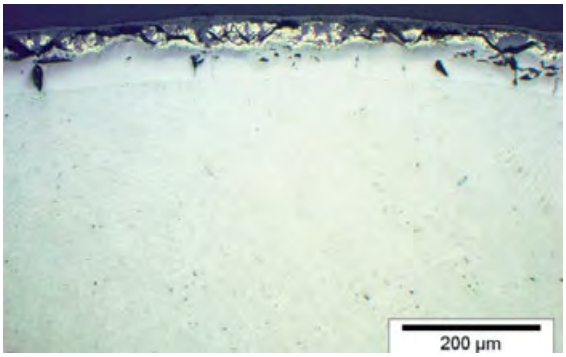

650 mm, 45°; 1660 K (TSH 10): moderate corrosion

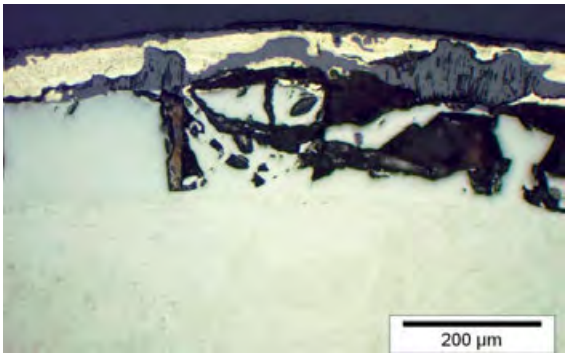

750 mm, 315°; 1735 (TSH 11): strong corrosion

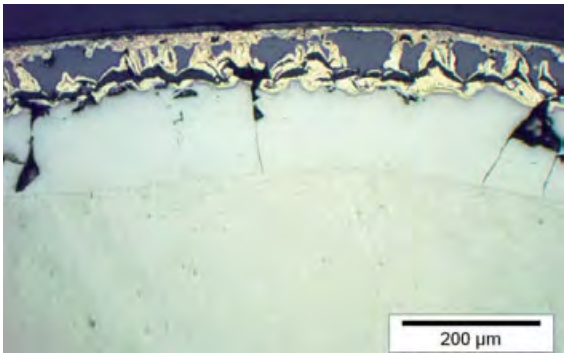

850 mm, 0°; 1844 K (TFS 10/12): strong corrosion

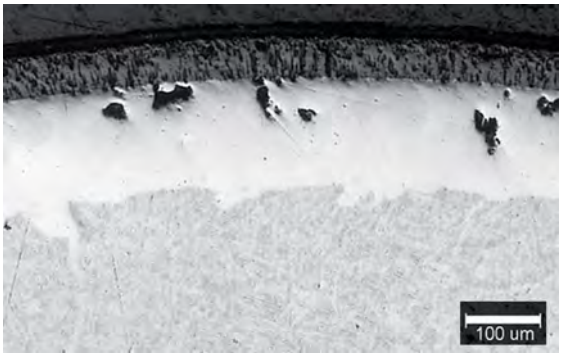

950 mm, 0°; 1434 K (TFS 11/13): no nitrides

Fig. 52: QUENCH-16; formation of nitrides for corner rod D (withdrawn before reflood initiation) at different bundle elevations with indication of temperature reached on the withdrawal time point.

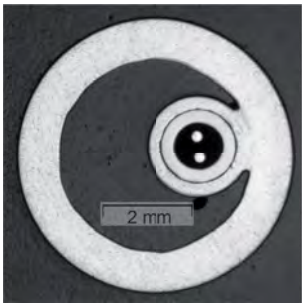

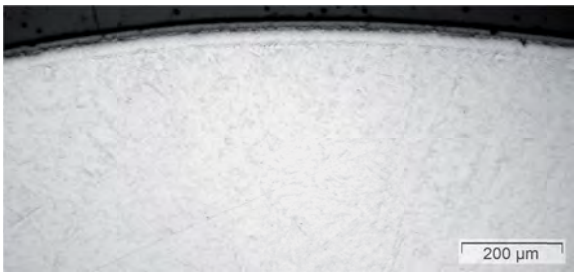

250 mm: δ_{ZrO2}=4.5 µm; α-Zr(O)=2.5 µm; T_{max}=945 K (TFS 12/7)

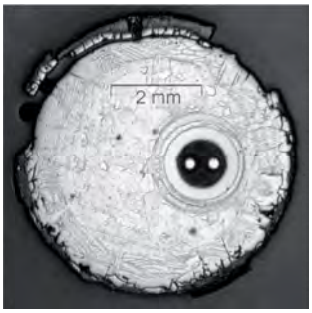

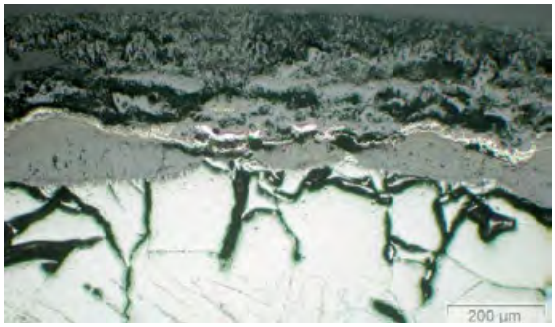

450 mm: relocated melt inside corner tube (left); δ_{ZrO2}=335 µm; α-Zr(O)=224 µm; residual nitrides

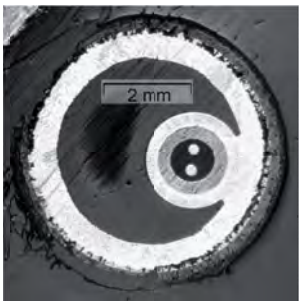

850 mm: δ_{ZrO2}=363 µm; α-Zr(O)=197 µm

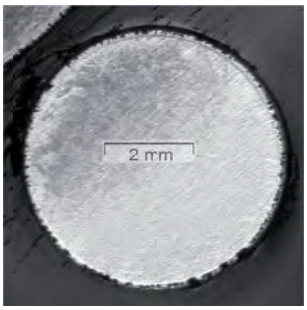

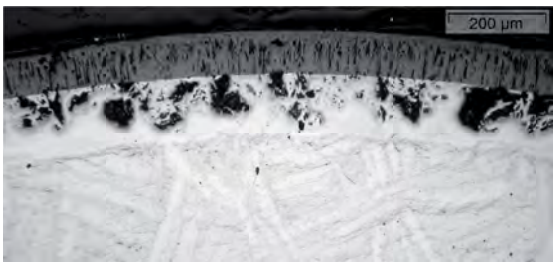

950 mm: δ_{ZrO2}=90 µm; α-Zr(O)=124 µm

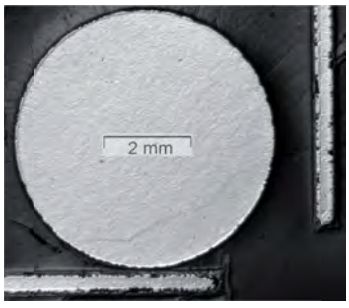

1050 mm: δ_{ZrO2}=30 µm; α-Zr(O)=53 µm

Fig. 53: QUENCH-16; metallography of corner rod A (tube up to 950 mm) withdrawn after the test.

Fig. 54: Neutron radiograph of rod B (axial range: 365 < z < 395 mm)

Fig. 55: Neutron radiograph of rod D (axial range: 355 < z < 385 mm)

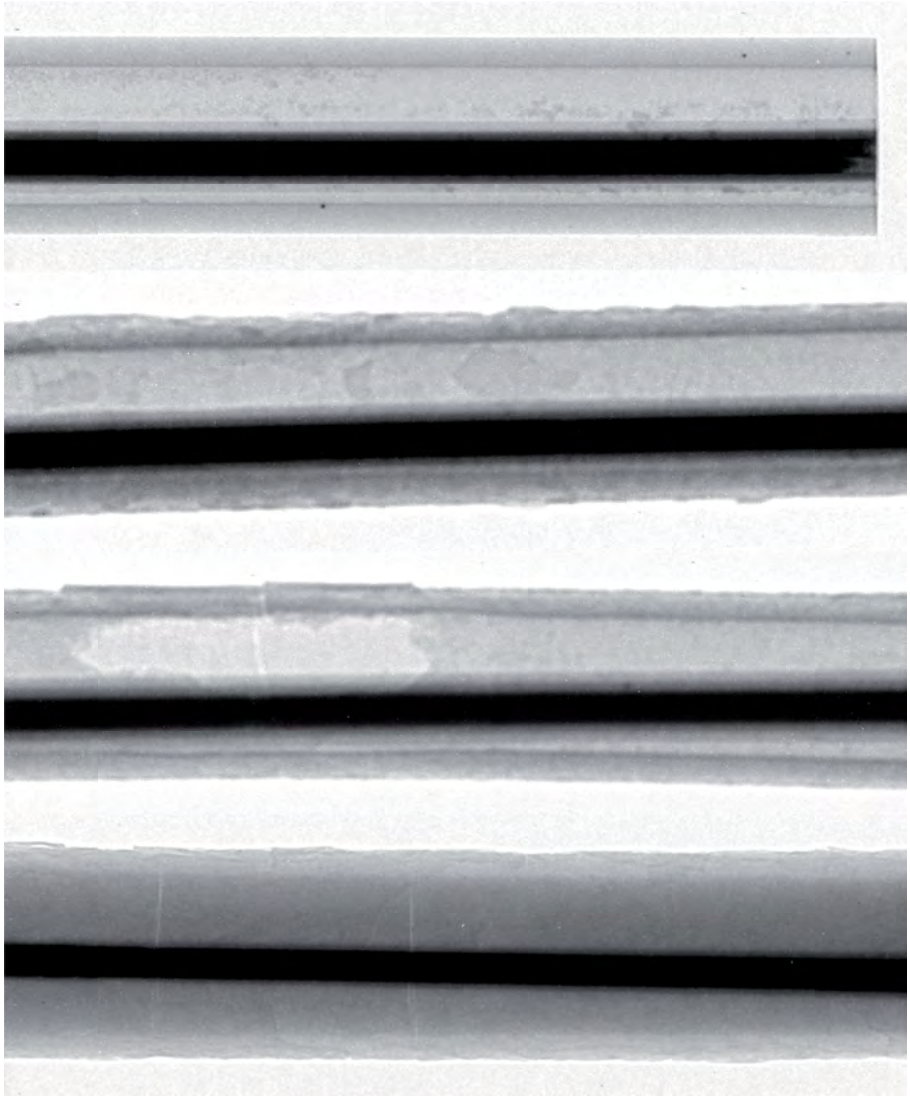

a) axial range: 214 < z < 240 mm

b) axial range: 270 < z < 300 mm

c) axial range: 340 < z < 370 mm

d) axial range: 460 < z < 480 mm

Fig. 56: Neutron radiograph of rod A (axial range: 210 < z < 480 mm)

Grid spacer #1 at -60 mm: frozen melt relocated from upper elevations

350 mm: oxide cracks; between rods – melt relocated from upper elevations

650 mm: absence of upper spalled oxide scales

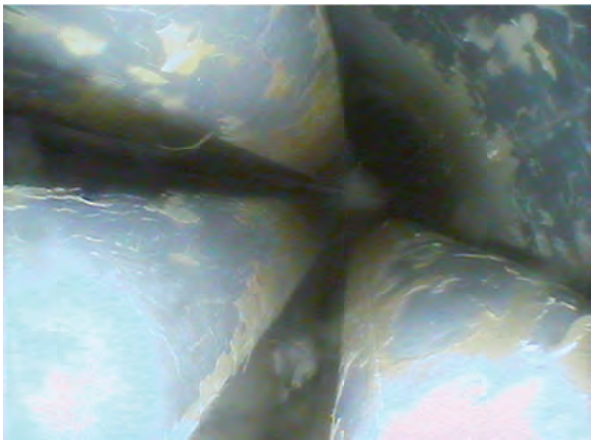

950 mm: spalling of coloured (yellow) surface layer of claddings

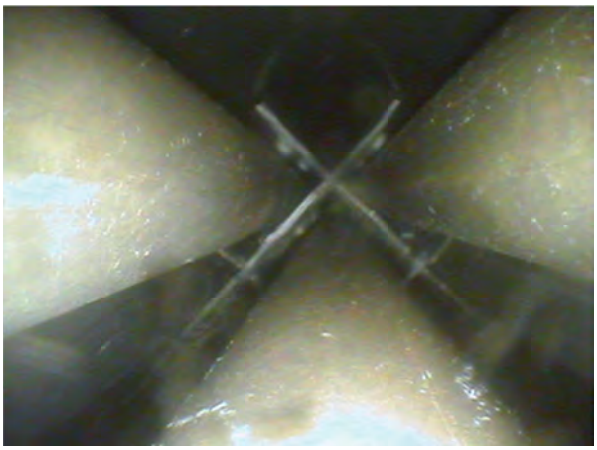

1050 mm: coloured (yellow) surface layer of claddings

1150 mm: intact dark oxidised surface of claddings

Fig. 57: QUENCH-16: Post-test visual investigations by endoscope introduced at the position of the corner rod B: front view.

250mm; cladding failure

350 mm: frozen metallic melt relocated from upper elevations

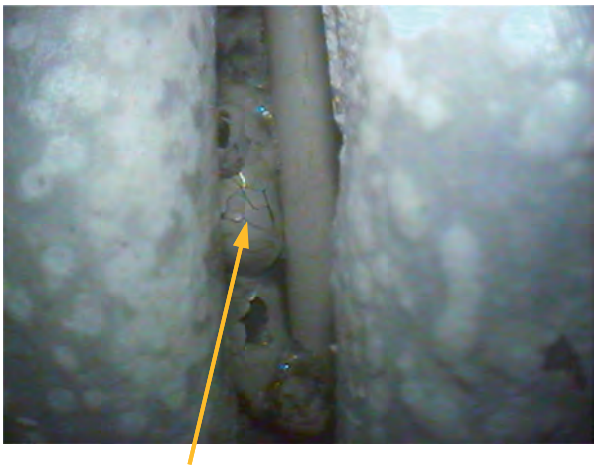

420 mm: oxidised melt droplets and rivulets

595 mm; palling of white oxide; cladding failure

600 mm: intensive cladding damaging

755 mm; spalling of thick oxide scales

Fig. 58: QUENCH-16: Post-test visual investigations by endoscope introduced at the position of the corner rod B: side view.

787mm; crack going through oxide layer

835mm; spalled yellowed scale

880mm; intact transparent yellowed scale

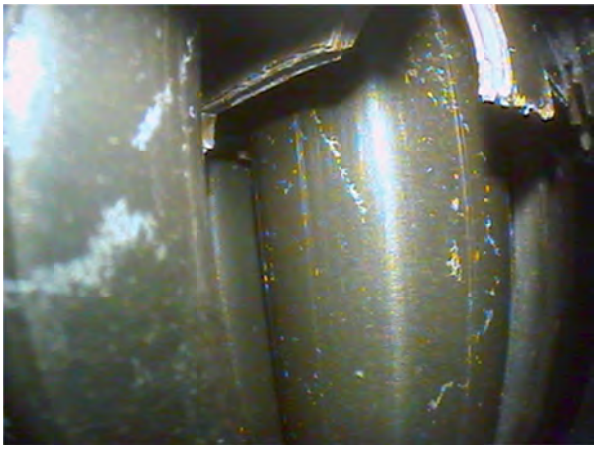

1050 mm: dark oxide of claddings, intact Grid Spacer #4

Fig. 59: QUENCH-16: Post-test visual investigations by endoscope introduced at the position of the corner rod B: side view 2.

0 mm: relocated small oxidised debris adhered to surface of lightly oxidised claddings

400 mm: breakup of cladding pieces

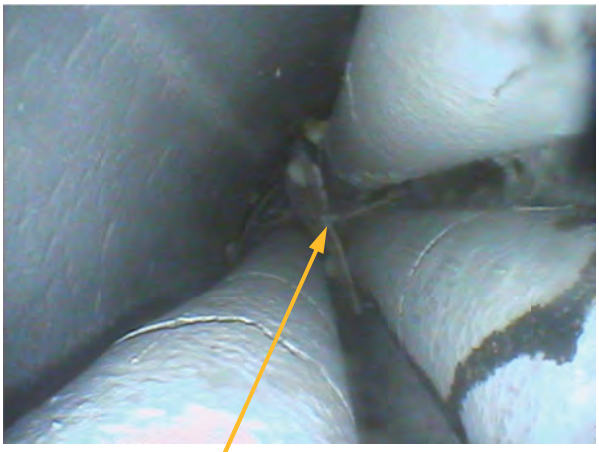

450 mm: cracks going through the oxidised cladding; piece of relocated oxidised GS#3

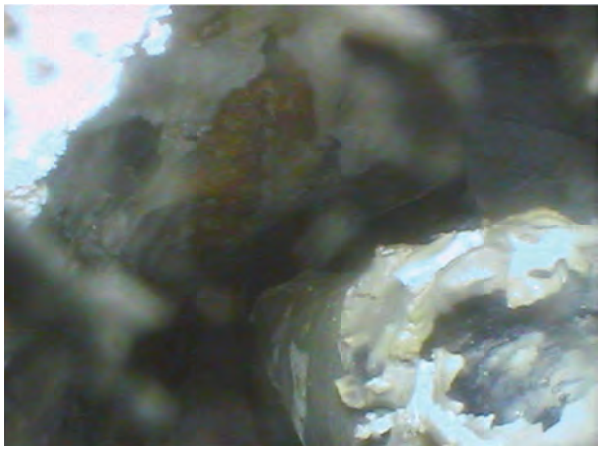

600 mm: cladding melted through

700 mm: spalling of yellowed ZrO2 scales from oxide layer

1000 mm: spalling of yellowed ZrO2 scales from oxide layer

Fig. 60: QUENCH-16: Post-test visual investigations by endoscope introduced at the position of the corner rod D: front view.

215 mm: relocated frozen melt between rod #21 and shroud

280mm, spalling at rods #9 and #21

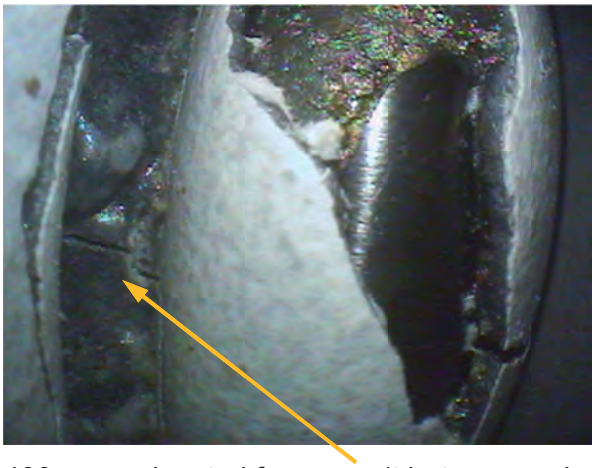

400 mm: relocated frozen melt between rods

550 mm: ZrO2 insulation damage under failed shroud

600 mm: damaging of cladding due to influence of melt

670 mm, spalling at rod#21; shroud

Fig. 61: QUENCH-16: Post-test visual investigations by endoscope introduced at the position of the corner rod D: side view.

775mm, spalling at rod#9 (centre); rod#21 (right); bottom of yellowed oxide

875mm; top of yellowed oxide; breakaway at TC

1050mm, rod #9; below GS#4; TFS 2/14

Fig. 62: QUENCH-16: Post-test visual investigations by endoscope introduced at the position of the corner rod D: side view 2.

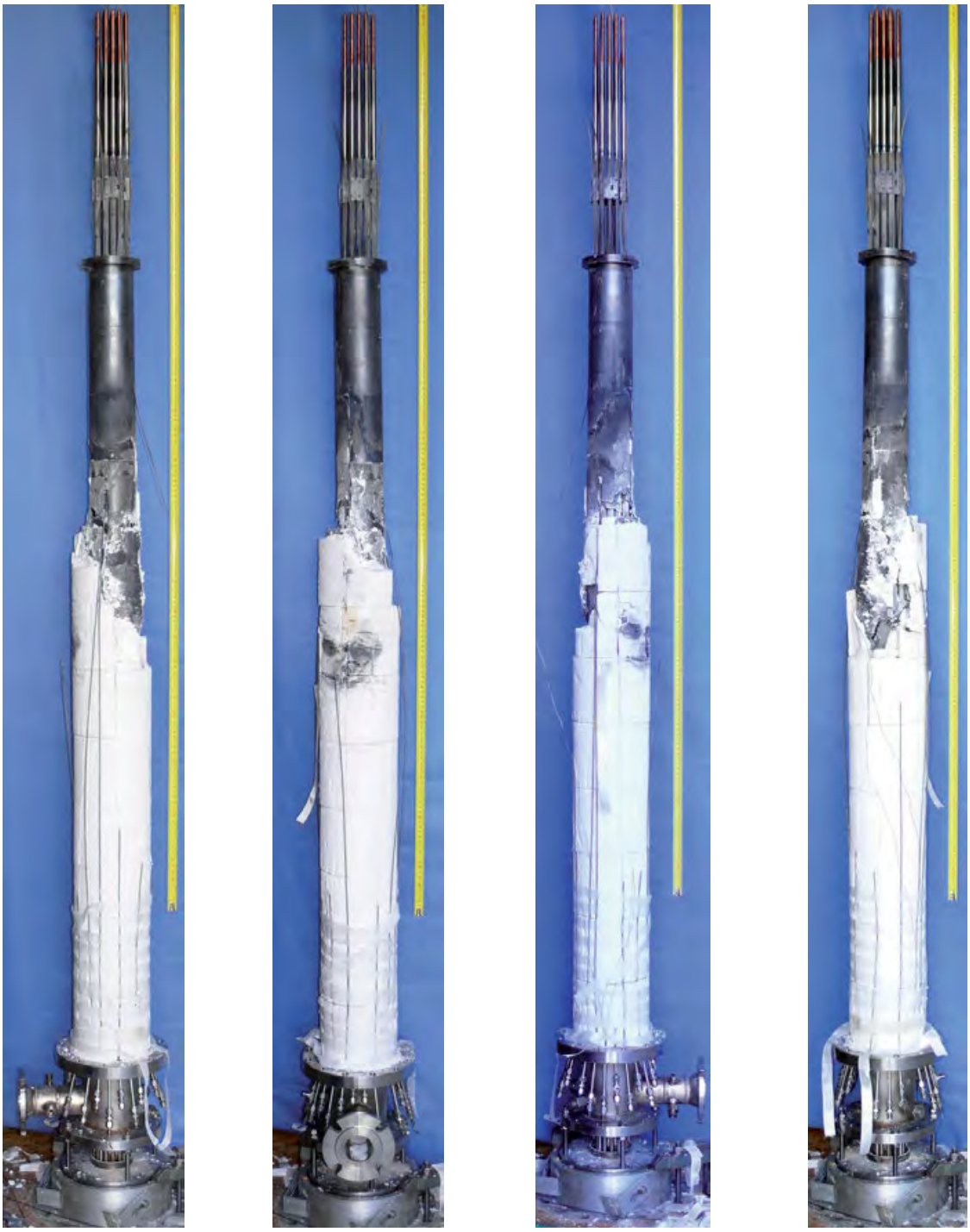

Fig.63: QUENCH-16; Bundle (with shroud and partially ZrO_2 insulation) withdrawn from cooling jacket.

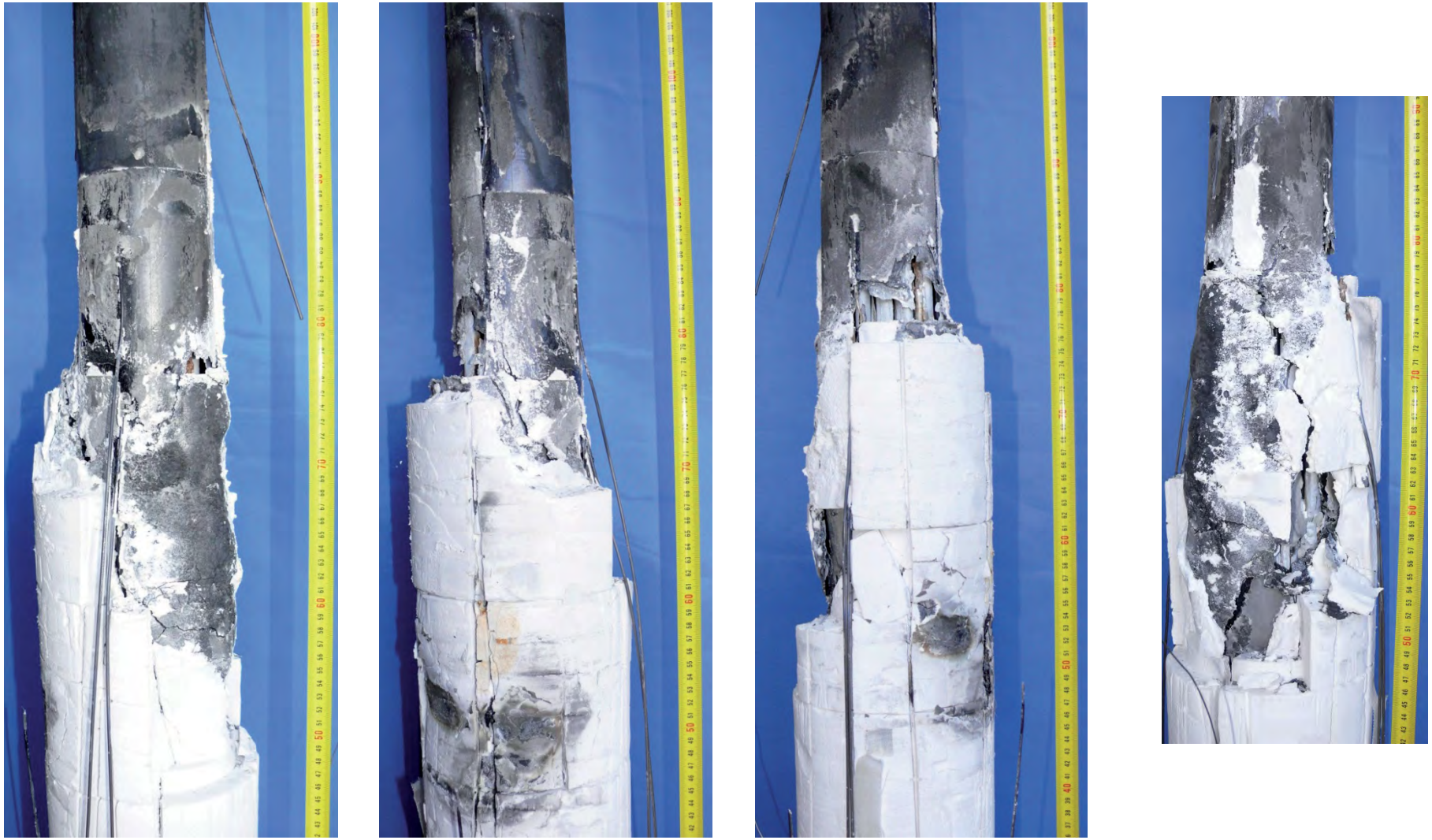

0° 90° 180° 270°

Fig.64: QUENCH-16; middle part of bundle (with shroud and ZrO_2) withdrawn from cooling jacket.

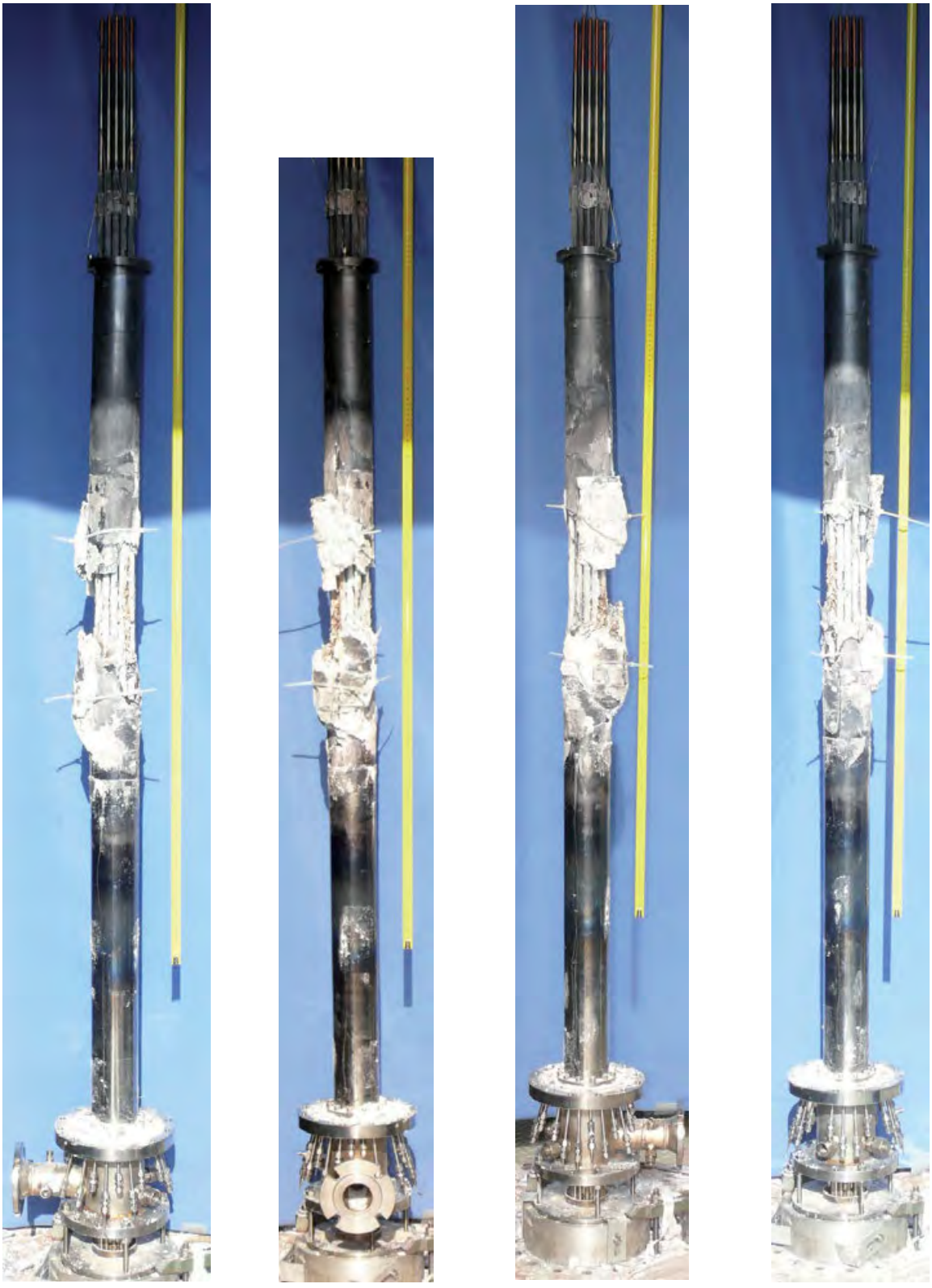

0° 90° 180° 270°

Fig. 65: QUENCH-16; Bundle (with shroud and partially ZrO_2 insulation) withdrawn from cooling jacket.

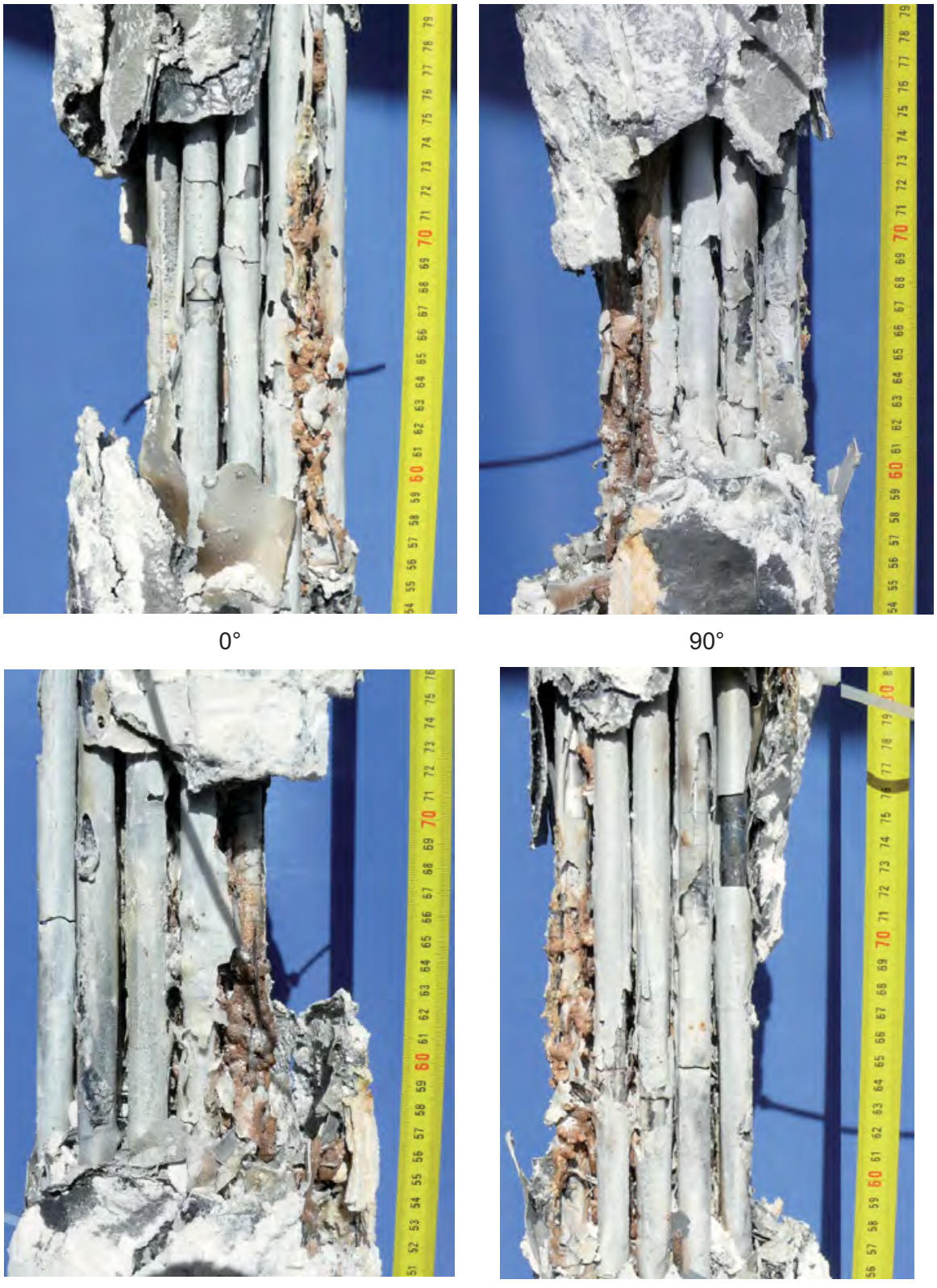

Fig.66: QUENCH-16; middle part of bundle after dismounting of ZrO_2 insulation (deleted together with shroud parts).

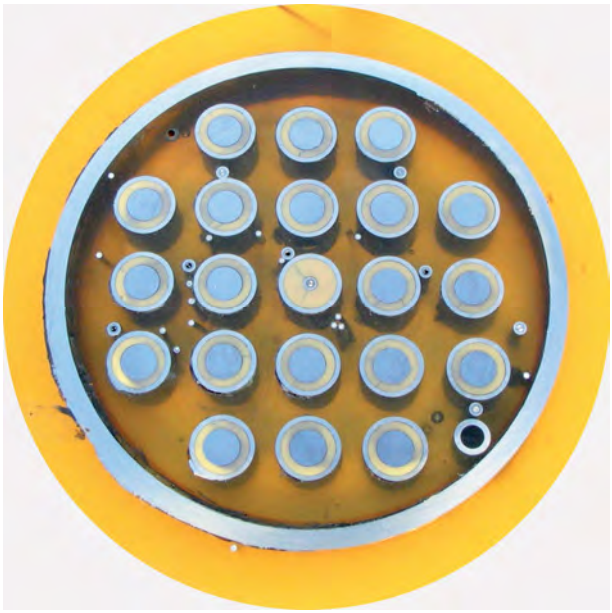

QUE-16-1 (**80 mm**, bottom)

QUE-16-1 (**100 mm**, top)

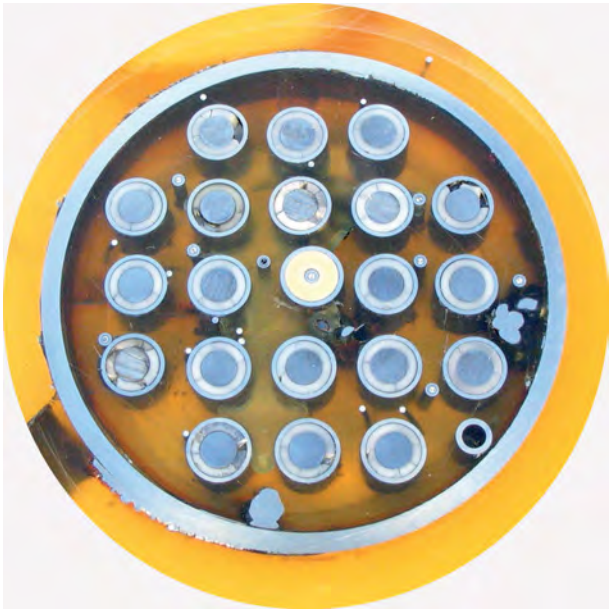

QUE-16-2 (**230 mm**, bottom)

QUE-16-2 (**250 mm**, top)

Fig. 67: QUENCH-16; Bundle cross sections at 80 mm, 100 mm, 230 mm and 250 mm.

QUE-16-3 (**330 mm**, bottom)

QUE-16-3 (**350 mm**, top)

QUE-16-4 (**430 mm**, bottom)

QUE-16-4 (**450 mm**, top)

Fig. 68: QUENCH-16; Bundle cross sections at 330 mm, 350 mm (normal magnification); 430 mm and 450 mm (reduced magnification).

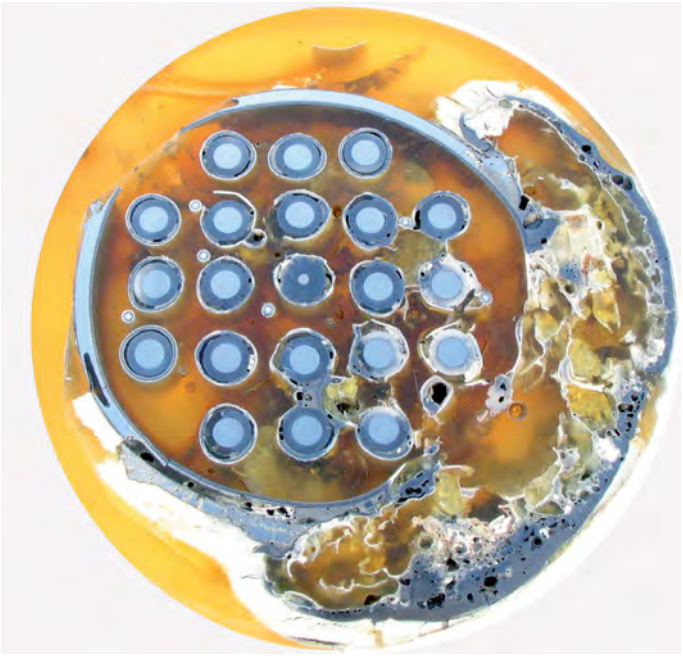

QUE-16-5 (**530 mm**, bottom)

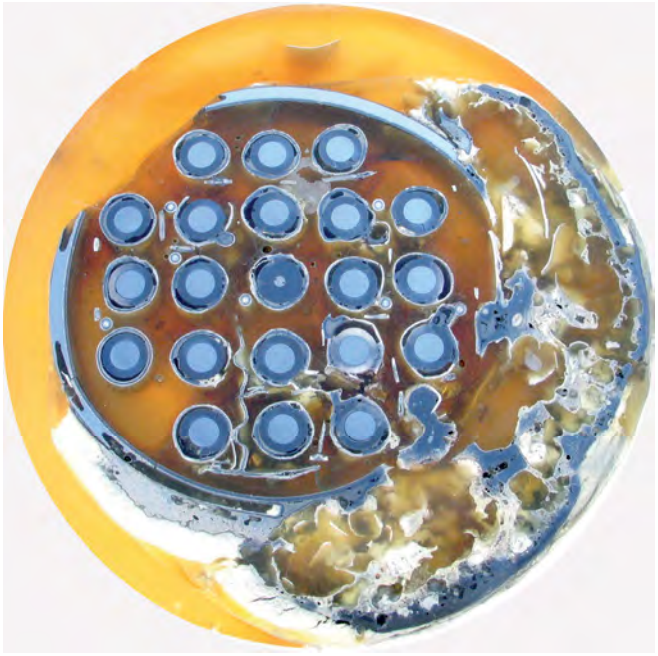

QUE-16-5 (**550 mm**, top)

QUE-16-6 (**630 mm**, bottom)

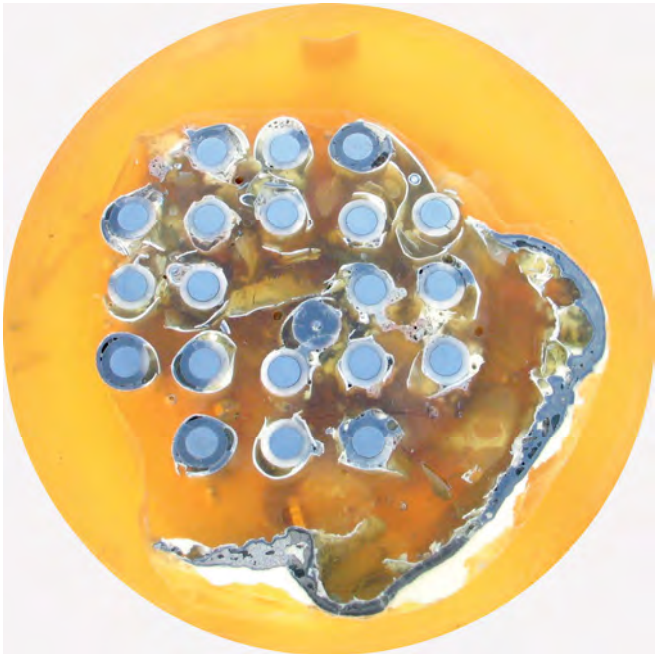

QUE-16-6 (**650 mm**, top)

Fig. 69: QUENCH-16; Bundle cross sections at 530 mm, 550 mm, 630 mm and 650 mm (reduced magnification).

QUE-16-7 (**730 mm**, bottom)

QUE-16-7 (**750 mm**, top)

QUE-16-8 (**830 mm**, bottom)

QUE-16-8 (**850 mm**, top)

Fig. 70: QUENCH-16; Bundle cross sections at 730 mm, 750 mm, 830 mm and 850 mm.

QUE-16-9 (**930 mm**, bottom)

QUE-16-9 (**950 mm**, top)

QUE-16-10 (**1030 mm**, bottom)

QUE-16-10 (**1050 mm**, top)

Fig. 71: QUENCH-16; Bundle cross sections at 930 mm, 950 mm, 1030 mm and 1050 mm.

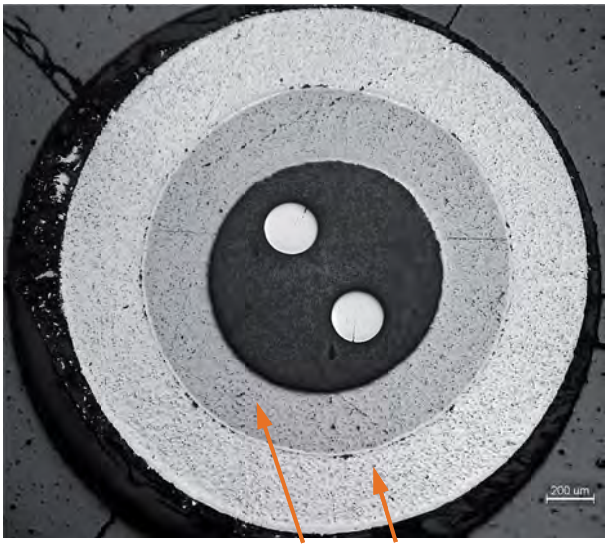

350 mm: intact solid Ta and Zr TC claddings

450 mm: intact solid Ta and Zr TC claddings

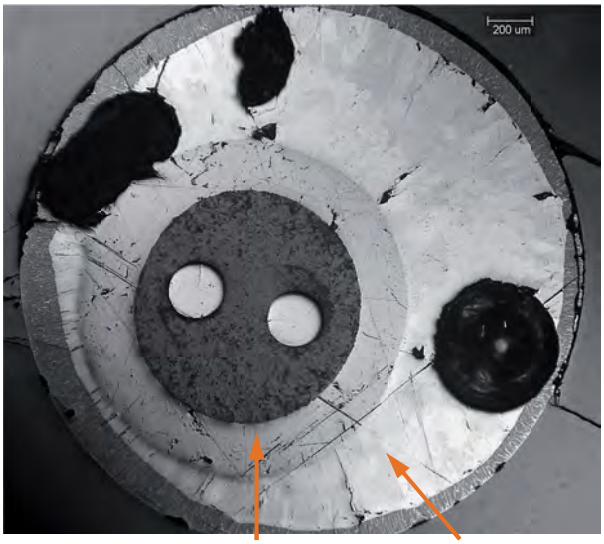

550 mm: intact Ta, relocated molten Zr oxidised at periphery

650 mm: intact Ta, relocated molten Zr completely oxidised

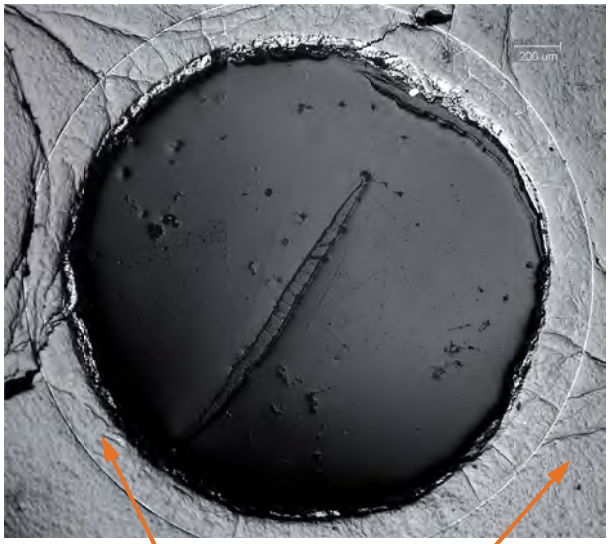

750 mm: residual completely oxidised Zr relocated from upper TCRC 13 and stuck at the surrounded ZrO_2 pellet

Fig. 72: QUENCH-16; thermocouple TCRC 10 inside the central rod.

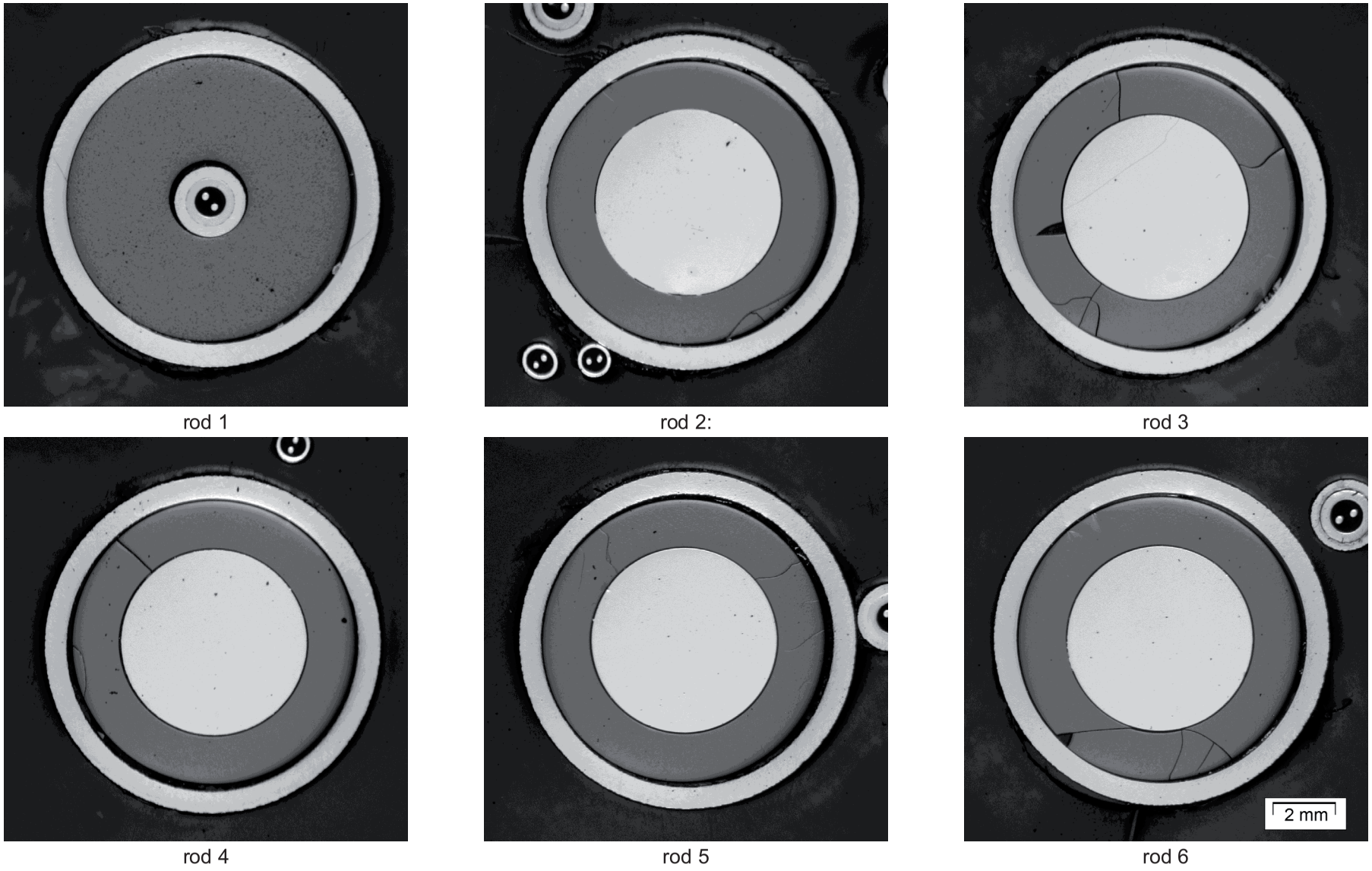

Fig.73: QUENCH-16; Cross section at elevation 250 mm depicting individual test rods 1-6.

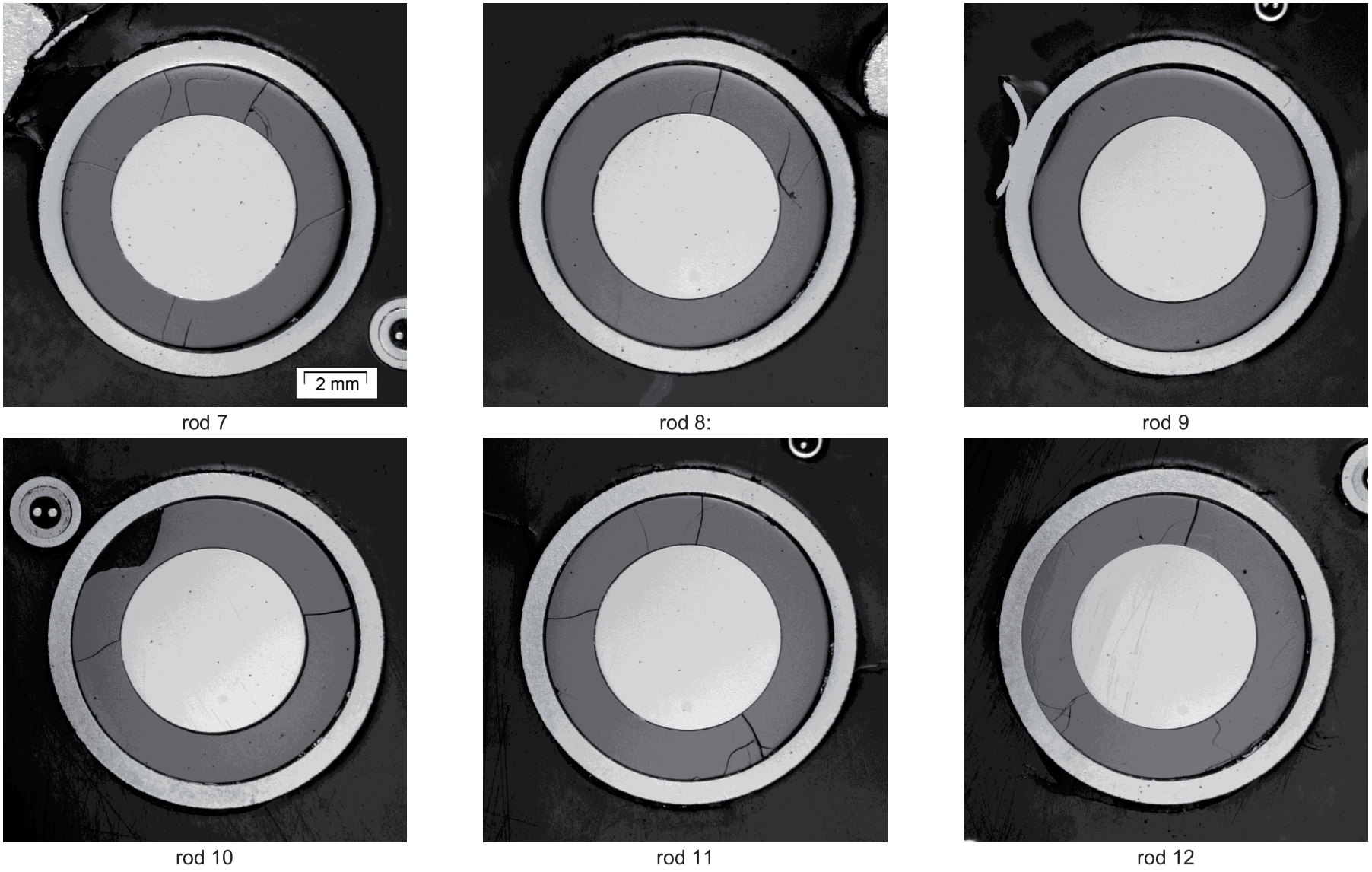

Fig.74: QUENCH-16; Cross section at elevation 250 mm depicting individual test rods 7-12.

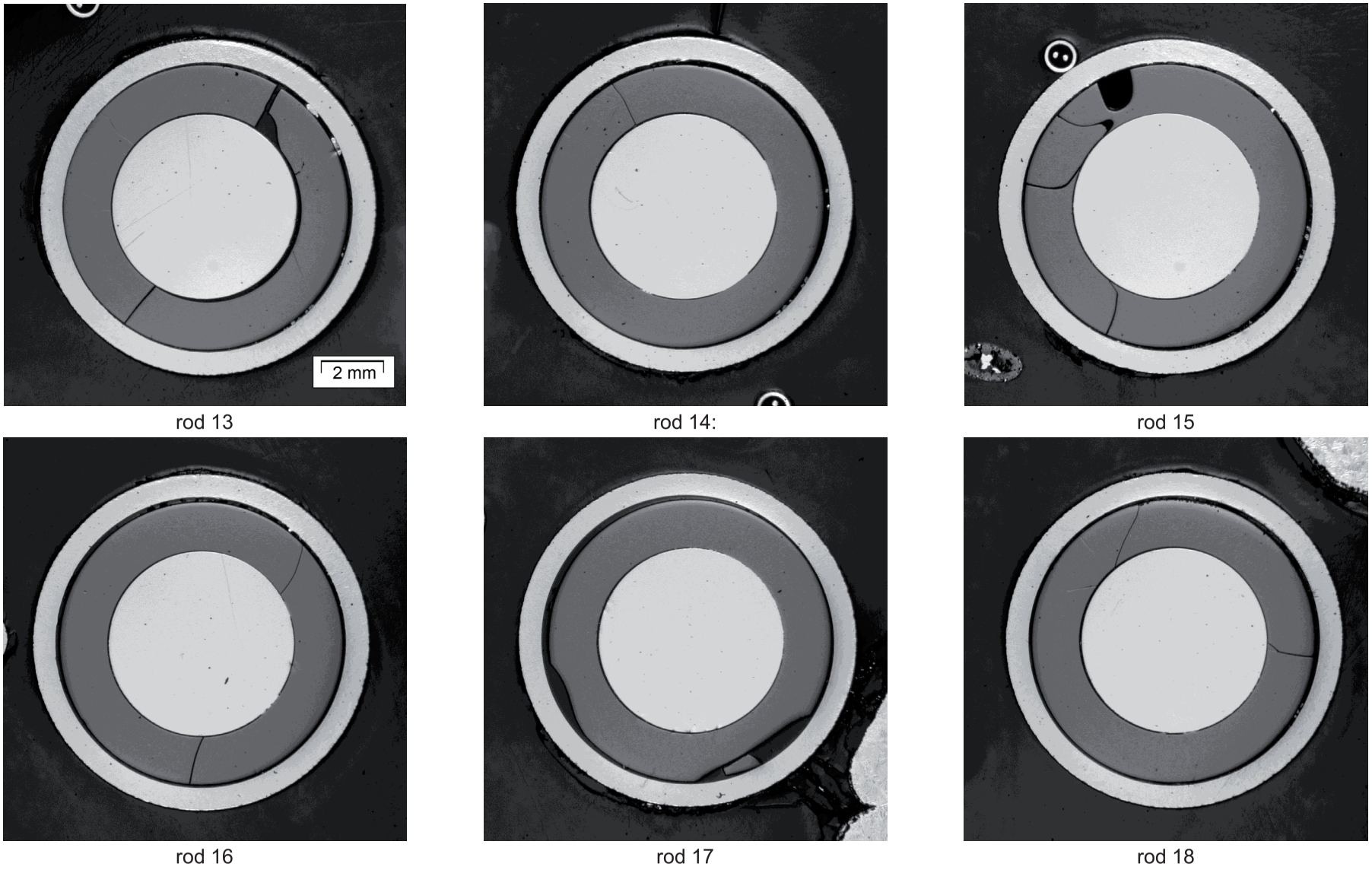

Fig.75: QUENCH-16; Cross section at elevation 250 mm depicting individual test rods 13-18.

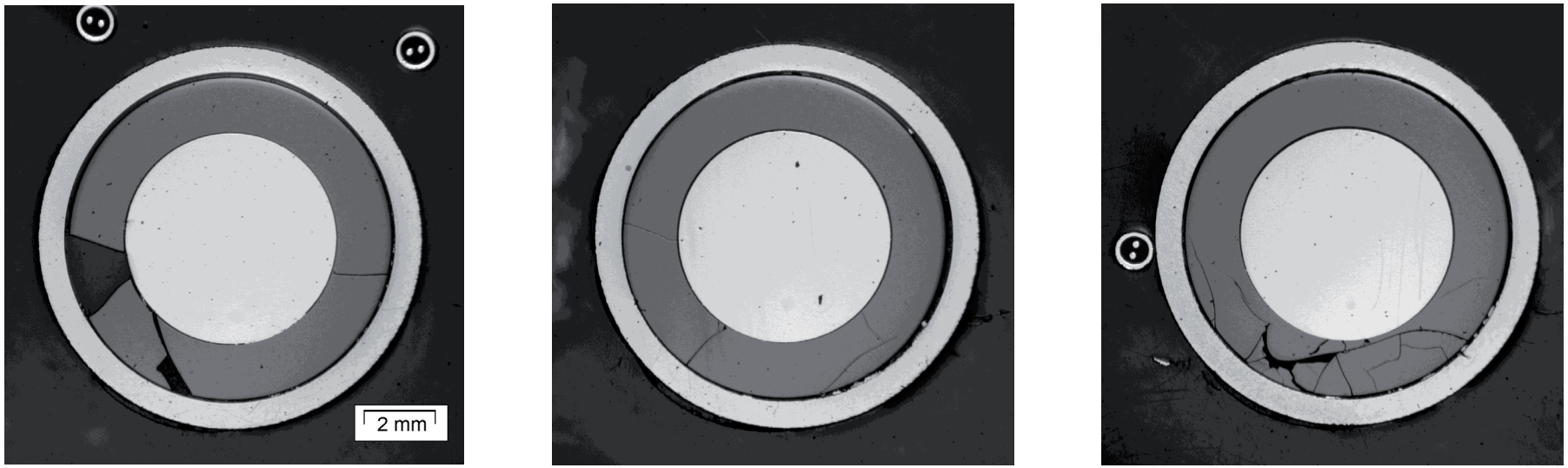

Fig.76: QUENCH-16; Cross section at elevation 250 mm depicting individual test rods 19-21.

rod 2, 270°: not oxidised melt

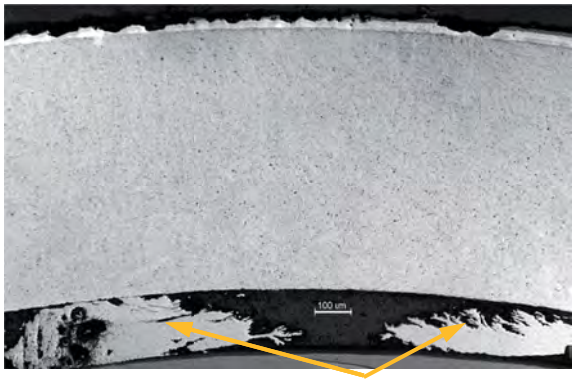

rod 3, 135°: melt

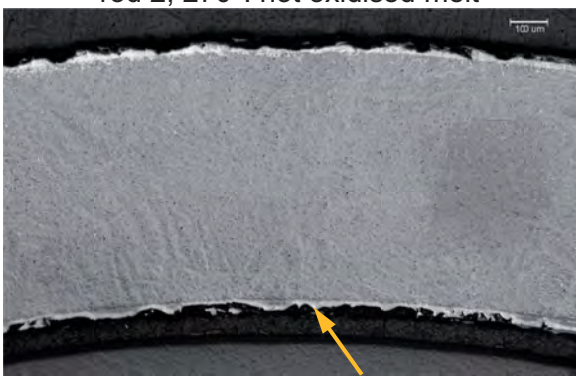

rod 4, 90°: melt

rod 5, 0°: melt

rod 13, 135°: melt

rod 14, 270°

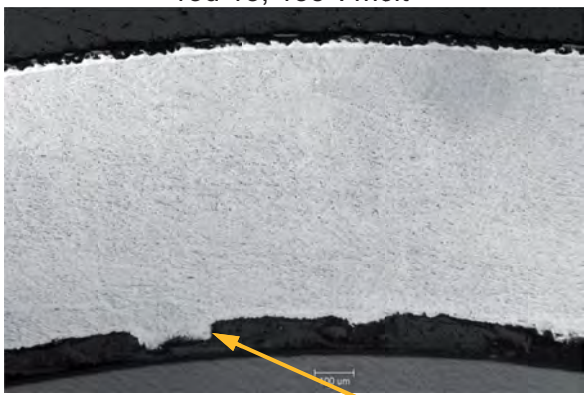

rod 15, 0°: melt

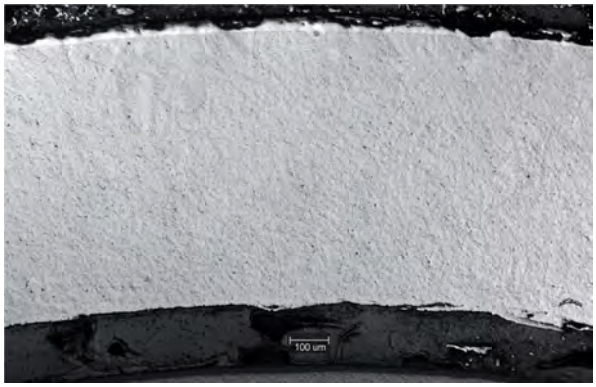

rod 16, 0°

Fig.77: QUENCH-16; cladding structure at 250 mm with melt fragments relocated from upper elevations between pellet and cladding.

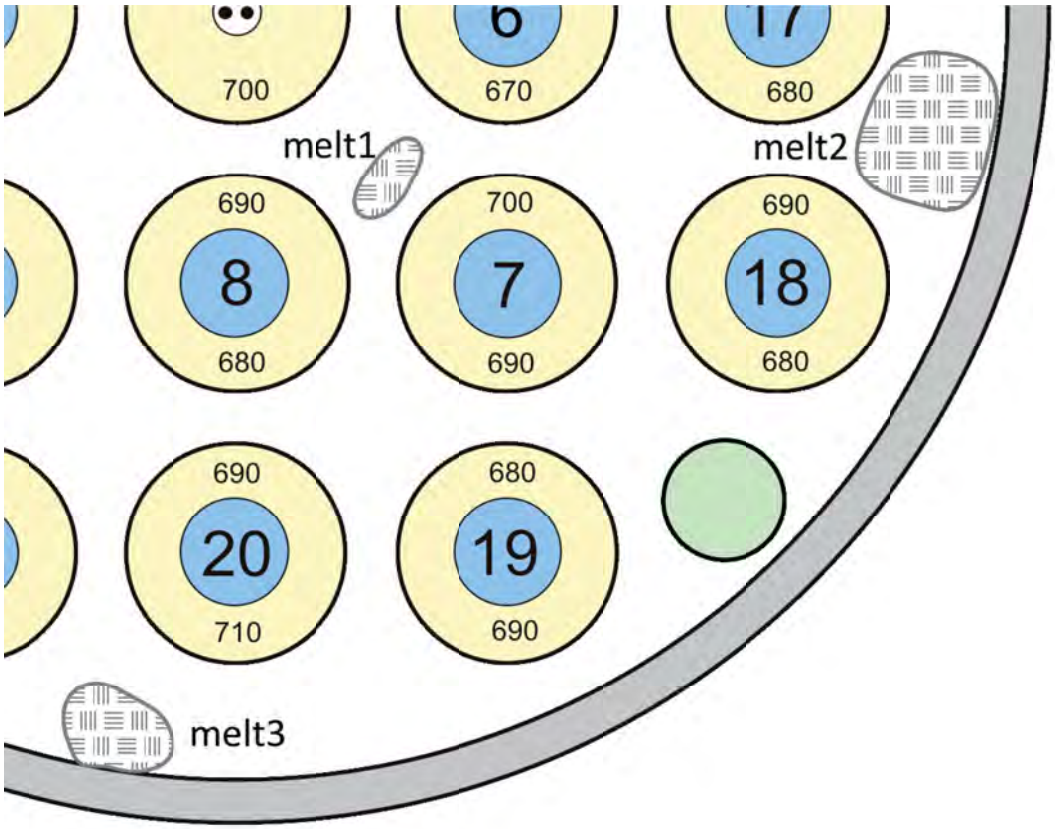

wt %	Zr	Fe	Cr	*Ni*	Sn	Hf	*Ta*	Total
shroud (Zr 702)	99.11	0.24	0	*0*	0	0.64	*0*	99.99
Zr 702 shroud product certification		0.11 (Fe + Cr)	0	*0*	0	0.7	*0*	
rod 8 (Zry-4)	98.35	0.24	0.12	*0*	1.29	0	*0*	100
melt1	97.99	0.52	0.15	*0.32*	0.3	0.48	*0.24*	100
melt2	99.24	0.15	0	*0*	0.15	0.46	*0*	100
melt3	97.62	0.41	0.17	*0.39*	0.54	0.51	*0.36*	100
possible source for melt	shroud +clad	shroud +clad	clad	*low T TC*	clad	shroud	*high T TC*	

Fig. 78: QUENCH-16; EDX analysis of shroud, cladding and relocated melt at elevation 250 mm

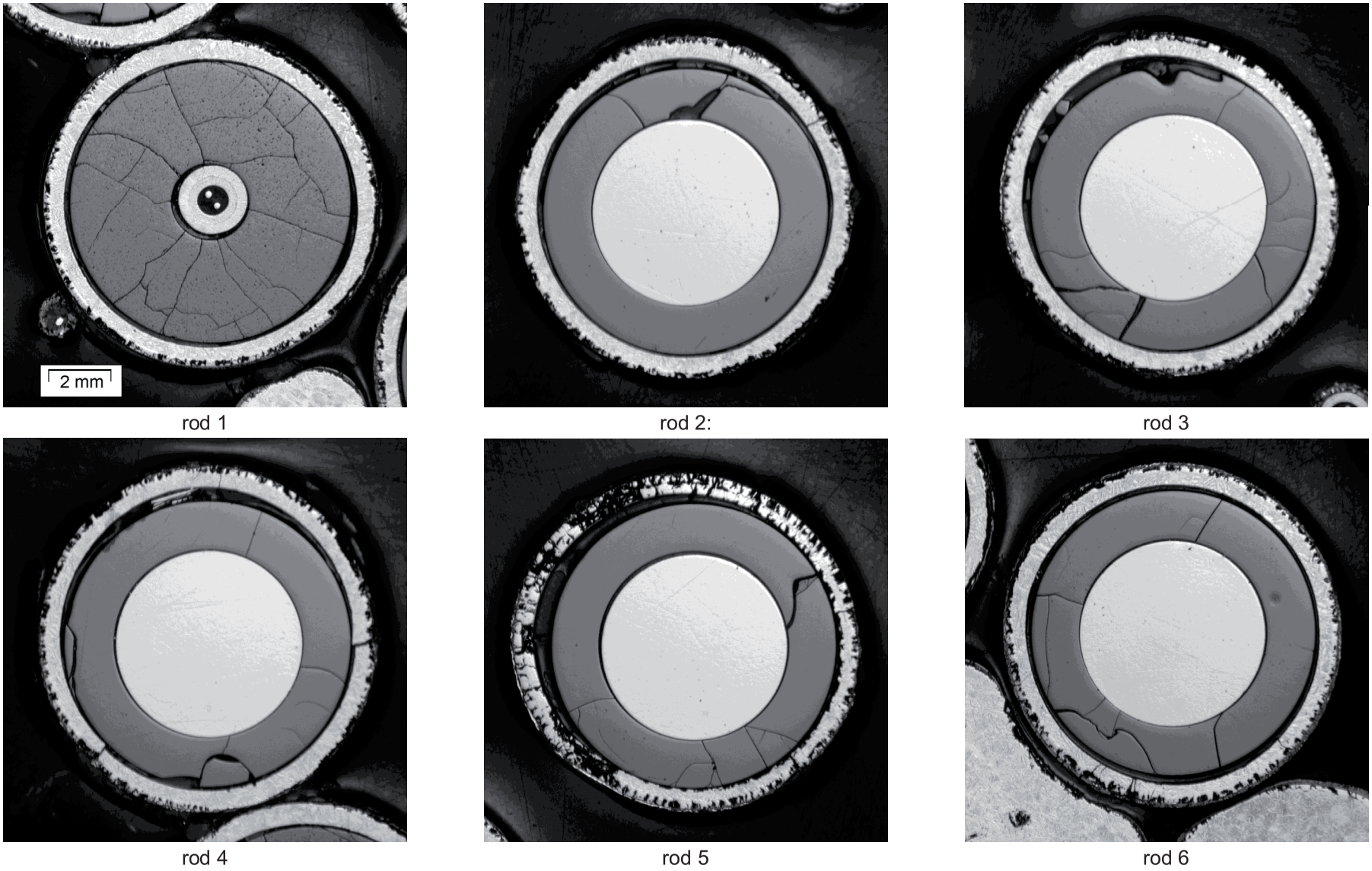

Fig.79: QUENCH-16; Cross section at elevation 350 mm depicting individual test rods 1-6.

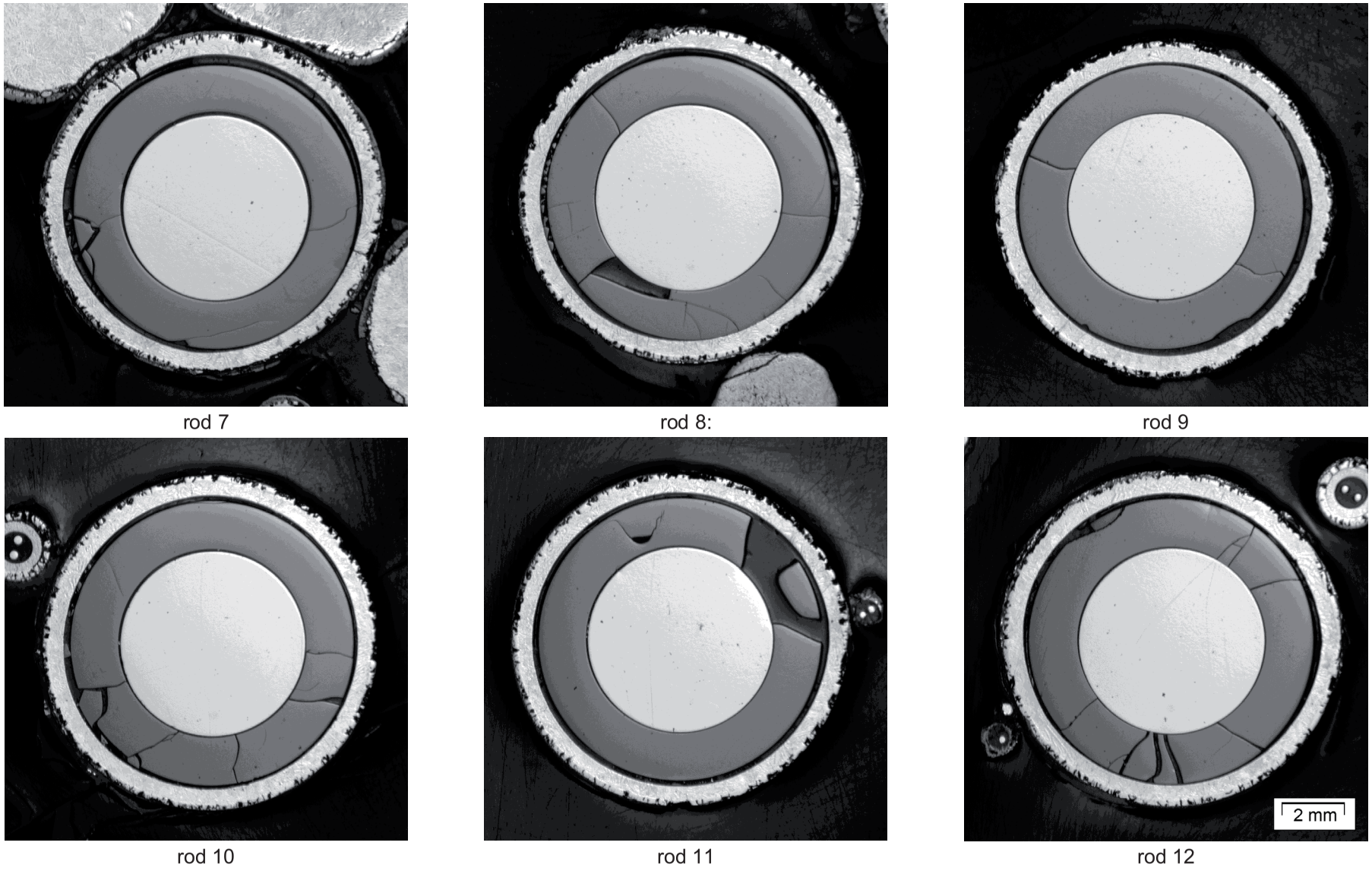

Fig.80: QUENCH-16; Cross section at elevation 350 mm depicting individual test rods 7-12.

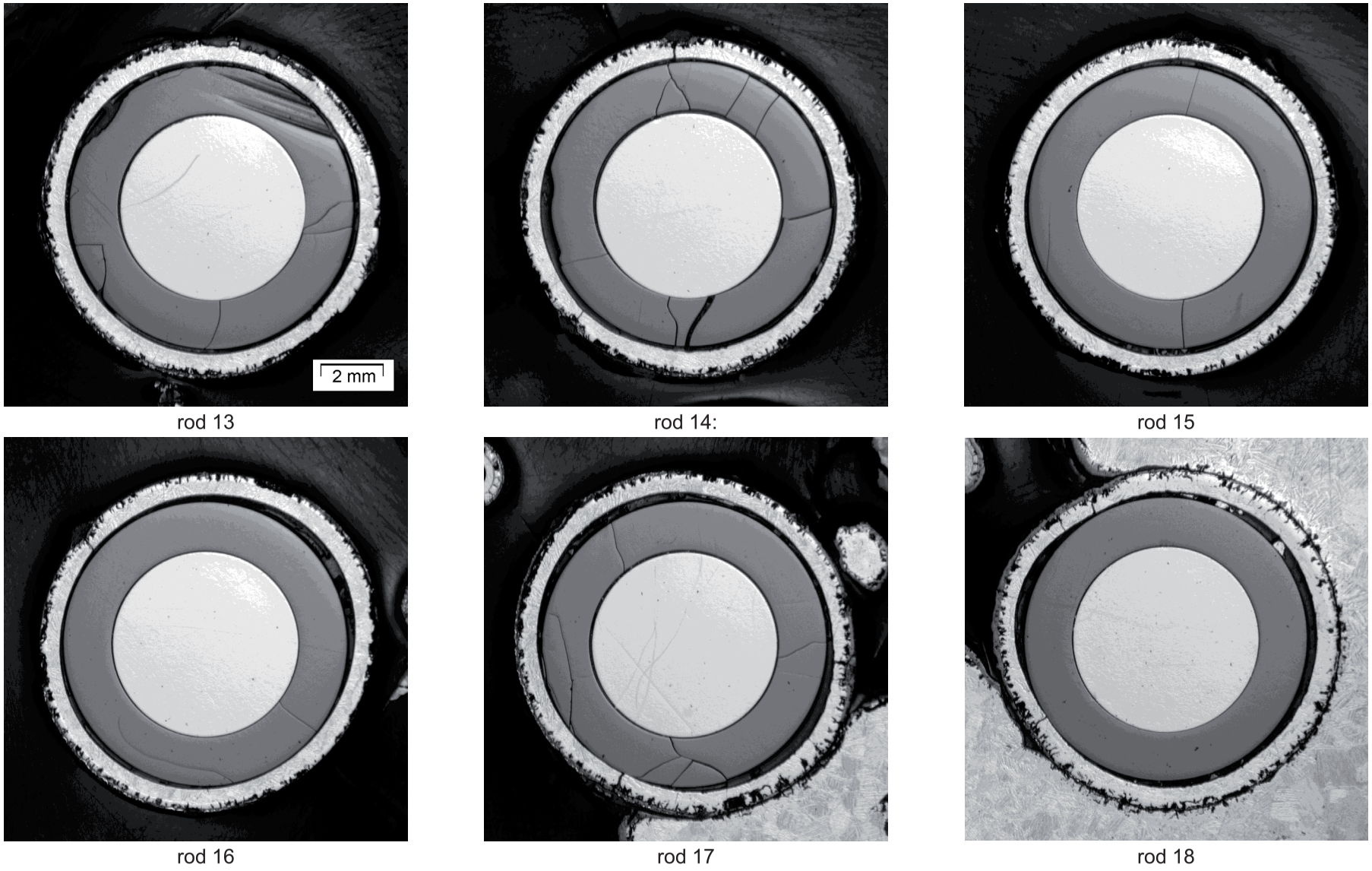

Fig.81: QUENCH-16; Cross section at elevation 350 mm depicting individual test rods 13-18.

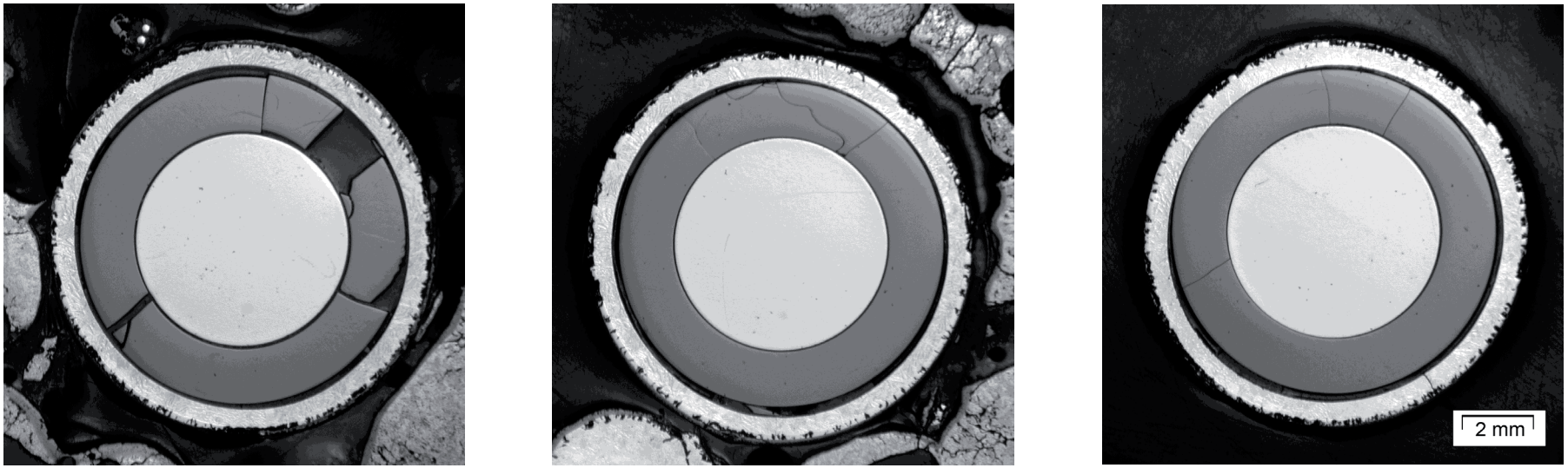

Fig.82: QUENCH-16; Cross section at elevation 350 mm depicting individual test rods 19-21.

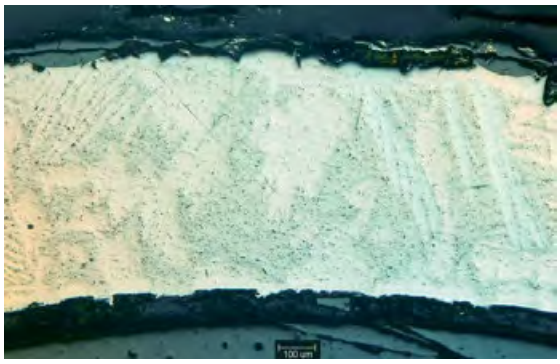

0°: nitrides; outer ZrO_2 spalled; homogeneous ZrO_2 developed during quench

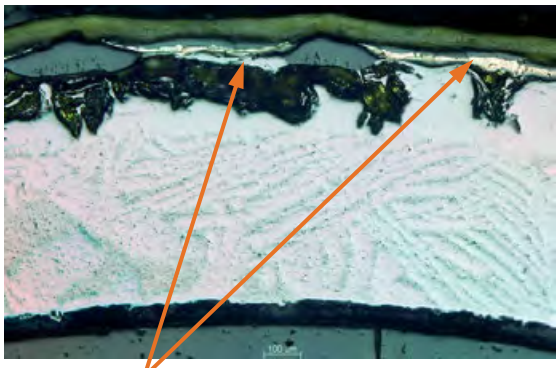

45°: nitrides; outer oxide sub-layer (yellowish); homogeneous ZrO_2 developed during quench

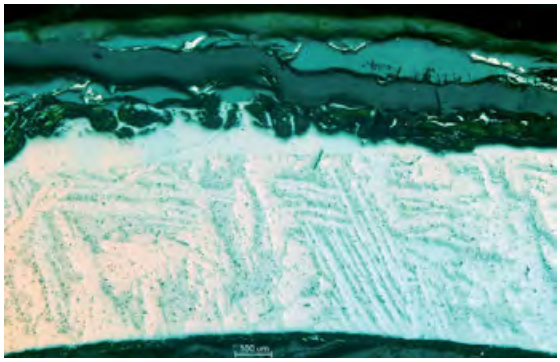

90°: nitrides; outer oxide sub-layer (yellowish); homogeneous ZrO_2 developed during quench

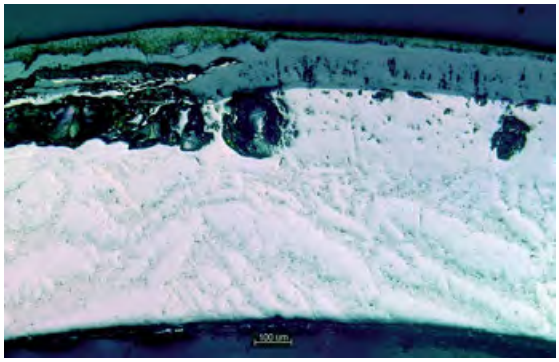

135°: nitrides; outer oxide sub-layer (yellowish); homogeneous ZrO_2 developed during quench

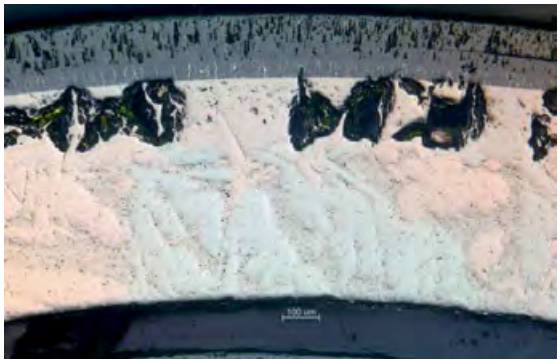

180°: regular ZrO_2

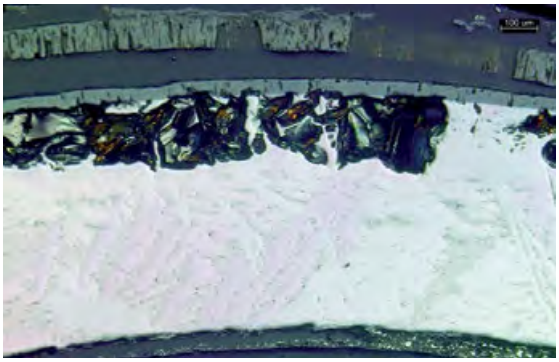

215°: regular ZrO_2

270°: regular ZrO_2

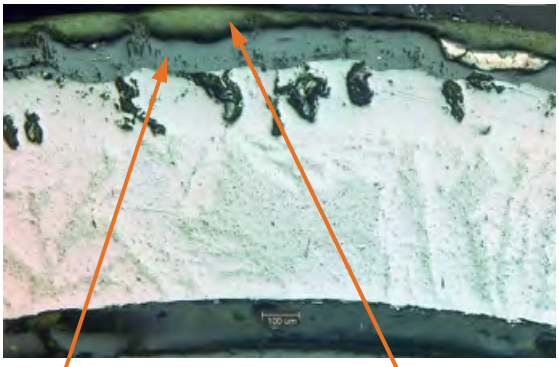

315°: nitrides; outer oxide sub-layer (yellowish); homogeneous ZrO_2 developed during quench

Fig. 83: QUENCH-16; cladding structure of rod #1 at elevation of 350 mm with nitrides (light strips) at the interface between two oxide sub-layers.

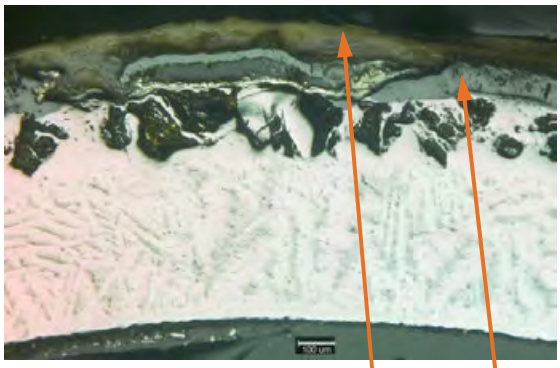

rod 2, 0°: nitrides between outer porous re-oxidised layer and internal secondary oxide

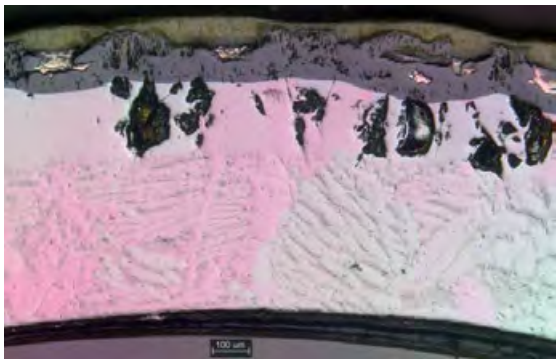

rod 3, 90°: nitrides between two oxide sub-layers

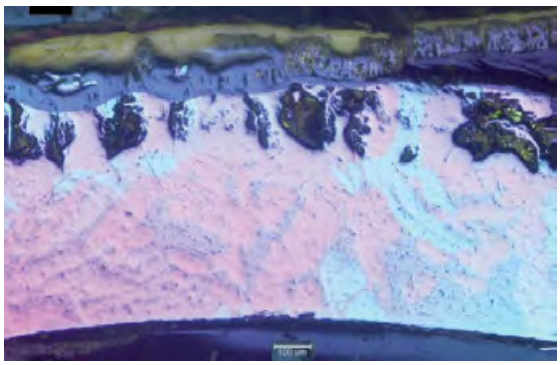

rod 4, 270°: nitrides between two oxide sub-layers

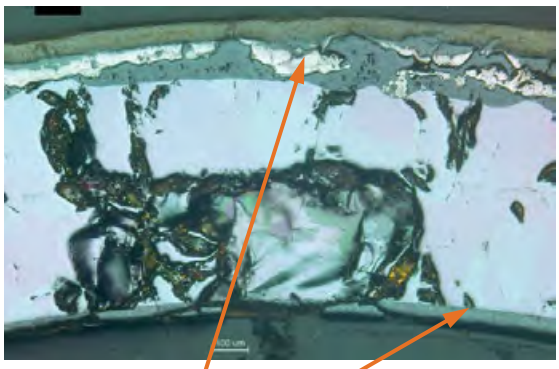

rod 5, 270°: nitrides between two oxide sub-layers; ZrO_2 ***at inner*** clad surface

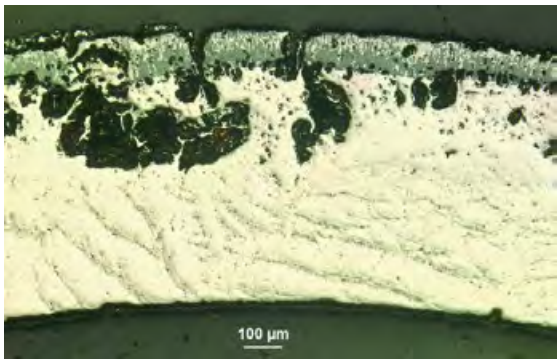

rod 6, 225°: *metallic precipitates inside* dense oxide layer due to local steam starvation

rod 7°, 270°: nitrides ***inside*** secondary oxide

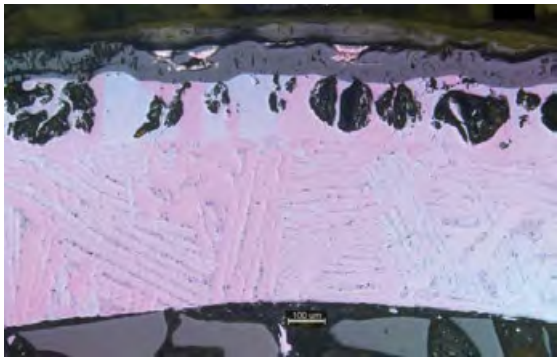

rod 8, 270°: nitrides between two oxide sub-layers

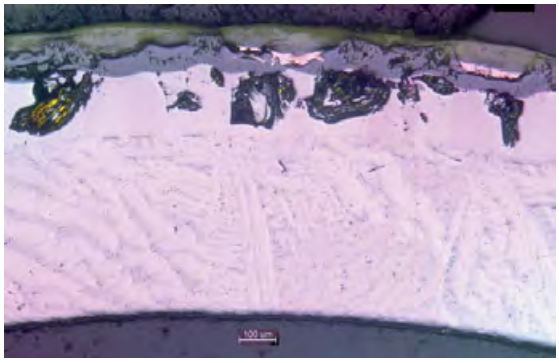

rod 9, 180°: nitrides between two oxide sub-layers

Fig. 84: QUENCH-16; cladding structure of internal rods #2 - #9 with outer oxide sub-layer (yellowish by epoxy resin) at elevation 350 mm

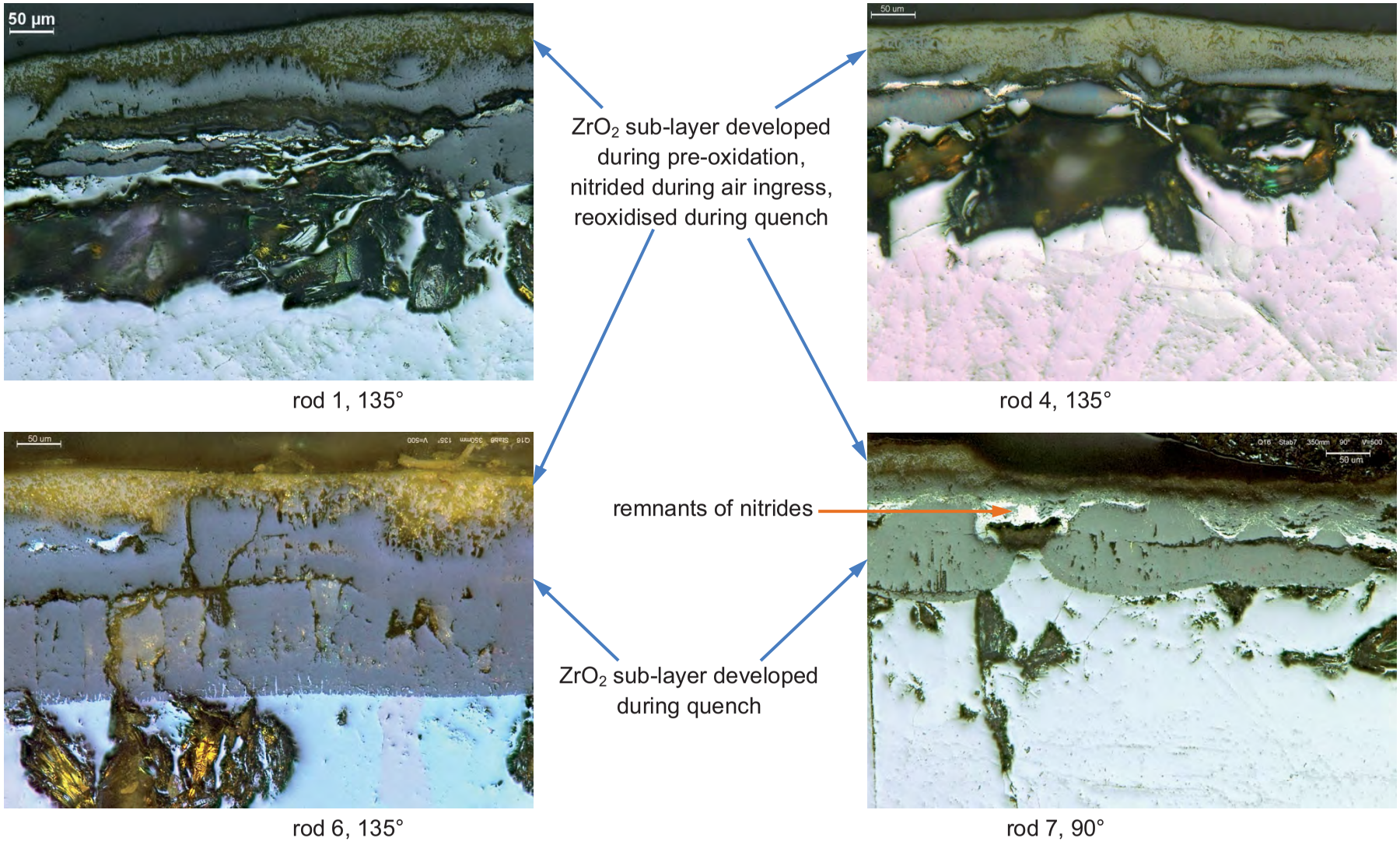

Fig. 85: QUENCH-16; structure of outer oxide layer with reoxidised porous sublayer coloured by epoxy resin for claddings at elevation 350 mm.

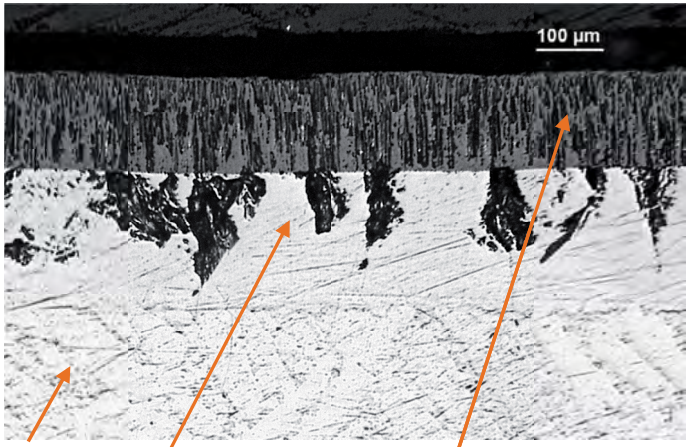

45°: prior β-Zr layer, α-Zr(O) layer, moderate oxide layer, absence of outer porous layer

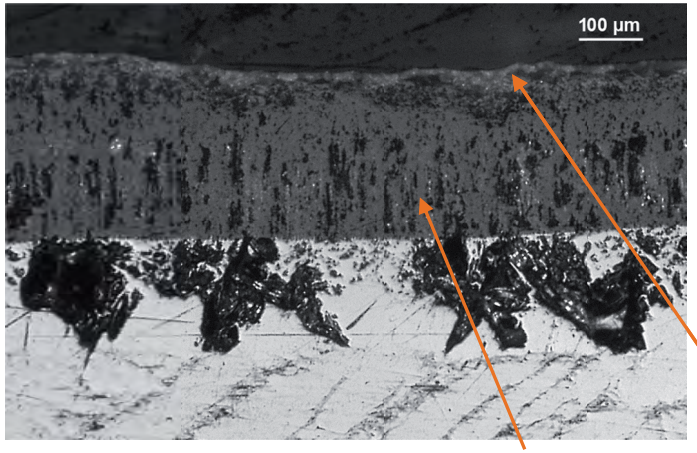

135° (highest circumference temperature): thick oxide layer with thin outer porous scale

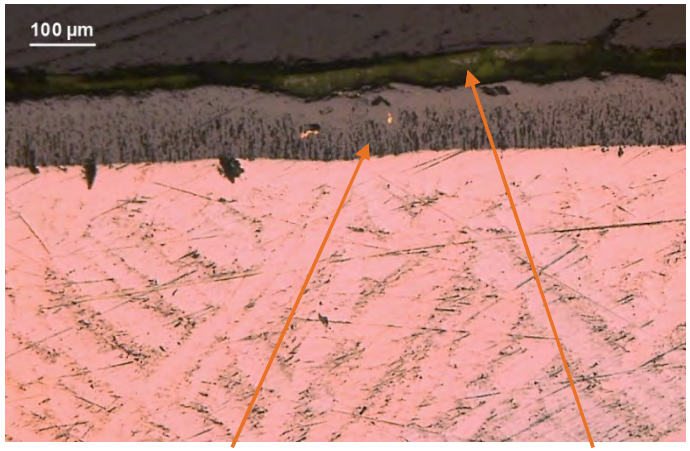

225°, polarised light: thin oxide layer, moderate outer porous layer (yellowed due to epoxy resin collected inside pores)

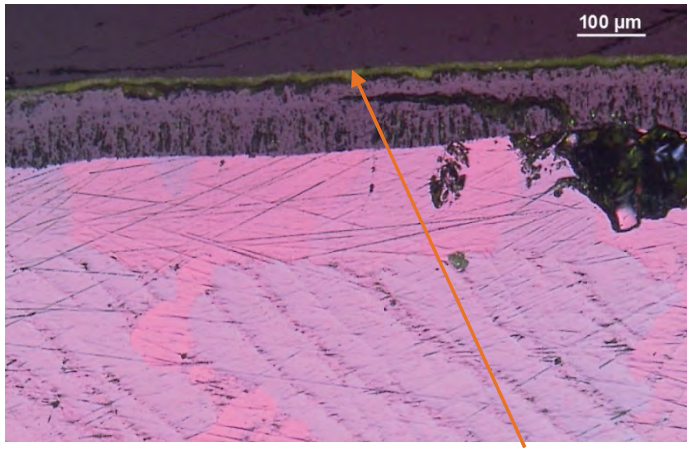

315°, polarised light: thin oxide layer, thin outer porous layer (yellowed due to epoxy resin)

Fig. 86: QUENCH-16; structure of inner (concave) surface of shroud at bundle elevation 350 mm.

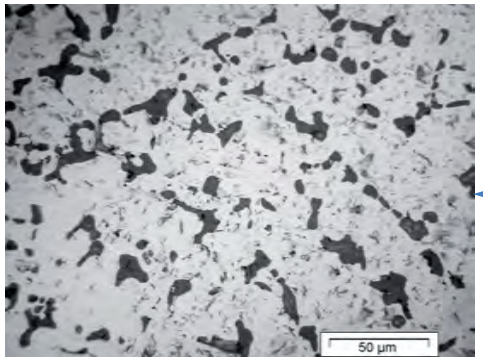

grey porous region; **precipitates area 10% → 8 wt% dissolved oxygen**

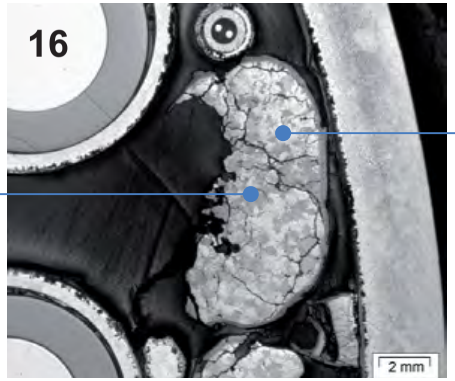

grey and light melt regions

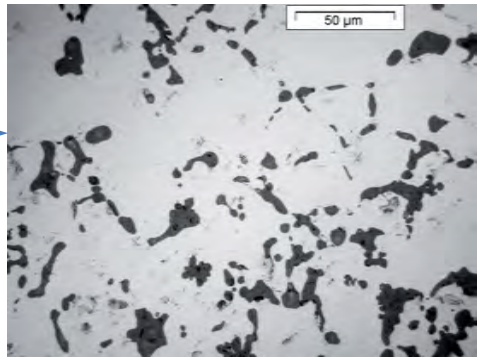

light non porous region; **p precipitates area 10% → 8 wt% dissolved oxygen**

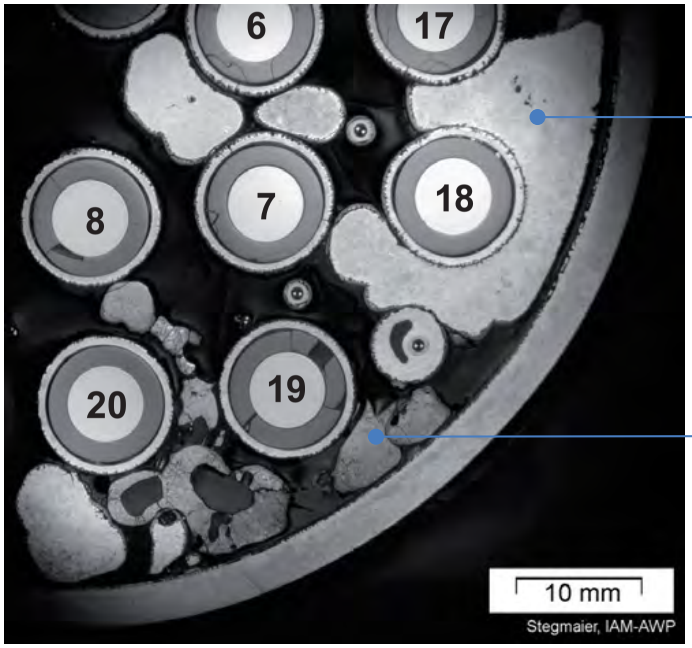

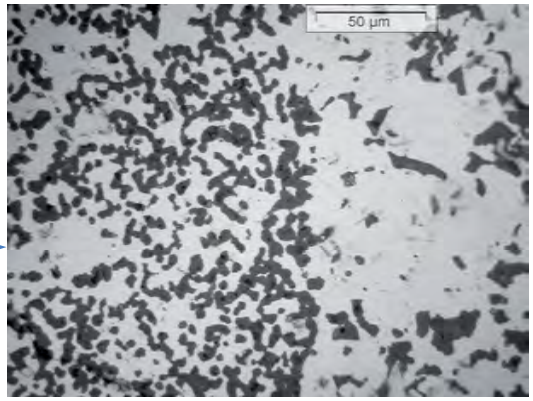

precipitates part 20% → 8 wt% dissolved oxygen

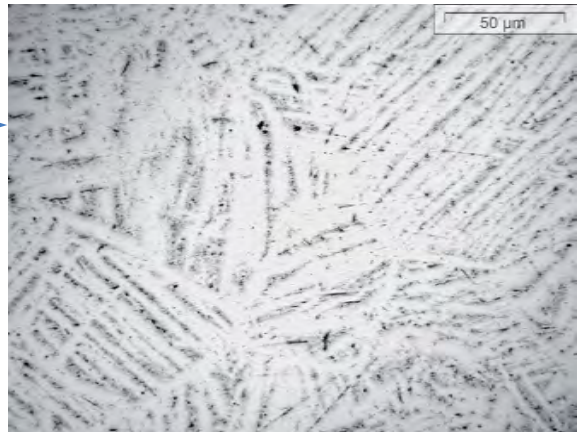

Widmanstätten pattern of frozen metallic melt

Fig. 87: QUENCH-16; Frozen melt at elevation 350 mm: not oxidised and oxidised melt

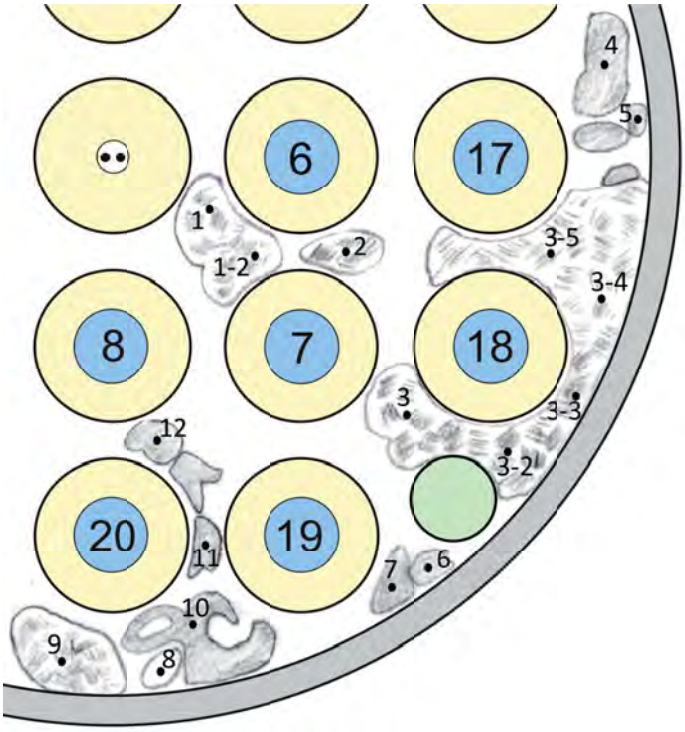

wt %	Zr	Fe	Cr	*Ni*	Sn	Hf	*Ta*	*Y*	Total
shroud Zr702	99.11	0.24	0	*0*	0	0.64	*0*	*0*	99.99
clad ZIRLO	98.35	0.24	0.12	*0*	1.29	0	*0*	*0*	100
melt 1	99.33	0.08	0	*0*	0.19	0.4	*0*	*0*	100
melt 1-2	97.79	0.86	0.32	*0.38*	0.14	0.5	*0*	*0*	99.99
melt 2	99.4	0	0	*0*	0.17	0.42	*0*	*0*	99.99
melt 3	98.57	0.37	0.19	*0.19*	0.27	0.41	*0*	*0*	100
melt 3-2	98.68	0.31	0.08	*0.17*	0.32	0.44	*0*	*0*	100
melt 3-3	99.33	0	0	*0*	0.21	0.46	*0*	*0*	100
melt 3-4	99.44	0	0	*0*	0	0.56	*0*	*0*	100
melt 3-5	99.33	0	0	*0*	0.14	0.53	*0*	*0*	100
melt 4	99.14	0	0	*0*	0	0.43	*0.44*	*0*	100
melt 5	98.94	0.1	0	*0*	0.11	0.47	*0.37*	*0*	99.99
melt 6	98.73	0	0	*0*	0.45	0.33	*0.49*	*0*	100
melt 7	96.89	0	0	*0*	0.45	0.47	*0.64*	*1.55*	100
melt 8	99.24	0	0	*0*	0.22	0.54	*0*	*0*	100
melt 9	98.8	0.12	0.06	*0.13*	0.45	0.44	*0*	*0*	100
melt 10	97.41	0.29	0.12	*0.14*	0.63	0.58	*0.82*	*0*	99.99
melt 11	98.54	0	0	*0*	0.35	0.41	*0.69*	*0*	99.99
melt 12	98.38	0	0.15	*0*	0.3	0.51	*0.66*	*0*	100
possible source for melt	shroud +clad	shroud +clad	clad	*low T TC*	clad	shroud	*high T TC*	*pellets*	

Fig.88: QUENCH-16; EDX analysis of shroud, cladding and relocated melt at elevation 350 mm.

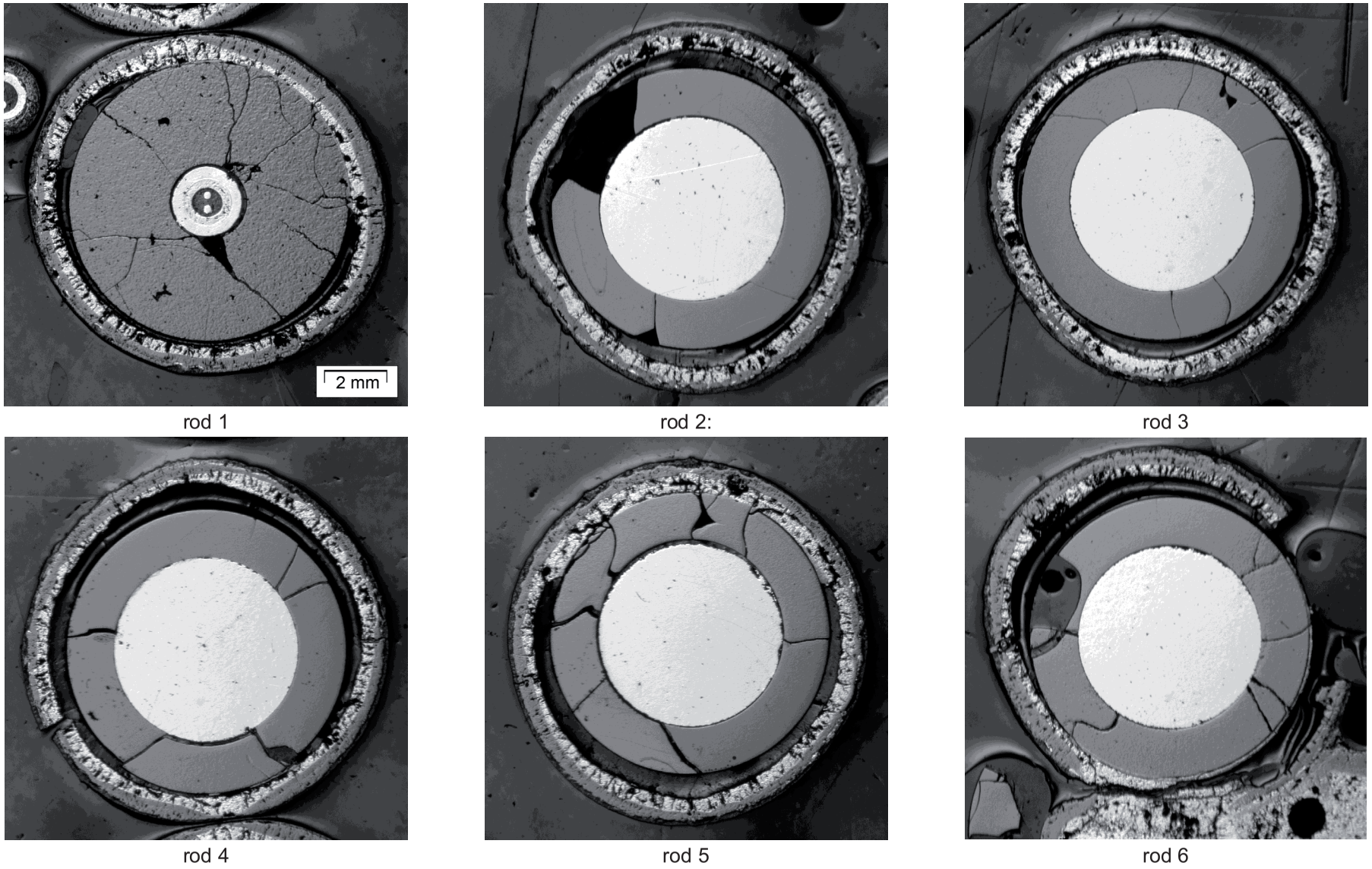

Fig.89: QUENCH-16; Cross section at elevation 450 mm depicting individual test rods 1-6.

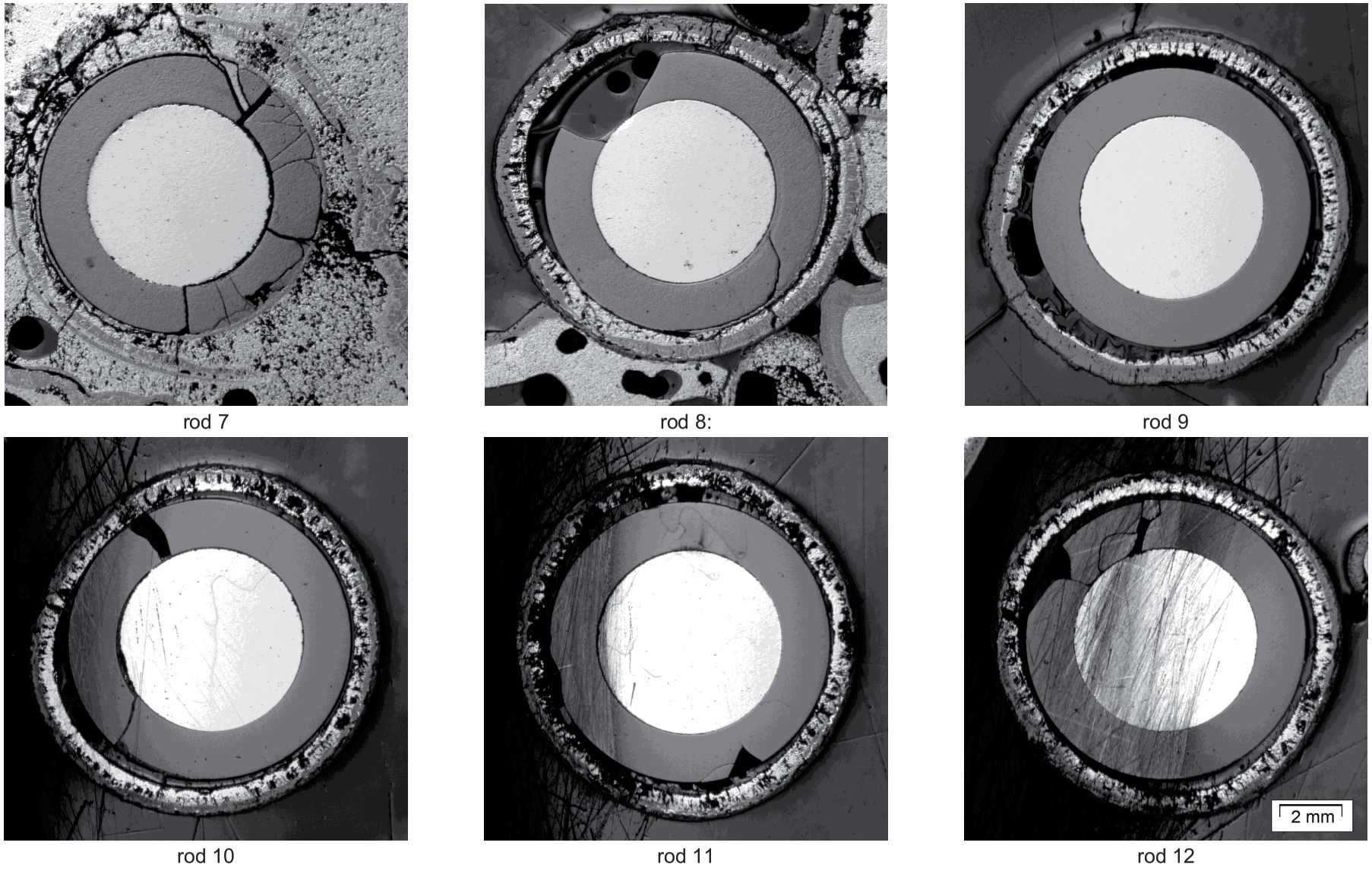

Fig.90: QUENCH-16; Cross section at elevation 450 mm depicting individual test rods 7-12.

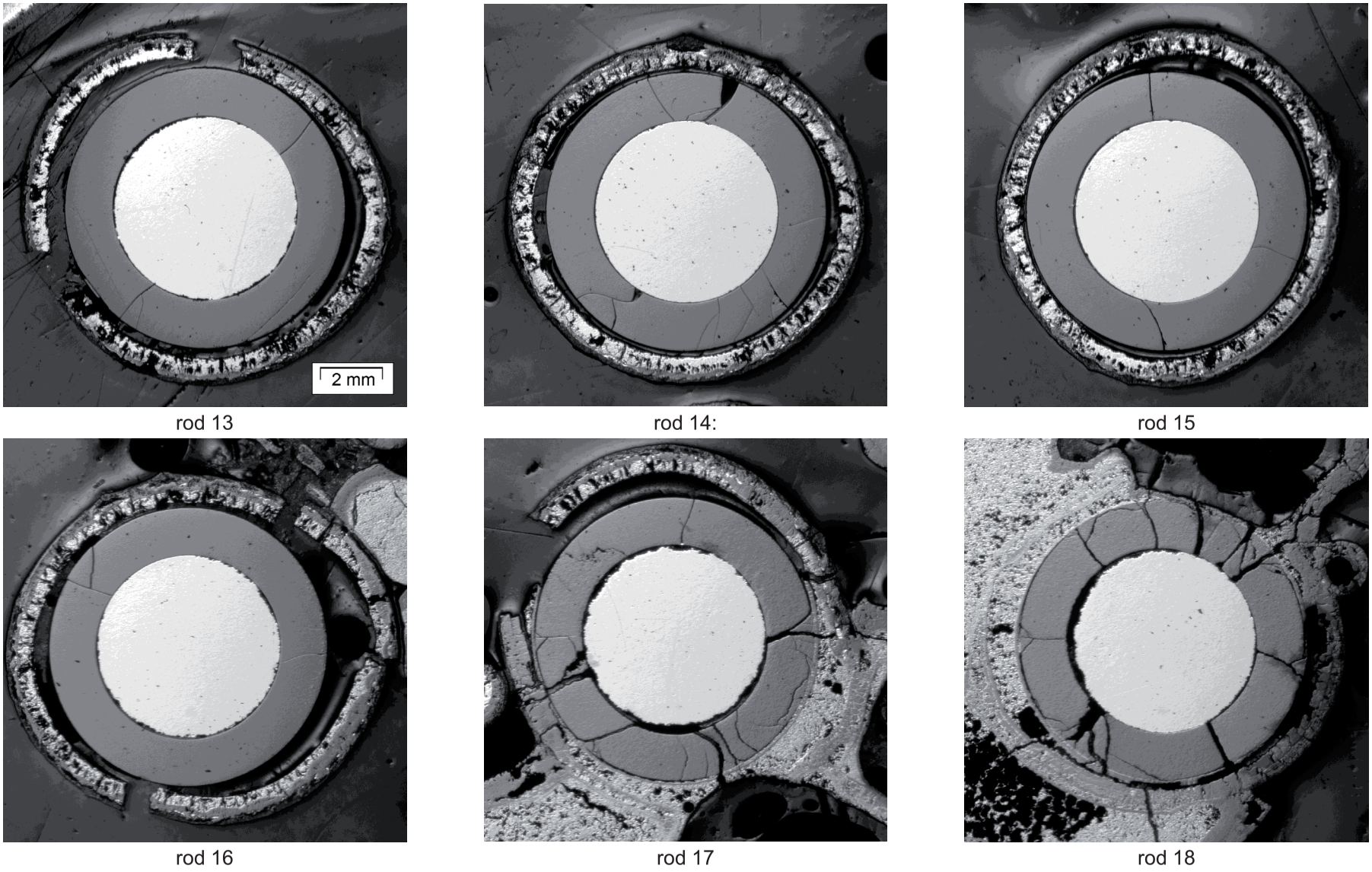

Fig.91: QUENCH-16; Cross section at elevation 450 mm depicting individual test rods 13-18.

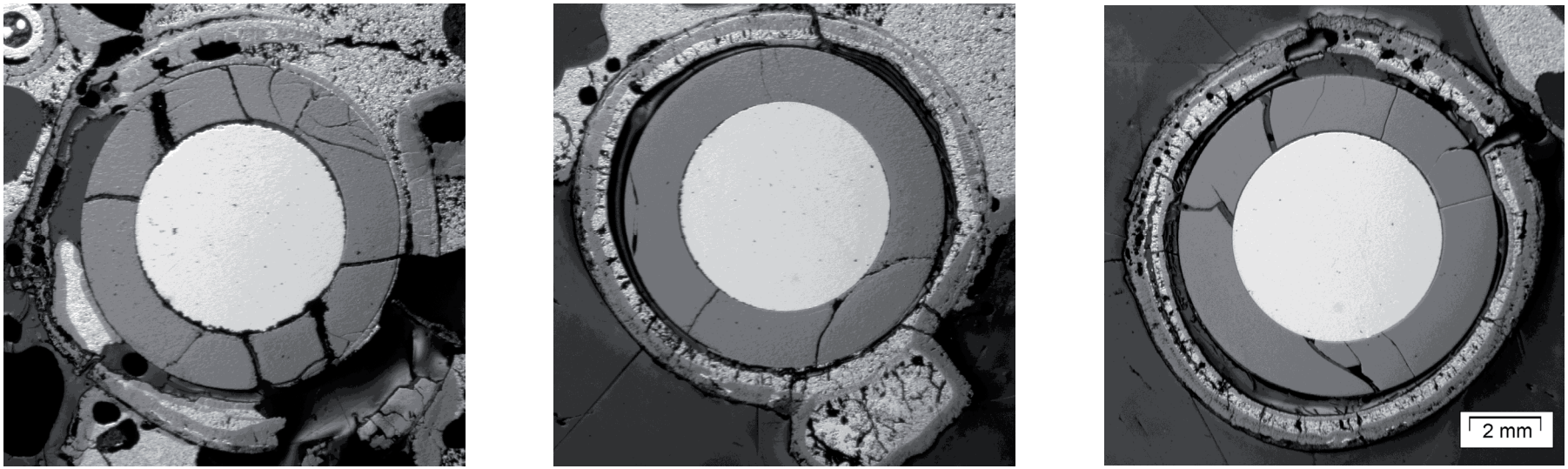

rod 19 rod 20 rod 21

Fig.92: QUENCH-16; Cross section at elevation 450 mm depicting individual test rods 19-21.

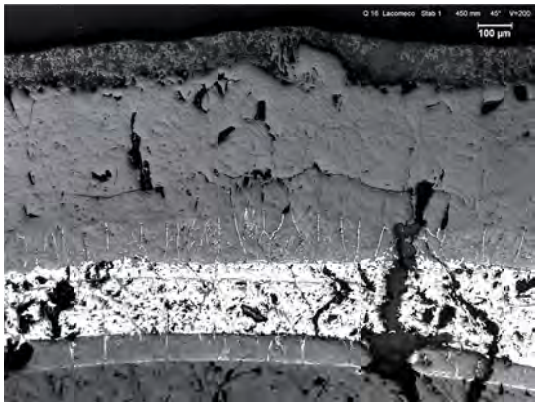

rod 1, 0°: no nitrides, inner oxide layer between partially oxidised melt (12 wt% oxygen) and pellet

rod 2, 45°: residual nitrides between two outer oxide sublayers, inner oxide at the melt boundary

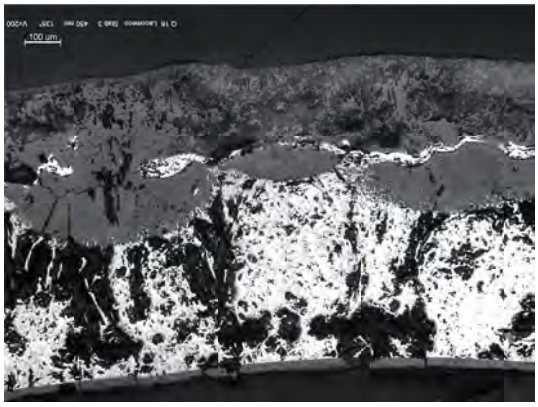

rod 3, 135°: residual nitrides, inner oxide layer

rod 9, 0°: residual nitrides

rod 15, 180°: residual nitrides

rod 16, 135°: residual nitrides

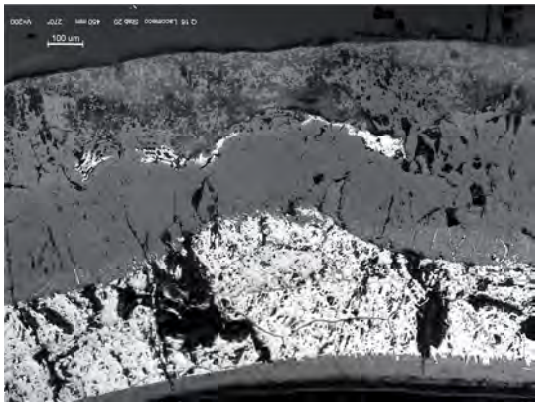

rod 20, 270°: residual nitrides, inner oxide layer,partially oxidised melt (15 wt% oxygen)

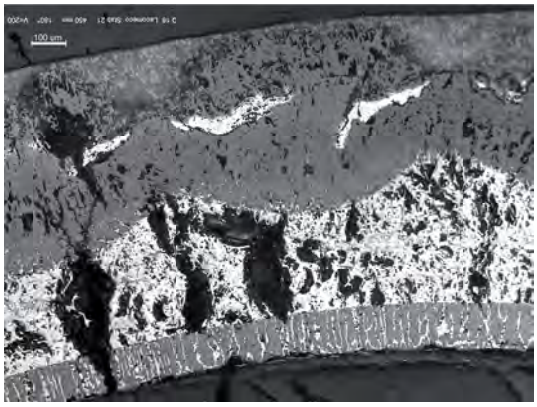

rod 21, 180°: residual nitrides, inner oxide layer, partially oxidised melt (17 wt% oxygen)

Fig. 93: QUENCH-16; cladding structure at elevation 450 mm.

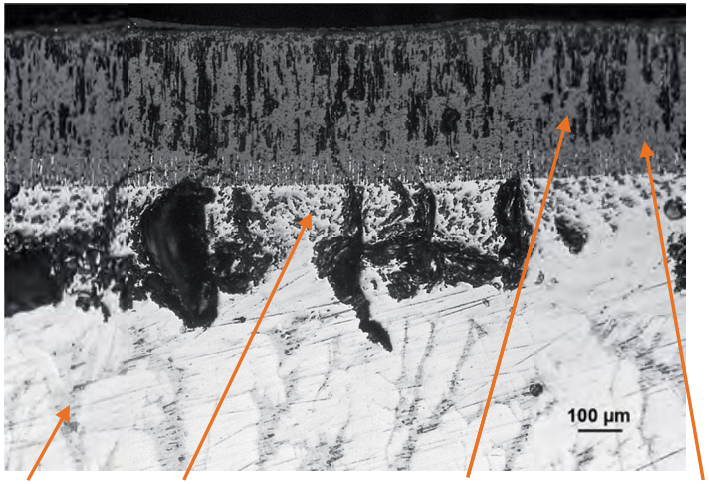

45°: prior β-Zr layer, α-Zr(O) layer, moderate oxide layer, thin outer porous layer

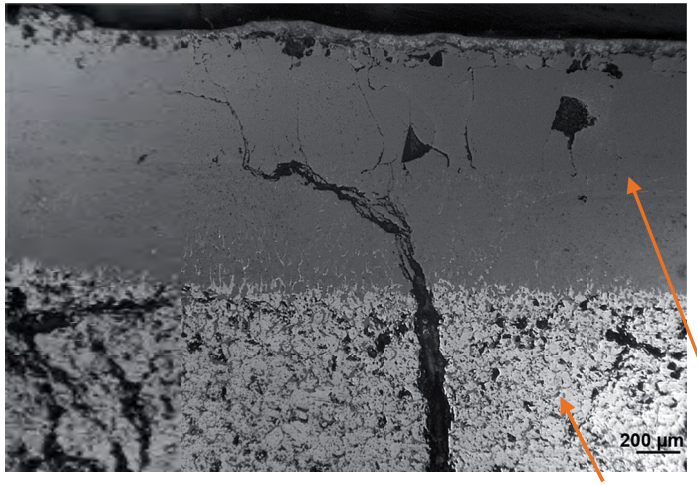

135° (highest circumference temperature): oxidised melt, very thick oxide layer with thin outer porous scale

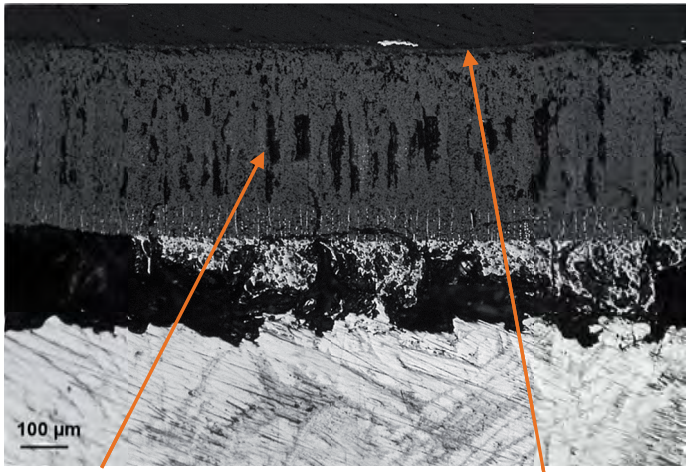

225°: moderate oxide layer, thin outer porous layer

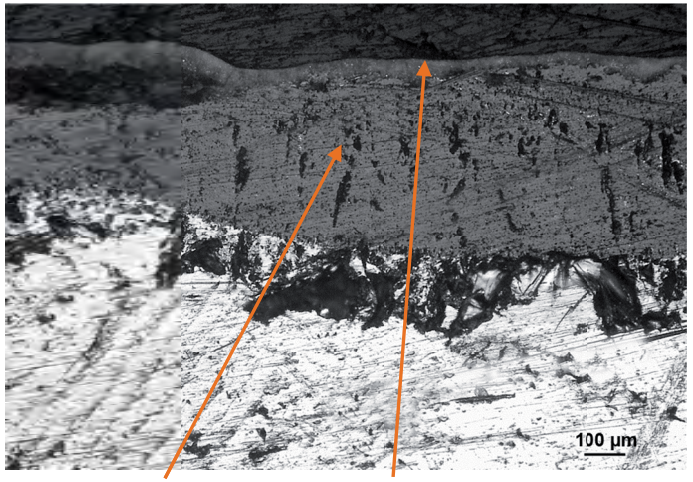

315°: moderate oxide layer, moderate outer porous layer

Fig. 94: QUENCH-16; structure of inner (concave) surface of shroud at bundle elevation 450 mm.

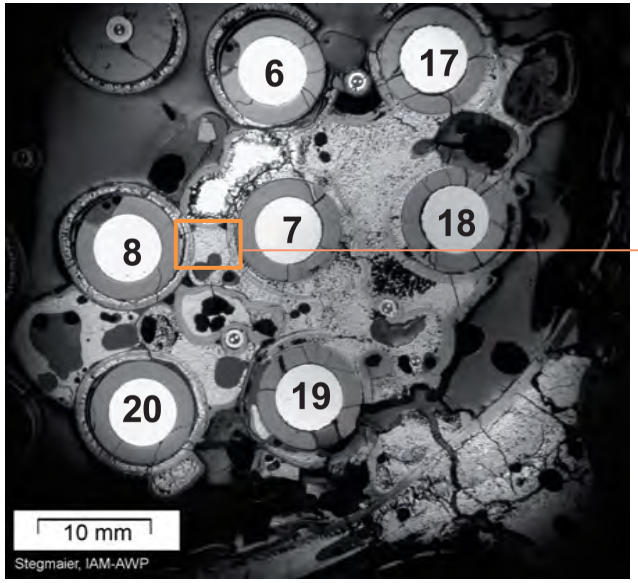

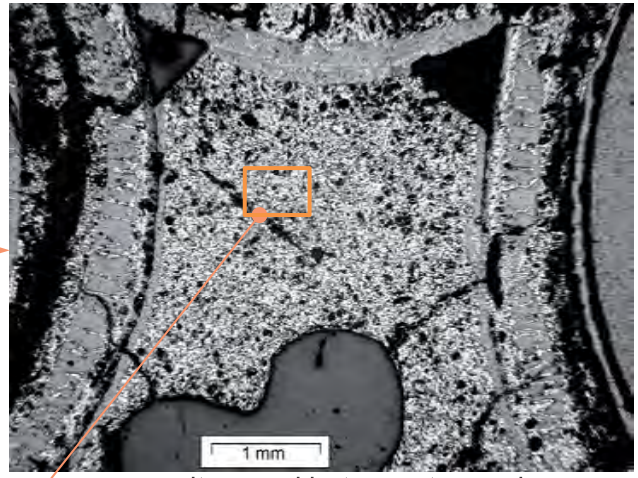

molten pool between two rods:
oxidation at melt periphery and ceramic precipitates inside melt

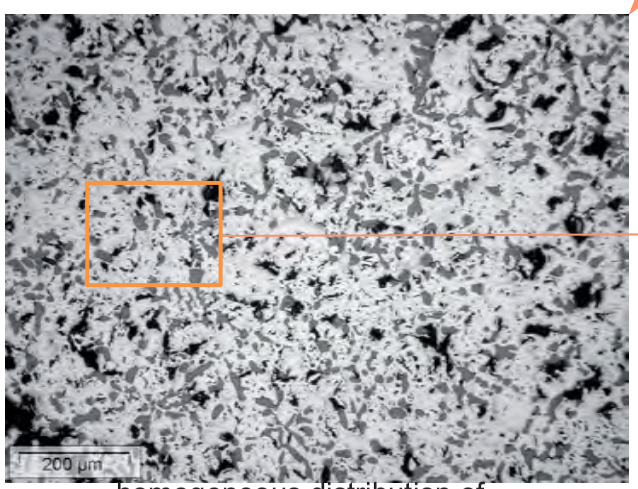

homogeneous distribution of ceramic precipitates in the melt

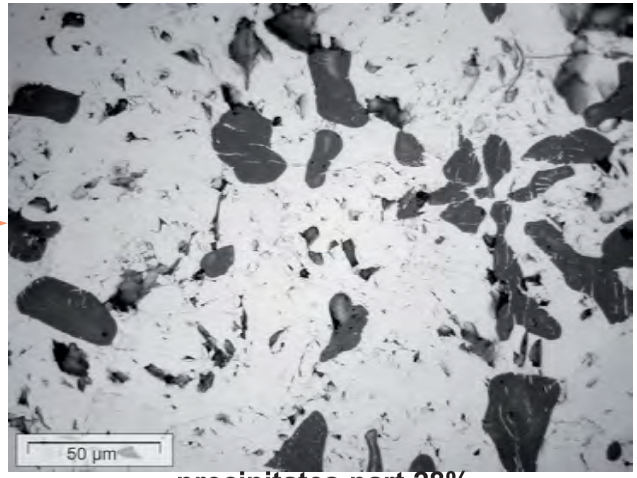

precipitates part 28% → 11.5 wt% dissolved oxygen

Fig. 95: QUENCH-16; Frozen melt at elevation 450 mm: mostly oxidised melt.

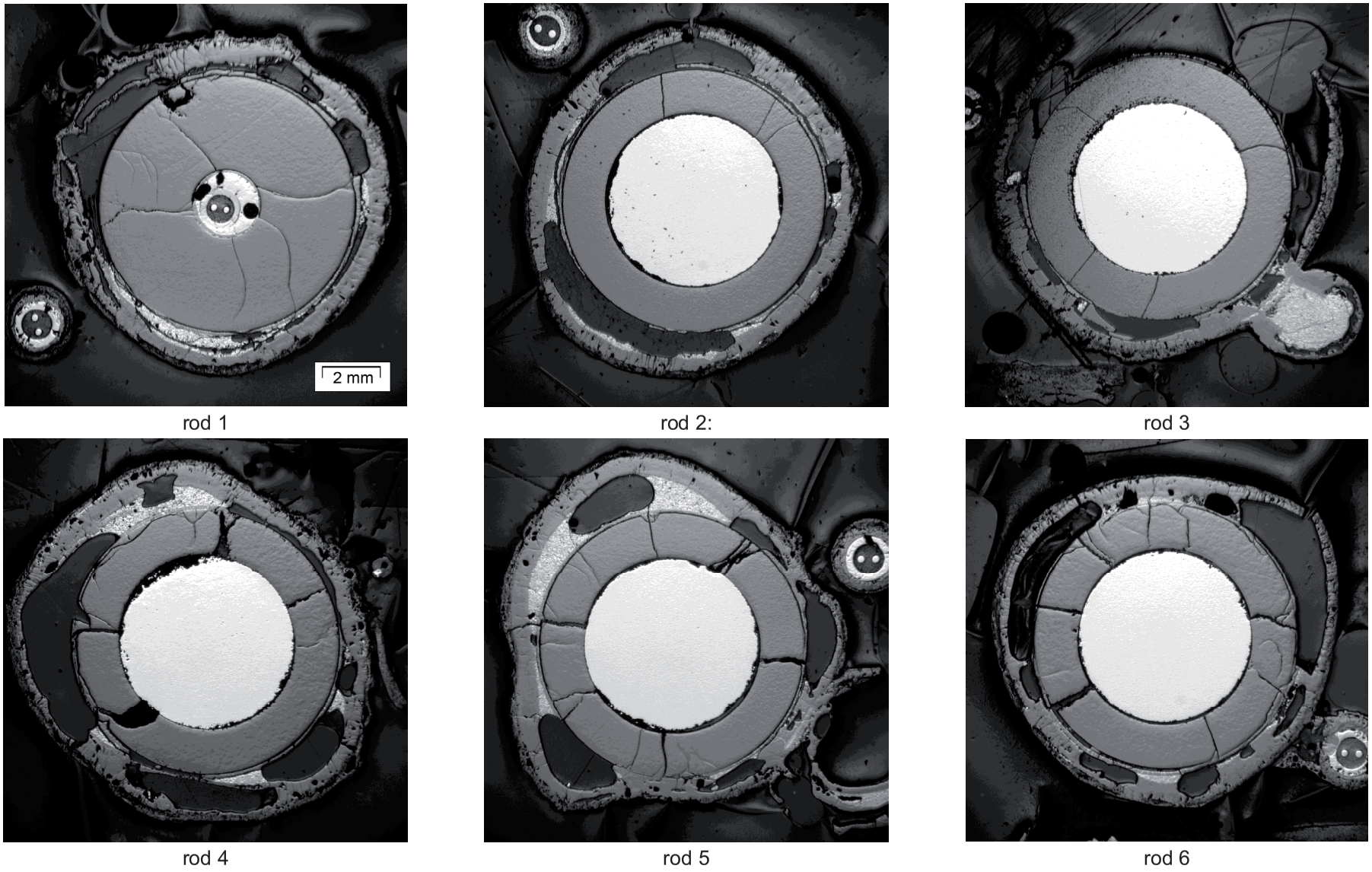

Fig.96: QUENCH-16; Cross section at elevation 550 mm depicting individual test rods 1-6.

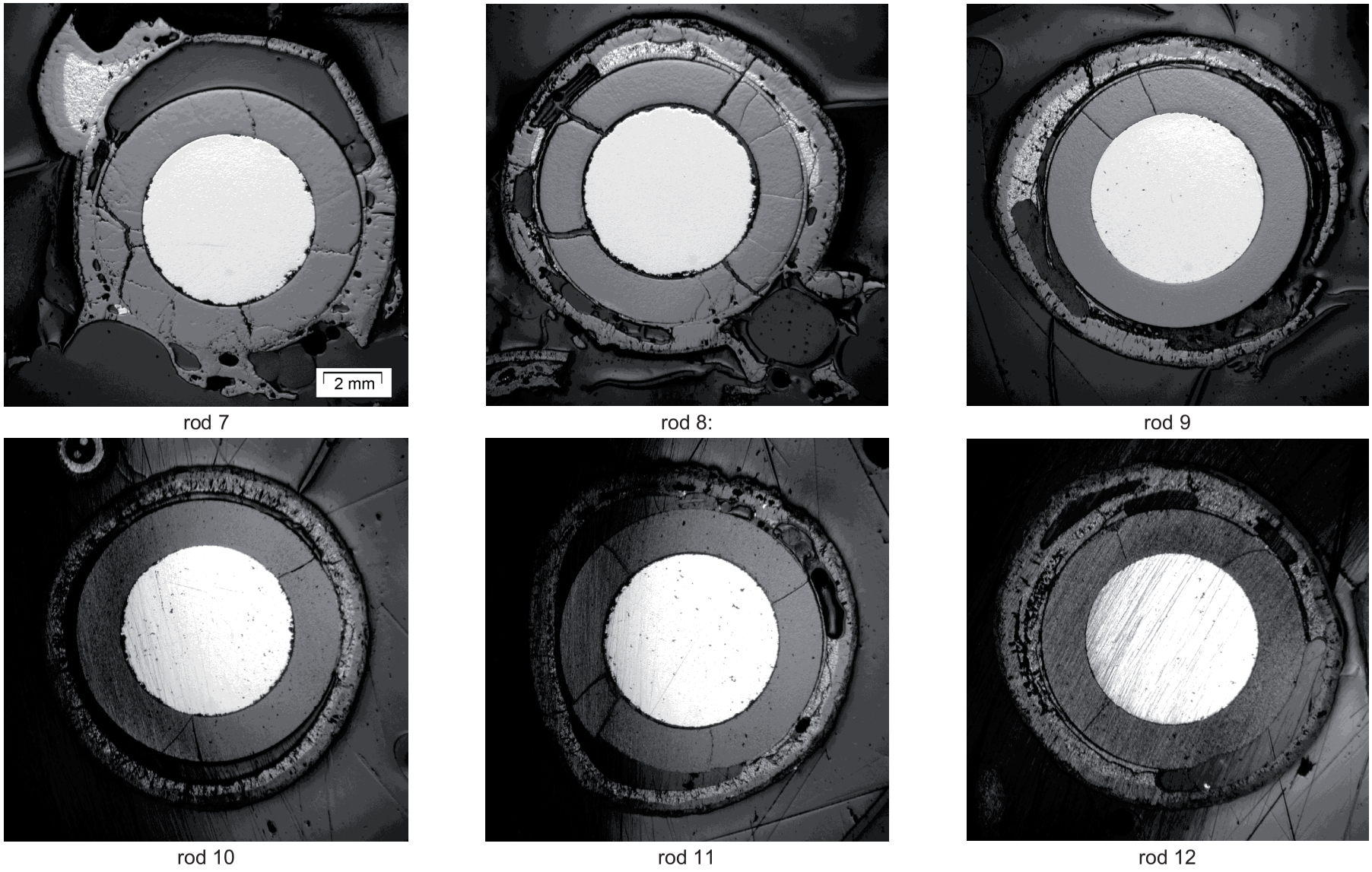

Fig.97: QUENCH-16; Cross section at elevation 550 mm depicting individual test rods 7-12.

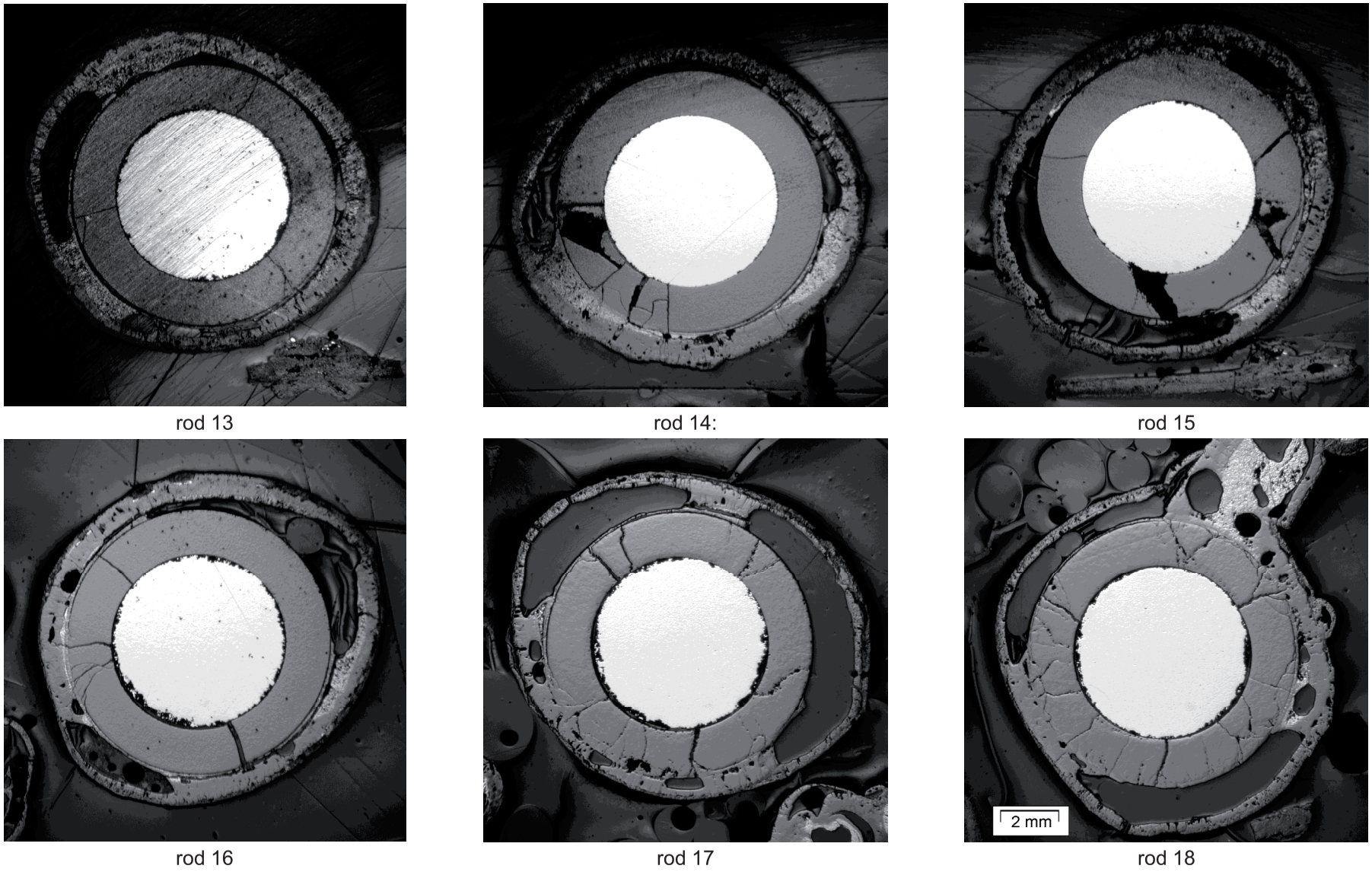

Fig.98: QUENCH-16; Cross section at elevation 550 mm depicting individual test rods 13-18.

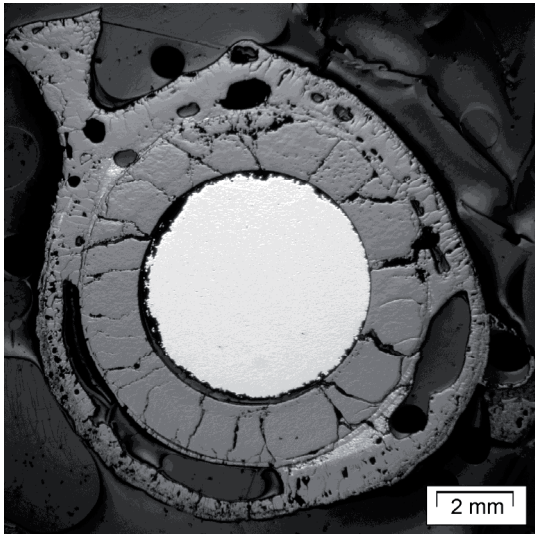

rod 19

rod 20

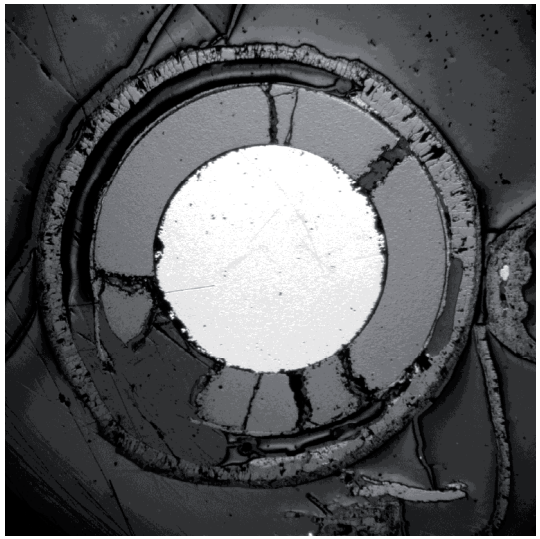

rod 21

Fig.99: QUENCH-16; Cross section at elevation 550 mm depicting individual test rods 19-21.

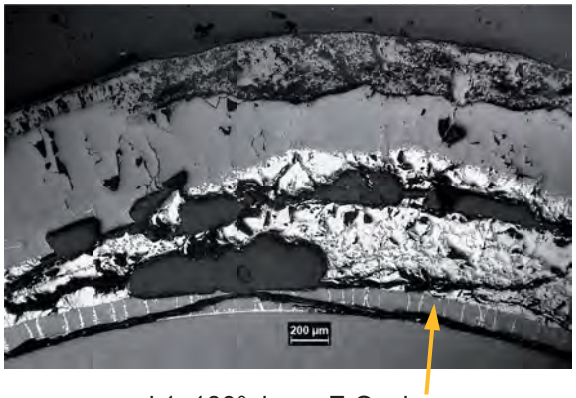

rod 1, 180°: inner ZrO_{2-x} layer

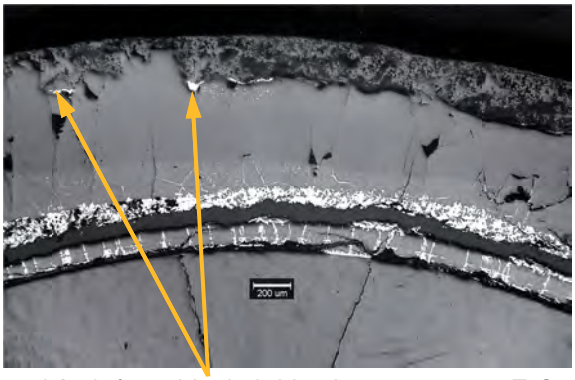

rod 2, 45°: residual nitrides between outer ZrO_2 sub-layers

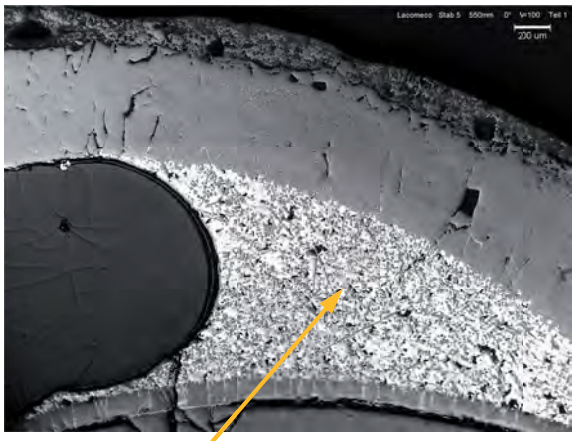

rod 5, 0°: melt with ceramic precipitates (oxygen content in prior melt 18 wt%)

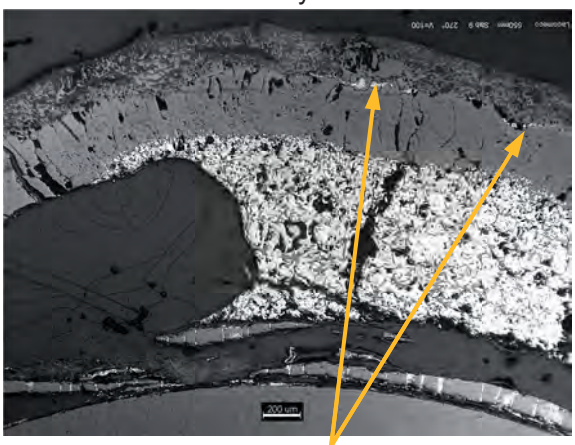

rod 9, 270°: residual nitrides between outer ZrO_2 sub-layers

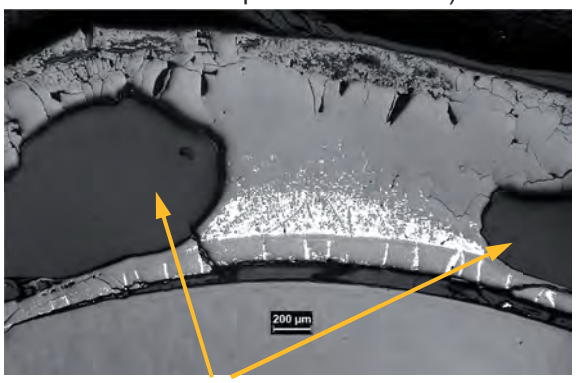

rod 6, 180°: voids from downwards relocated melt

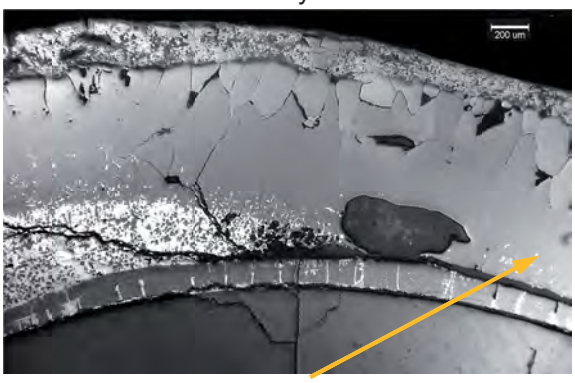

rod 8, 90°: complete melt oxidation

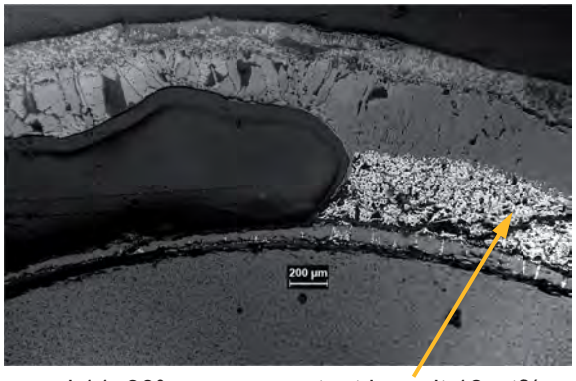

rod 11, 90°: oxygen content in melt 18 wt%

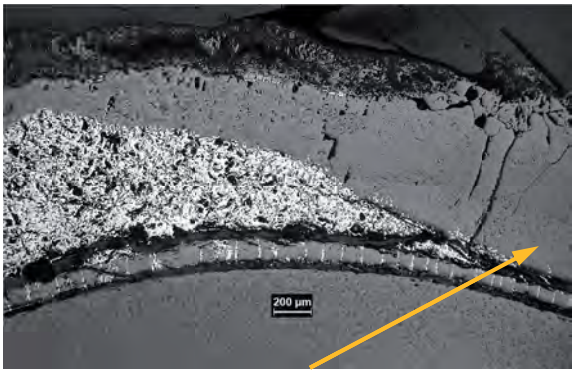

rod 14, 135°: complete melt oxidation

Fig.100: QUENCH-16; cladding structure at 550 mm with two outer ZrO_2 sub-layers, frozen molten layer and inner ZrO_{2-x} layer.

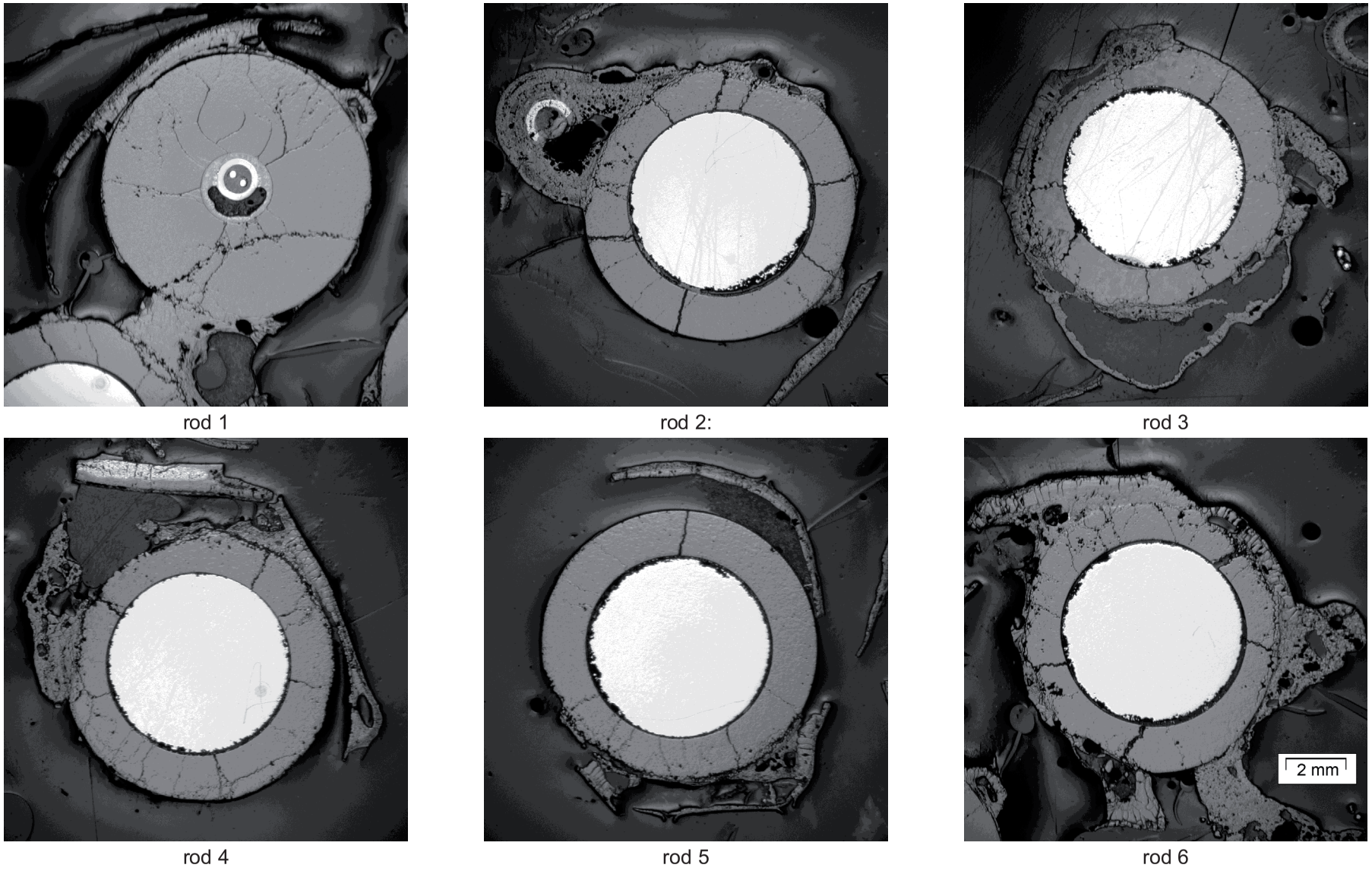

Fig.101: QUENCH-16; Cross section at elevation 650 mm depicting individual test rods 1-6.

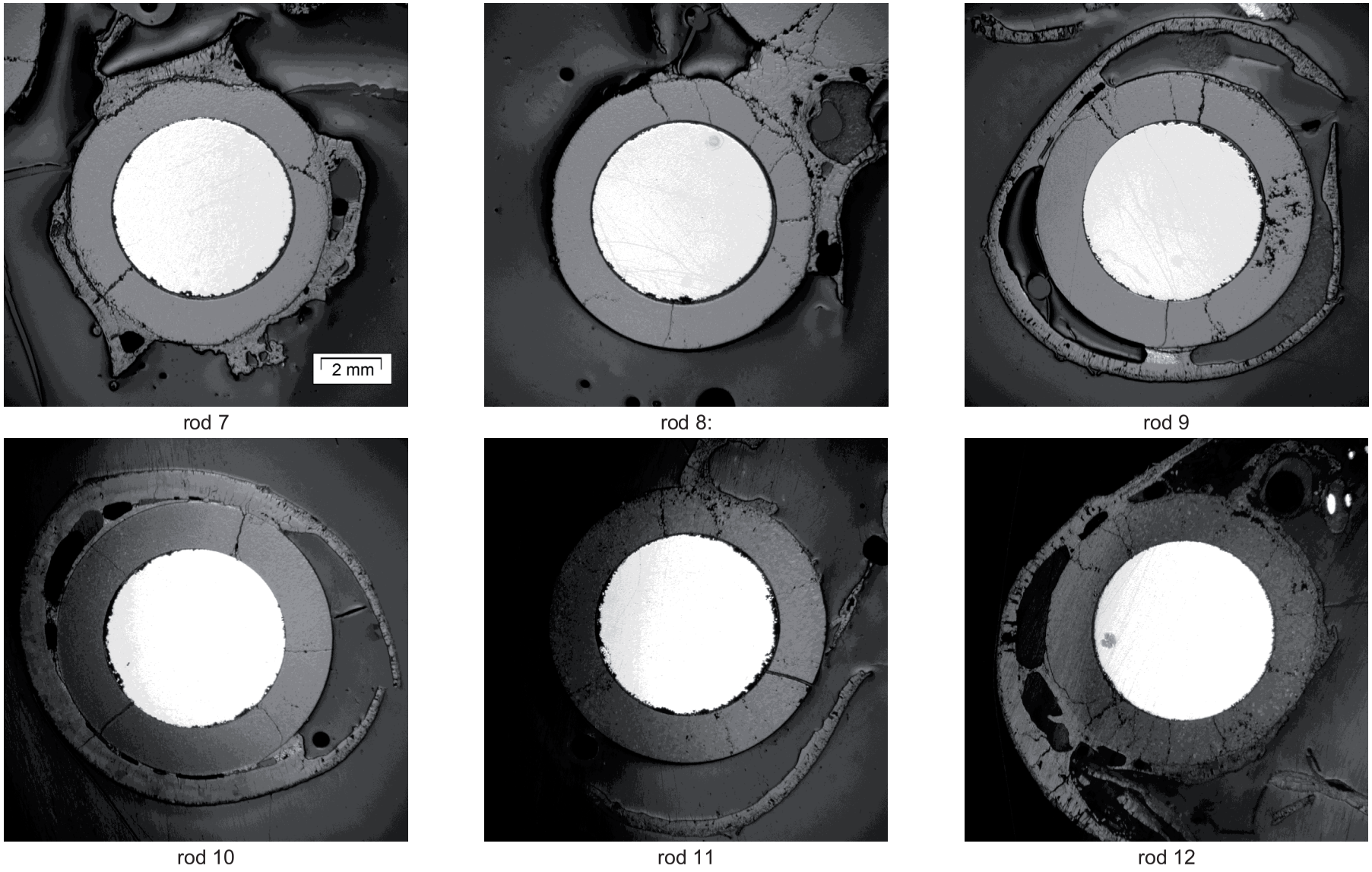

Fig.102: QUENCH-16; Cross section at elevation 650 mm depicting individual test rods 7-12.

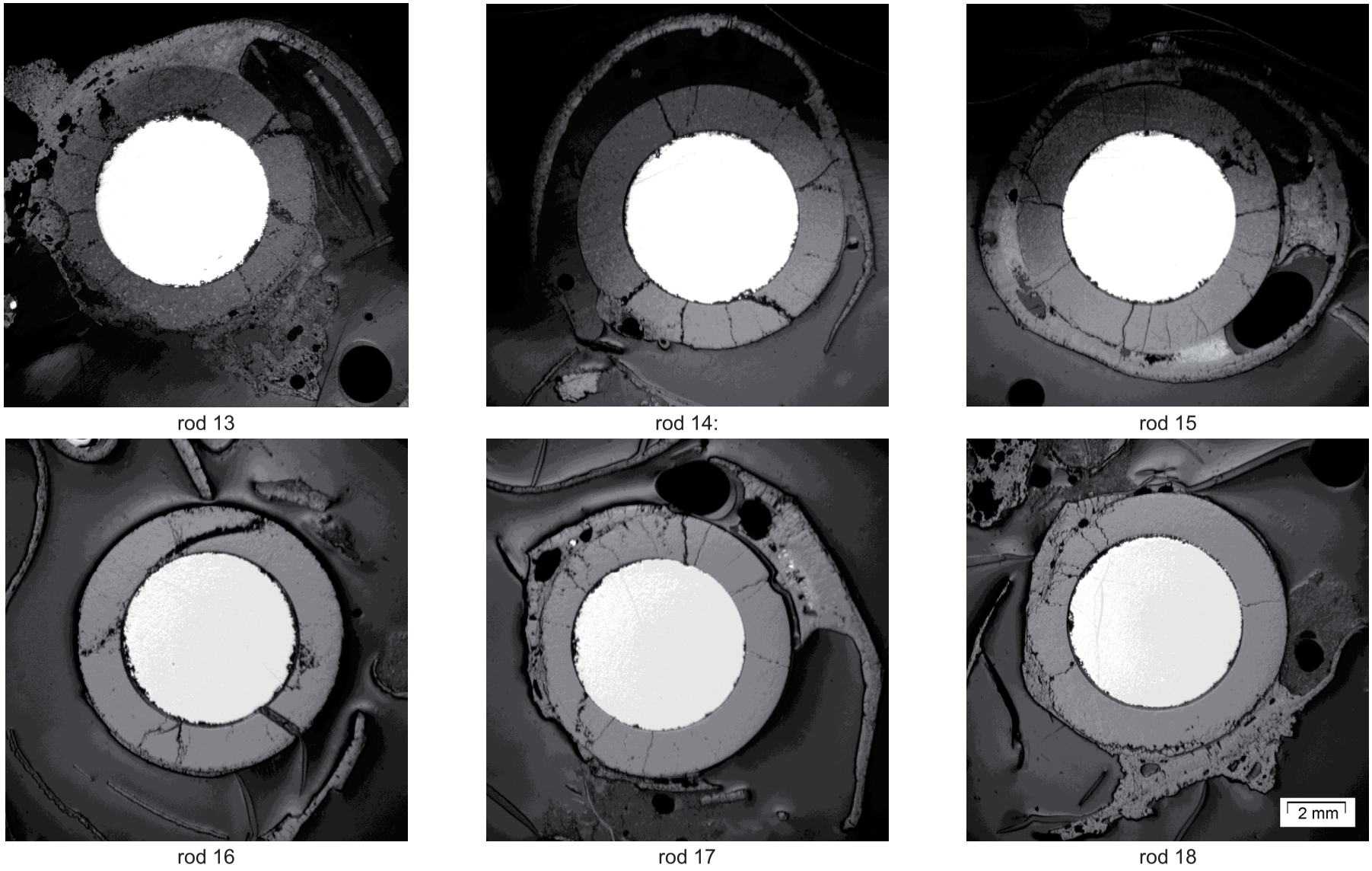

Fig.103: QUENCH-16; Cross section at elevation 650 mm depicting individual test rods 13-18.

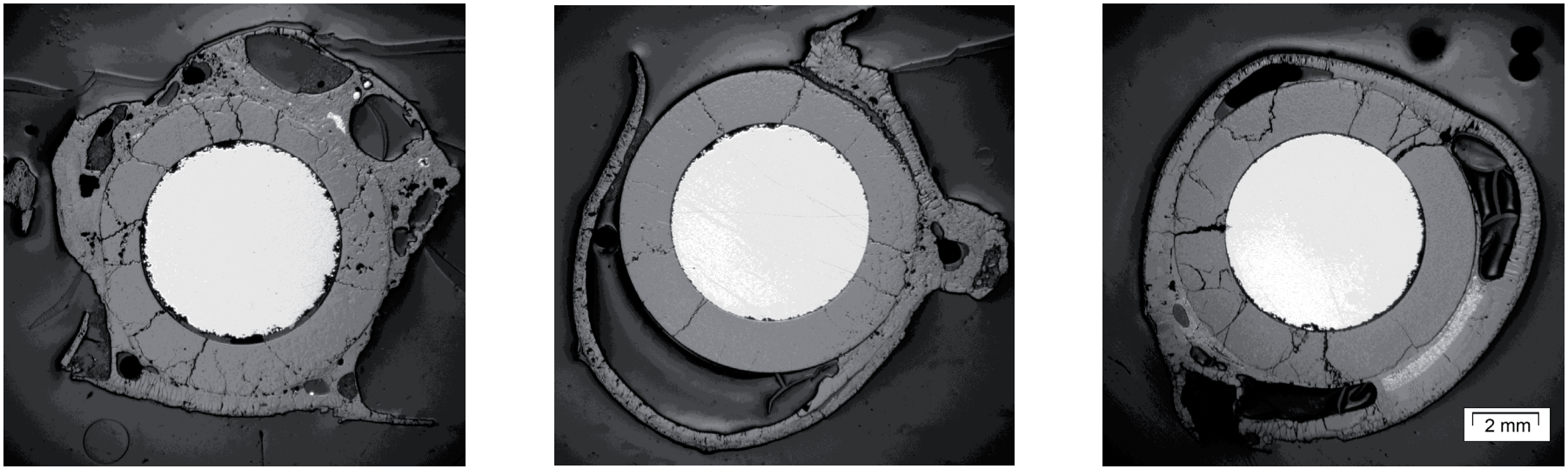

rod 19 rod 20 rod 21

Fig.104: QUENCH-16; Cross section at elevation 650 mm depicting individual test rods 19-21.

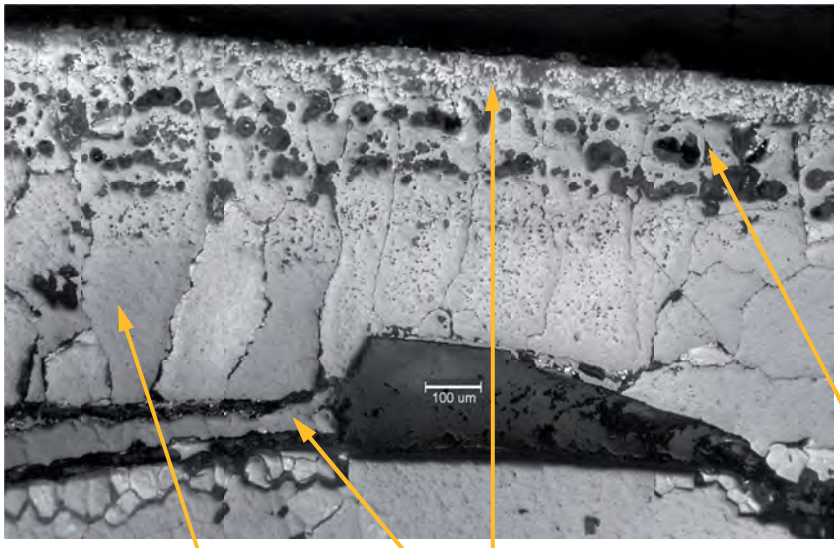

rod 1, 315°: completely oxidised cladding with porous upper sub-layer, prior metal molten sub-layer, dense inner sub-layer, oxide on the boundary to pellet

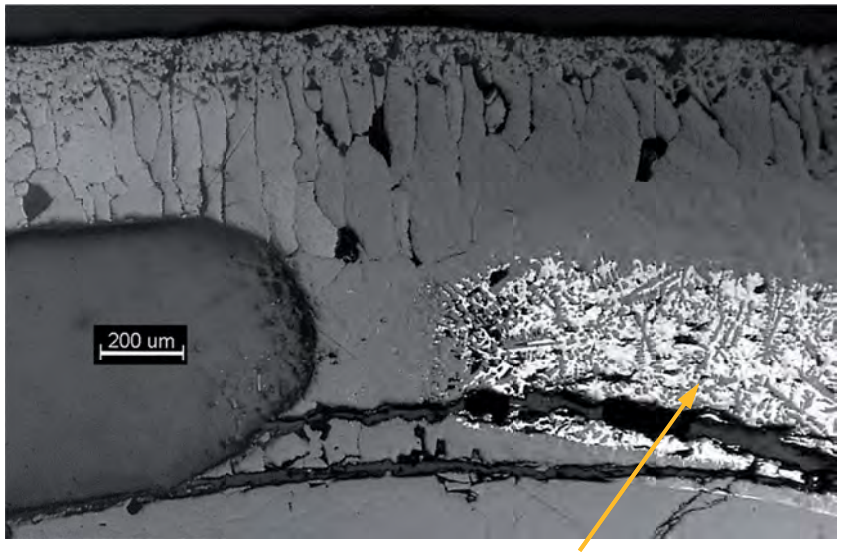

rod 9, 180°: partially oxidised melt (oxygen content 15 wt%)

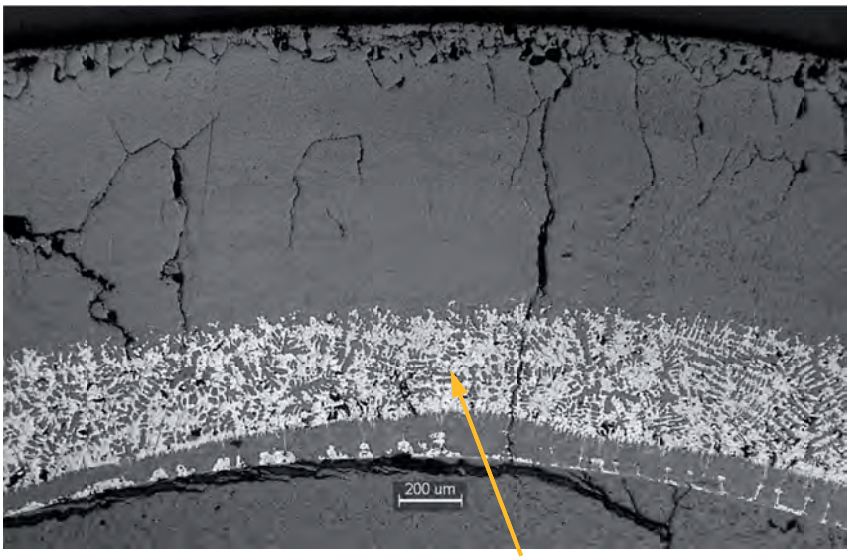

rod 21, 135°: partially oxidised melt (oxygen content 17 wt%)

Fig. 105: QUENCH-16; strong oxidation of claddings at 650 mm.

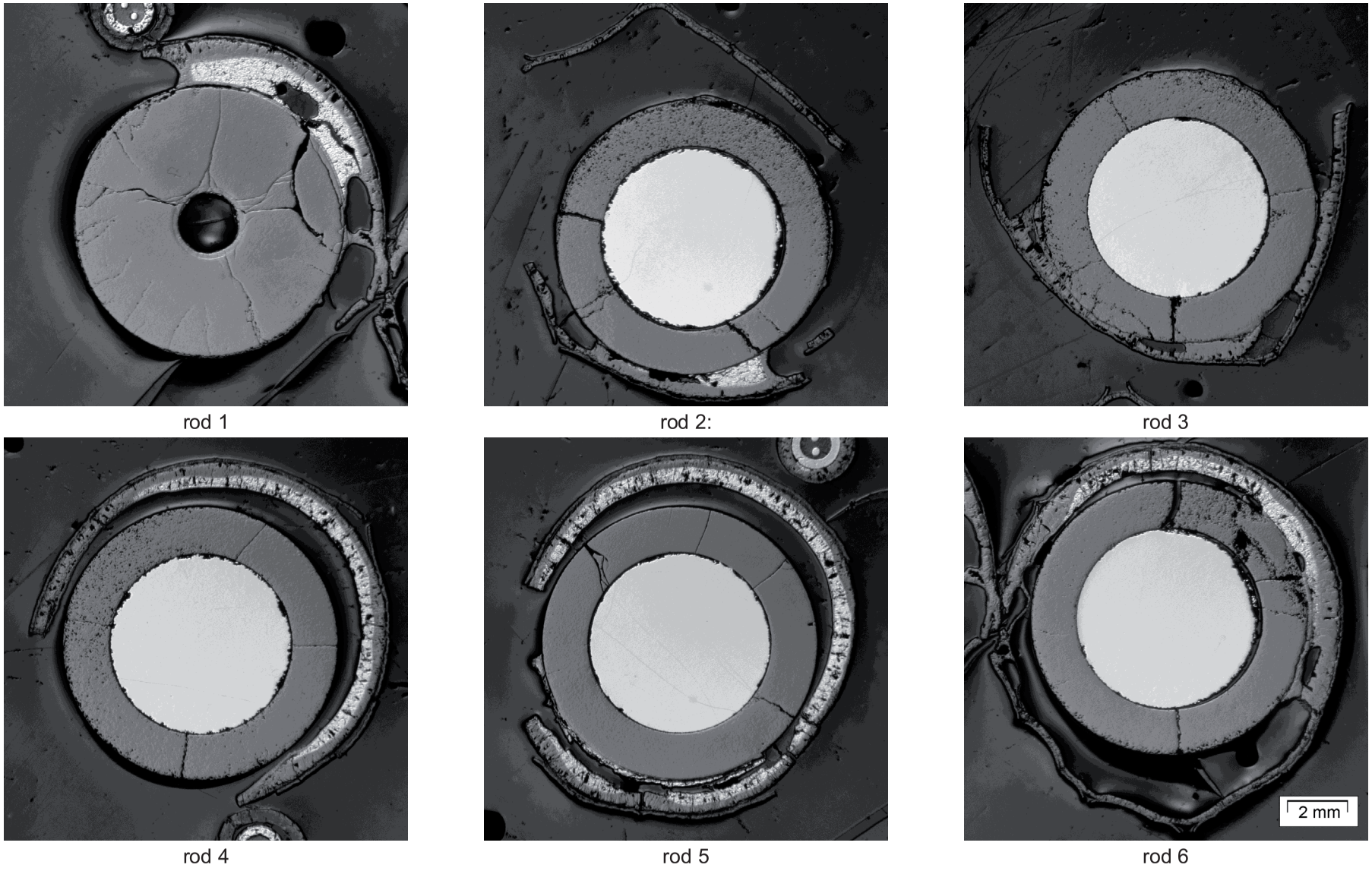

Fig.106: QUENCH-16; Cross section at elevation 750 mm depicting individual test rods 1-6.

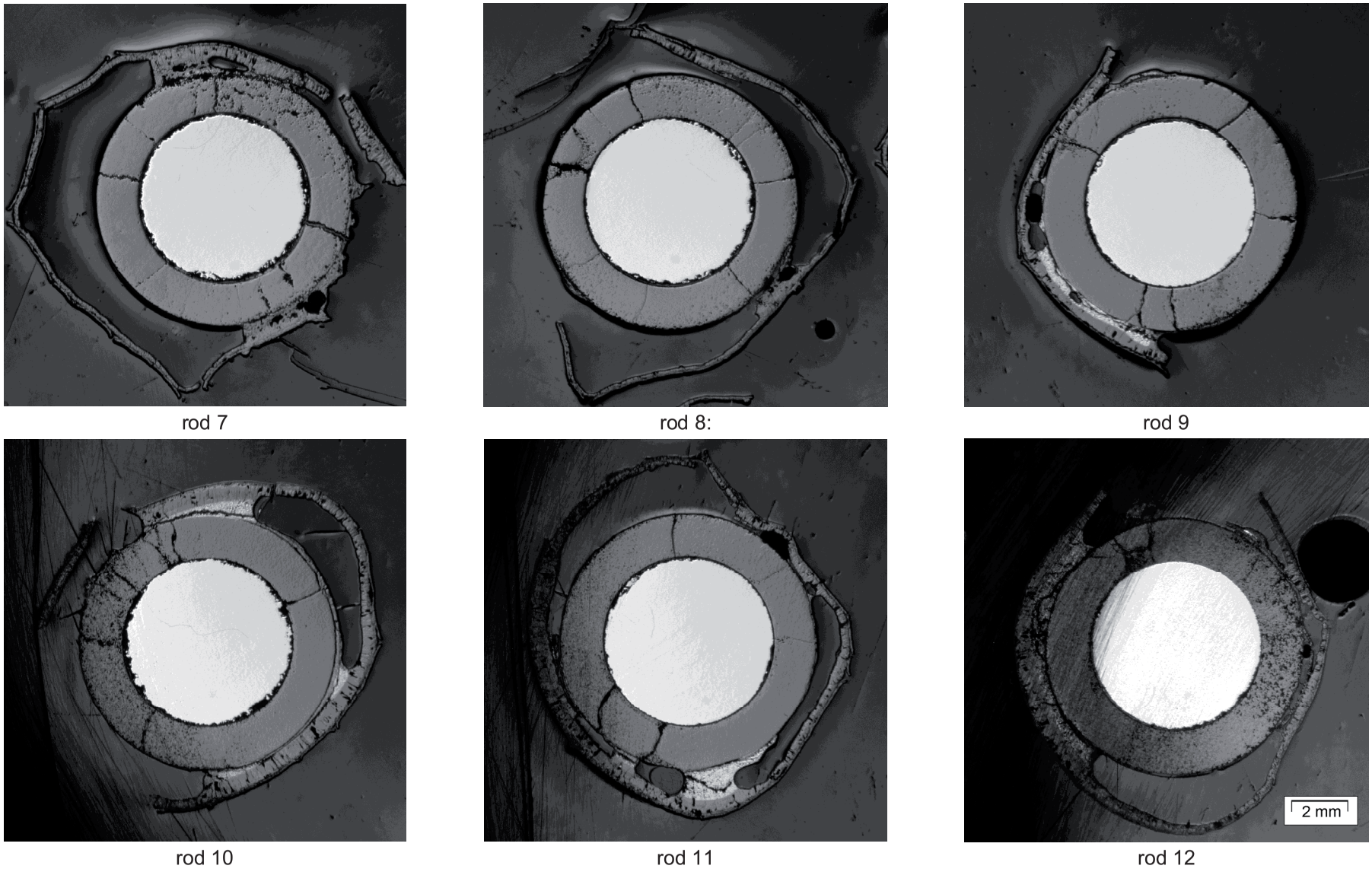

Fig.107: QUENCH-16; Cross section at elevation 750 mm depicting individual test rods 7-12.

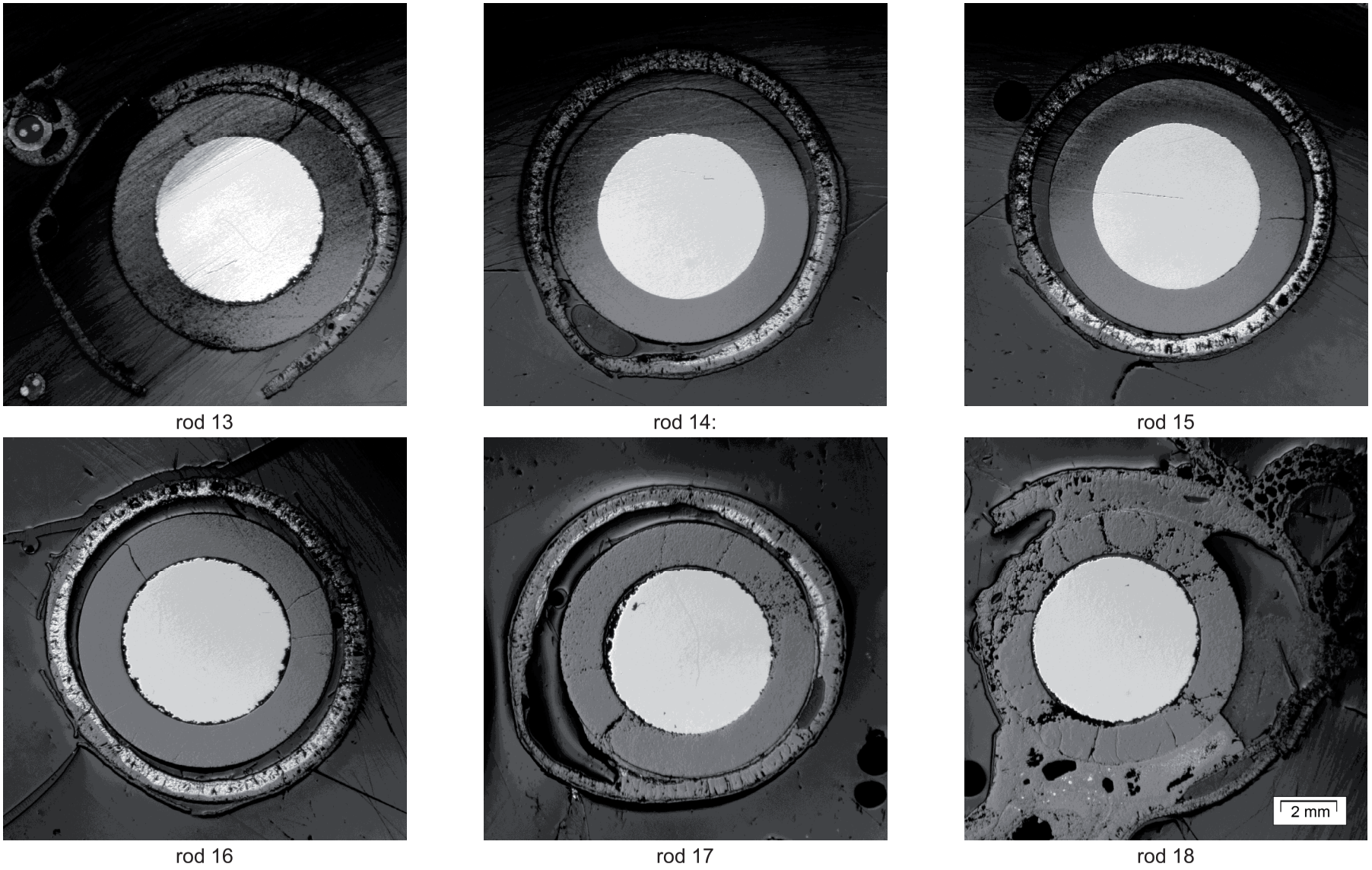

Fig.108: QUENCH-16; Cross section at elevation 750 mm depicting individual test rods 13-18.

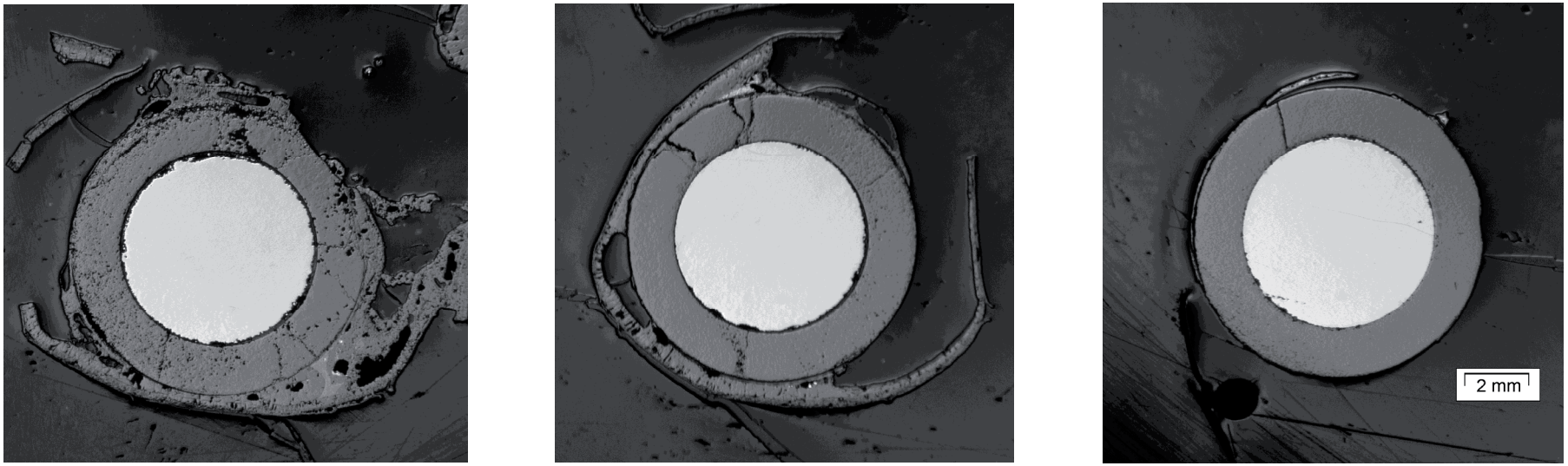

rod 19 rod 20 rod 21

Fig.109: QUENCH-16; Cross section at elevation 750 mm depicting individual test rods 19-21.

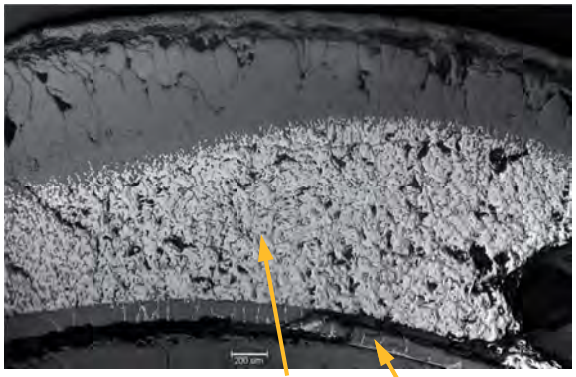

rod 1, 0°: oxidised melt (oxygen content 16 wt%) between outer and inner ZrO2

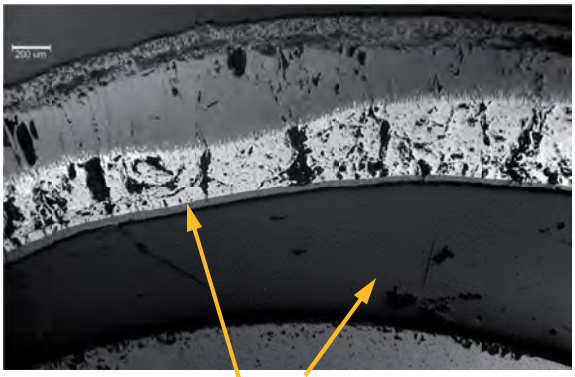

rod 4, 0°: significant gap between pellet and clad, inner oxide layer

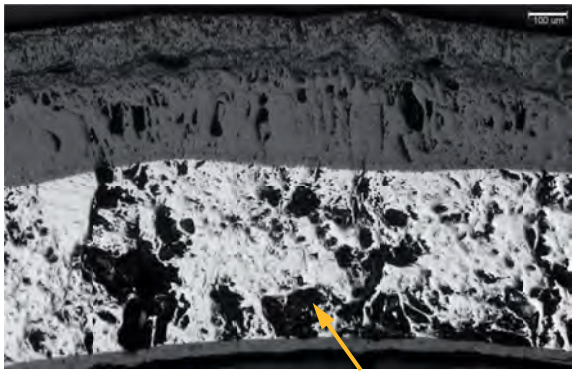

rod 5, 0°: metal melt

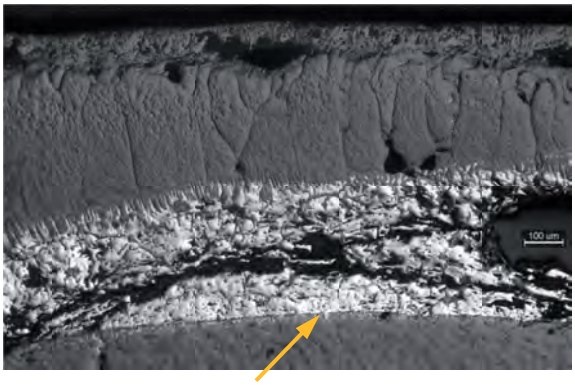

rod 9, 225°: transient zone between pellet and melt

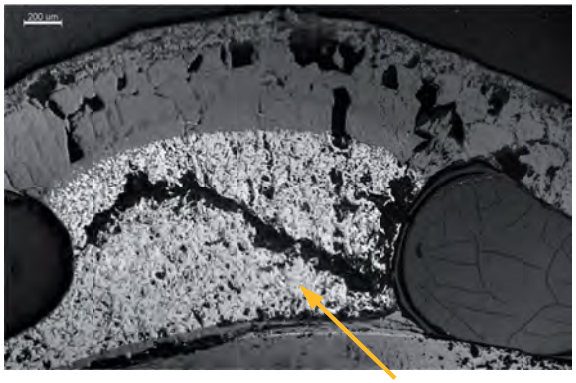

rod 11, 225°: oxidised melt (oxygen content 15 wt%)

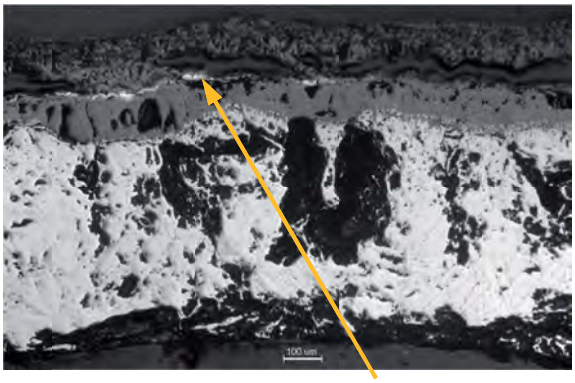

rod 15, 180°: residual nitrides between porous and dense oxide layers

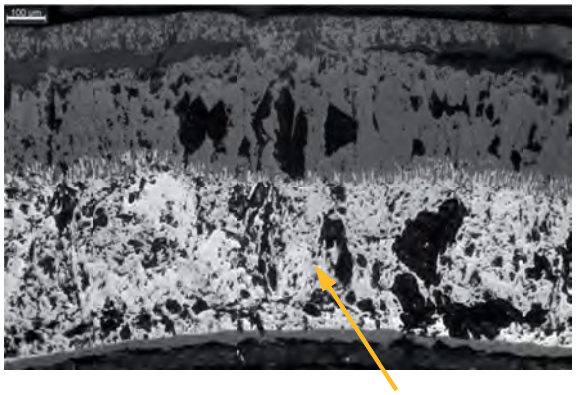

rod 16, 135°: metal melt

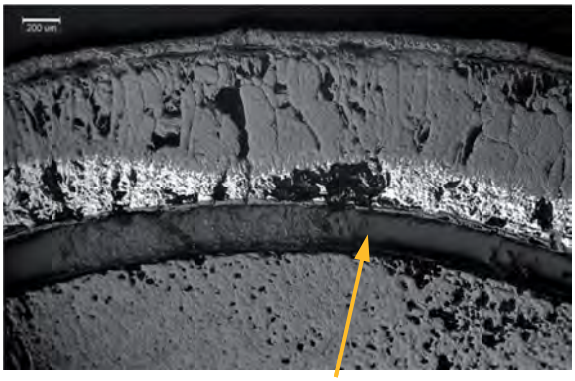

rod 17, 45°: significant gap between pellet and clad, oxygen content in melt 16 wt%

Fig.110: QUENCH-16; cladding structure at 750 mm with significant melt formation.

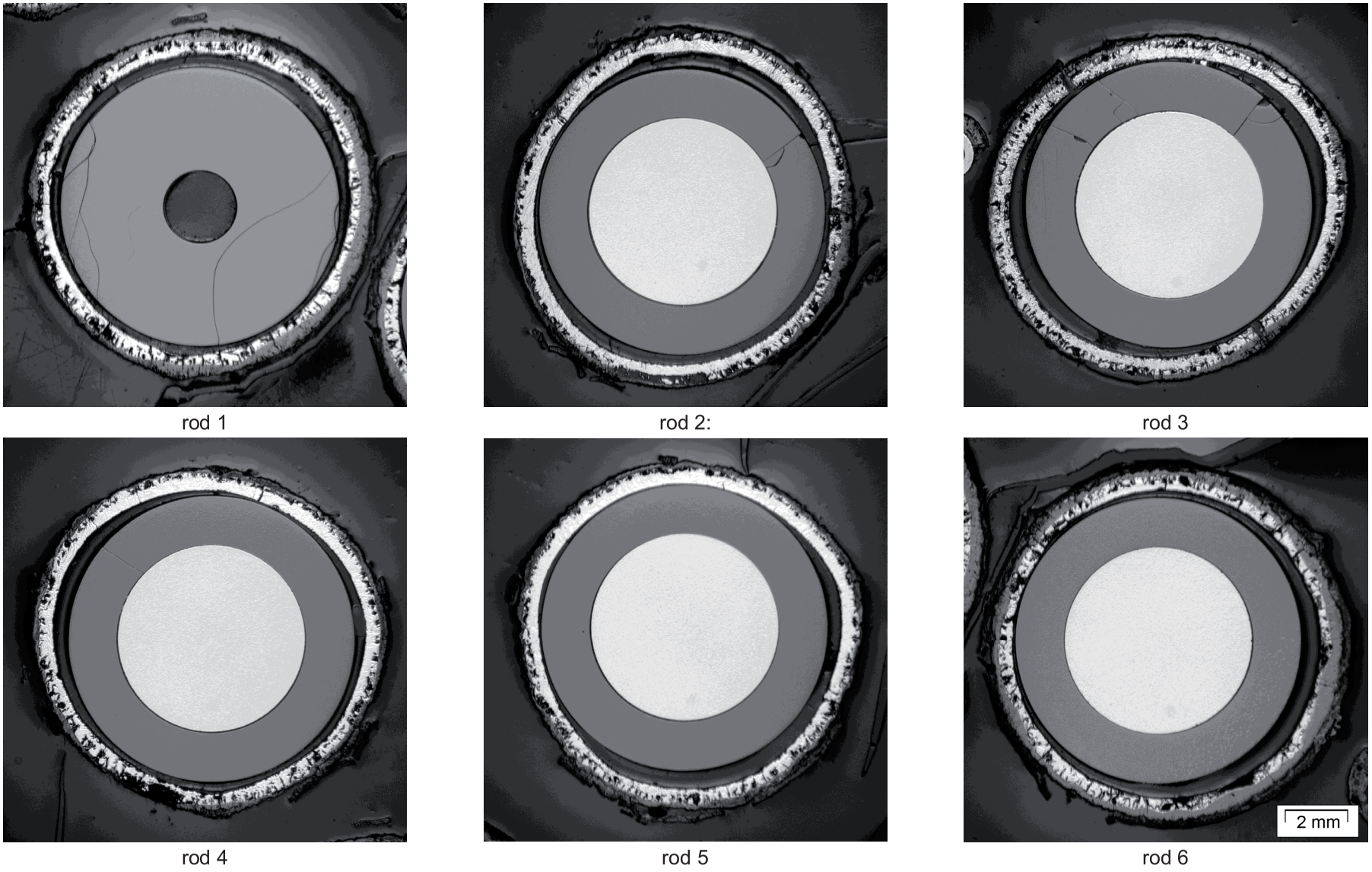

Fig.111: QUENCH-16; Cross section at elevation 850 mm depicting individual test rods 1-6.

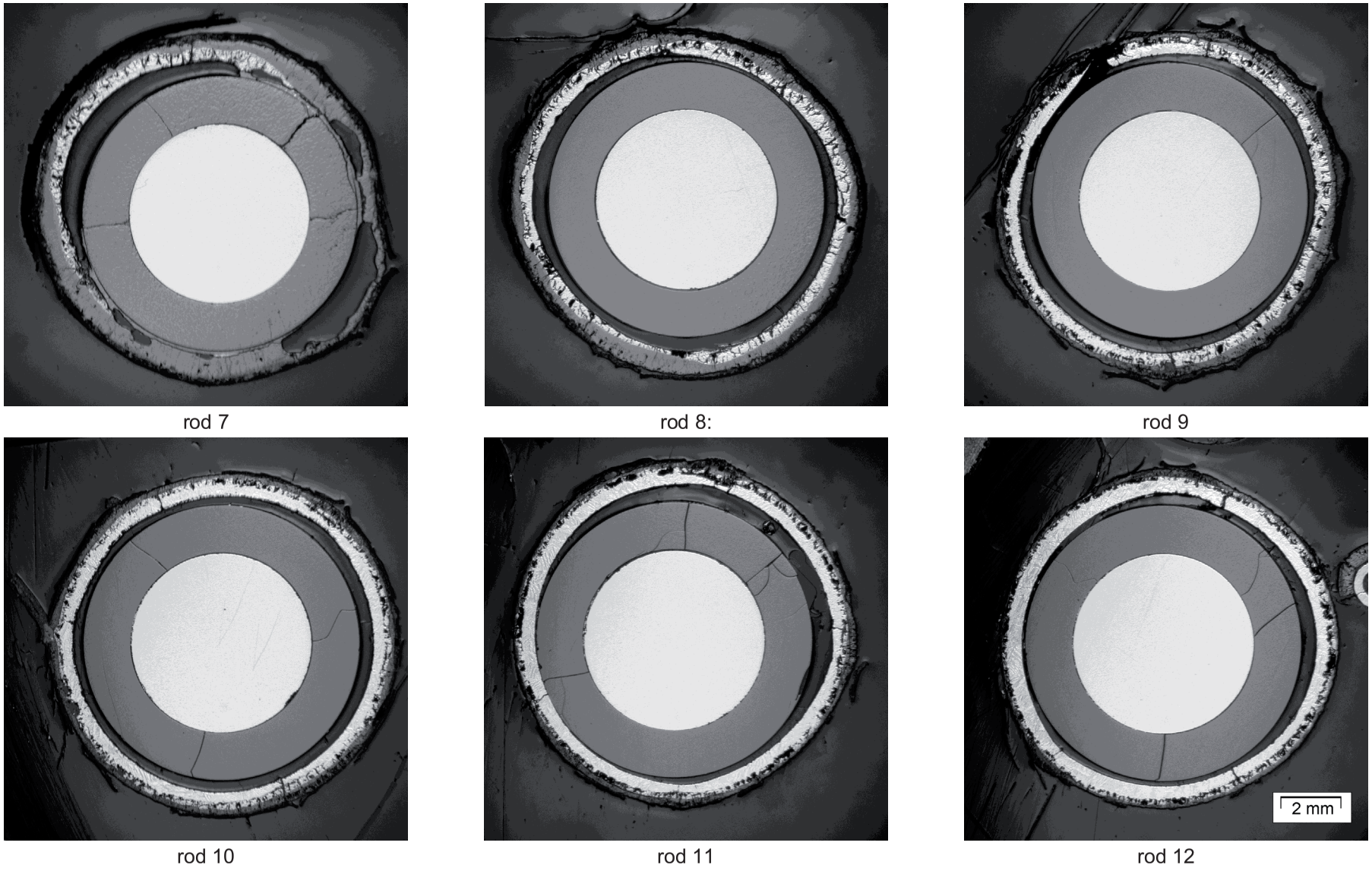

Fig.112: QUENCH-16; Cross section at elevation 850 mm depicting individual test rods 7-12.

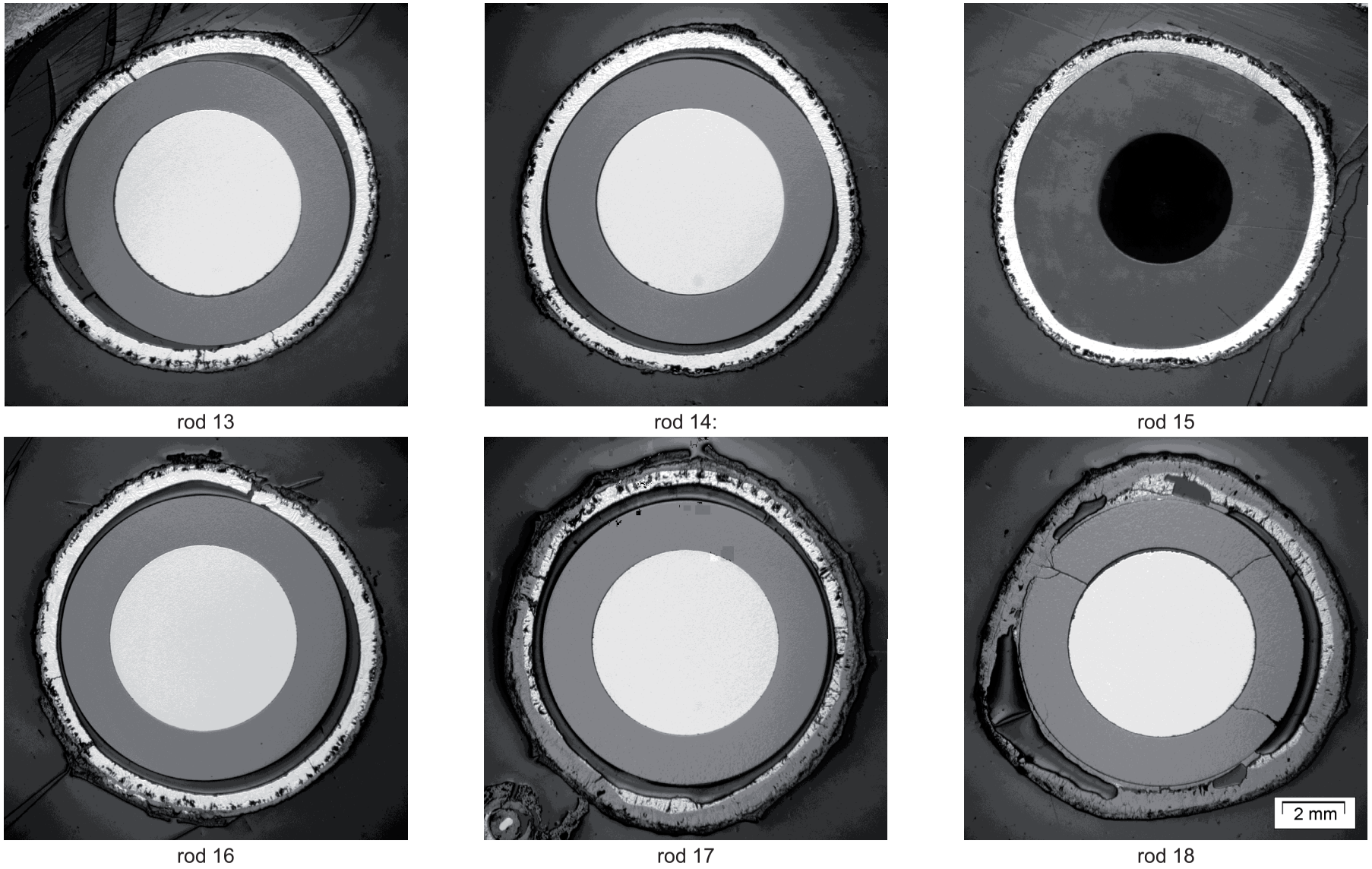

Fig.113: QUENCH-16; Cross section at elevation 850 mm depicting individual test rods 13-18.

rod 19 rod 20 rod 21

Fig.114: QUENCH-16; Cross section at elevation 850 mm depicting individual test rods 19-21.

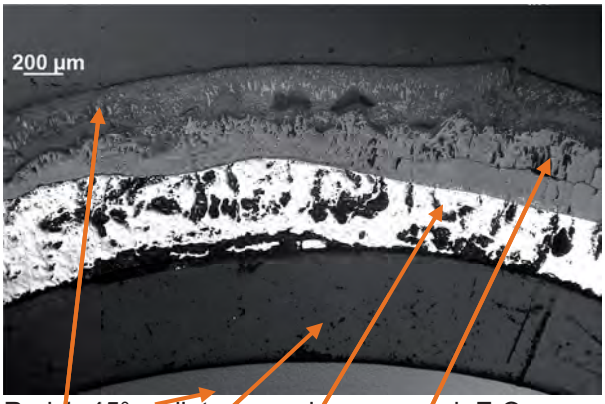

Rod 1, 45°: pellet, gap, α-layer, quench ZrO_2, primary ZrO_2

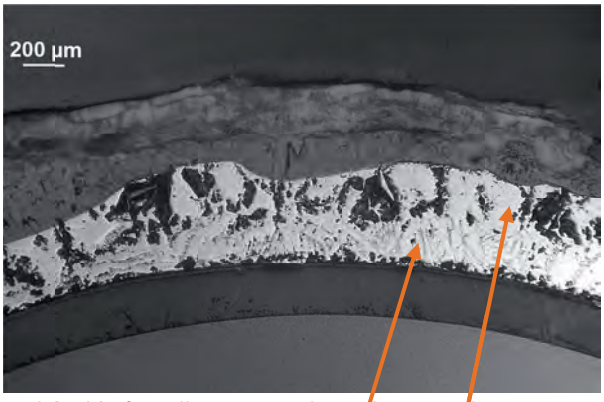

rod 2, 135°: pellet, gap, prior β-layer, α-layer, quench ZrO_2, primary ZrO_2

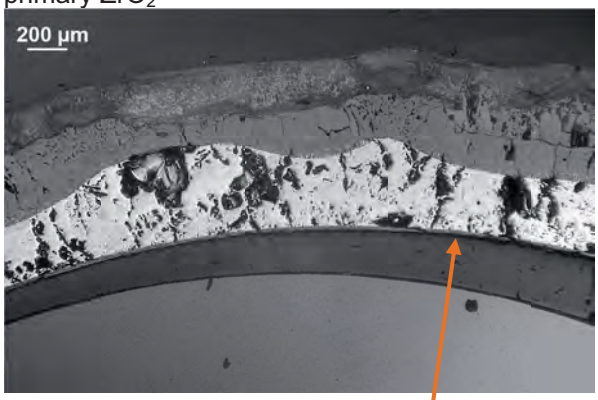

rod 3, 135°: pellet, gap, α-layer, inner ZrO_2, quench ZrO_2, primary ZrO_2

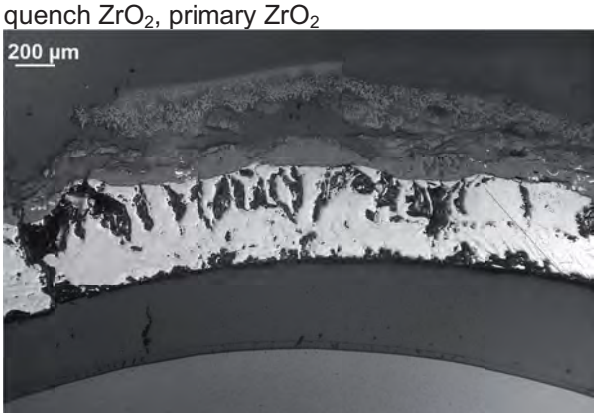

rod 5, 135°: pellet, gap, prior β-layer, α-layer, quench ZrO_2, spalling of primary ZrO_2

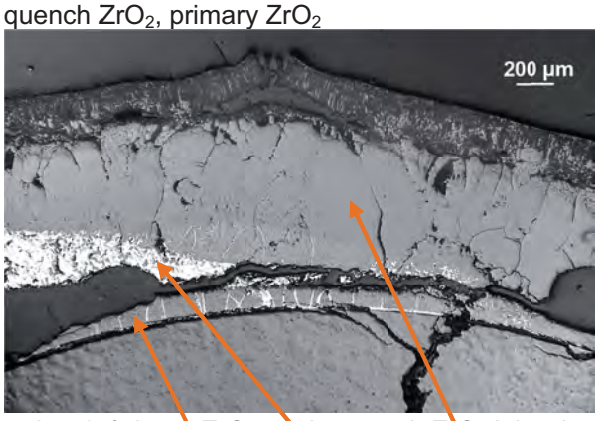

rod 7, 45°: inner ZrO_2, melt, quench ZrO_2 joined with completely oxidised melt, primary ZrO_2

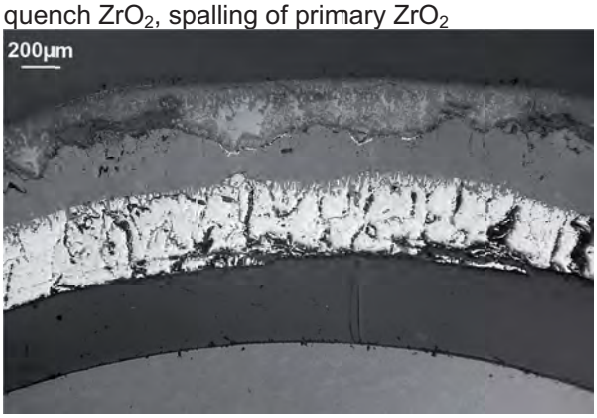

rod 5, 135°: pellet, gap, partially molten α-layer, quench ZrO_2, primary ZrO_2

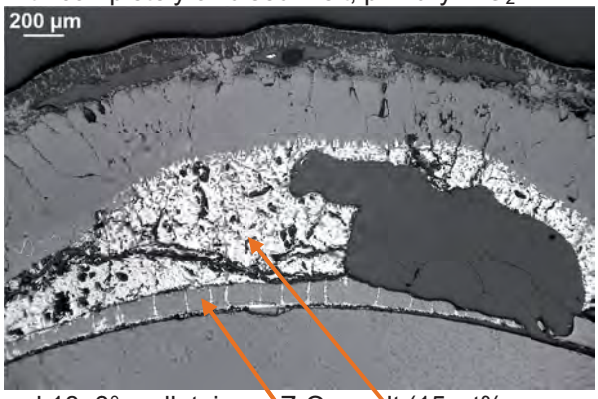

rod 18, 0°: pellet, inner ZrO_2, melt (15 wt% oxygen) with void, quench ZrO_2, primary ZrO_2

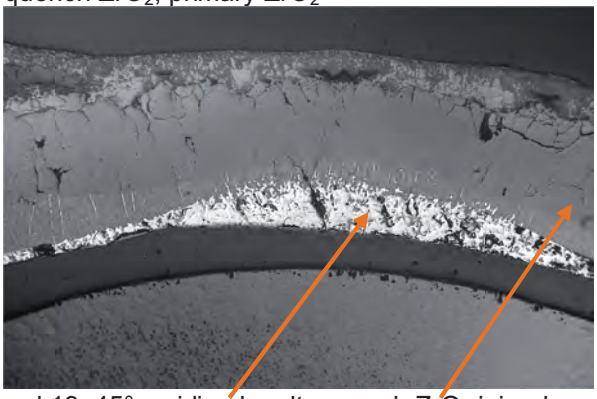

rod 19, 45°: oxidised melt, quench ZrO_2 joined with completely oxidised melt, primary ZrO_2

Fig.115: QUENCH-16; sequence of structure elements for different rods of elevation 850 mm.

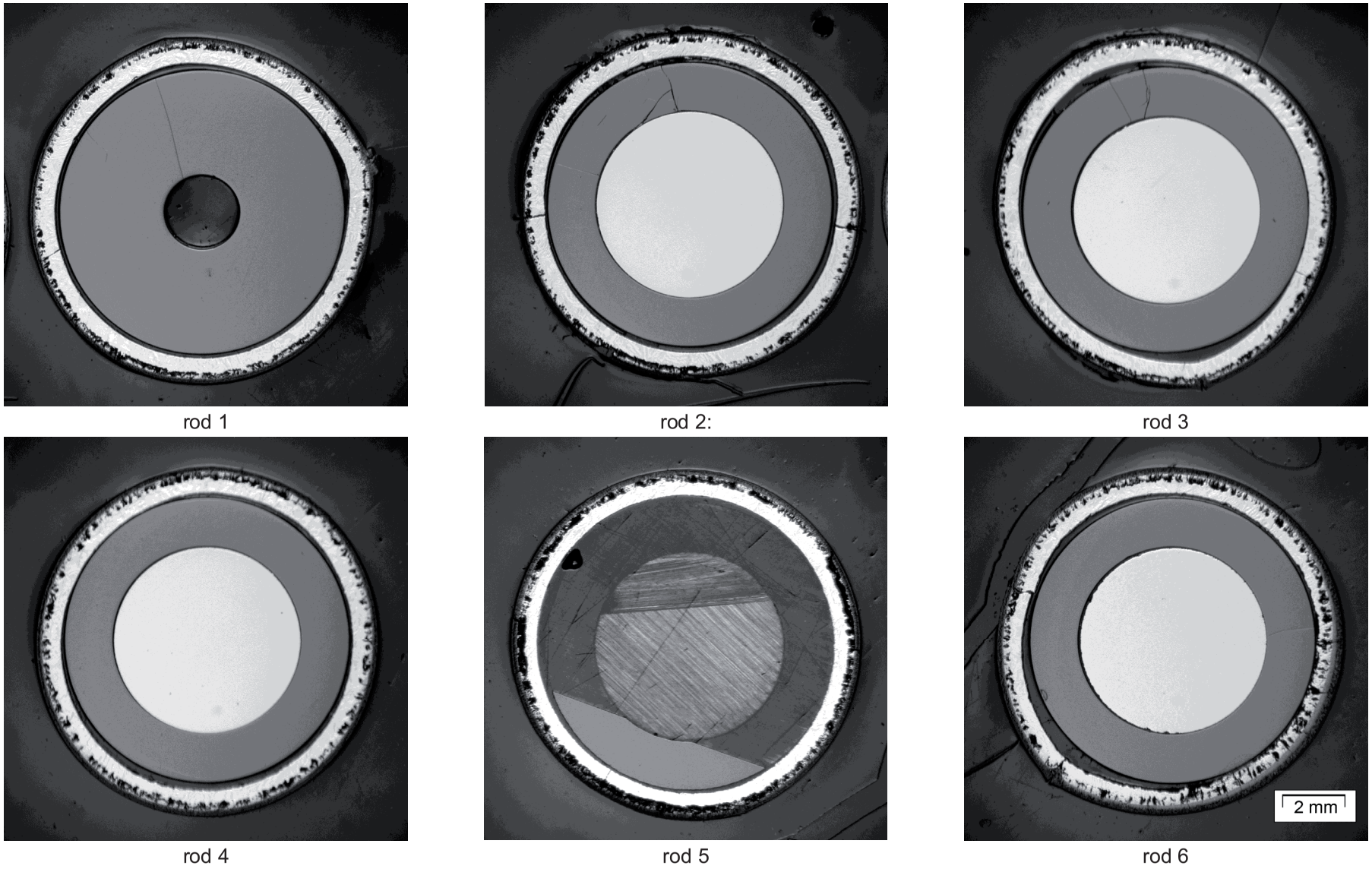

Fig.116: QUENCH-16; Cross section at elevation 950 mm depicting individual test rods 1-6.

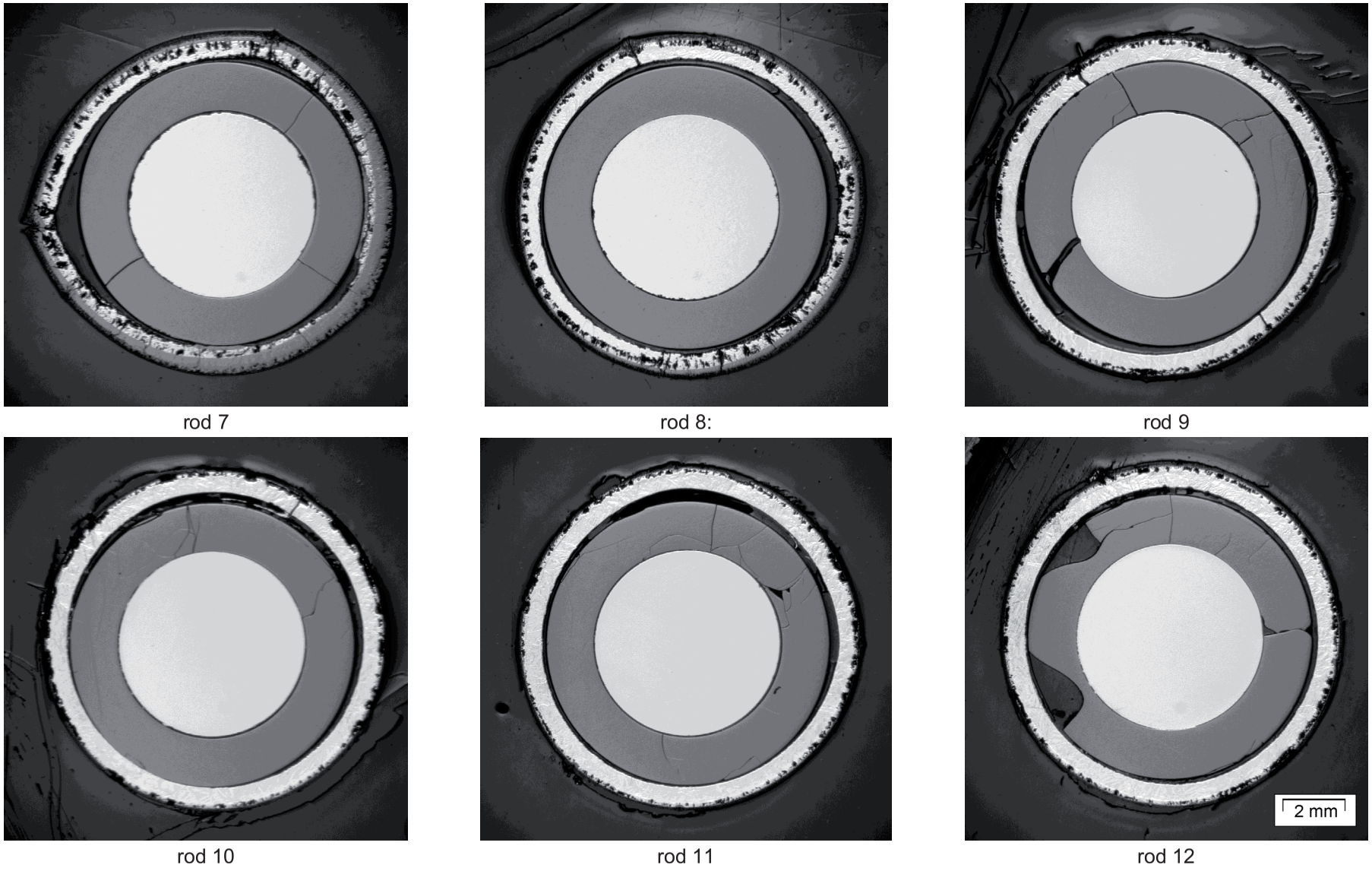

Fig.117: QUENCH-16; Cross section at elevation 950 mm depicting individual test rods 7-12.

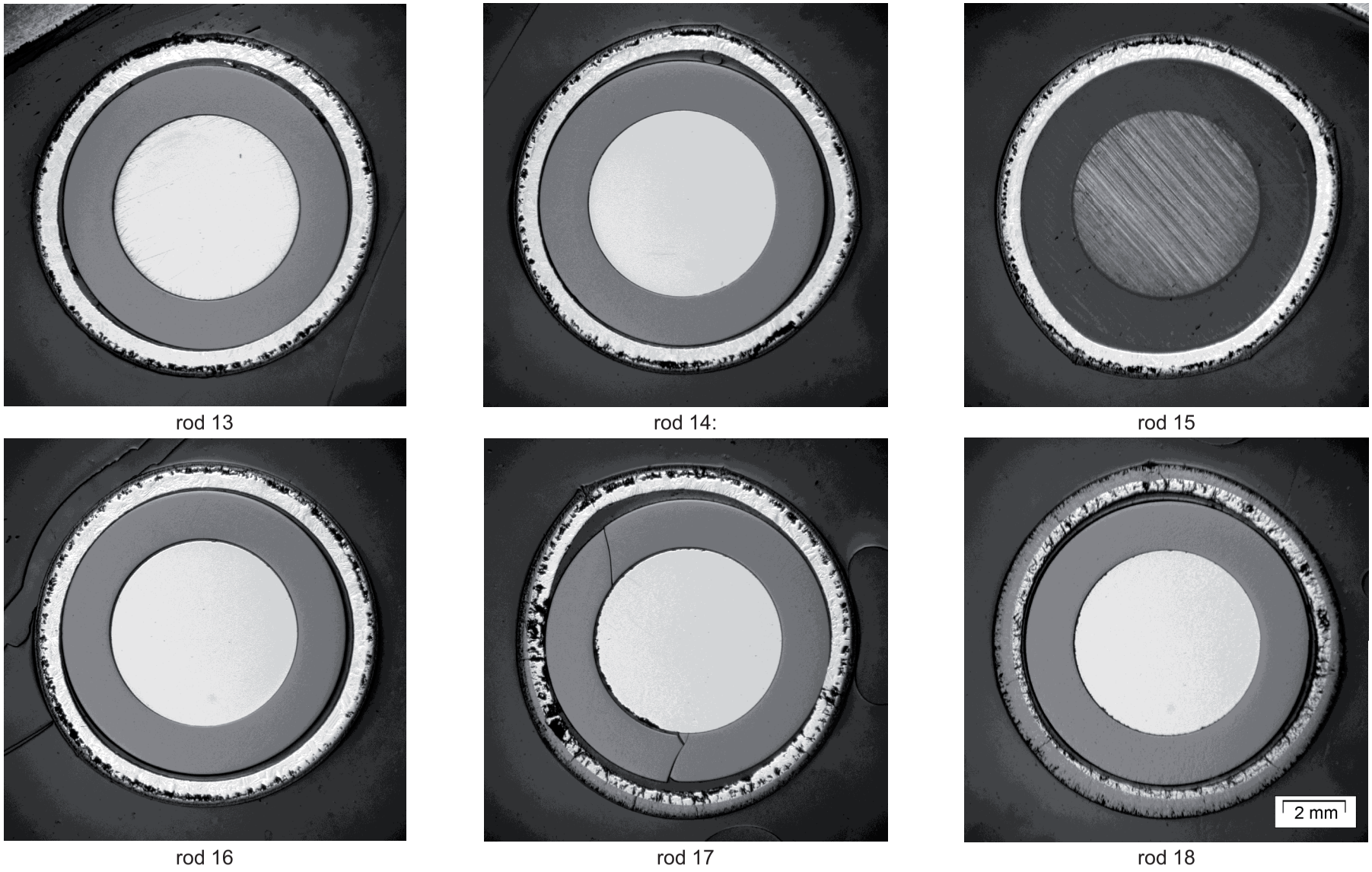

Fig.118: QUENCH-16; Cross section at elevation 950 mm depicting individual test rods 13-18.

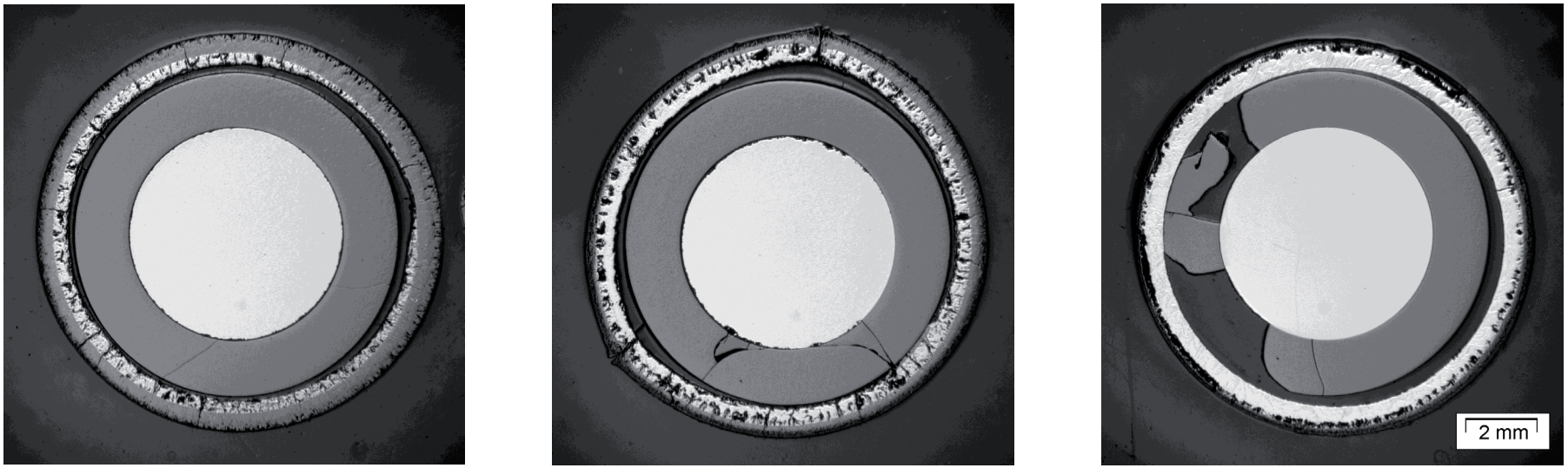

rod 19 rod 20 rod 21

Fig.119: QUENCH-16; Cross section at elevation 950 mm depicting individual test rods 19-21.

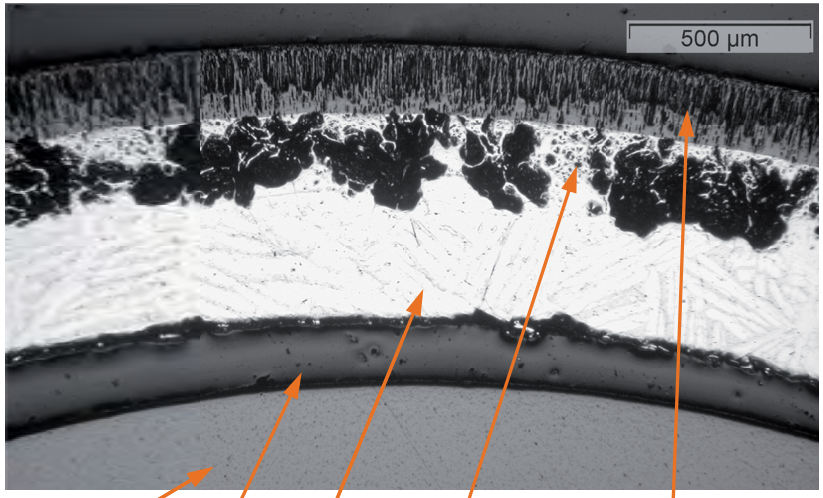

rod 6, 0°; pellet, gap, prior β-Zr, α-Zr(O): 266 µm, ZrO_2: 196 µm

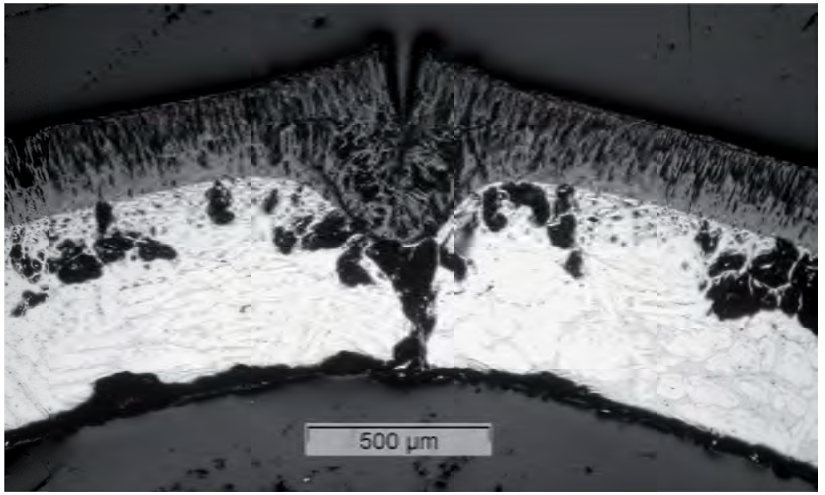

rod 6, 225°; gap, prior β-Zr, α-Zr(O): 240 µm, ZrO_2: 240 µm, wedge-shape crack

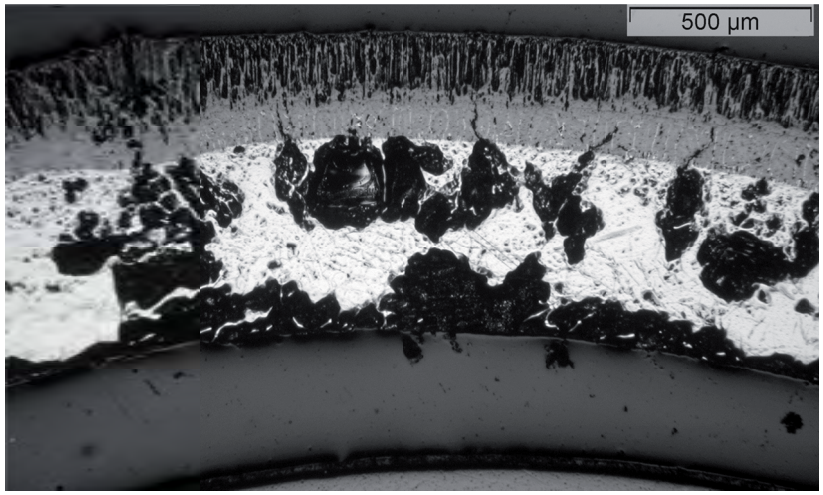

rod 8, 90°; pellet, gap, α-Zr(O): 511 µm, ZrO_2: 291 µm

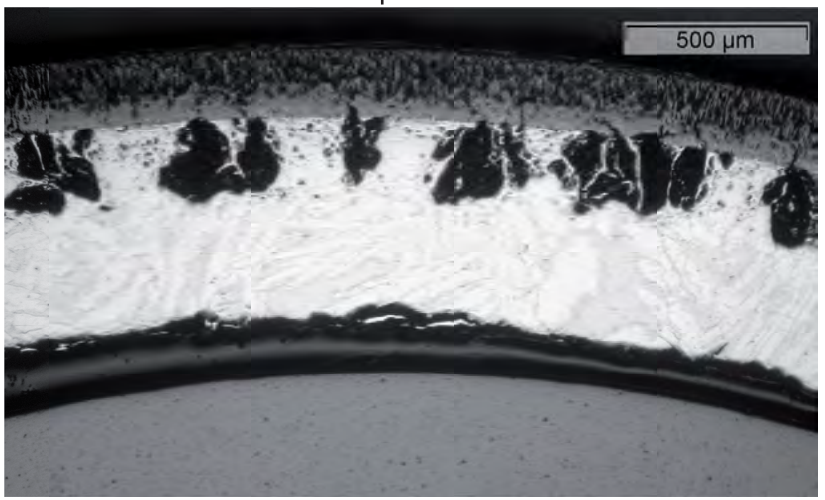

rod 8, 270°; pellet, gap, prior β-Zr, α-Zr(O): 223 µm, ZrO_2: 204 µm

Fig.120: QUENCH-16; structure of simulator rods at elevation 950 mm: absence of nitrides; formation of axial wedge-shape cracks predetermine the “flowering effect”.

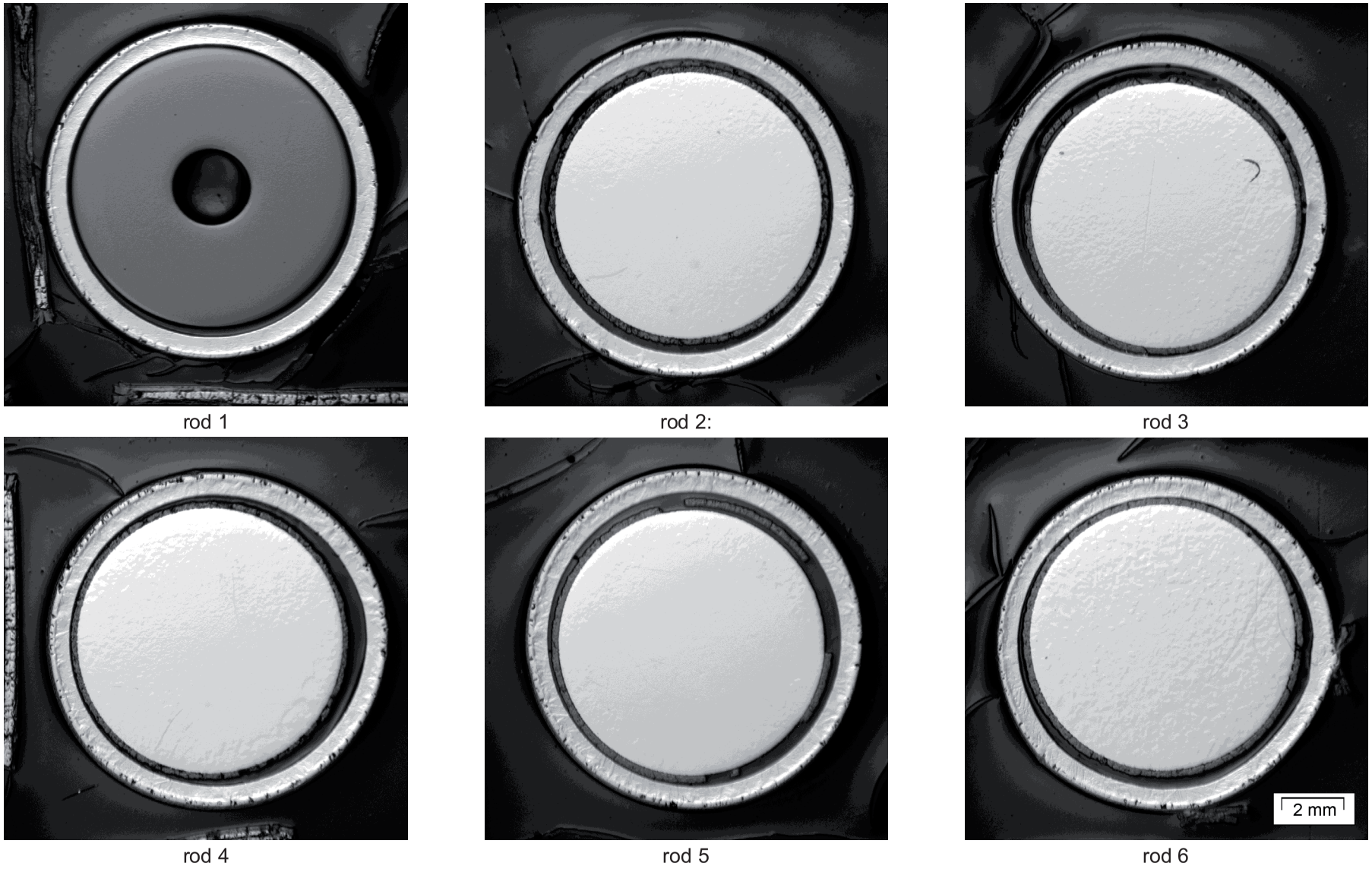

Fig.121: QUENCH-16; Cross section at elevation 1050 mm depicting individual test rods 1-6.

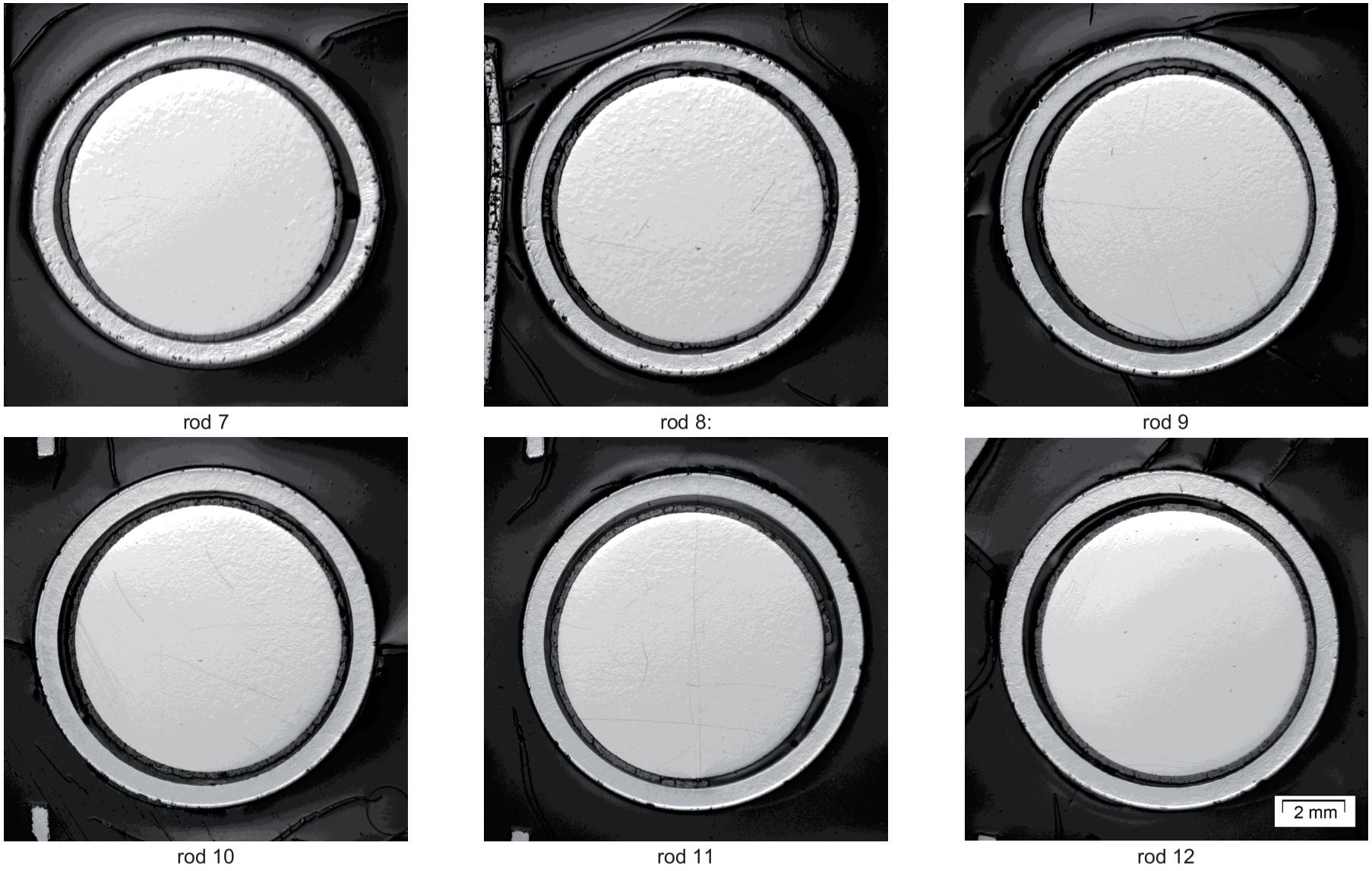

Fig.122: QUENCH-16; Cross section at elevation 1050 mm depicting individual test rods 7-12.

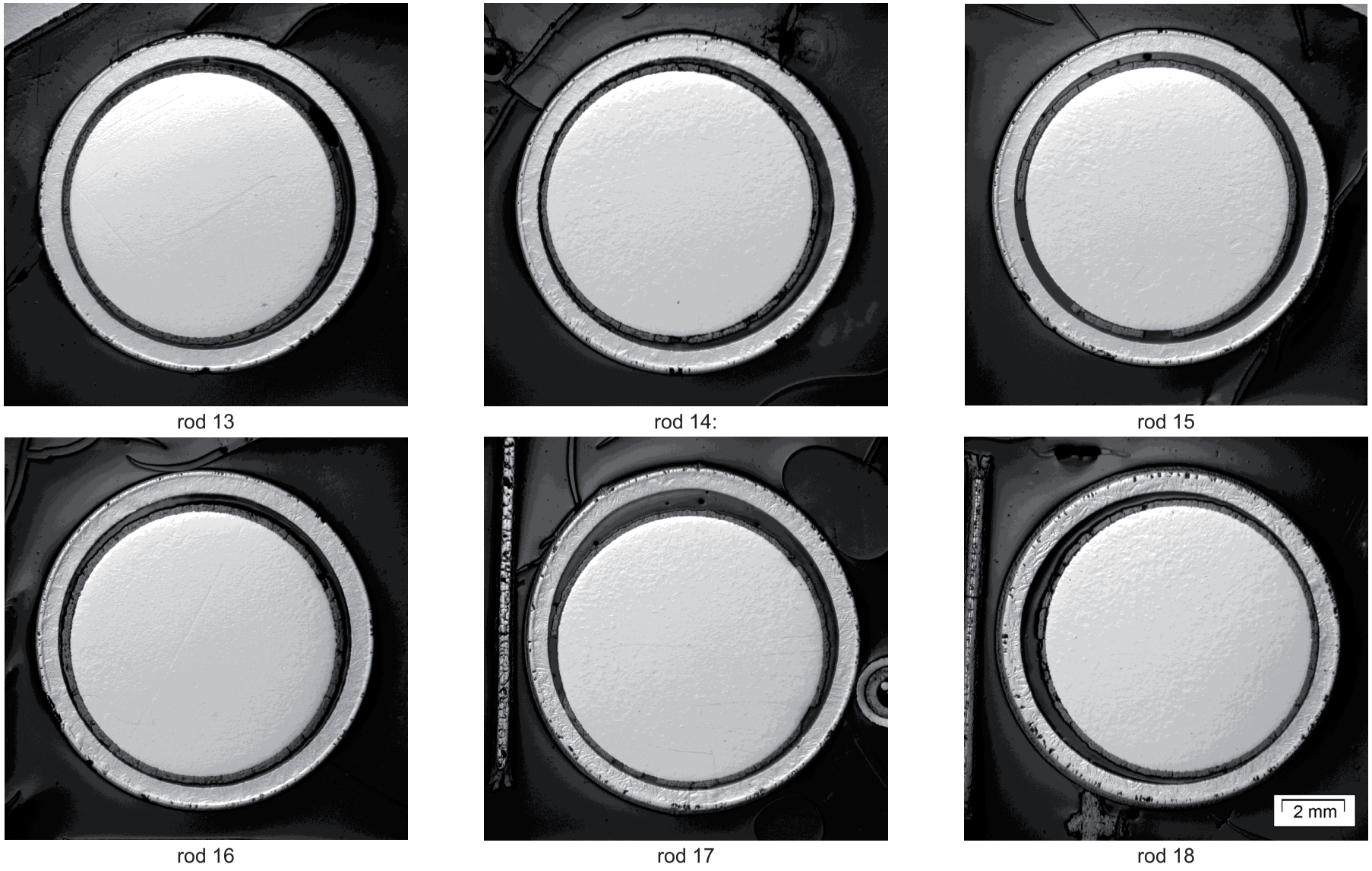

Fig.123: QUENCH-16; Cross section at elevation 1050 mm depicting individual test rods 13-18.

rod 19 rod 20 rod 21

Fig.124: QUENCH-16; Cross section at elevation 1050 mm depicting individual test rods 19-21.

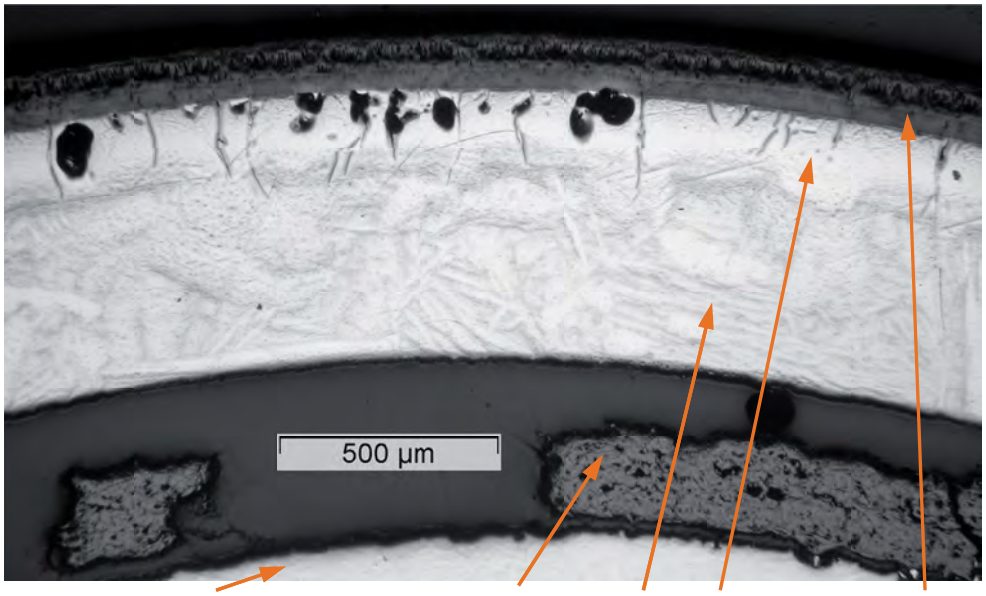

rod 5, 180°: Mo-heater, residual ZrO_2-coating, prior β-Zr, α-Zr(O): 165 µm, ZrO_2: 130 µm

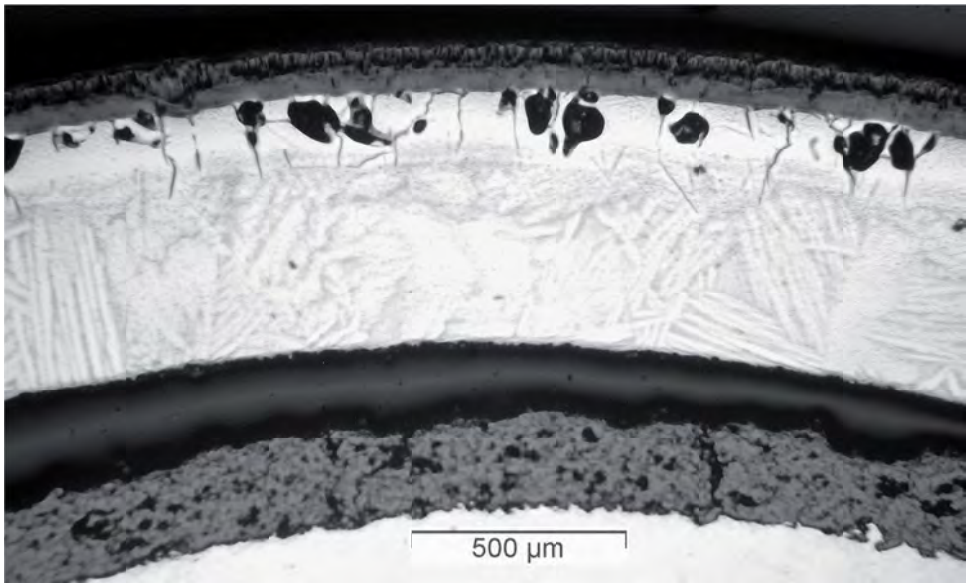

rod 6, 270°: Mo-heater, ZrO_2-coating, prior β-Zr, α-Zr(O): 154 µm, ZrO_2: 122 µm

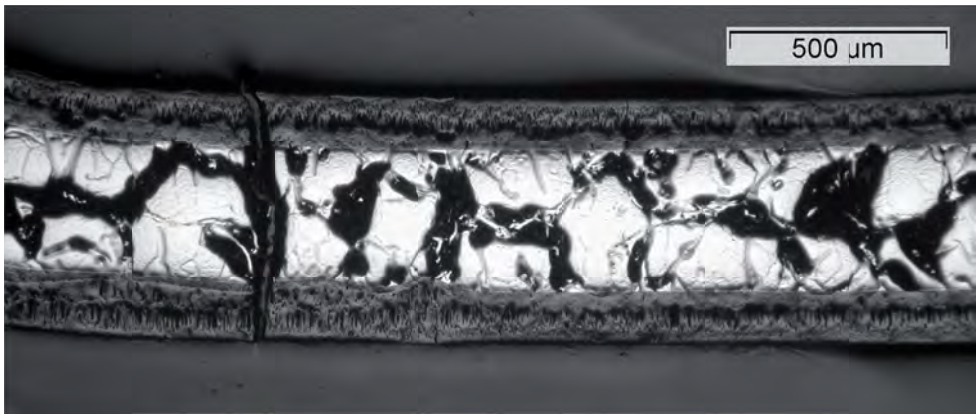

grid spacer: ZrO_2: 120 µm, α-Zr(O): 325 µm; ZrO_2: 120 µm

Fig.125: QUENCH-16; structure of simulator rods and grid spacer at elevation 1050 mm.

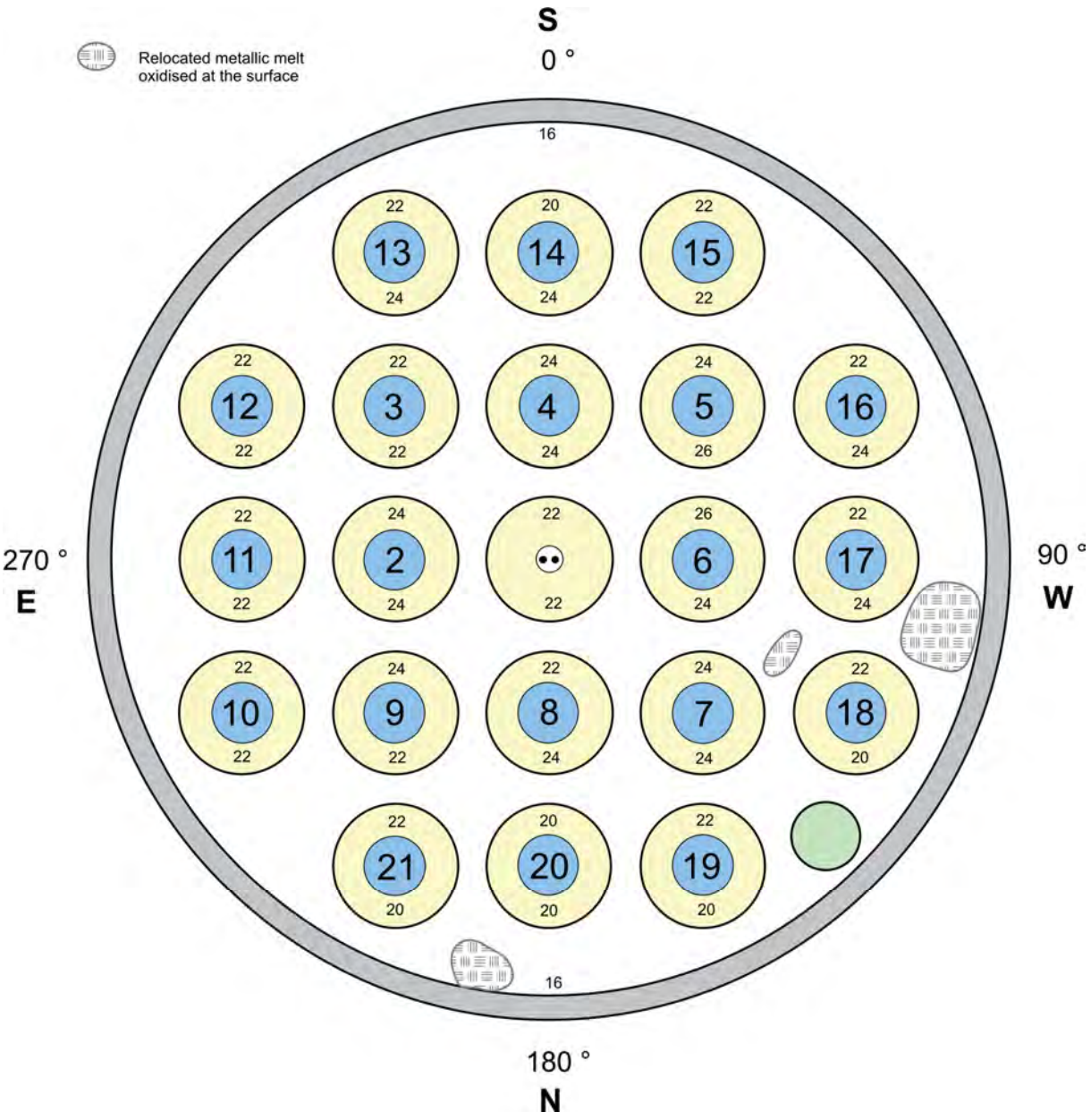

Fig.126: QUENCH-16; Alpha-phase layer thickness at bundle elevation 250 mm (Cross section QUE 16-2-250).

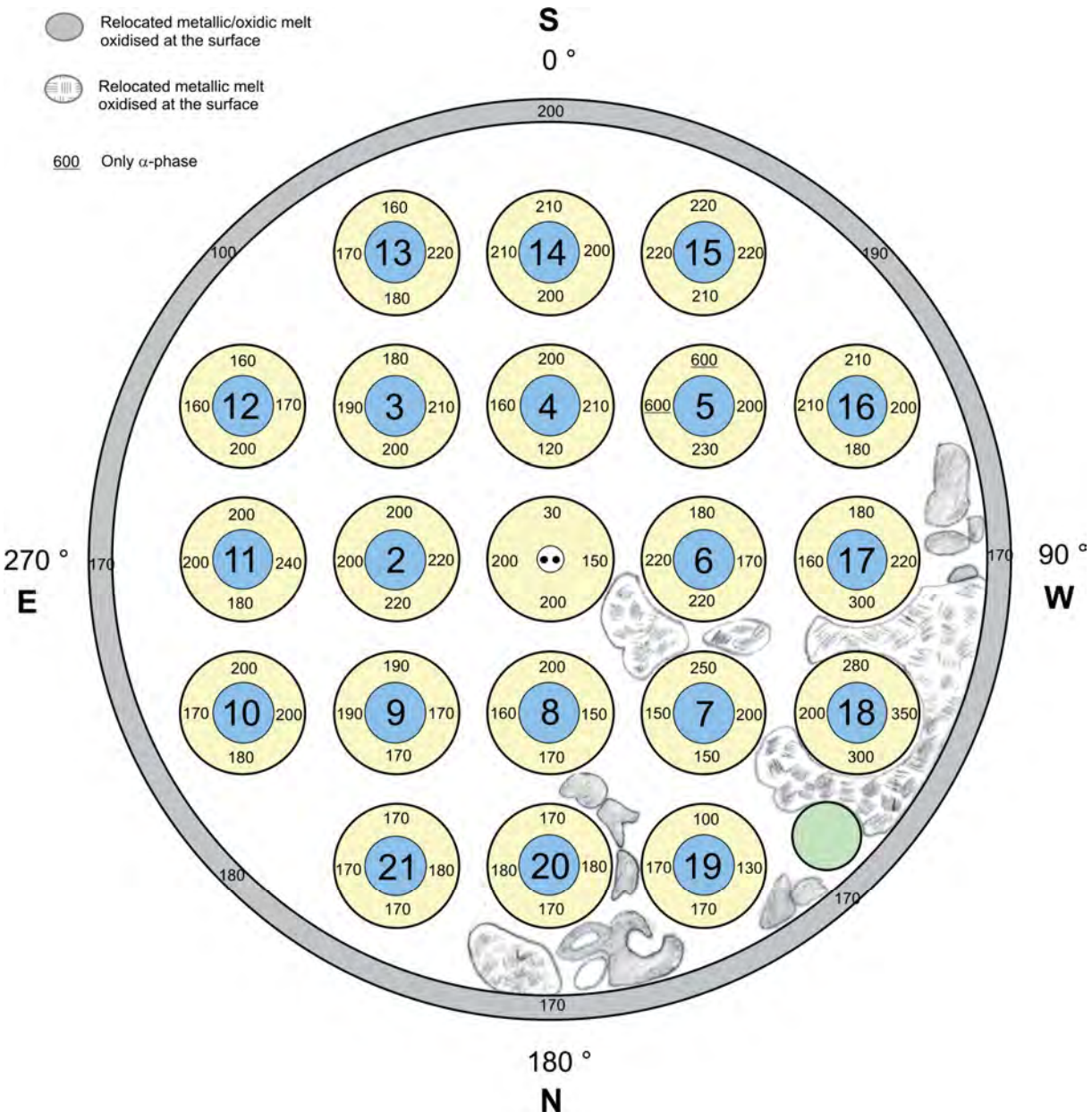

Fig.127: QUENCH-16; Alpha-phase layer thickness at bundle elevation 350 mm (Cross section QUE 16-3-350).

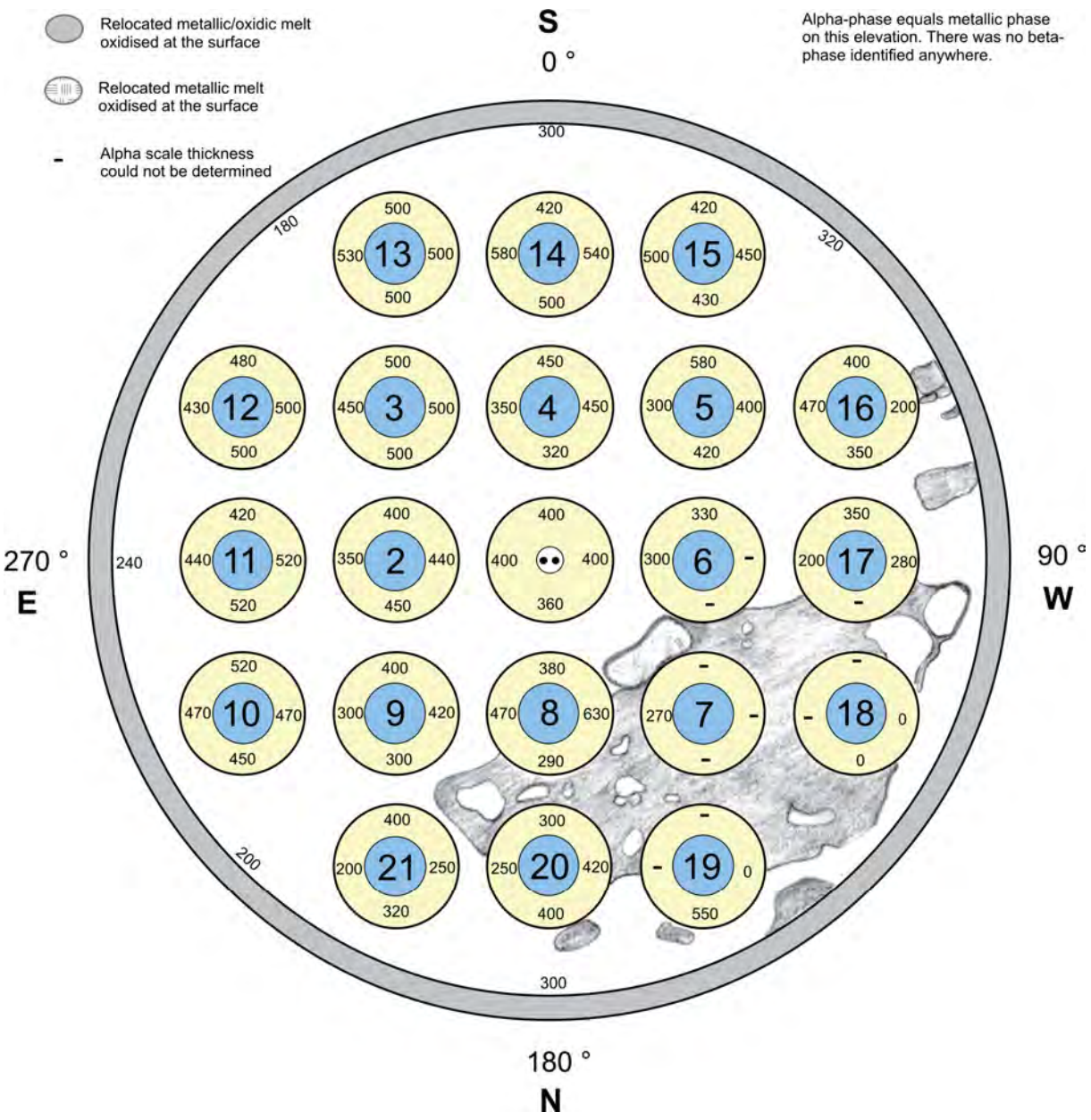

Fig.128: QUENCH-16; Alpha-phase layer thickness at bundle elevation 450 mm (Cross section QUE 16-4-450).

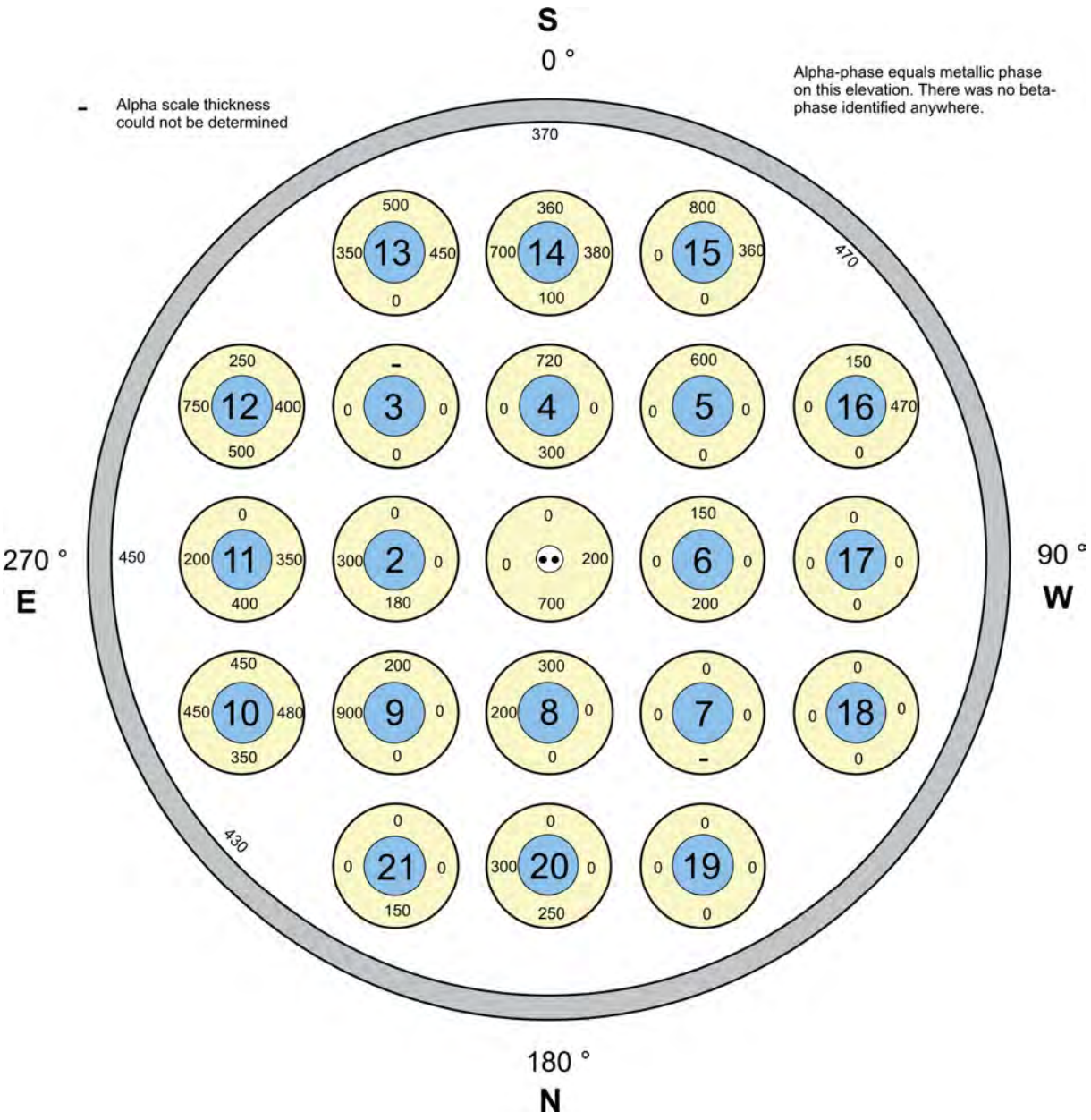

Fig.129: QUENCH-16; Alpha-phase layer thickness at bundle elevation 550 mm (Cross section QUE 16-5-550).

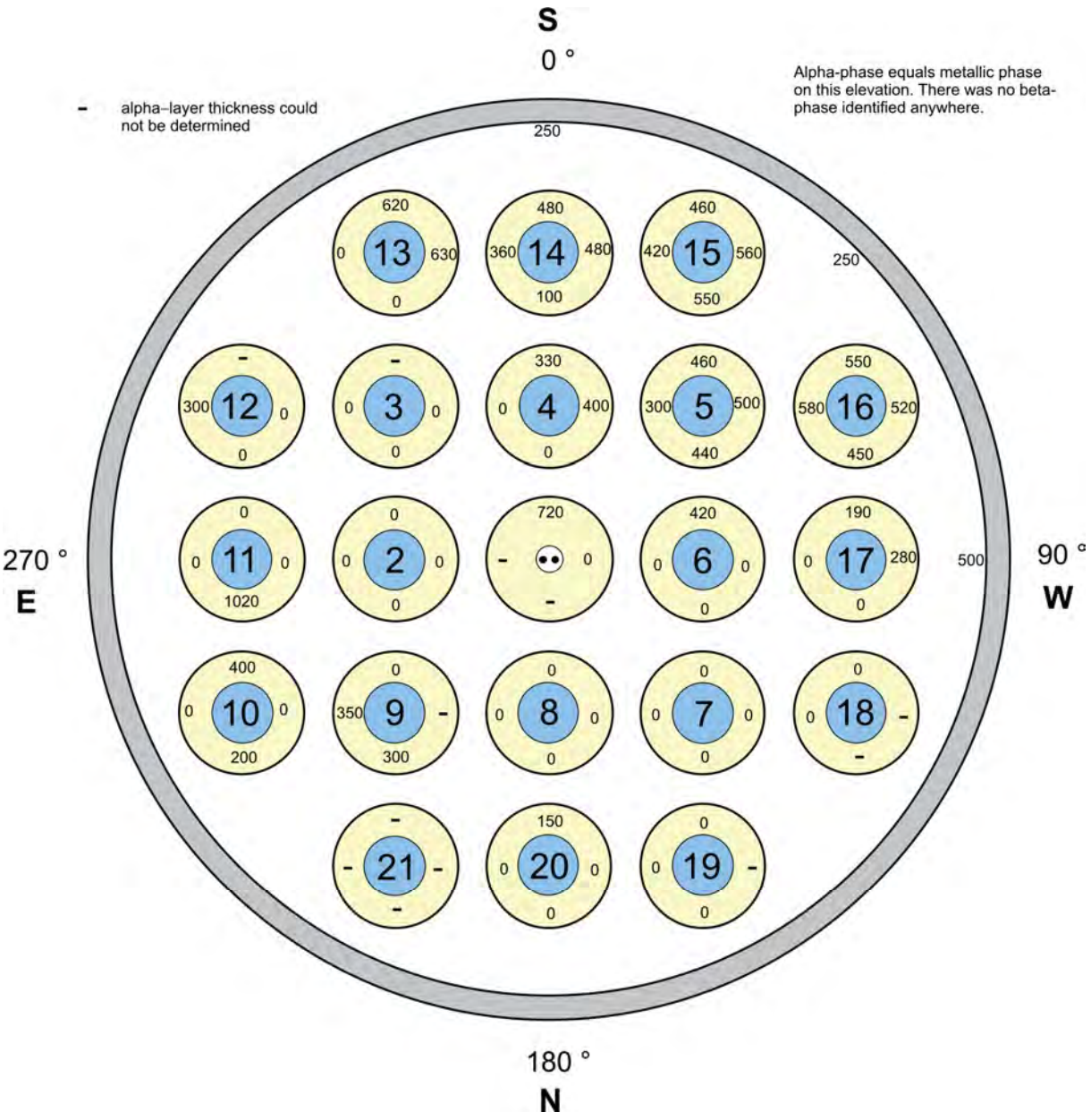

Fig.130: QUENCH-16; Alpha-phase layer thickness at bundle elevation 750 mm (Cross section QUE 16-7-750).

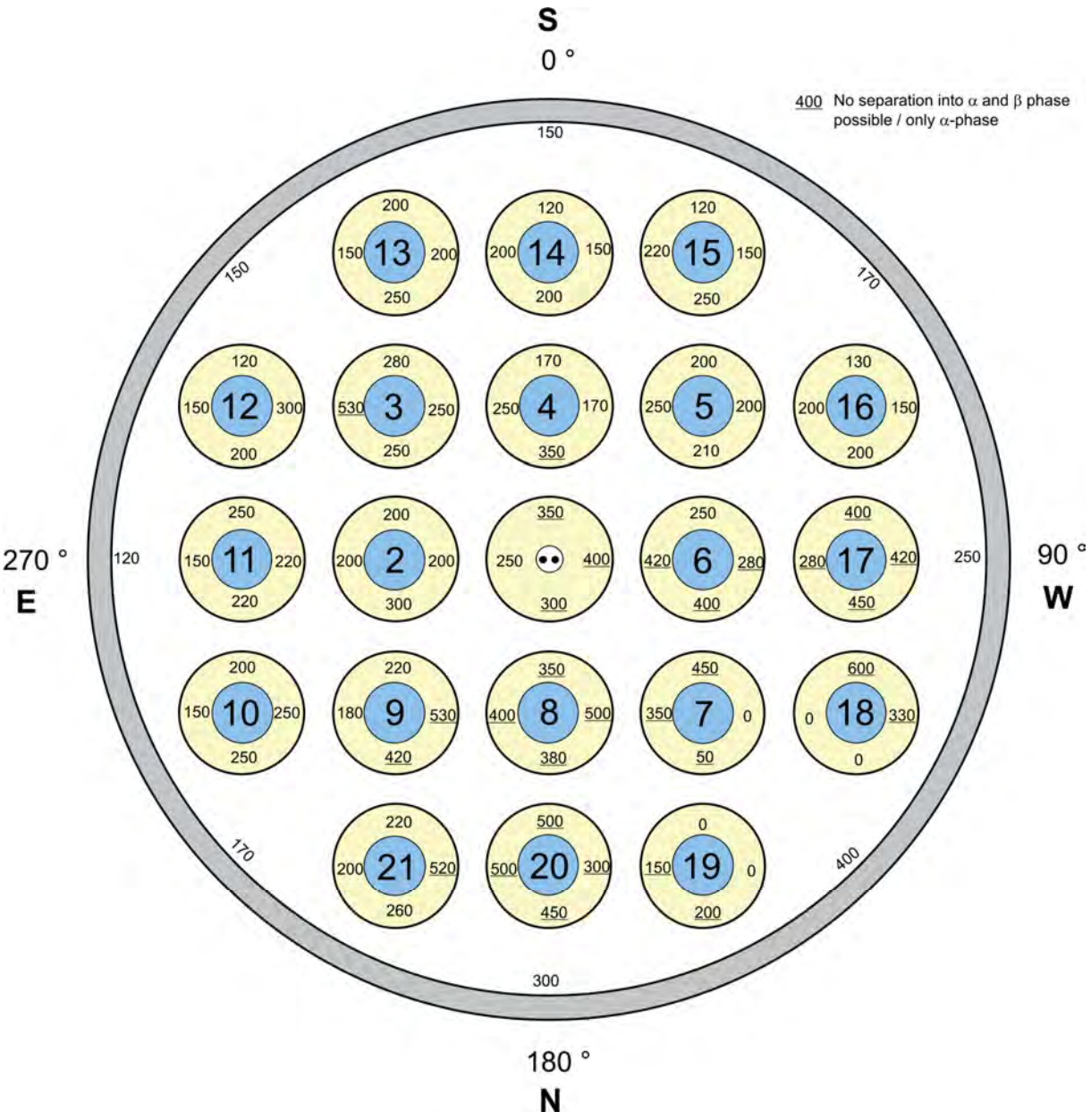

Fig.131: QUENCH-16; Alpha-phase layer thickness at bundle elevation 850 mm (Cross section QUE 16-8-850).

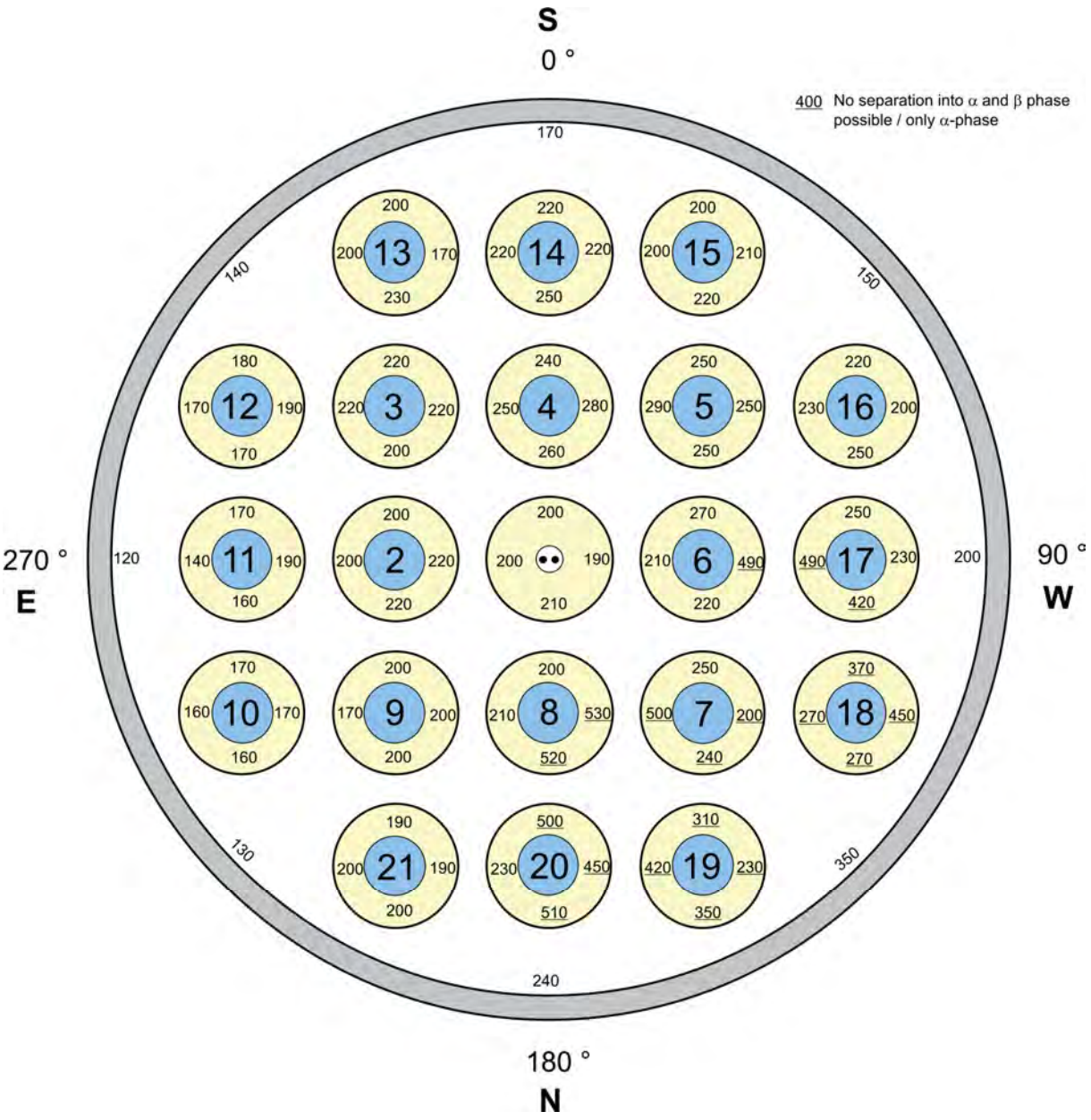

Fig.132: QUENCH-16; Alpha-phase layer thickness at bundle elevation 950 mm (Cross section QUE 16-9-950).

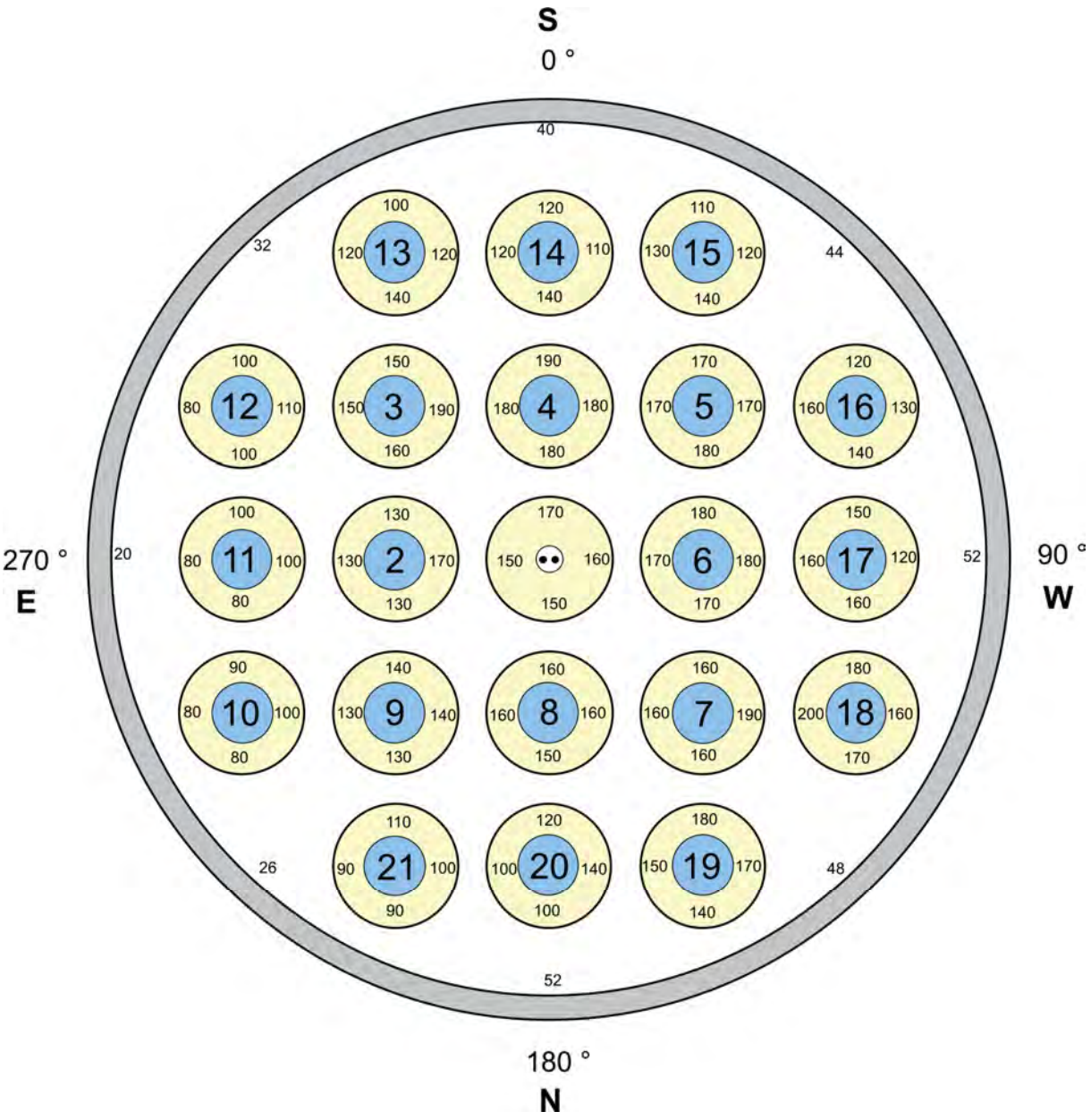

Fig.133: QUENCH-16; Alpha-phase layer thickness at bundle elevation 1050 mm (Cross section QUE 16-10-1050).

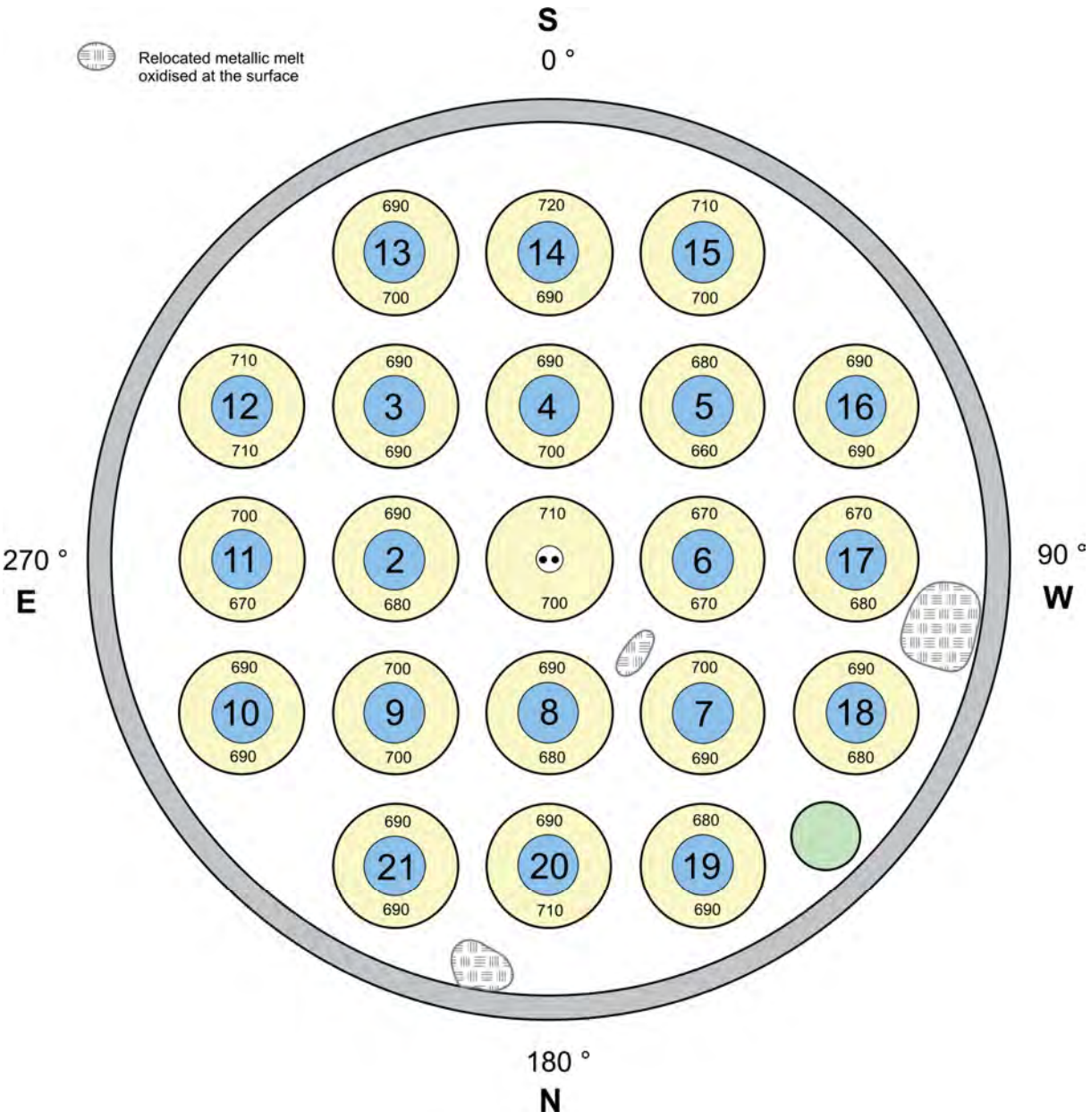

Fig.134: QUENCH-16; Beta-phase layer thickness at bundle elevation 250 mm (Cross section QUE 16-2-250).

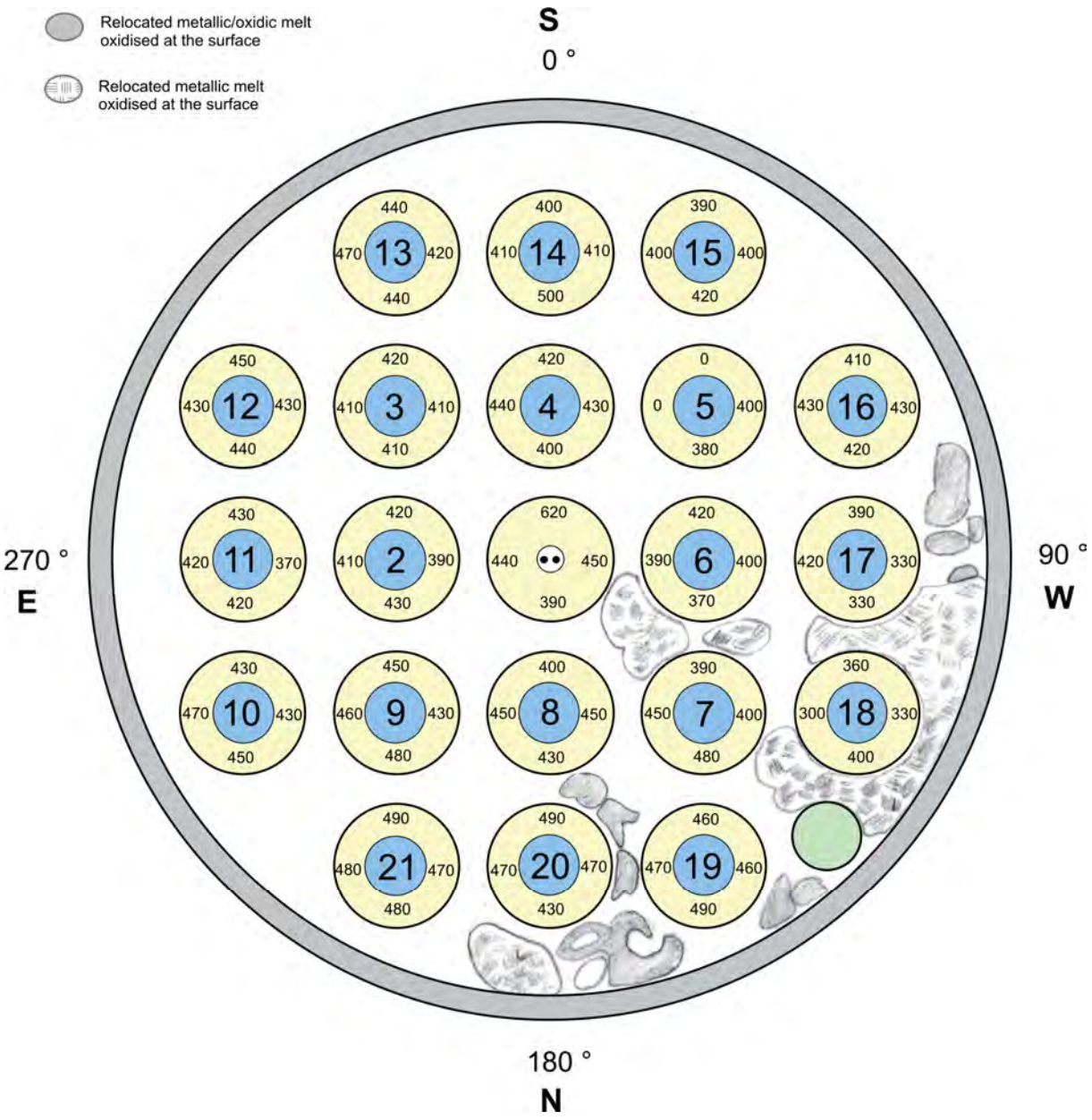

Fig.135: QUENCH-16; Beta-phase layer thickness at bundle elevation 350 mm (Cross section QUE 16-3-350).

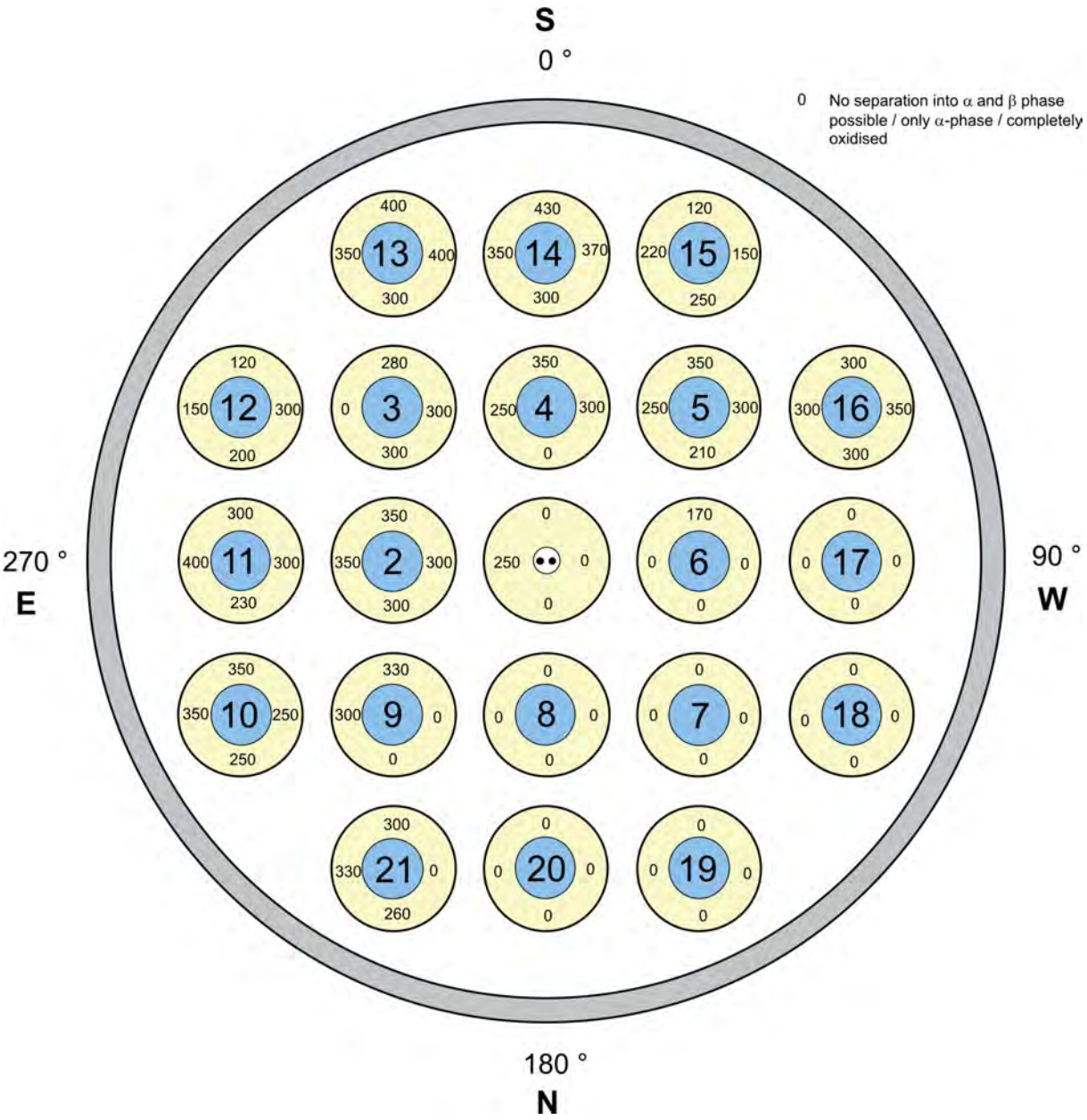

Fig.136: QUENCH-16; Beta-phase layer thickness at bundle elevation 850 mm (Cross section QUE 16-8-850).

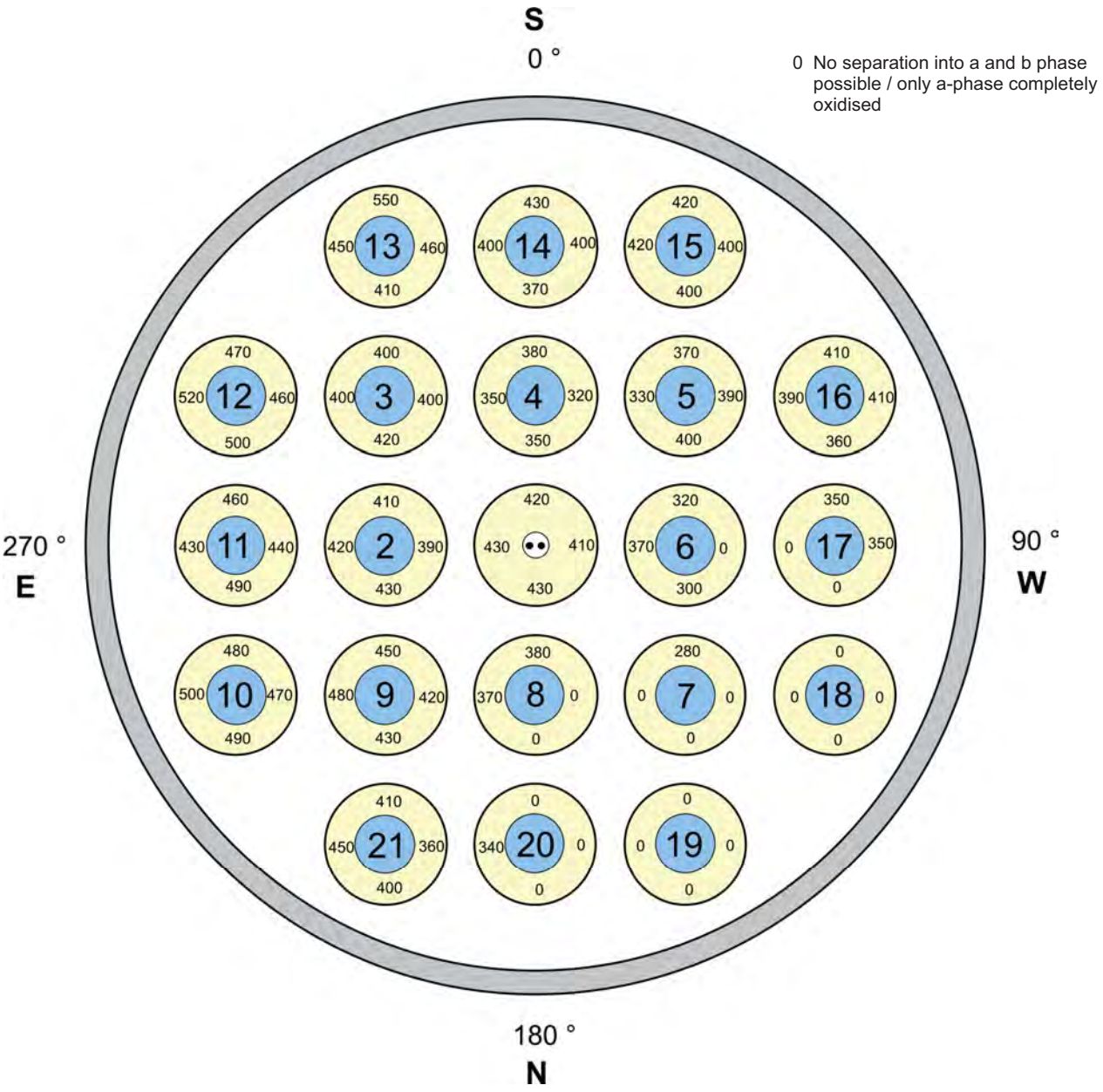

Fig.137: QUENCH-16; Beta-phase layer thickness at bundle elevation 950 mm (Cross section QUE 16-9-950).

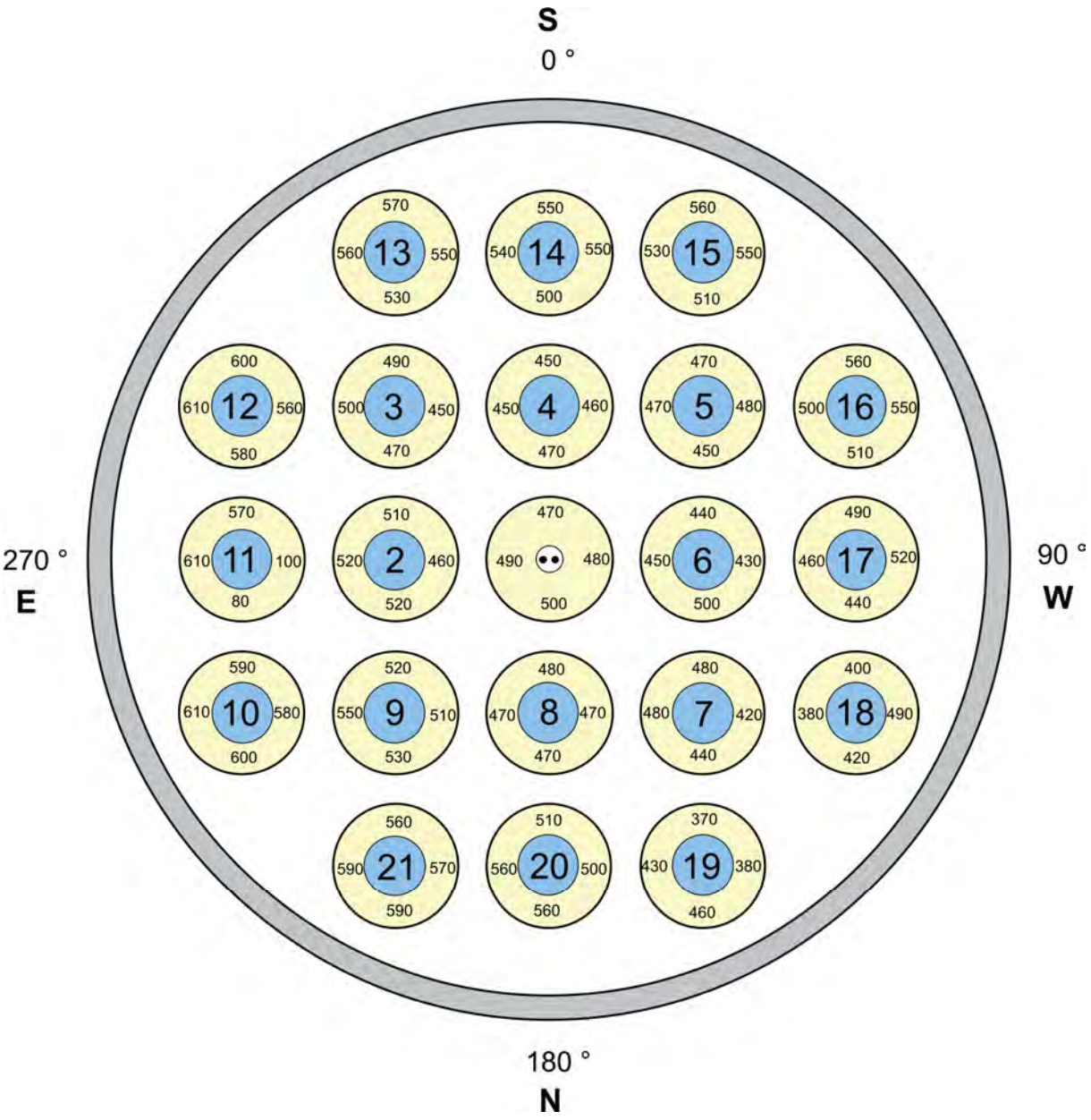

Fig.138: QUENCH-16; Beta-phase layer thickness at bundle elevation 1050 mm (Cross section QUE 16-10-1050).

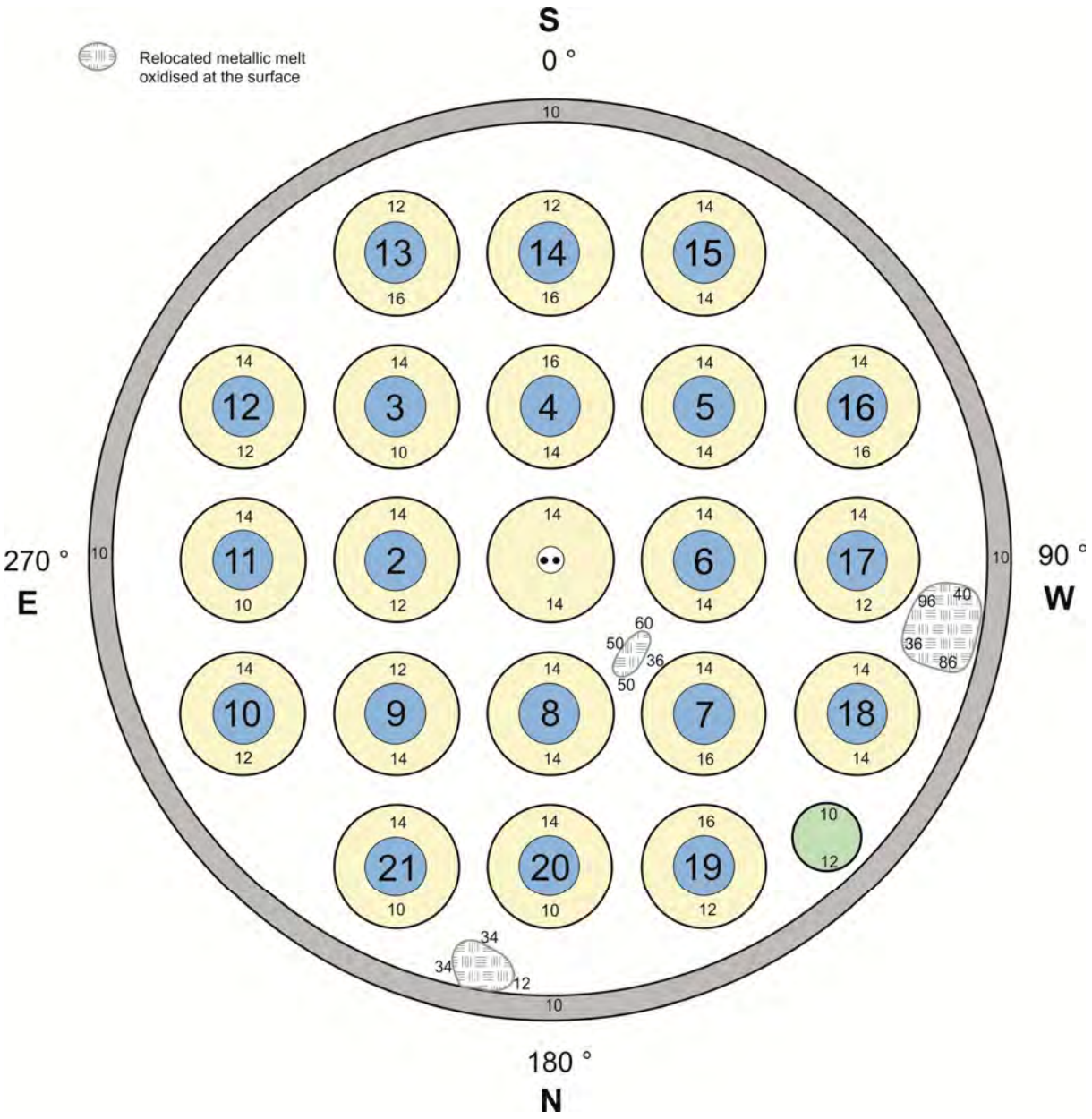

Fig.139: QUENCH-16; Oxide layer thickness at bundle elevation 250 mm (Cross section QUE 16-2-250).

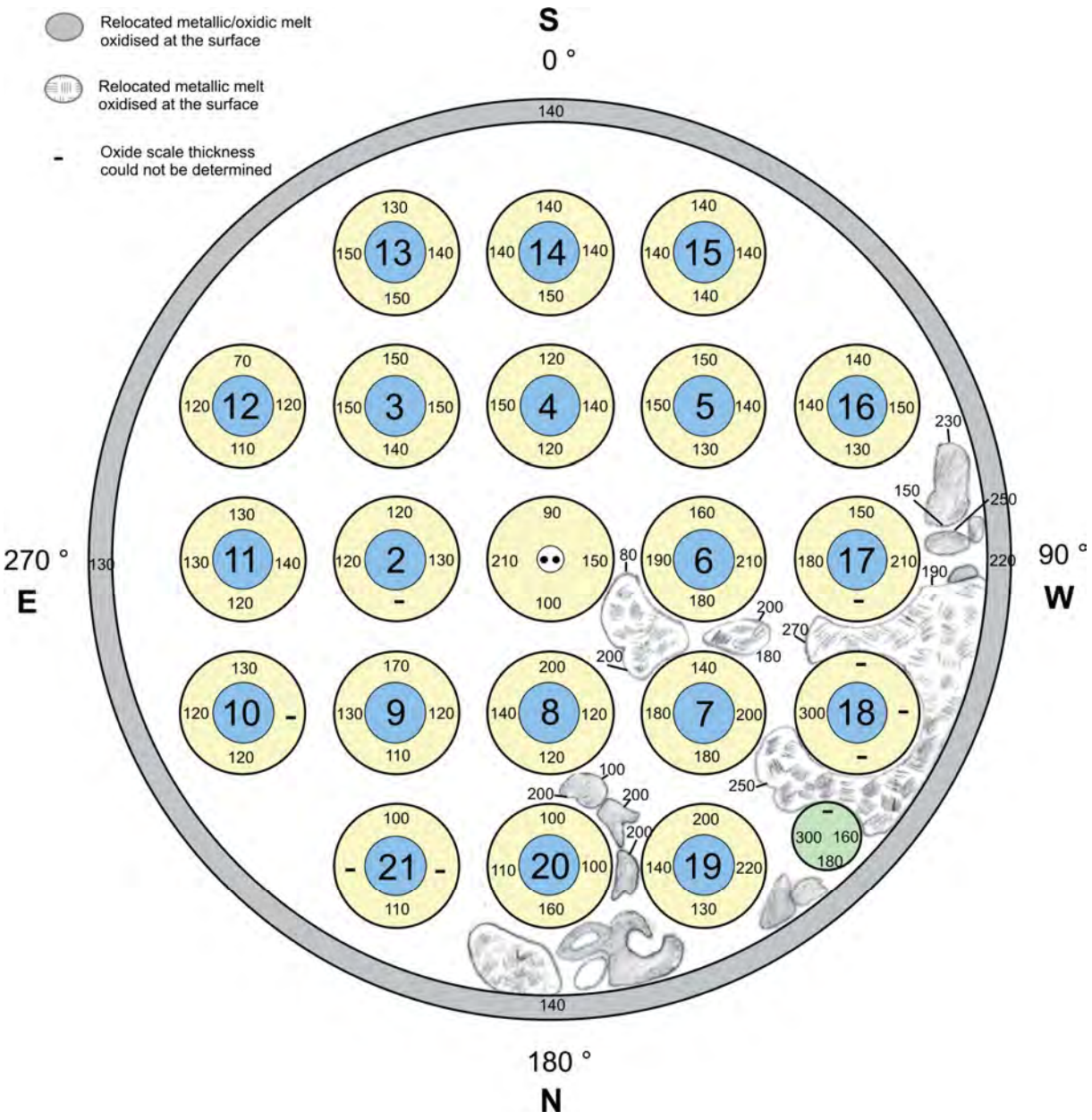

Fig.140: QUENCH-16; Oxide layer thickness at bundle elevation 350 mm (Cross section QUE 16-3-350).

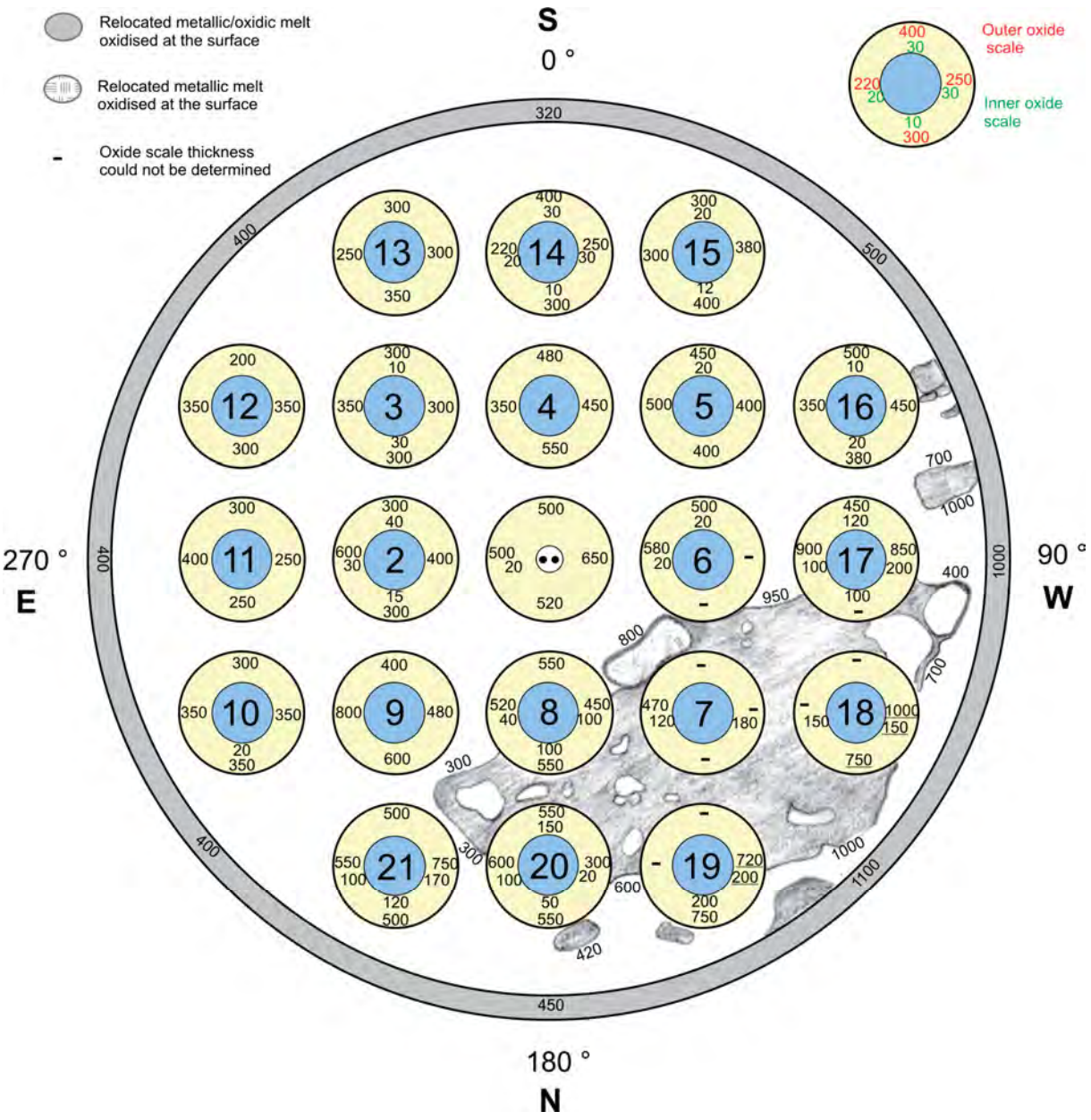

Fig.141: QUENCH-16; Oxide layer thickness at bundle elevation 450 mm (Cross section QUE 16-4-450).

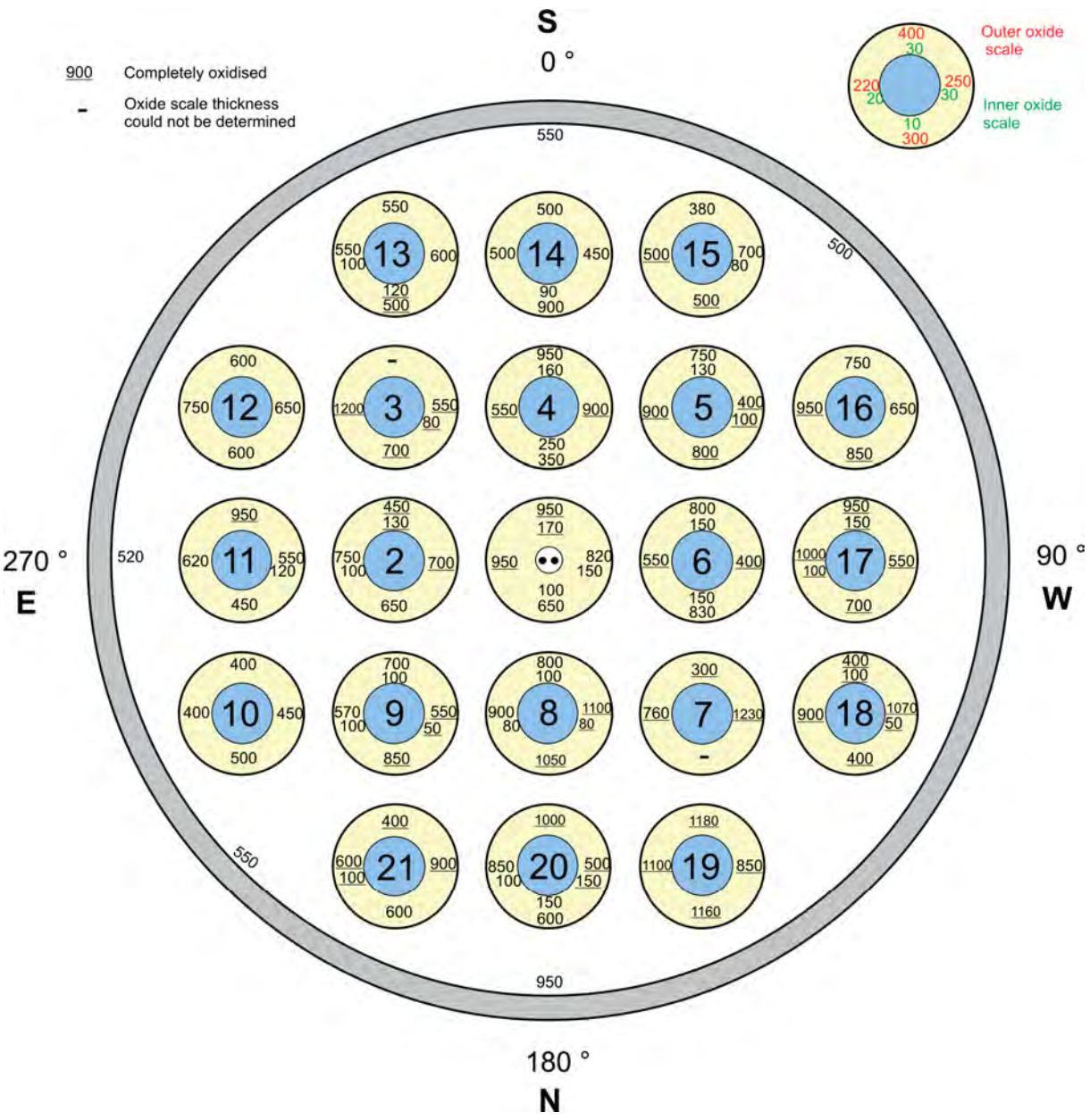

Fig.142: QUENCH-16; Oxide layer thickness at bundle elevation 550 mm (Cross section QUE 16-5-550).

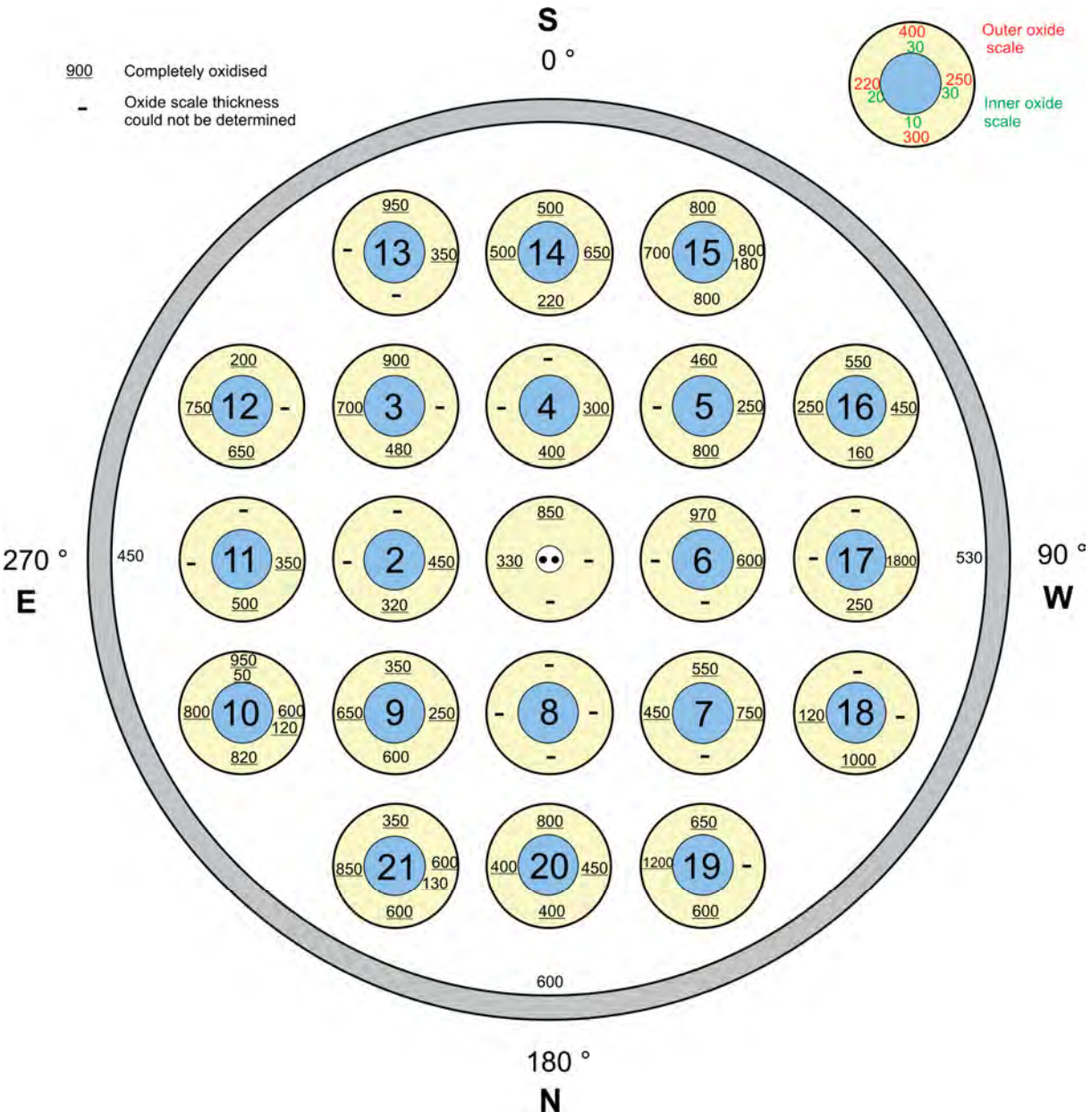

Fig.143: QUENCH-16; Oxide layer thickness at bundle elevation 650 mm (Cross section QUE 16-6-650).

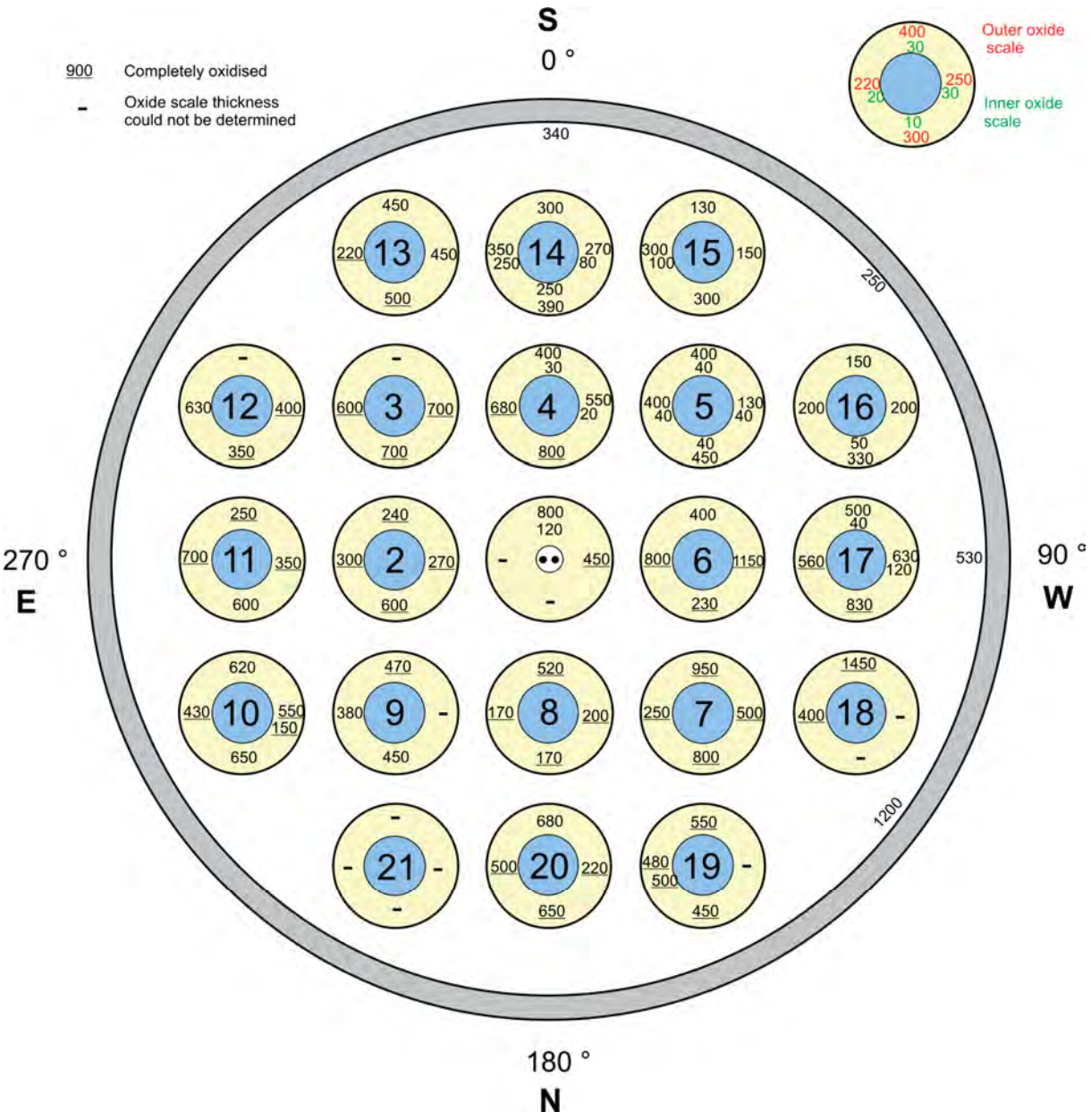

Fig.144: QUENCH-16; Oxide layer thickness at bundle elevation 750 mm (Cross section QUE 16-7-750).

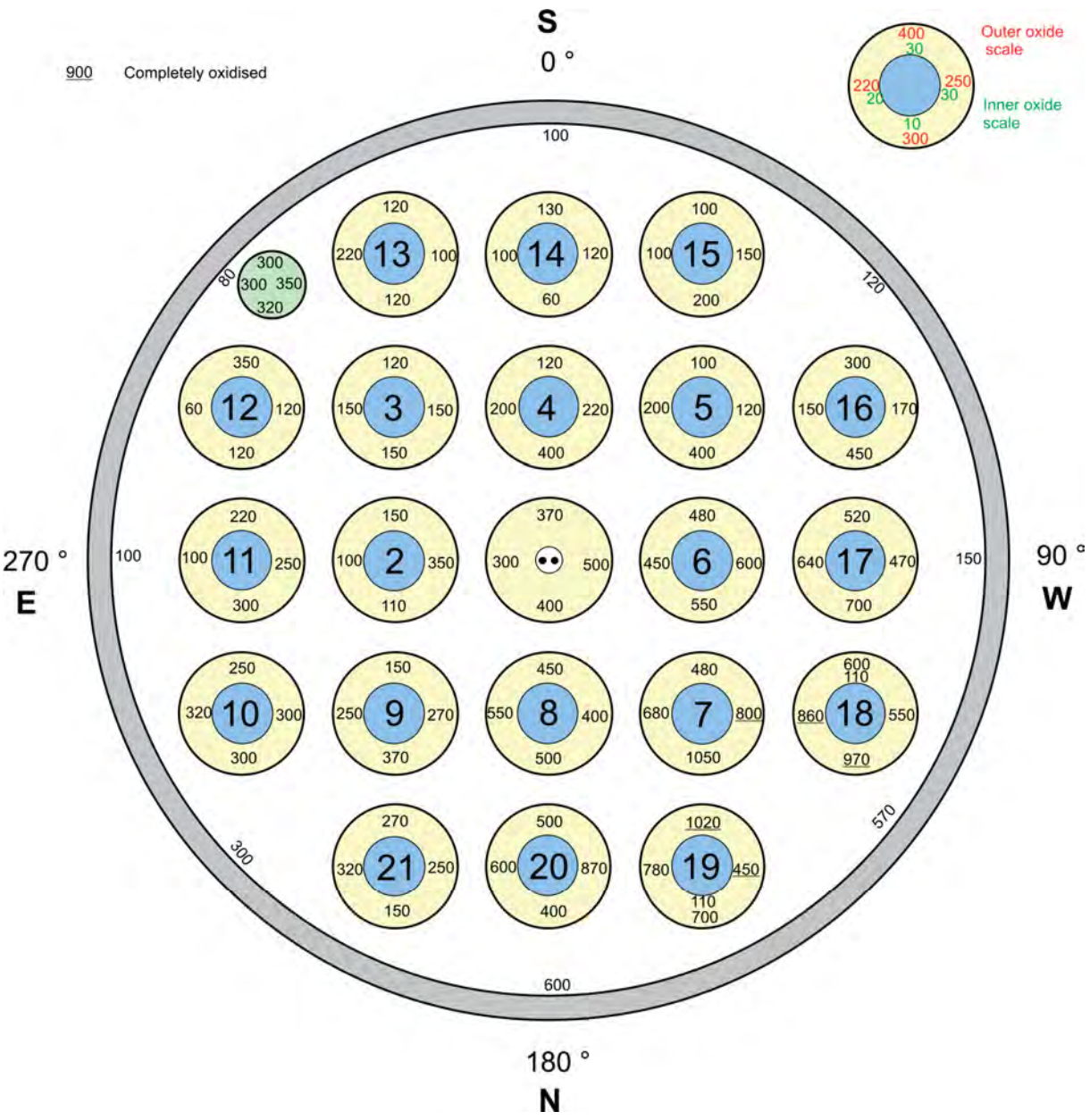

Fig.145: QUENCH-16; Oxide layer thickness at bundle elevation 850 mm (Cross section QUE 16-8-850).

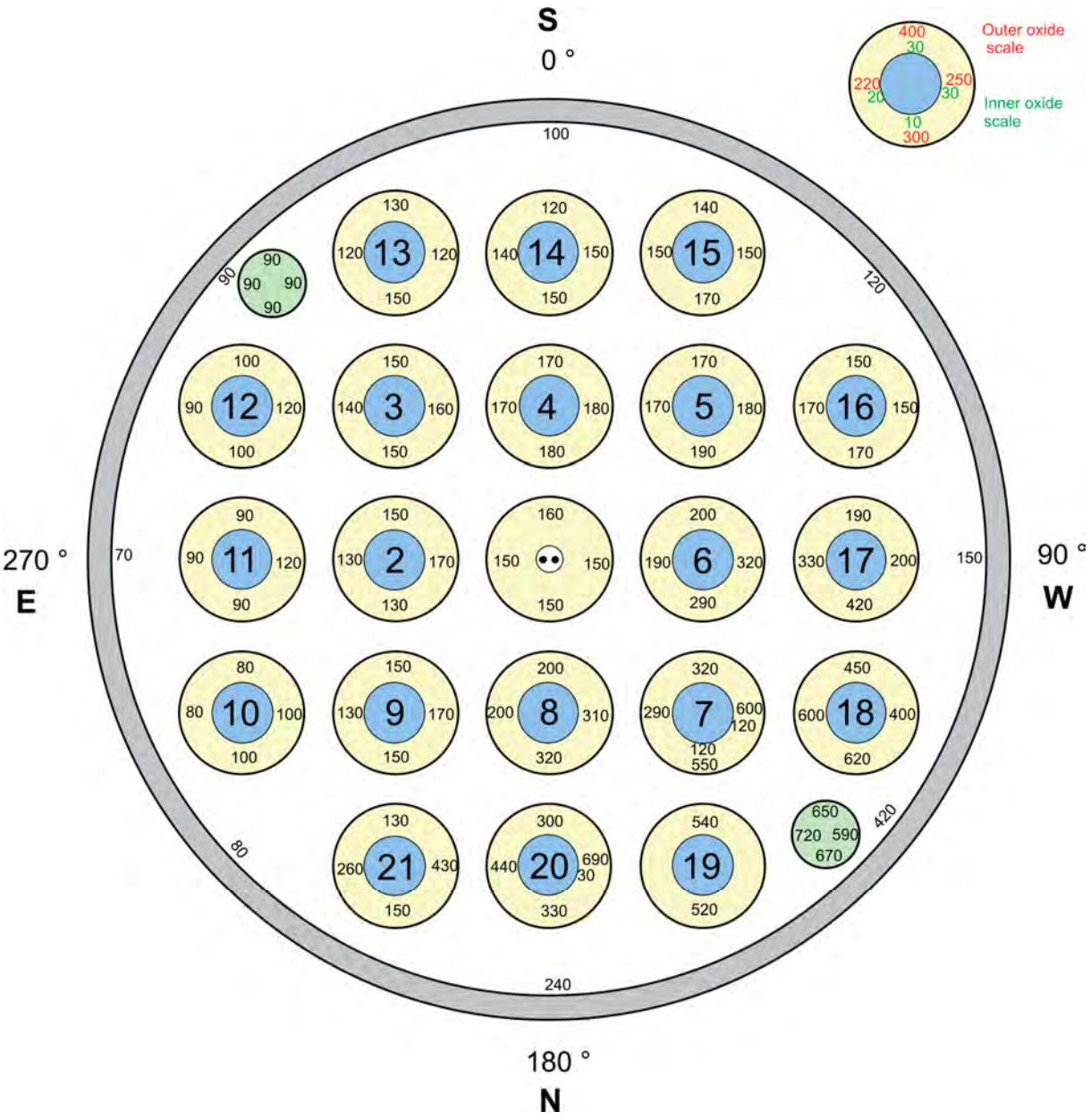

Fig.146: QUENCH-16; Oxide layer thickness at bundle elevation 950 mm (Cross section QUE 16-9-950).

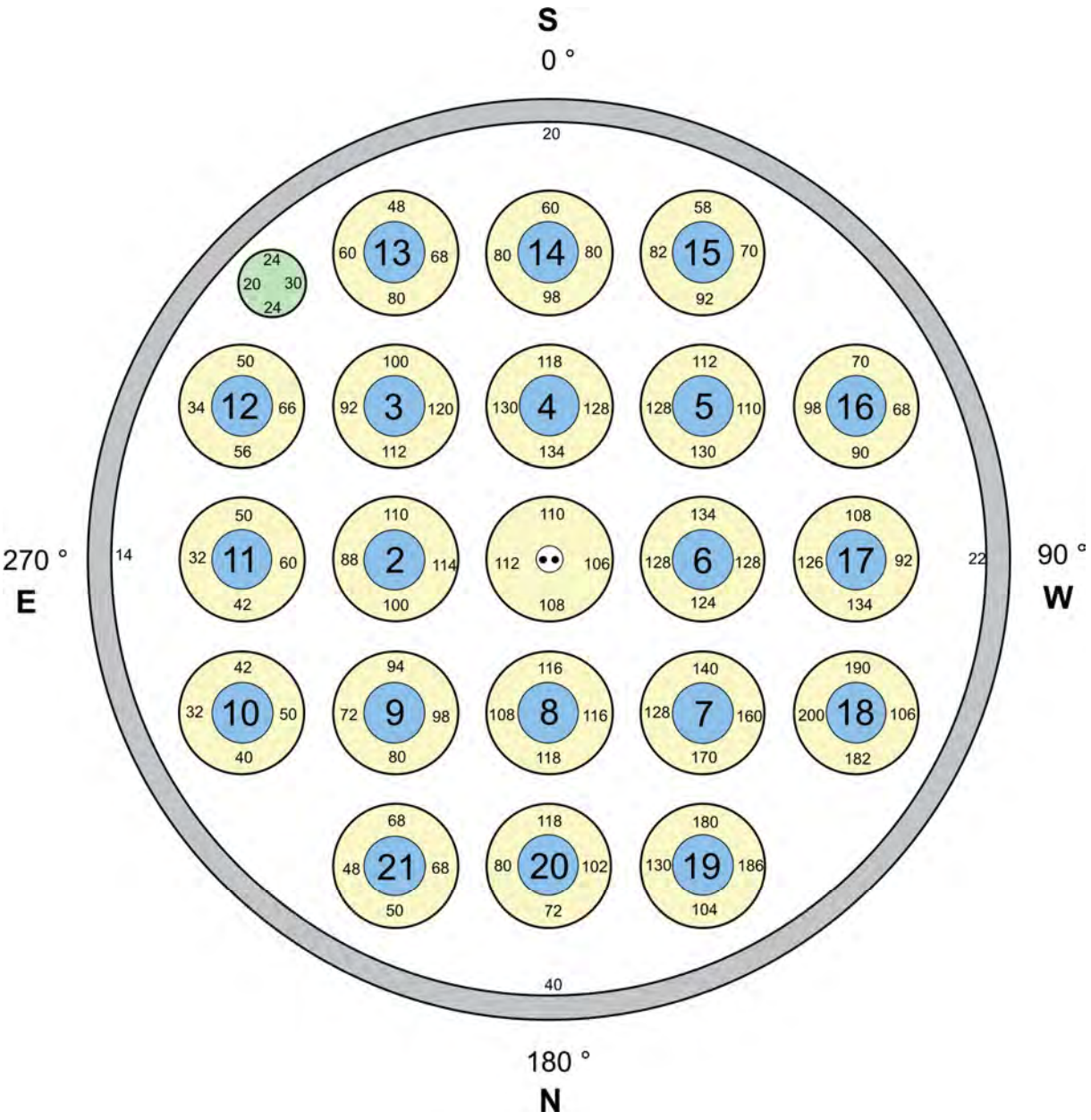

Fig.147: QUENCH-16; Oxide layer thickness at bundle elevation 1050 mm (Cross section QUE 16-10-1050).

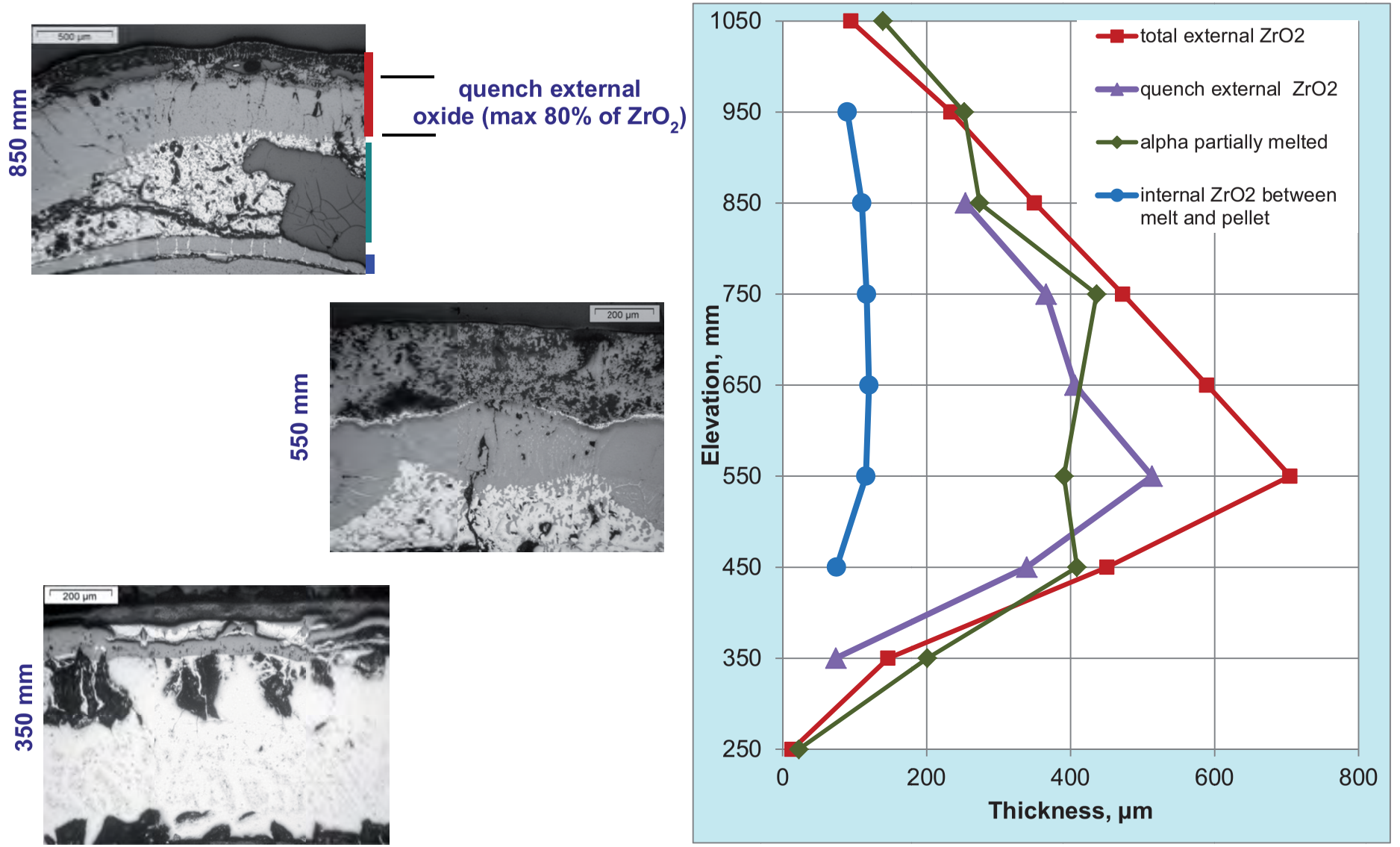

Fig.148: QUENCH-16; axial distribution of cladding oxidation rate.

Air ingress issues have received considerable attention in recent years in view of the likely acceleration of the cladding oxidation, fuel rod degradation, and the release of some fission products, most notable ruthenium. The accident at Fukushima Daiichi drew attention to the possibility of overheated fuel assemblies becoming exposed to air outside of the reactor.

Experimental and analytical works on air ingress were performed within the EC 4th and 6th Framework Programs. A number of previous out-of-pile bundle air ingress tests have been performed under a range of configurations and oxidizing conditions, namely CODEX AIT-1, AIT-2 with small 9-rod bundles, QUENCH-10 with 21-rod strong preoxidized bundle and PARAMETER-SF4 with finally molten 19-rod bundle. The accumulated data have demonstrated that air oxidation of cladding is a quite complicated phenomenon governed by numerous processes whose role can depend on the oxidizing conditions, the oxidation history and the details of the cladding material specification. The models for air oxidation do not yet cover the whole range of representative conditions.

The out-of-pile bundle experiment QUENCH-16 on air ingress was conducted in the electrically heated 21-rod QUENCH facility at KIT in July 2011. It was performed in the framework of the EC supported LACOMECO program. The primary aims were to examine the oxidation of the Zircaloy-4 claddings in air following a limited pre-oxidation in steam, and to achieve a long period of oxygen starvation to promote interaction with the nitrogen. QUENCH-16 was thus a companion test to the earlier air ingress experiment, QUENCH-10, which was performed with strongly pre-oxidized bundle. Unlike QUENCH-10, significant temperature escalation and intensive hydrogen release were observed during the reflood phase. Three contributors for intensive hydrogen production during reflood were identified: (i) re-oxidation of nitrides, (ii) secondary oxidation of cladding metal by steam penetrated through the porous re-oxidized scales and (iii) melt oxidation.

ISSN 1869-9669
ISBN 978-3-7315-0008-7